

COUNTER FLOW SILICA-TITANIA PHOTOCATALYTIC REACTOR FOR THE  
SIMULTANEOUS TREATMENT OF AIR AND WATER CONTAMINATED WITH  
VOLATILE ORGANIC COMPOUNDS

By

CHRISTINA AKLY

A DISSERTATION PRESENTED TO THE GRADUATE SCHOOL  
OF THE UNIVERSITY OF FLORIDA IN PARTIAL FULFILLMENT  
OF THE REQUIREMENTS FOR THE DEGREE OF  
DOCTOR OF PHILOSOPHY

UNIVERSITY OF FLORIDA

2009

© 2009 Christina Akly

To my parents, Bethsy and Salomon

## ACKNOWLEDGMENTS

I would like to thank Dr. Paul A. Chadik, my committee chair and advisor. If I had to name one person from whom I have learned the most about engineering and scientific research, he would be that person. His teaching has always been challenging, his guidance and support has always gone beyond expectations and his advice has always encouraged me to go the extra mile. I would like to thank both Dr. Chadik and Dr. David Mazyck for encouraging me to pursue a doctorate degree. Without their advice and support, I probably would have not followed this path, which has been an incredibly rewarding learning experience. I am also thankful to my other advisory committee members, Dr. Chang-Yu Wu and Dr. Spyros Svoronos for their guidance and suggestions during the completion of this work. I attribute my success to the many teachers I have learned from throughout my years at the University of Florida.

I would like to thank some of my fellow researchers at the Environmental Engineering Department in UF for providing advice, lab support and in general good research discussions that have significantly contributed to the progress of my work: Mauricio Arias, Felipe Behrens, Gordon Brown, Heather Byrne, Tim English, Heather Fitzpatrick, Beau Kosted, Jennifer Stokke, and Mike Witwer. Also, I would like to give special thanks to Dr. Hwidong Kim at UF and Rick Loftis at Mazyck Technology Solutions for providing analytical support. They have always gone out of their way to teach me and help me out with the GC, so I am grateful for their time and patience. Randy Switt and Dr. Ben Koopman provided important advice related to my model, so I am grateful for their help. Very importantly, I would like to thank my family for their unconditional love and support, especially my father who is has always encouraged me to follow my dreams, my friends for their continuous support, even from many miles away; my fiancé, Gordon, for always being there for me. Thank you all for listening and being there.

## TABLE OF CONTENTS

|   | <u>page</u> |
|---|-------------|
| ACKNOWLEDGMENTS.....  | 4           |
| LIST OF TABLES.....   | 8           |
| LIST OF FIGURES.....  | 10          |
| ABSTRACT .....  | 15          |
| <b>CHAPTER</b>  |             |
| 1    INTRODUCTION .....   | 17          |
| 2    LITERATURE REVIEW .....  | 23          |
| Heterogeneous Photocatalysis.....   | 23          |
| Titanium Dioxide as Catalyst .....  | 26          |
| Catalyst Support: Silica-Titania Composites.....  | 28          |
| Photocatalysis of Organic Compounds with TiO <sub>2</sub> .....   | 33          |
| Photocatalytic Oxidation (PCO) of Toluene with TiO <sub>2</sub> : Mechanisms and Intermediate Formation ..... | 36          |
| Gaseous and Aqueous Phase Toluene Kinetics.....   | 42          |
| Effect of Initial Concentration .....   | 47          |
| Effect of Light Intensity .....   | 48          |
| Effect of Superficial Velocity .....  | 49          |
| Effect of Temperature.....  | 49          |
| Effect of Relative Humidity.....  | 50          |
| Mass Transfer .....   | 51          |
| Equilibrium Partitioning of Volatile Organic Compounds between Air and Water .....                            | 51          |
| Mass Transfer Principles .....  | 52          |
| Mass Transfer Operations: Packed Tower Aerator (PTA) .....  | 54          |
| 3    MATERIALS AND METHODS .....  | 63          |
| Pilot-Scale Reactor: Two-Phase Photocatalytic Oxidation Tower (TPOT) .....                                    | 63          |
| Bench-Scale Reactor for Gas Phase Studies.....  | 65          |
| UV Irradiance Distribution in the Reactor.....  | 67          |
| Synthesis of the Silica-Titania Composites (STCs) .....   | 71          |
| Characterization of the STCs.....   | 72          |
| Analytical Methods for Toluene and Oxidation Byproducts .....   | 74          |
| 4    CHARACTERIZATION OF SILICA-TITANIA COMPOSITES .....  | 88          |
| 5    GAS PHASE TOLUENE DEGRADATION STUDIES.....   | 93          |

|   |            |
|---|------------|
| Bench-Scale Studies.....  | 93         |
| Gas Phase Toluene Studies Using Dry STCs.....   | 93         |
| Adsorption of toluene in a packed bed reactor .....   | 93         |
| PCO of toluene: Effect of water vapor .....   | 94         |
| PCO of toluene: Effect of space time ( $\tau$ ).....  | 95         |
| Kinetic analysis .....  | 96         |
| Gas Phase Toluene Studies Using Wetted STCs.....  | 100        |
| Toluene adsorption in a batch reactor .....   | 100        |
| Toluene adsorption in a continuous flow packed-bed reactor.....                                     | 102        |
| Pilot-Scale Studies .....   | 103        |
| Toluene Adsorption Using TPOT .....   | 104        |
| Adsorption of toluene using dry STCs.....   | 104        |
| Adsorption of toluene using wetted STCs .....   | 105        |
| Toluene PCO Using TPOT .....  | 106        |
| PCO of toluene using dry STCs .....   | 106        |
| PCO of toluene using wetted STCs.....   | 109        |
| <b>6 AQUEOUS PHASE TOLUENE DEGRADATION STUDIES .....</b>  | <b>121</b> |
| Bench-Scale Studies.....  | 121        |
| Pilot-Scale Studies .....   | 123        |
| Adsorption of Toluene Using TPOT .....  | 123        |
| PCO of Toluene Using TPOT .....   | 124        |
| TPOT Hydrodynamics .....  | 124        |
| Liquid-Solid Mass Transfer Coefficient ( $K_{LSaC}$ ) .....   | 130        |
| <b>7 SIMULTANEOUS GAS AND AQUEOUS PHASE TOLUENE DEGRADATION USING THE PILOT-SCALE REACTOR .....</b> | <b>143</b> |
| Gas-Liquid Mass Transfer Coefficient ( $K_{GLa_w}$ ) .....  | 143        |
| Simultaneous Two-Phase Degradation Studies.....   | 147        |
| <b>8 MATHEMATICAL MODELING AND SIMULATION OF THE TPOT .....</b>                                     | <b>165</b> |
| Model Development.....  | 165        |
| Model Simulation.....   | 169        |
| Effects of Operating Parameters on the TPOT Performance .....                                       | 171        |
| <b>9 CONCLUSIONS .....</b>  | <b>184</b> |
| <b>APPENDIX</b>   |            |
| <b>A PRELIMINARY STUDIES .....</b>  | <b>189</b> |
| Studies on System's Integrity .....   | 189        |
| System Losses .....   | 189        |
| Losses Due to Photolysis.....   | 189        |

|  |            |
|--|------------|
| Stripping.....   | 190        |
| Absorption .....                                       | 192        |
| <b>B ASSESSMENT OF LEACHING OF NANOMATERIALS .....</b> | <b>197</b> |
| <b>LIST OF REFERENCES .....</b>                        | <b>200</b> |
| <b>BIOGRAPHICAL SKETCH .....</b>                       | <b>208</b> |

## LIST OF TABLES

| <u>Table</u> |  | <u>page</u> |
|--------------|--|-------------|
| 2-1          | Oxidation power of various species commonly used in treatment applications .....   | 59          |
| 2-2          | Properties of Degussa P25 .....  | 60          |
| 3-1          | Calculated average UV intensity through the commingled packing at different annuli distances from the UV lamps. ....                             | 77          |
| 3-2          | Chemicals used in the STC formulation to produce one batch of 140Å STC with 30% by mass titania loading.....                                     | 77          |
| 3-3          | Conditions of the GC/MS and Purge & Trap used for the analysis of gas and aqueous phase toluene. ....  | 78          |
| 4-1          | Properties of STCs .....   | 90          |
| 4-2          | Phosphorus content from ICP – AES results and accessible TiO <sub>2</sub> surface area.....  | 90          |
| 5-1          | Summary of experimental conditions for the bench-scale gas phase PCO experiments using dry STCs .....  | 110         |
| 5-2          | Mears ( $C_M$ ) and Weisz-Prater ( $C_{WP}$ ) criteria for the determination of mass transfer influences. ....                                   | 110         |
| 5-3          | Experimental conditions for the adsorption experiments using dry STCs in the TPOT .  | 111         |
| 6-1          | Langmuir and Freundlich isotherms fitting parameters for the aqueous phase toluene adsorption data obtained in batch experiments. ....           | 134         |
| 6-2          | Mean residence time and dispersion coefficients for the high flow rings only packing and commingled packing obtained from the tracer tests. .... | 134         |
| 6-3          | Rate constants and Mears ( $C_M$ ) criterion for the determination of external mass transfer influences in the aqueous phase.. ....              | 135         |
| 6-4          | Experimental conditions for the aqueous phase PCO experiments in the TPOT. ....  | 135         |
| 7-1          | Individual and averaged properties for the two different packing materials used to pack the TPOT.....  | 153         |
| 7-2          | Summary of operational conditions and toluene removals for the simultaneous two-phase experiments. ....  | 153         |
| 8-1          | Summary of correlations used to determine the parameters involved in the solution to the differential equations developed to model the TPOT..... | 174         |

|     |   |     |
|-----|---|-----|
| 8-2 | Comparison of the actual net toluene removal to the net removal predicted by the two-phase model using different calibration methods.....                     | 175 |
| 8-3 | Comparison of the mass transfer coefficients calculated using the correlations developed for the aqueous phase and those found by calibrating the model. .... | 175 |
| 8-4 | Operating conditions selected for the simulation of the system's performance.....   | 175 |
| 8-5 | Reactor characteristics for the end polishing sections of the treatment system. ....  | 175 |

## LIST OF FIGURES

| <u>Figure</u> |  | <u>page</u> |
|---------------|--|-------------|
| 1-1           | Conceptual design of the photocatalytic system .....   | 22          |
| 2-1           | Energy band diagram of a spherical titania particle showing the basic reaction mechanism of TiO <sub>2</sub> photocatalysis.....                         | 60          |
| 2-2           | Structures and properties of rutile and anatase titanium dioxide .....   | 61          |
| 2-3           | Linkages of SiO <sub>2</sub> tetrahedras .....   | 61          |
| 2-4           | Silanol groups on the silica surface.....  | 62          |
| 2-5           | Diagram describing the equilibrium partitioning of a contaminant between the air and water phases using the two film theory. ....                        | 62          |
| 3-1           | CAD drawings of the reactor.....   | 78          |
| 3-2           | Dimensions of the TPOT reactor shown in horizontal configuration.....  | 79          |
| 3-3           | Picture of the two different packing materials that make up the commingled packing in the TPOT .....   | 79          |
| 3-4           | Photograph of the reactor (TPOT) during a typical experimental run.....  | 80          |
| 3-5           | Emission spectrum of UV-C lamps: A) ordinary and B) non-ozone producing UV-C lamps. ....   | 81          |
| 3-6           | Reactor setup for a typical experimental run.....  | 81          |
| 3-7           | Gas phase experimental setup and reactor.....  | 82          |
| 3-8           | UV irradiance as a function of lamp length measured in ambient air with the UV radiometer sensor placed at 0.95cm and 6.25 cm from the lamp.....         | 82          |
| 3-9           | Top view of the box setup used to measure the UV intensity as a function of different packing materials at different “X” distances from the lamp. ....   | 83          |
| 3-10          | UV irradiance as a function of distance to the lamp through ambient air using the set up of Figure 3-9 for different extents of reflective surfaces..... | 83          |
| 3-11          | UV intensity as a function of the distance from the UV lamp through different packing materials.....   | 84          |
| 3-12          | Enlarged version of Figure 3-11 .....  | 84          |

|      |  |     |
|------|--|-----|
| 3-13 | Actual placement of the five UV lamps inside the TPOT measured after packing the reactor with the commingled packing.....  | 85  |
| 3-14 | Fit of the data obtained for UV intensity through the commingled packing.....  | 85  |
| 3-15 | UV irradiance distribution inside the reactor.. .....  | 86  |
| 3-16 | Drying schedule for cylindrical STCs of 9 mm in diameter by 8 mm in height used to pack the TPOT.....  | 87  |
| 4-1  | Typical nitrogen adsorption/desorption isotherm for the STCs used to pack the pilot-scale reactor .....  | 91  |
| 4-2  | Typical pore size distributions of the STCs used to pack the pilot-scale reactor.....  | 91  |
| 4-3  | Comparison of the accessible titanium dioxide surface area for different STC shapes. ....  | 92  |
| 5-1  | Gas phase adsorption of toluene followed by PCO using dry STCs and low relative humidity conditions in the bench scale reactor .....                                 | 111 |
| 5-2  | Normalized effluent toluene concentration during simultaneous adsorption and PCO experiments at different water vapor concentrations as a function of run time ..... | 112 |
| 5-3  | Normalized effluent toluene concentrations as a function of run time at various space times .....  | 112 |
| 5-4  | Linear regression of the Langmuir-Hinshelwood model.....   | 113 |
| 5-5  | Plan view of the experimental setup of the batch experiments to assess adsorption under different STCs wetting conditions. ....                                      | 113 |
| 5-6  | Gas phase adsorption of water vapor and toluene to STCs under different wetting conditions.....  | 114 |
| 5-7  | Adsorption of gas phase toluene to STCs under different wetting conditions in a continuous flow reactor. ....  | 114 |
| 5-8  | Adsorption breakthrough curves for toluene on the dry STCs in the commingled packing of the pilot-scale reactor. ....  | 115 |
| 5-9  | Adsorption breakthrough curves for water vapor on the dry STCs in the commingled packing of the pilot-scale reactor. ....  | 115 |
| 5-10 | Comparison of gas phase toluene adsorption using the TPOT with dry versus pre-wetted STCs.....   | 116 |
| 5-11 | Adsorption of gas phase toluene followed by PCO in the TPOT using dry STCs and ambient relative humidity. ....   | 117 |

|      |   |     |
|------|---|-----|
| 5-12 | Conversion of toluene by PCO in TPOT for 3 studies performed using the same initial conditions: .....   | 118 |
| 5-13 | Conversion of gas phase toluene by PCO in the TPOT after catalyst regeneration. ....  | 118 |
| 5-14 | Water vapor concentration profile in the TPOT at various run times for the experiment corresponding to the 2 <sup>nd</sup> regeneration study.. ....  | 119 |
| 5-15 | Relative output of the UV-C lamps used in this research as a function of temperature..  | 120 |
| 5-16 | Effect of wetting of the packing on gas phase toluene removal by PCO in the TPOT. ..  | 120 |
| 6-1  | Removal of toluene due to adsorption in batch experiments as a function of STCs mass for different initial aqueous phase toluene concentrations.....  | 135 |
| 6-2  | Adsorption isotherm for the aqueous phase toluene – STCs system. ....   | 136 |
| 6-3  | Aqueous phase toluene adsorption for different liquid loading rates. ....   | 136 |
| 6-4  | Toluene removal as a function of inlet toluene concentration in the TPOT at a flowrate of 3.8 L/min. ....   | 137 |
| 6-5  | Aqueous phase toluene removal in the TPOT as a function of flowrate. ....   | 137 |
| 6-6  | Cumulative RTD ( $F(t)$ ) and RTD ( $E(t)$ ) functions obtained from the tracer test analysis for the TPOT at different flowrates and packed with different packing styles..  | 138 |
| 6-7  | Dispersion coefficients for the TPOT with commingled packing obtained from the tracer tests (data) and determined by the empirical correlation fitted to the data. ....   | 139 |
| 6-8  | Mean residence time as a function of liquid loading rate for the TPOT packed with the commingled packing.....   | 139 |
| 6-9  | Aqueous phase toluene concentrations predicted using the PFD model as a function of the depth of the packing for different liquid loading rates ( $L_m$ ).....  | 140 |
| 6-10 | Aqueous phase toluene concentrations predicted using the PFD model as a function of the depth of the packed tower for different initial toluene concentrations ( $C_{in}$ ).....  | 140 |
| 6-11 | Liquid-solid mass transfer coefficient as a function of the Reynolds number.....  | 141 |
| 6-12 | Liquid-solid mass transfer coefficient as a function of the inlet toluene concentration..   | 141 |
| 6-13 | Actual versus liquid-solid mass transfer coefficients calculated from the correlation in Equation 6-19 as a function of Re and $C_{IN}$ .....   | 142 |
| 7-1  | Comparison of the measured overall gas-liquid mass transfer coefficients to the coefficients predicted by the Onda correlation and by the Modified Onda correlation for different liquid flowrates and packing styles as a function of air to water ratio ..... | 154 |

|      |   |     |
|------|---|-----|
| 7-2  | Comparison of the predicted wetted surface area of the packing calculated using the Onda correlation and the Modified Onda correlation as a function of liquid flowrate for the tower packed with the commingled packing..... | 155 |
| 7-3  | Comparison of overall gas-liquid mass transfer coefficients for the tower packed with high flow rings only and the commingled packing as a function of air to water ratio for a liquid flowrate of 4.0 L/min.....             | 155 |
| 7-4  | Overall gas-liquid mass transfer coefficients as a function of air to water ratio for different liquid flowrates for the tower packed with commingled packing.....  | 156 |
| 7-5  | Effect of the liquid flowrate on $K_{GLa_w}$ for different gas flowrates for the tower packed with the commingled packing.....  | 156 |
| 7-6  | Comparison of actual saturation conditions in the reactor for the different experimental runs and the equilibrium concentrations predicted by the Henry's law.....  | 157 |
| 7-7  | Results for two-phase experiments using saturated conditions : Experiment (a) .....   | 158 |
| 7-8  | Results for two-phase experiments using saturated conditions : Experiment (b). ....   | 159 |
| 7-9  | Results for two-phase experiments using saturated conditions : Experiment (c) .....   | 160 |
| 7-10 | Results for two-phase experiments using saturated conditions : Experiment (d). ....   | 161 |
| 7-11 | Results for two-phase experiments using saturated conditions : Experiment (e) .....   | 162 |
| 7-12 | Results for two-phase experiments using undersaturated conditions : Experiment (f)...   | 163 |
| 7-13 | Comparison of the removal of toluene in the two-phase experiments to the expected removal in the aqueous phase only .....   | 164 |
| 8-1  | Schematics of the reactor and differential volume used to determine toluene's mass balance equations. ....  | 176 |
| 8-2  | Gas, liquid and solid phases resistances and concentration profiles in the TPOT.....  | 176 |
| 8-3  | Comparison of concentration profiles obtained from the model using the correlation derived for the aqueous phase (1) and the one fitted to the two-phase data (2).....  | 177 |
| 8-3  | Continued.....  | 178 |
| 8-4  | Effects of dispersion coefficient on the aqueous and gas phases profiles obtained from the models using the K's calculated from the correlations.....   | 179 |
| 8-5  | Actual net toluene removal versus the net removal predicted by the two-phase model using different mass transfer coefficients. ....   | 179 |

|      |   |     |
|------|---|-----|
| 8-6  | Concentration profile for toluene in the TPOT present in the gas and aqueous phases in the presence of PCO (UV lamps on) and due to mass transfer only (UV lamps off) ..... | 180 |
| 8-7  | Net toluene removal in the TPOT as a function of packed bed depth .....   | 180 |
| 8-8  | Complete treatment system showing the simulation results.....   | 181 |
| 8-9  | Effect of different operating parameters on the aqueous phase profile concentrations in the TPOT .....  | 182 |
| 8-10 | Effect of different operating parameters on the gas phase profile concentrations in the TPOT. ....  | 182 |
| 8-11 | Effect of different operating parameters on the net toluene conversion in the TPOT as a function of packed bed depth. ....  | 183 |
| A-1  | System losses in the gas phase due to potential leaks.....  | 193 |
| A-2  | System losses in the aqueous phase due to volatilization and/or leaks. ....   | 193 |
| A-3  | Photolysis of toluene in the gas phase. ....  | 194 |
| A-4  | Photolysis of toluene in the aqueous phase. ....  | 194 |
| A-5  | Toluene stripping in the TPOT packed with high flow rings only using the UV lamps off and on and having the air flow free of contaminant.....                               | 195 |
| A-6  | Toluene absorption in the TPOT packed with plastic high flow rings only and the water flow free of contaminants.....  | 196 |
| B-1  | Effects of the UV radiation on the leaching of silica and titania from the TPOT packing.....  | 198 |
| B-2  | Effect of the flowrate on the leaching of silica and titania from the packing on the TPOT.....  | 199 |
| B-3  | Leaching of silica and titania from the packing in the TPOT for several experiments performed at various dates.....   | 199 |

Abstract of Dissertation Presented to the Graduate School  
of the University of Florida in Partial Fulfillment of the  
Requirements for the Degree of Doctor of Philosophy

**COUNTER FLOW SILICA-TITANIA PHOTOCATALYTIC REACTOR FOR THE  
SIMULTANEOUS TREATMENT OF AIR AND WATER CONTAMINATED WITH  
VOLATILE ORGANIC COMPOUNDS**

By

Christina Akly

August 2009

Chair: Paul A. Chadik

Cochair: David W. Mazyck

Major: Environmental Engineering Sciences

The photocatalytic oxidation (PCO) of VOCs was investigated using a novel countercurrent flow reactor designed to enable the treatment of toluene present in the gas and the aqueous phases simultaneously. The reactor was packed with silica-titania composites (STCs) commingled with plastic high flow rings. Using this mixed packing style was advantageous as it resulted in a higher UV penetration throughout the reactor. The average UV intensity in the reactor was 220 uW/g irradiated titania.

Under dry conditions, the STCs had a high adsorption capacity for toluene; however, this adsorption was completely inhibited by the wetting of the STCs when the two phases were flowing simultaneously. The lack of adsorption hindered the PCO of toluene in the gas phase as it was found to be negligible during the two-phase operation.

Likewise, the adsorption of toluene in the aqueous phase was negligible likely due to the short mean residence time in the pilot reactor (< 60 s). However, the PCO of toluene in the aqueous phase linearly increased with concentration due to the larger driving force and decreased as function of liquid loading rate.

In the presence of both phases, toluene destruction was only observed under conditions in which the solution was initially supersaturated with respect to the gas phase. Under these conditions, the net destruction of toluene in the system reached a maximum of about 68%. For the most part, the destruction occurred in the aqueous phase, and it was observed that high gas phase flowrates could be detrimental to the toluene destruction in the two-phase reactor.

The reactor was modeled using a one dimensional plug flow with dispersion model for the aqueous phase and a plug flow model for the gas phase. The dispersion coefficient and gas-liquid and liquid-solid mass transfer coefficients were determined from correlations developed in this study. The model was calibrated using the two-phase experiments data by fitting the mass transfer coefficients. The mathematical model is a useful tool to simulate the reactor's performance for a given set of operating conditions and investigate the effects of the different variables on the net toluene conversion.

## CHAPTER 1

### INTRODUCTION

Many organic compounds are currently regulated by the Environmental Protection Agency (EPA) under the National Primary Drinking Water Regulations (NDWRs) due to the threat they pose to human health. Among these compounds are volatile organic compounds (VOCs), which cover a significant portion of these regulated organic chemicals. Many VOCs can be toxic to humans in both the air and the water phase and cause environmental problems. Some of the more alarming chronic effects from VOC exposure are the increased risk of cancer and problems with the nervous system, blood, liver, and kidney, among others. Some VOCs cause cancer in animals and some are suspected or known to cause cancer in humans such as benzene, trichloroethylene, vinyl chloride and carbon tetrachloride. Short term exposure to sufficiently high concentrations of these contaminants may cause fatigue, nausea, weakness, and confusion (USEPA, 2007a).

Environmentally, VOCs can be involved in the production of photochemical oxidants such as ozone which can be toxic to humans when present in the troposphere, they can be implicated in acid rain formation and even the depletion of stratospheric ozone (Japar et al, 1991; Cortese, 1990). Many VOCs are used as solvents for adhesives, and in the production of rubber, drugs, and paints. The majority of them are used in the production of other chemicals, and fewer are used as flocculants, gasoline additives, or insecticides. Their release to the environment is mostly through emissions and wastewater discharges by production and manufacturing facilities and spills. Since these compounds are very volatile, they will quickly partition to the gas phase, becoming an air pollution problem. Consequently, many of these compounds are also regulated under the Clean Air Act (CCA) and the Occupational Safety and Health Administration (OSHA) as air pollutants. When VOCs do not completely volatilize, they can reach groundwater by leaching through the soil where they may be anaerobically degraded; however, biodegradation is

usually slow. Toluene, one of the regulated VOCs, is the target compound for this research. Like other VOCs, it can potentially cause serious health effects from acute exposures at levels above the regulated maximum contaminant levels (MCL); in drinking water, the MCL is 1 mg/L while the air standards recommend a concentration below 300 µg/m<sup>3</sup> to prevent risk of adverse effects by inhalation (USEPA, 2007b; OEHHA, 2002).

VOCs regulations are becoming more stringent because of the increased awareness and evidence of the potential adverse effects from exposure to these contaminants. The Clean Air Act of 1990 for example, set the goal of reducing the emissions of 189 toxic chemicals over a period of 8 years, 70% of these chemicals being VOCs (Armor, 1992). In 1998, EPA issued a rule limiting VOC emissions from consumer products that requires many United States manufacturers, importers, and distributors to limit the VOC content of their products. In addition, another rule was issued limiting emissions from exterior and interior house paints, wood and roof coatings (USEPA, 2007c). As a result, these more rigorous regulations need to be addressed by improvements in treatment techniques. Conventional process for air and water treatment include phase transfer, chemical treatment using strong oxidizing agents such as chlorine, potassium permanganate, ozone, hydrogen peroxide and ultraviolet light, thermal and catalytic oxidation, and biological treatment. Such VOCs treatment technologies are currently implemented in potable water treatment plants, groundwater remediation systems, industrial facilities for both gas and aqueous phase emissions, spills, and indoor air pollution, to mention a few. All these traditional treatment processes have limitations of their own. For example, phase transfer methods such as stripping, absorption and adsorption, remove undesired contaminants from one phase but transfer them to another without elimination of the problem. Biological treatments that transform the VOCs can only be applied under very specific conditions because of the sensitivity

of microorganisms to undesired toxic compounds. The oxidation methods use either strong oxidants that present serious hazards during practical applications or high energy intensive UV light. Some of the newest technologies investigated for the removal of VOCs are advanced oxidation processes (AOP) involving a solid phase catalyst. These processes are usually preferred over conventional VOCs treatment technologies because they completely oxidized the contaminants to carbon dioxide and water. One of the AOPs that have shown promising results is heterogeneous photocatalysis with titanium dioxide ( $\text{TiO}_2$ ). There is a vast research literature database on the removal of VOCs using  $\text{TiO}_2$ . The results have shown this technology to be effective at completely oxidizing the target contaminants from the gaseous phase and at a slower rate from the aqueous phase. Despite its potential, the feasibility for implementing this technology in large scale systems, particularly those that treat both air and water phases, has not been successfully demonstrated. The research efforts have aimed at two major issues concerning photocatalysis with  $\text{TiO}_2$ : (1) the identification of reaction intermediates, detailed reaction mechanisms, and reaction kinetics; and (2) the optimization of reaction conditions to enhance the photoreaction rate and yield. These issues, which are key factors to large scale implementation, have been broadly investigated; however, they have not been yet resolved.

In addition to the lack of evidence supporting the intrinsic mechanisms and kinetics of VOCs reactions on the catalyst surface, a full size practical reactor configuration and catalyst support for such reactor to implement this technology have not been developed. The reactor needs to be both efficient at achieving the required removal and cost effective compared to currently available technologies. Several factors have impeded the design of effective photocatalytic reactors. Since heterogeneous photocatalysis requires light irradiation to initiate the reactions, sufficient illumination distribution inside the reactor that will activate most of the

catalyst is of utmost importance. Another barrier to the development of the photocatalytic reactor is the incorporation of the catalyst inside the reactor. Several configurations have been used in lab-scale experiments, but most of them are usually inconvenient and expensive when considered for large scale systems. Finally, the reactor has to be able to handle fluctuations in flowrates and concentrations that are typical in full-scale applications (Ray, 1999).

In this work, silica-titania composites capable of simultaneous adsorption and photocatalytic destruction of organic compounds were developed and used in a specially-designed counter-flow packed bed reactor capable of treating both the gas and aqueous phase of the desired contaminant. Toluene was the target volatile organic compound commonly found as a water and air contaminant. The proposed technology can handle the air emissions and contaminated water within one reactor. The overall proposed system, shown in Figure 1-1, consists of three treatment stages. Given that using a countercurrent flow configuration with both streams being contaminated could cause the undesired transfer of contaminants at both ends of the tower where treated streams meet the contaminated ones, two additional packed sections were included in the final system. The concentrations exiting both ends of the tower were expected to be very low. Therefore, treating these trace level contaminants should required smaller size packed beds. Additionally, since these polishing sections would be treating only one phase of the contaminants, they would be packed only with the silica-titania composites (STC). This part of the system was not be a priority in this research because the treatment of single phase organic contaminants in air or water using STCs has already been proven feasible by other researchers (Holmes et al., 2004; Londeree, 2002; Ludwing, 2004; Pintioniak et al., 2003; Stokke et al., 2006). Therefore, most of the efforts in this work focused on investigating the mechanisms on the section where the two contaminant phases were treated together.

The objectives of this research were the following:

1. Design and optimize the performance of a countercurrent flow reactor packed with engineered silica-titania composites to enable the simultaneous treatment of gas phase and aqueous phase VOCs, using toluene as the target compound.
2. Determine the main factors that affect the toluene removal efficiency (eg. residence time, water vapor concentration, mass transfer, influent contaminant concentration, etc.) in the gas and aqueous phases separately.
3. Determine the main operating factors that affect the toluene removal efficiency (eg. residence time, air to water ratio, inlet gas and aqueous phase concentrations, etc.) in the gas and aqueous phases simultaneously.
4. Investigate the effect of the simultaneous two-phase flow in the individual adsorption and photocatalytic efficiencies of the two fluid phases.
5. Determine the effect of the commingled packing on the overall UV distribution in the reactor.
6. Investigate the presence of potential byproducts in the effluent flows and adsorbed to the catalyst surface.
7. Determine the overall mass transfer coefficient, gas-liquid and liquid-solid, for the commingled packing in the reactor and compare it to known mass transfer correlations.
8. Model the reactor mathematically by using operating parameters as the main inputs and calibrate the model using collected data for toluene

The following hypotheses were investigated in this research:

1. The removal of aqueous phase VOCs will be enhanced in the presence of the air stream in the proposed countercurrent flow reactor configuration.
2. The UV light distribution will be improved by the use of the commingled packing.
3. The expected presence of a liquid film around the catalyst pellets during the removal of gas-phase VOCs will hinder the adsorption of toluene on the STC. However, decreased adsorption will not result in decreased photocatalysis of toluene in the gas phase, since the reaction can still occur in the bulk air.
4. The photocatalytic oxidation mechanism for the destruction of VOCs involves the hydroxyl radical attack using the abundant O<sub>2</sub> as the scavenger specie since water is pre-adsorbed to the catalyst and continuously supplied in the system together with air.

- Despite the short retention time, the contaminants will be completely mineralize to  $\text{CO}_2$  and water due to excess hydroxyl radical, so no byproducts other than  $\text{CO}_2$  will be present in the effluent streams
- Deactivation of the catalyst can be overcome using the two-phase system configuration.

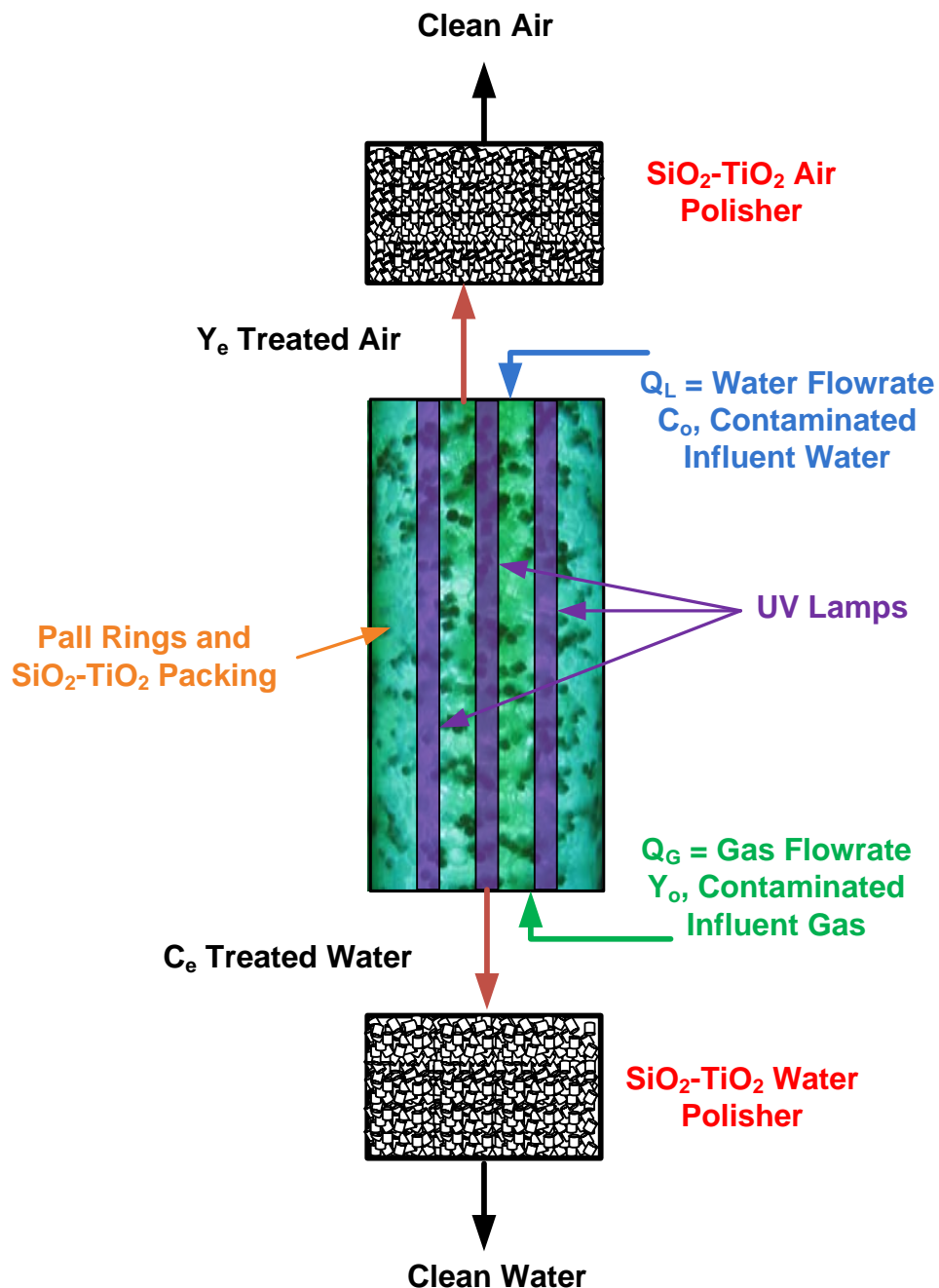


Figure 1-1. Conceptual design of the photocatalytic system

## CHAPTER 2

### LITERATURE REVIEW

#### **Heterogeneous Photocatalysis**

In heterogeneous photocatalysis, photoinduced reactions take place on the surface of the catalyst while the catalyst remains intact. Interest in heterogeneous photocatalysis started with the discovery of the photocatalytic splitting of water by Fujishima and Honda in 1972. Semiconductors have been widely studied because of their application in photocatalysis. They can act as sensitizers due to their electronic structure. Different from metals, semiconductors possess a band gap, which is a void energy region where no energy levels are available to promote recombination of the electron and hole produced by photoactivation in the solid. The band gap extends from the filled valence band (VB) to the vacant conduction band (CB). Semiconductor photocatalysis can be more appealing than conventional oxidation methods because semiconductors are usually inexpensive, nontoxic, and capable of extended use without substantial loss of photocatalytic activity. One of the most commonly used semiconductors in environmental applications with sufficient band-gap energy to catalyze different chemical reactions is titanium dioxide ( $\text{TiO}_2$ ). The band gap energy for  $\text{TiO}_2$  is 3.2 eV compared to the normal hydrogen electrode (NHE) (Hoffmann et al., 1995).

The initial process in heterogeneous photocatalysis, presented in Equation 2-1, is the generation of electron-hole pairs in the semiconductor particles by the excitation of an electron with photons of energy,  $h\nu$ , greater than the bandgap energy ( $h\nu > 3.2 \text{ eV}$  or  $\lambda < 388 \text{ nm}$  for  $\text{TiO}_2$ ). In this process, an electron from the CB ( $e_{\text{CB}}^-$ ) is promoted to the VB, creating a hole in the VB ( $h_{\text{VB}}^+$ ). The electron in the CB can act as a reductant while the hole in the VB acts as oxidant (Linsebigler et al., 1995). This photoexcitation process is shown in Figure 1-1.



Upon excitation, the electron and hole can follow different pathways (Linsebigler et al., 1995, Hoffmann et al., 1995, Herrmann et al., 2005):

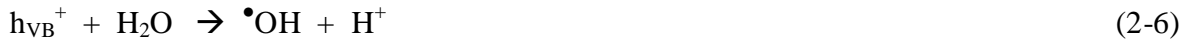
**Bulk Recombination:** Some of the electron hole pairs generated may recombine within the volume or on the surface of the semiconductor dissipating the input energy as heat.



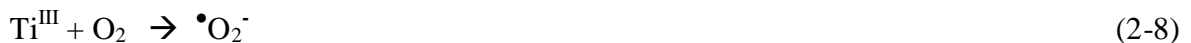
**Surface Recombination:** There is a high probability that the electron-hole pairs which migrate to the surface may recombine with species such as hydroxyl ions ( $OH^-$ ) and hydroxyl radicals ( $\cdot OH$ ), thus limiting the efficiency of photocatalysis.



**Surface Trapping:** The electron hole pairs, which migrate to the surface of the catalyst, are trapped and form primary hydroxyl radicals. Additionally, the electron can get trapped irreversibly to form  $Ti^{3+}$  defects.



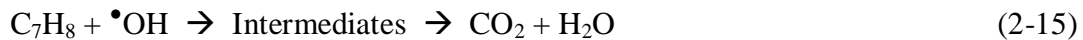
**Electron Scavenging:** Oxygen ( $O_2$ ) scavenges the conduction band electrons through the following consecutive reactions to form multiple peroxide radicals.



**Interfacial Charge Transfer and Back Reactions:** Some of the radicals as generated above may recombine at the surface of titanium dioxide through a multi-step charge transfer reaction. These back reactions are simply an electron transfer between the surface radicals and the titanium dioxide surface. The back reactions become important when these reactive radicals are trapped near the catalyst surface.



**Degradation:** The highly reactive radicals that escape the back reactions lead to complete degradation of the organic (or inorganic) compound, either by initiating an oxidation or reduction pathway. For example,



The efficiency of photocatalysis can be measured by the number of events occurring per photon absorbed, which is known as the quantum yield. Since measuring the light absorbed in a photocatalytic process is very difficult, it is assumed that all light is absorbed, and the resulting value is defined as the apparent quantum yield. The quantum yield ( $\Phi$ ) can be described by the relationship given in Equation 2-16:

$$\Phi \propto k_{CT} / (k_{CT} + k_R) \quad (2-16)$$

where  $k_{CT}$  is the rate of the charge transfer process and  $k_R$  is the rate of the hole recombination (Linsebigler et al., 1995). For an ideal system, the quantum yield would be equal to 1 (rate of hole recombination is either zero or negligible). However, the efficiency of the photocatalytic processes decreases by the recombination of the electron and hole. This recombination process can be retarded by promoting electron and hole traps in the system, either as electron acceptor or

donor species or as catalyst surface defects. During catalyst preparation, ideal semiconductors' crystal lattices are not always produced resulting in natural surface and bulk irregularities. These defects are associated with surface electron states which differ in their energy from the bands present in the bulk semiconductor and serve as charge carrier traps that help suppress electron-hole recombination. Hindering such recombination increases the probability for oxidation and reduction processes to take place, hence increasing the efficiency of photocatalysis. (Fox and Dulay, 1993).

### **Titanium Dioxide as Catalyst**

By far,  $\text{TiO}_2$  is the most used photocatalyst for air and water treatment applications. This semiconductor is preferred among others because it is chemically and biologically inert; and thus, it does not undergo photo or chemical corrosion. It is also inexpensive when compared to other available catalysts. The photogenerated holes are highly oxidizing while the photogenerated electrons are sufficiently reducing to produce superoxide from dioxygen. After reaction with water, the holes can produce hydroxyl radicals. The hydroxyl radical oxidation potential is more positive than that for ozone (See Table 2-1). The reduction potential for conduction band electrons is in principle negative enough to evolve hydrogen from water, though the electrons can become trapped and lose some of their reducing power (Fox and Dulay, 1993).

Two different crystal structures of  $\text{TiO}_2$ , rutile and anatase, are commonly used in photocatalysis. Of these two forms, anatase shows the higher photocatalytic activity. The structures of rutile and anatase  $\text{TiO}_2$  are shown in Figure 2-2. Both structures consist of titanium ( $\text{Ti}^{4+}$ ) atoms surrounded by six oxygen ( $\text{O}^{2-}$ ) atoms forming an octahedron. The differences between the two crystal structures are the distortion of each octahedron and the assembly pattern of the octahedra chains. The Ti-Ti distances in anatase are greater whereas the Ti-O distances are shorter than in rutile. Additionally, the rutile octahedron is connected to 10 neighboring oxygen

atoms while the anatase structure is in contact with only eight. These structural differences are responsible for the differences in their band electronic structures and mass densities (Linsebigler et al., 1995).

Of the commercially available titanium dioxides, Degussa's P25 is the most researched for its photocatalytic ability. Table 2-2 shows some of the physico-chemical characteristics of Degussa P25. Commercial P25 is produced from high-temperature flame hydrolysis of  $\text{TiCl}_4$  in the presence of oxygen and hydrogen followed by a steam treatment to remove HCl. The resulting product is a catalyst consisting of 70% anatase and 30% rutile phases of  $\text{TiO}_2$  (Degussa Technical Bulletin, 1990). The anatase phase of  $\text{TiO}_2$  is considered the more photoreactive of the two. The difference in reactivity of the phases is attributed to: (1) the more positive conduction band of the rutile phase that can prevent molecular oxygen from acting as an electron acceptor, and (2) the difference in surface properties between the two phases (Tanaka et al., 1991). Tanaka et al. (1991) showed that the photocatalytic ability of a  $\text{TiO}_2$  catalyst is foremost affected by the anatase content and secondarily affected by the size of the crystal. Under equal percentages of anatase phase, a  $\text{TiO}_2$  catalyst containing larger crystals is more efficient than one with smaller crystals. This could be due to the larger migration distance of the holes and electrons to the surface of the catalyst, thereby decreasing the possibility of recombination (Tanaka et al., 1991). Furthermore,  $\text{TiO}_2$  in the form of pure anatase might be deactivated to a lesser extent than the combined phase  $\text{TiO}_2$  for some organic compounds. Marci et al. (2003), for example, showed that when using a titanium dioxide catalyst made of 100% anatase phase no deactivation of the catalyst was encountered. However, when Degussa P25 was used under the same conditions, the catalyst was completely deactivated after 20 h of operation. The types of byproducts found in the

photooxidation of organic chemicals might be also influence by the type of TiO<sub>2</sub> phase used for the reactions (Marci et al., 2003).

### **Catalyst Support: Silica-Titania Composites**

Nanosized titania particles come in the form of a very fine white powder, so developing practical catalyst supports is a challenge for the application in TiO<sub>2</sub> photocatalytic systems. Common methods of implementing this catalyst in gas phase reactors treating VOCs include depositing the titania on substrate particles for packed beds (Kobayakawa et. al., 1998) or on reactor tube walls as a thin film (Maira et. al., 2001). Both of these options can be disadvantageous to the photocatalytic process because in the first case, there is only an effective thin layer exposed to the light, and in the second case, the immobilization of titania particles on tube walls limits the mass transfer. Furthermore, tube wall films do not always provide homogenous coating, and there is a high chance of detachment from the surface. One means to overcome immobilization is to use a fluidized bed. However, this bed will eventually fail as a result of attrition. For the treatment of aqueous phase pollutants, titania slurry is the most commonly applied method (Crittenden et. al., 1997). However, due to the small particle sizes, the removal of the semiconductor from solutions is difficult and energy intensive. Additionally, this effective water treatment solution would be difficult to implement for the treatment of air in a reactor system that attempts to treat both phases.

Since catalytic reactions occur at the fluid-solid interface, a large interfacial area can be advantageous in attaining a significant reaction rate. Large surface areas are usually provided by porous structures. Mesoporous materials have attracted considerable attention after the discovery of M41S family of silicates, which were determined to possess large surface areas, narrow pore distributions and controllable pore sizes (Kresge et al, 1992). Immobilization of titanium dioxide by embedding it in a silica matrix (SiO<sub>2</sub>) having a large surface area has shown to be an effective

catalyst support for treatment of gas and aqueous phase VOCs (Belhekar et al.,2002; Boonamnuayvitaya et al, 2006; Holmes, 2003; Kang et al.,2004; Londree, 2002; Ludwig et al 2008; Stokke, 2008). Arai et al. (2006) showed that loading silica to TiO<sub>2</sub> using a sol-gel method resulted in 1.5 to 2 times increase in reaction rate constants for the photocatalytic oxidation of phenol, nitrobenzene, propionic acid and benzyltrimethylammonium chloride as compared to pure TiO<sub>2</sub> suspensions. Similar improvements have been observed in the PCO of toluene in the gaseous phase. Zhang (2005), for example, determined that the overall removal of toluene increased by about 30% when silica embedded titania was used as the catalyst instead of simply pure TiO<sub>2</sub>. Likewise, Zou et al (2006) showed that the conversion of toluene reached a steady state at 51% when using Degussa P25 and it increased by 14% when high surface area SiO<sub>2</sub>-TiO<sub>2</sub> pellets were used under the same operational conditions. Neither of these studies accounted for adsorption and photo-oxidation removal separately, so the enhanced conversion might be partially attributed to an increased adsorption due to the greater surface area of the SiO<sub>2</sub> -TiO<sub>2</sub> catalyst.

Silica exists as a SiO<sub>4</sub> tetrahedron where Si atoms are connected to four oxygen atoms one of which is bounded to another Si atom from another tetrahedron, as shown in Figure 2-3. Silica forms a clear network, transparent to UV radiation, so it does not hinder the absorption of photons by the TiO<sub>2</sub> semiconductor. Furthermore, silica has a high adsorptive capacity for many organic contaminants since it is commonly the fixed phase in the columns used for gas chromatography (Miyabe and Guiochon, 2004). Therefore, incorporating TiO<sub>2</sub> to the silica matrix can improve the photocatalytic process by adsorbing the contaminants to the silica surface which will provide longer time for interaction with the catalyst. As a result, the probability of the compound to be degraded by the active species formed in the surface is increased.

There have been many research studies investigating methods to prepare SiO<sub>2</sub>-TiO<sub>2</sub> composites with photocatalytic properties. The synthesis conditions of these materials have an important impact on the final properties of such composites. Silica-titania composites can be formed by two types of interaction between Si and Ti atoms: (1) physical interactions, such as van der Waals attractions and (2) chemical interactions, such as the creation of Ti-O-Si bonds. There are few methods widely used for the preparation of mixed oxides (chemically bonded composites) such as sol-gel hydrolysis, coprecipitation, impregnation and chemical vapor deposition. Each of these methods has different advantages and disadvantages which are related to the difficulties in attaining homogeneous coatings, controlling changes in titania crystal phases between rutile and anatase, and limiting the TiO<sub>2</sub> content in the mixture. In all these methods, titania is incorporated into the silica matrix by replacing a Si atom from the silica network by a Ti atom. Among all the available methods, a sol-gel synthesis was selected since it has shown to overcome most of the common problems encountered in the preparation of SiO<sub>2</sub>-TiO<sub>2</sub> composites and has proven to produce materials that can effectively remove organic compounds from gas and aqueous phases under the influence of UV radiation while enabling the casting of the composites to almost any desired shape (Holmes et al., 2004; Londeree, 2002; Ludwing, 2004; Pitoniak et al., 2003; Stokke et al., 2006).

During the sol-gel synthesis, a sol-gel, which is a stable dispersion of colloidal particles in a continuous liquid phase, is formed. These silica-gels are derived from silicon alkoxides such as tetraethoxy orthosilicate (TEOS) and tetramethoxy orthosilicate (TMOS). TEOS is desired over TMOS because, even though the latter hydrolyzes faster, it produces methanol as a byproduct of the process. TEOS, on the other hand, has longer hydrolysis rates but it produces ethanol instead. If workers are exposed to the emissions during the manufacturing process, ethanol emissions are

less toxic than methanol. The steps involved in the processing of silica gels generally include hydrolysis, condensation, gelation, aging, drying and curing. Initially, the alkoxide used as precursor is mixed with water to undergo hydrolysis. Ethanol is added together with the alkoxide for cosolvency purposes because the alkoxide has low water solubility. During hydrolysis the alkoxide group is replaced by a hydrogen ion by a nucleophilic attack of water on the silicon atom (Equation 2-17). Hydrolysis can be catalyzed by either acid or bases. In general, acid catalysis increases hydrolysis rate while base catalysis favors condensation. Depending on the concentrations and conditions, re-esterification, i.e. the reverse reaction for hydrolysis and condensation, can occur (Hench and West, 1990).



Following hydrolysis condensation reactions occur with siloxane bonding. There are two types of condensation, water condensation and alcohol condensation. In the first case, condensation occurs between two silanol groups (Equation 2-18) while the latter involves a silanol and alkoxide group (Equation 2-19). Water and alcohol are the respective byproducts for each reaction. Fluoride is added to the process since it is an important catalyst of silica reactions. Under acidic conditions, fluoride has the ability of catalyzing both hydrolysis and condensation reactions. It is believed that fluoride makes the silicic acid monomer more susceptible to nucleophilic attack by expanding its coordination sphere (Powers, 1998)



Additional polycondensation occurs to form the  $\text{SiO}_2$  network, which still contains the alcohol and water within the pores. At this point, during cross-linking, the low viscosity liquid like sol is cast into a special mold that prevents adhesion of the sol. After hydrolysis, gelation

occurs as colloidal particles grow by polymerization or aggregation. During this step, the viscosity increases sharply and a solid object results in the shape of the mold. Aging or syneresis is the next step in the process. Additional network linkages are formed resulting in the shrinkage of the gel which forces some of the liquid out of the pores. The aged gel has to be strong enough to resist possible cracking during drying. The drying step has an important influence on the final pore size of the sol-gel. This stage involves the removal of the liquid from the pores of the network. Drying has to be closely controlled to avoid cracking. For xerogel formation, the selected type of sol-gel for this research, the removal of the liquid from the pores is achieved by evaporation at ambient temperatures and pressures below the critical temperature of the liquid (Hench and West, 1990).

The last step to form a mechanically strong gel is curing. This final heat treatment influences the surface chemistry of the gels. Water retained on the surface of the silica can be present in two forms: (1) physisorbed, free water within the ultraporous gel structure, or (2) chemisorbed, as hydroxyl groups associated with the gel surface. Heat treatments using temperatures in the 180°C – 200°C range can remove physisorbed species while dehydroxylation, i.e. removal of chemisorbed species requires temperatures above 200°C. Rehydroxylation of the silica surface in the presence of water occurs reversible up to 600°C, such that the surface characteristics are not significantly changed. However, above this temperature, rehydroxylation is less likely and decreases in surface area due to sintering are observed (Londeree, 2002).

The surface functional groups are the main features of a hydrated silica surface and are responsible for the hydrophilic nature of most silica gels. Two functional groups are observed on the silica surface: silanol groups (-Si-O-H) and siloxane groups (-Si-O-Si-). Silanol groups,

shown in Figure 2-4, act as active adsorption sites while siloxane groups are non-reactive. The average silanol concentration of fully hydroxylated surfaces is about 4.9 silanols/nm<sup>2</sup> (Legrand, 1998).

### Photocatalysis of Organic Compounds with TiO<sub>2</sub>

Although it is well established that the initial step for the photooxidation process on TiO<sub>2</sub> is the excitation of the surface to produce an electron-hole pair, the subsequent chemical events at the fluid-solid interface remain an ambiguous and controversial issue. Different authors have postulated a wide variety of mechanistic pathways to explain the photodegradation of organic compounds and have attempted to determine the rate limiting reactions for these processes. Once the semiconductor has been photoexcited, the organic compound can be either oxidized directly by the trapped holes or indirectly by species formed on the surface of the catalyst such as hydroxyl radicals which are strong oxidizing agents (Hoffmann et al., 1995).

The photochemical reaction on TiO<sub>2</sub> catalyst in the aqueous phase is generally believed to involve radical species. Most studies have proposed hydroxyl radicals derived from hole-trapping by surface hydroxyl groups as the primary oxidizing agent and oxygen as a scavenger for photogenerated electrons. These surface trapping and electron scavenging reactions were previously presented in Equations 2-5 to 2-10. Turchi and Ollis (1990) proposed four cases in which a hydroxyl radical can oxidize an organic molecule in the aqueous phase. These cases are represented by Equations 2-20 to 2-23.

Case 1: The reaction occurs while both species, hydroxyl radical (Ti<sup>IV</sup>- •OH) and organic molecule (X<sub>1,ads</sub>), are adsorbed resulting in adsorbed products (X<sub>2,ads</sub>).



Case 2: The reaction occurs between a nonbound radical (•OH) and an adsorbed organic molecule (X<sub>1,ads</sub>).



Case 3: The reaction occurs between an adsorbed radical and a free organic molecule ( $\text{X}_1$ ) arriving at the surface of the catalyst and producing a molecule in the bulk phase ( $\text{X}_2$ )



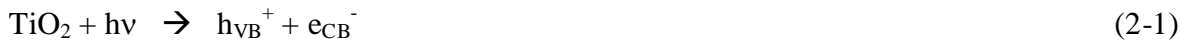
Case 4: The reaction occurs between two free species in the fluid phase



The extensive research on photodecomposition of water and photooxidation of organics has provided some evidence of hydroxylated intermediates which in principle, can be formed either by homolytic attack by a hydroxyl radical or by hydration of a singly oxidized intermediate (Fox and Dulay, 1993; Linsenbigler et al., 1995). For the case of gas-solid photocatalysis, however, the evidence for  $\cdot\text{OH}$  attack is not as definite. Either radical formation for organic oxidation or direct hole oxidation has been postulated as plausible mechanisms. Because gas phase molecules can move more freely, hole-electron recombination and hole-organic molecule oxidation can be kinetically competitive. Similarly, the abundance and availability of water molecules in the gas phase is severely diminished as compared to the aqueous phase resulting in a decreased probability of hydroxyl radical formation (Fox and Dulay, 1993). Nonetheless, there is currently no agreement regarding which species are more extensively active in the degradation of organic molecules. Furthermore, it has been difficult to establish an unambiguous mechanism to explain the photocatalytic oxidation (PCO) of organics because the data for direct hole oxidation as well as hydroxyl radical attack can result in similar reaction intermediates (Fox and Dulay, 1993; Hoffmann et al., 1995). Nevertheless, some of the mechanisms found in the literature that are widely accepted as possible photocatalytic pathways are presented below (adapted from Serpone and Emelie, 2002):

## Direct Pathways

**The Langmuir-Hinshelwood Process:** Some researchers have suggested that because photogenerated electron-hole recombination is so fast, interfacial electron transfer is kinetically competitive only when the electron donor or acceptor is preadsorbed on the catalyst surface. Preadsorption has been also suggested as a prerequisite for the reaction to occur at significant high rates (Fox and Dulay, 1993). Consequently, the Langmuir-Hinshelwood (LH) mechanism has been proposed as a possible pathway for the PCO of organic compounds using TiO<sub>2</sub>. The LH mechanism described by Equations 2-24 to 2-28, proposes as the initial step the adsorption and desorption of the organic molecule of interest (X) on the catalyst surface (S) based on Langmuir equilibrium. During the next step, the VB hole ( $h_{VB}^+$ ) is trapped by the adsorbed organic molecule ( $X_{ads}$ ) forming a reactive radical state ( $X_{ads}^+$ ). This species can either decay when electron recombination occurs (Equation 2-26) or undergo chemical reactions to regenerate the original surface state and yield products (Equation 2-27)



**The Eley-Rideal Process:** The Eley-Rideal process has been described by Serpone and Emeline (2002). After the hole-electron pair generation (Equation 2-1), the hole is trapped by surface defects (S) producing surface active centers ( $S^+$ ) which can either decay by recombination (Equation 2-29) or act as adsorption sites where the organic compounds can

chemisorb to form reactive species  $(S-X)^+$  that can further decompose yielding products (Equations 2-30 and 2-31, respectively).



### Indirect Pathways

The photocatalytic destruction of organic compounds by reactions with unstable species formed as the result of the surface activation is the indirect pathway most commonly considered (Equation 2-32). Researches that have investigated indirect pathways include Turchi and Ollis (1990), Fan and Yates (1996), and Hennezel et al. (1998), to name a few. The oxidants formed by water and oxygen adsorption and photodecomposition found in most of the literature are  $\cdot OH$ ,  $\cdot O_2^-$ ,  $HO_2^\bullet$ ,  $H_2O_2$  and intermediates such as  $\cdot O^-$  among others (Hoffmann et al., 1995; Yue et al., 2002). Some of the proposed reactions for their formation were presented in Equations 2-6 and 2-8 to 2-10.



### **Photocatalytic Oxidation (PCO) of Toluene with $TiO_2$ : Mechanisms and Intermediate Formation**

There seems to be an agreement in the literature that the initial PCO of toluene with  $TiO_2$  is very fast. However, the oxidation rate decreases dramatically within the first 30 to 60 minutes. During toluene photocatalysis, most research studies have shown that there is a high potential for catalyst deactivation depending on the experimental conditions (Alberci and Jardim, 1997; Boonamnuayvitaya et al., 2006; Hennezel et al., 1998; Maira et al., 2001a). This phenomenon is not true for all VOCs, and it seems to be most evident for the case of aromatic compounds such

as toluene and benzene (Alberci and Jardim, 1997; Lebrawski and Ollis, 2003a.). The deactivation of TiO<sub>2</sub> during toluene photocatalysis is usually visually supported by a change in color of the catalyst from white to yellow or brown (Alberci and Jardim, 1997; Eianga et al., 2002). Deactivation does not seem to be strongly related to the concentration of toluene since most studies on gas-phase toluene have reported some degree of deactivation. For example, Alberci and Jardim (1997) observed decreases in toluene conversion yields from about 80% to 21% after 150 minutes of continuous operation, attributed to catalyst deactivation, for initial concentrations of 17 ppm<sub>v</sub> as well as 500 ppm<sub>v</sub>. Deactivation was less evident for lower concentrations, but it was still observed. Similar results were found by Sauer et al. (1995) and Luo and Ollis (1996) under conditions of lower concentrations and shorter contact times. Many other studies have encountered severe deactivation after 3 hours of catalyst use (Blount et al., 2001; Hennezel et al., 1998; Maira et al., 2001). Literature indicates that the deactivation of the catalyst decreases with increasing humidification of the air. The actual effect of water and mechanisms for this phenomenon have not been well documented. Similarly, after catalyst poisoning, the catalytic surface can be regenerated by illumination of the photocatalyst in the presence of pure air (Peral and Ollis, 1992). For long term deactivations, however, stronger oxidants such as H<sub>2</sub>O<sub>2</sub> might be required (Alberci and Jardim, 1997). Catalyst deactivation has been attributed to the accumulation of recalcitrant intermediate species strongly bound to the catalyst surface limiting the oxidation of toluene. The oxidation rate of these intermediates is much slower, and therefore, the overall PCO of toluene takes longer than for other organic compounds (Ameen and Raupp, 1999; Augugliario et al., 1990; Blount and Falconer, 2002; Hennezel et al., 1998; Larson and Falconer, 1997). Characterization of the potential intermediates causing catalyst deactivation is very important because it is related to the

photocatalyst lifetime which is a factor of the process economics of photocatalysis (Sauer and Ollis, 1996).

Earlier studies by Larson and Falconer (1997) on the PCO of toluene in the gas phase showed that this compound reacted quickly to form strongly bound intermediates more difficult to degrade and their rate for degradation to CO<sub>2</sub> and H<sub>2</sub>O was much slower. Based on their results, they proposed that the first product from the oxidation of toluene is benzyl alcohol, which further reacts to form benzaldehyde and CO<sub>2</sub>. They were not able to identify the strongly bound intermediates because the ones they found, benzyl alcohol and benzaldehyde were not considered as plausible limiting reactions due to their high rate of oxidation to form CO<sub>2</sub> when tested separately. These rates were 20 and 10 times faster than the oxidation rate of toluene. On the other hand, they suggested that a possible intermediate was benzoic acid since it has been reported by others as a byproduct but they were not able to test for this compound based on the nature of their experiments (Larson and Falconer, 1997).

Another group of researchers, Mendez-Roman and Cardona-Martinez (1998), further supported benzoic acid as the strongly bound intermediate in the degradation of gaseous toluene. In their study, they identified benzaldehyde and benzoic acid as intermediates using the Fourier-Transform Infrared (FTIR) spectrum technique, and to a lesser extent, benzyl alcohol using methanol extraction. They proposed that toluene was oxidized to benzaldehyde, which was further oxidized to benzoic acid. They attributed the surface deactivation of the catalyst to benzoic acid, and they found that this deactivation was retarded when the system was humidified. Their explanation for this phenomenon was that the formation of benzoic acid, which accumulates on the surface and degrades at very slow rates, was slowed down by the water. The water had two possible roles: competition with species that were forming on the

surface, or partial regeneration of some of the active sites on the catalyst (Mendez-Roman and Cardona-Martinez, 1998).

Refuting the arguments that suggested benzoic acid as the strongly bound species, is the study of Augugliaro et al. (1990), who found that benzoic acid seems to be an active species on the catalyst surface. Significant amounts of benzene and CO<sub>2</sub> were produced by PCO when benzoic acid was reacted separately under the same conditions as toluene. The intermediates found in this work were benzaldehyde, benzene, benzyl alcohol, and trace amounts of benzoic acid. The proposed path for toluene degradation was the hydroxyl radical attack to the toluene molecule forming benzaldehyde, which further reacted with •OH to form benzoic acid, and the latter decomposed to benzene and CO<sub>2</sub>. Benzene was found as a transient product present only at the beginning of the PCO. Among the strongly bound intermediates suggested to decrease the activity of the catalyst were benzyl alcohol, phenol and benzoate-like species. These species would hinder the formation of benzoic acid, and consequently, benzene and CO<sub>2</sub> production would decline in the first few hours. Similar to the other authors, they also found that the catalyst deactivation was retarded upon humidification, with the catalyst activity lasting about 20 hours for the case of unhumidified systems versus 70 hrs for humidified conditions. Additionally, it was suggested that benzaldehyde does not oxidize any further in the absence of •OH, deactivating the catalyst (Augugliario et al., 1990).

Blount and Falconer (2002), on the other hand, found that benzaldehyde oxidation was possible even in the absence of water; therefore, they excluded this species as the responsible for catalytic deactivation. Their findings did not contribute any other possible explanation for the deactivation of the catalyst other than the already mentioned strongly bound species in the surface of TiO<sub>2</sub>. However, based on their results from Temperature-Programmed Hydrogenation

(TPH) used to characterize byproducts, they suggested that the intermediates deactivating the catalyst do not appear to be graphitic structures.

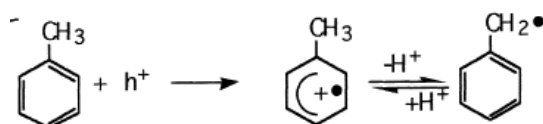
Matra et al. (1999) identified benzaldehyde as the main photo-oxidation path of toluene. Small amounts of benzene, benzyl alcohol and traces of benzoic acid and phenol were also detected. In their studies they determined that in the presence of water, no decrease of photoreactivity of toluene was observed at steady-state conditions. By removing water vapor from the feed, the conversion of toluene to benzaldehyde was almost completely inhibited, and an irreversible deactivation of the catalyst occurred. Similar to the Blount and Falconer results, their investigations using FTIR techniques indicated that benzaldehyde is produced on the TiO<sub>2</sub> surface even in the absence of water vapor. However, exposure of the catalyst to the UV light in a dry atmosphere results in an irreversible consumption of surface hydroxyl groups. This dehydroxylation should be the reason of deactivation of the catalyst under dry conditions (Matra et al., 1999).

Most of the articles presented in the literature do not seem to state a clear understanding and explanation for the intermediates strongly bound to the surface that hinder the activation of the photocatalyst. However, some mechanistic pathways have been postulated to describe the formation of those other intermediates that have been mostly characterized in the different studies. Some of these pathways, as described by Hennezel et al. (1998), are presented below:

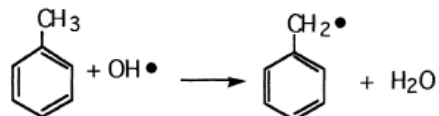
- a. The primary proposed toluene PCO pathway involves the initial formation of the benzyl radical from the abstraction of the hydrogen from the methyl group in toluene.

There are 2 pathways that have been proposed for this radical formation:

1. Direct hole transfer to toluene: electron transfer from toluene to the VB hole to form the benzyl radical.

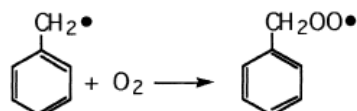


2. Hydrogen abstraction by a  $\bullet\text{OH}$ : electron transfer from the methyl group in the toluene molecule to the  $\bullet\text{OH}$  formed by water adsorbed to the catalyst surface.

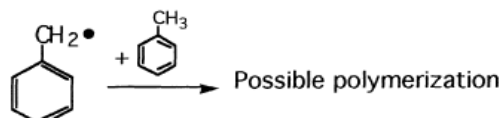


- b. Once the benzyl radical is formed, the reaction can follow two other pathways:

1. The benzyl radical can react with  $\text{O}_2$  to form a benzylperoxy radical.

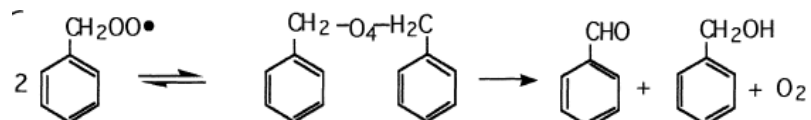


2. The benzyl radical can react with another toluene molecule to initiate a polymerization reaction.

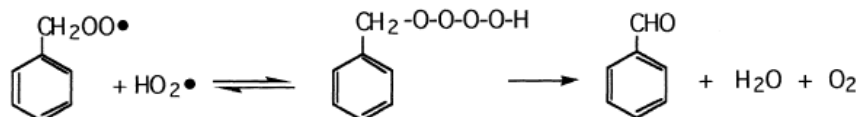


- c. The benzylperoxy radicals can form the commonly found intermediates in toluene PCO by two different pathways:

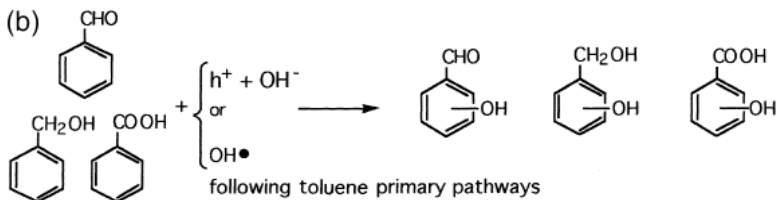
1. It can couple and form tetroxide, which further decomposes to benzaldehyde, benzyl alcohol and molecular oxygen



2. It can react with a hydroperoxy radical forming monalkyltetroxide, which further decomposes to benzaldehyde, water and, molecular oxygen.



- d. A plausible pathway for degrading the most common intermediates is a direct attack on the ring by hydroxyl radicals, VB holes or hydroxide ion. This attack would form mono-hydroxylated isomers (hydroxybenzaldehyde, hydroxybenzoic acid, and hydroxybenzyl alcohol). These hydroxylated compounds are not found in significant amounts, so this pathway is considered to be of secondary importance.



Conditions that influence intermediate formation include the contact time between the catalyst and toluene, the percent relative humidity in the influent stream, and some studies have also indicated light intensity as a possible factor (Alberci and Jardim, 1997; Peral and Ollis, 1992). Lebrawski and Ollis (2003a and b) developed a two-site kinetic model to simulate and predict the deactivation of TiO<sub>2</sub> during photocatalysis of aromatic compounds. The model is based on the assumption that there are two types of catalyst sites in the TiO<sub>2</sub> surface: (1) sites that can be occupied by the aromatic contaminants, water molecules or some reaction intermediates and (2) sites that can be only occupied by reaction intermediates or water due to the more hydrophilic nature of these sites and the fact that most of the intermediates are more polar than the original reactant aromatic compound. The model calculates different surface coverages which are used in rate expressions to finally determine effluent concentrations of the aromatic compounds. It also accommodates for catalyst regeneration and reuse when applicable. Although the model does not provide information about the intermediates or possible reaction mechanisms, the results show reasonable agreements with experimental data, so the model can be used as a rough estimate of the potential catalyst deactivation in the presence of toluene. (Lebrawski and Ollis, 2003a and b).

### Gaseous and Aqueous Phase Toluene Kinetics

Literature suggests major differences between the kinetics of heterogeneous photocatalytic reactions of organic compounds present in water and in the gas phase. The liquid-solid interface might appear more complex for kinetic studies since more variables need to be controlled, as

compared to gas-solid systems. Such variables include the surface composition, surface area and preparation procedures of the catalyst, solution characteristics, such as pH and its effects on the solid surface structure, oxygen partial pressure, and diffusion rates in solution and near the catalysts surface among others (Anpo et al., 1991). Despite all the possible parameters involved in liquid-solid photocatalysis, most of the variables determining the rate of gas phase photocatalysis are the same as in liquid-phase photocatalysis. The main difference between liquid-solid and gas-solid photocatalysis of toluene is that the reaction rates for the latter can be orders of magnitude larger (Lichtin and Avudaithai, 1996). However, deactivation of the catalyst during gas phase photocatalysis presents a disadvantage compare to aqueous phase photocatalysis. Except for few papers, research studies have not focused on directly comparing gas phase and aqueous phase reactions on TiO<sub>2</sub>. Most differences have been observed by collecting results from individual phase studies, which are harder to compare due to differences in operational conditions. With the objective of constructing more impartial comparisons, Lichtin and Avudaithai (1996) studied the photocatalysis of some chemicals in aqueous and gas phases under similar conditions. The chemicals included in the study were acetonitrile, methanol, trichloroethylene and methylene chloride. Their results show that the photoefficiencies for the removal of such organics, defined as the number of molecules of organic reactant removed per number of photons incident on catalyst, was from 2 to 300 times larger for gas-solid systems as compared to liquid-solid systems.

Not only has the kinetic comparisons between gas-solid and liquid-solid photocatalysis been neglected, but studies on the simultaneous PCO of contaminants in both phases are virtually nonexistent. The kinetics of reactions in both phases is of great importance in the design of processes, reactors, and the respective scale-up of photocatalytic systems. Accordingly, a short

review of the main factors affecting the oxidation rate of toluene in the aqueous and gaseous phases based on the currently available literature is presented in this section.

The rate equations for heterogeneous photocatalysis are traditionally dependent on the intrinsic catalyst characteristics as well as mass transfer considerations in the system. The common steps considered in heterogeneous catalyzed reactions are the following (Satterfield, 1969):

- 1) Mass transfer (diffusion) of the reactants from the bulk fluid to the external surface of the catalyst pellet.
- 2) Diffusion of the reactant from the pore mouth through the catalyst pores to the immediate vicinity of the internal catalytic surface.
- 3) Adsorption of reactant A onto the catalyst surface
- 4) Reaction on the surface of the catalyst ( $A \rightarrow B$ )
- 5) Desorption of the products from the surface
- 6) Diffusion of the products from the interior of the pellet to the pore mouth at the external surface.
- 7) Mass transfer of the products from the external pellet surface to the bulk fluid.

The overall rate of the reaction is equal to the rate of the slowest step in the mechanism, given that such step is much slower than the other steps. Typically the rate can be dictated by the extent of reaction or the mass transfer. If the reaction rate is controlling, the diffusion steps (1, 2, 6, 7) are very fast compared with the reaction steps (3-5), so the concentrations in the immediate vicinity of the active sites are indistinguishable from those in the bulk fluid. For mass transfer limited reactions, the reaction steps are very fast compared to the diffusion steps, so mass transport affects the reaction rate. In mass transfer limited reactions such as systems affected by diffusion from the bulk gas or liquid to the catalyst surface or to the mouth of the catalyst pores, changes in the flow conditions past the catalyst should change the overall reaction rate. For systems where the diffusion within the pores of the catalyst limits the reaction rate, changes in the external flow conditions will not have any effect on the overall reaction rate.

As many heterogeneous catalytic reactions such as the PCO of VOCs on TiO<sub>2</sub> are apparently zero order at high reactant concentration and first order at lower concentrations, the Langmuir-Hinshelwoold (LH) rate form, given by Equation 2-33, is the most commonly assumed for fitting kinetics data.

$$r = -\frac{d[c]}{dt} = k_{LH}\theta = \frac{k_{LH}K_{ads}C}{1 + K_{ads}C} \quad (2-33)$$

The terms in the equation are the rate of the reaction,  $r$ , the concentration of the contaminant in solution,  $C$ , time,  $t$ , the reaction rate constant,  $k_{LH}$ , the fraction of the surface covered by the reactant,  $\theta$ , and the adsorption coefficient of the reactant  $K_{ads}$ . When low concentrations are considered ( $K_{ads}C \ll 1$ ), this equation becomes pseudo first order ( $r = k_{LH}KC$ ), and when high concentrations are used ( $KC \gg 1$ ), the reaction simplifies to a zero order reaction ( $r = k_{LH}$ ).

Although most of the observed kinetic data fit this rate form, it is not a sufficient condition to assume the Langmuir-Hinshelwood mechanism, which assumes the adsorption of the contaminant to the catalyst surface, as the actual pathway of the reaction. Recent studies have demonstrated that other mechanisms, including different modifications of the Eley–Rideal mechanism, can result in the same kinetics of photodegradation as represented by Equation 2-33 (Turchi and Ollis, 1990, Emeline et al. 1998). It has been shown that the contaminant's interaction with photoactivated oxygen via the most common rate-limiting steps described by the four cases presented in previous sections and postulated by Turchi and Ollis (1990) can result in overall reaction rate equations that have the same dependence on reactant concentration as the one modeled by the LH form. Accordingly, the LH equation does not provide any insight of the mechanisms between contaminant and excited oxygen (Turchi and Ollis, 1990). Ollis (2005) recently proposed that the apparent simple LH rate form has several origins which are hard to

study because of the various kinetic ‘disguises’ that exist in photocatalysis. He showed that out of the two most common assumptions for kinetic mechanism, pseudo-steady state and slow step assumptions, the former is the only one that explains the data available on light intensity dependence. His conclusions illustrate that the studied photocatalyzed reactions do not reach adsorption/desorption equilibrium because the significant reactivity of the active adsorbed species, such as hydroxyl radical, continuously shift from equilibrium (Ollis, 2005).

Although the best kinetic model has not been decided upon, common factors influencing the kinetics of toluene in the gas and aqueous phases have been indicated to be, by many researchers, the initial toluene concentration, the UV intensity, the flowrate and to a lesser extent the temperature. For gas-phase PCO, the relative humidity also plays a key role in the kinetics of the reaction, whereas for aqueous phase PCO, pH is usually considered. However, a common feature of photocatalytic reactions on  $\text{TiO}_2$  powders suspended in aqueous solution is the weak dependence of the reaction rate on solution pH (Fox and Dulay, 1993). The isoelectric point for  $\text{TiO}_2$  in water is about pH = 6, meaning that the surface charge is positive at pH values lower than 6 and negative at higher pH. Despite the evidence showing the importance of pH on the particle size, surface charge, and band edge positions of  $\text{TiO}_2$ , photocatalysis of toluene is found to occur at both low and high pH at comparable reaction rates (Fox and Dulay, 1993). The major trends and effects of the mentioned factors for gas phase and aqueous phase toluene kinetics are described below. Direct comparisons among rate constants, however, even in the same phase are not always possible due to the differences in operational conditions among the studies and calculations parameters arbitrarily selected. For example, studies that use the LH rate form to describe the kinetics of toluene PCO may choose to include or exclude the formation of intermediates. If intermediates are included in the calculations, their  $K_{ads}C$  terms must be present

in the L-H rate equation, even when their adsorption on the surface of TiO<sub>2</sub> might be rather weak. However, for simplicity, many studies employ the initial toluene rate for the application on the equation by assuming that intermediates formation at the beginning of the process is negligible (Xu and Langfordl, 2000). As a result, discrepancies among the LH rate constants determined by different studies can easily occur because the selected time intervals might be different.

### **Effect of Initial Concentration**

Most studies have found that the decomposition and mineralization of toluene decreases as the initial concentration of the contaminant increases and the rates of decomposition increase accordingly. There is no consensus on the reaction order as a function of concentration since several trends on the increase of reaction rate has been observed for concentration ranges between 0.5 to 2400 ppm<sub>v</sub> (Buozaza et al., 2006; Maira et al., 2001b; Obee and Brown, 1995; Pengyi et al., 2003). Fewer studies determined that increasing the initial concentration of toluene had a negative effect on the pseudo first order reaction constant (Buozaza and Laplanche, 2002; Wang and Ray, 2000). These studies also included a wide range of concentrations, between 20 to 800 ppm<sub>v</sub>. In general, increasing the concentration of toluene increases the number of molecules that can be adsorb on the surface of the catalyst and thus, oxidized. However, the surface active area of the catalyst is limited, so overloading the system is likely to deactivate the catalyst more rapidly resulting in adverse effects on the oxidation rate despite the positive order kinetics involved. Furthermore, the divergent results with respect to the initial toluene concentration might be attributed to the differences in catalyst characteristics among the studies as well as operational conditions of the systems.

## **Effect of Light Intensity**

Higher UV wavelengths usually result in higher intensities. The wavelength of the UV lamps does not seem to change the kinetics of the PCO of toluene in the aqueous phase at low concentrations. For example, Holmes et al.(2004) tested the PCO of toluene in the aqueous phase in concentrations below 200 µg/L by using UV sources that produced 365 nm and 254 nm wavelengths and no changes in the rate constants were observed. Thus, it was concluded that as long as the light source provided radiant energy greater than  $5.12 \times 10^{-19}$  J (i.e.  $> 3.2\text{eV}$  or  $\lambda < 388$  nm) which is the minimum photon energy required to excite the electrons in the TiO<sub>2</sub> surface, increasing the radiant energy did not further contribute to kinetic improvements. Studies comparing the effects of UV intensity on higher concentrations of toluene were not found in the literature for the aqueous phase.

On the other hand, the irradiance usually referred to as light intensity, significantly influences the oxidation rate of toluene in gas phase. In general, it has been observed that for systems that are not mass transfer limited, the reaction rate ( $r$ ) increases linearly with UV intensity ( $I$ ) if the intensity is below 10-20 mW/cm<sup>2</sup>. For higher intensities, greater than 10-20 mW/cm<sup>2</sup> the oxidation rate is directly proportional to the square root of the intensity meaning that the recombination of photoinduced charges predominates, and accordingly the quantum efficiency decreases (D'Oliveira et al., 1990). These results have been validated for systems treating gas phase toluene. Hager and Bauer (1999) and Wang and Ray (2000) used intensities between 0.3 and 20 mW/cm<sup>2</sup> and found that the reaction rate of gas phase toluene increased linearly with UV intensity. Furthermore, it has been shown that at high enough intensities the reaction rate does not depend on  $I$  anymore and it is instead mass transfer limited. The quantum efficiency ( $\phi$ ), i.e. the number of molecules transformed per number of photons adsorbed is also

a function of intensity, but it follows the opposite trends of the reaction rate because the absorption of photons follows a first order rate in intensity. Hence, at low intensities,  $\phi$  is constant; at higher intensities ( $> 10\text{-}20 \text{ mW/cm}^2$ ),  $\phi$  is inversely proportional to the square root of the intensity, and at values of  $I$  that are high enough not to influence the rate,  $\phi$  varies as the inverse of  $I$  (Ollis et al. 1991).

### **Effect of Superficial Velocity**

The superficial velocity affects the mass transfer and transport of pollutants to the catalyst surface. The mass transfer of the reactants to the catalyst can be the rate limiting step in photocatalytic processes. During immobilization of the catalyst, one of the disadvantages is the decreased contact area between catalyst and reactants that can result in lower mass transfer rates. When the reaction is mass transfer limited, the reaction rate increases with increasing velocity. For the case of toluene, many studies in the gas phase have shown that toluene is mass transfer limited for low superficial velocities, usually below 10 cm/min (Alberci and Jardim, 1997; Marci et al., 2003). At higher velocities, the oxidation rate does not increase anymore and remains constant, so the reaction becomes kinetically controlled instead of mass transfer limited. Higher superficial velocities are usually desired to overcome mass transfer limitations; however, increasing the velocities decreases the residence time in the reactor resulting in a decrease in toluene conversion. Accordingly, an optimum combination of velocity and residence time is expected to result in a maximum pollutant removal.

### **Effect of Temperature**

It is well accepted that increasing the temperature increases the reaction rate as described by the Arrhenius equation. This tendency has been widely observed in photocatalytic reactions. Hager and Bauer (1999), for example, found that toluene conversion increased when the

temperature was raised from 7°C to 27°C; however, the conversion significantly decreased when the temperature was raised further up to 75°C. They concluded that at lower temperatures, desorption of the toluene molecules from the catalyst was the limiting step, whereas at higher temperatures, adsorption of these molecules became the rate limiting step. Similarly, the adsorption of water molecules might be also hindered at higher temperatures. Wang and Ray (2000) found only small increases in reaction rates for the three temperatures they investigated, 25°C, 35°C and 45°C. They calculated the activation energy of toluene by using a  $k$  versus  $1/T$  plot and determined this value to be 31.42 kJ/mol. This value was the largest activation energy found compared to the other compounds studied, which included benzene and 1,2-dichloroethylene.

### **Effect of Relative Humidity**

Relative humidity (RH) plays a key role in the oxidation of toluene in the gas-phase. Some authors consider this parameter a requirement to achieve complete oxidation of toluene (Augugliaro et al., 1999). Most literature agrees that increasing the relative humidity of the influent air increases the oxidation rate (Augugliaro et al., 1999; Hennenzel et al., 1998; Luo and Ollis, 1996; Pengyi et al., 2003; Wang and Ray, 2000). In general, it is well documented that for low concentrations of toluene (< 3 ppm), the rate increases with relative humidity up to about 30% RH, with an optimum between 20% and 30% RH. However, higher RH has a detrimental effect in the oxidation rate, so above 30% RH, the rate rapidly declines. A possible explanation for this phenomenon is that at such low concentrations of contaminant, competition effects predominate and the water molecules can reach the catalyst easier than the toluene molecules adversely affecting the oxidation of toluene (Obee and Brown, 1995). For higher toluene concentrations, the optimum relative humidity is closer to 40% (Hennenzel et al., 1998; Luo and Ollis, 1996; Obee and Brown, 1995; Pengyi et al., 2003; Wang and Ray, 2000). Above this

value, the rate does not increase any further, but it remains constant. Achieving optimum relative humidity enhances the complete mineralization of toluene while reducing the accumulation of intermediates. Increasing relative humidity increases the overall initial conversion of toluene as well as the conversion obtained at steady state (Augugliaro et al., 1999; Maira et al., 2001). Although the importance of the presence of water for the oxidation of toluene is unquestionable, the actual role of water on the reaction pathway is still not well understood.

### Mass Transfer

Understanding the equilibrium partitioning of chemicals between air and water and the mass transfer across the air-water interface is of utmost importance for the purpose of this research.

#### **Equilibrium Partitioning of Volatile Organic Compounds between Air and Water**

Systems are constantly moving towards the final state of equilibrium. Once equilibrium is attained, the transfer stops. (Hand et al., 1999). Henry's law is used to describe the equilibrium of the contaminants between air and water phases. The law can be assumed to follow a linear trend with respect to the solute's concentration for low concentrations. If the concentration is too high, possible deviations from linearity should be accounted for. In general, the expression is given by Equation 2-34:

$$Y_s = H \times C_s \quad (2-34)$$

where  $Y_s$  is the gas phase concentration at the interface [Mass/Length<sup>3</sup>],  $H$  is Henry's constant [dimensionless], and  $C_s$  is the aqueous phase concentration at the interface [Mass/Length<sup>3</sup>].

The equilibrium partitioning between air and water,  $H$ , can be influenced by temperature, pressure, ionic strength, surfactants and the solution pH for the case of ionizable species. Given that most treatment operations are carried out at atmospheric pressure, the impact of pressure on the Henry's constant can be considered negligible. Temperature, however, influences the

aqueous solubility of compounds and their vapor pressure. The changes of  $H$  with temperature can be predicted by the van't Hoff's equation (Equation 2-35), assuming that the standard state enthalpy change ( $\Delta H^\circ$ ) is constant over the temperature range of interest.

$$H_2 = H_1 \exp\left[\frac{-\Delta H^\circ}{R}\left(\frac{1}{T_2} - \frac{1}{T_1}\right)\right] \quad (2-35)$$

$\Delta H^\circ$  is the standard state enthalpy change in water due to the dissolution of a compound in water and  $R$  is the universal gas constant.  $H$  and  $T$  are the Henry's constant and temperature, respectively with the subscripts representing different conditions. The other factors influencing  $H$  do not have a pronounced effect unless extreme conditions are present. Thus, their influence will not be assessed in detail in this review. Hand et al. in the book by AWWA (1999) describes most effects of these parameters and provides a large set of references on the topic.

### Mass Transfer Principles

The rate at which a component is transferred from one phase to another depends upon the degree of departure of the systems from equilibrium. Whether mass transfer occurs from air to water or vice versa, the mechanisms and assumptions are basically the same. The two film theory, developed by Lewis (1916) and Whitman (1923), is the basis for most mass transfer correlations. According to this theory, turbulence in the two phases dies out near the interface, so equilibrium occurs at the gas/liquid interface, as illustrated in Figure 2-5. Consider for example that a contaminant present in the aqueous phase is in contact with the air phase, as depicted by Figure 2-5. The tendency of the system to reach equilibrium is sufficient for the molecules in the bulk aqueous phase ( $C_b$ ) to diffuse in the air phase ( $Y_b$ ). First, the contaminant in the bulk water phase will move towards the air-water interface due to the concentration difference in this film ( $C_b > C_s$ ). Similarly, the concentration in the air phase at the air-water interface ( $Y_s$ ) is larger than

the bulk air phase concentration, providing the driving force for the contaminant to move to the bulk air phase (AWWA,1999)

The entire resistance to transfer is considered to be contained at the two films near the interface where the transfer occurs by purely molecular diffusion. Local equilibrium is assumed at the interface and concentration gradients at this interface are established much faster than common steady-state diffusion assumes (Skelland, 1985). The overall resistance to mass transfer ( $R_T$ ) is considered to be the sum of the liquid phase ( $R_L$ ) and the gas phase ( $R_G$ ) resistances (Equation 2-36). These resistances can be defined as the reciprocal of the liquid phase and gas phase rate constant, respectively (2-37) (McCabe et al., 2005):

$$R_T = R_L + R_G \quad (2-36)$$

$$\frac{1}{K_L a_w} = \frac{1}{k_l a_w} + \frac{1}{H k_g a_w} \quad (2-37)$$

The rate of transfer of a VOC from the aqueous phase to the gas phase can be described by the linear simplification of Fick's Law (Equation 2-38):

$$J = K_L a_w [C^* - C_s] \quad (2-38)$$

where  $J$  = mass transfer rate [Mass/time/Length<sup>2</sup>]

$K_L$  = liquid side mass transfer coefficient [Length/time]

$a_w$  = wetted interfacial area per volume of tower [Length<sup>2</sup>/Length<sup>3</sup>]

$C^*$  = equilibrium concentration in aqueous phase [Mass/Length<sup>3</sup>]

According to Equation 2-38, the factors influencing the rate of transfer of a contaminant from the aqueous to the air phase are:

- the driving force for mass transfer, i.e. the concentration gradient
- the wetted interfacial area
- the mass transfer coefficient

The driving force of the system can be increased by shifting the systems from equilibrium. In general, increasing the temperature causes shifts from equilibrium. When considering the product of the wetted area and the mass transfer coefficient, ( $K_L a_w$ ), the term is known as the overall mass transfer coefficient. This term will depend on the system and chemical characteristics. All these factors are used and optimized in the design of mass transfer operations, such as strippers and absorbers. Packed towers aerators (PTAs) are mass transfer units commonly used for the stripping of volatile compounds from the aqueous phase and absorption of gases from the gas phase. Because their principles of operation have been implemented on the design of the reactor used for this research, some of their design considerations are included below.

### **Mass Transfer Operations: Packed Tower Aerator (PTA)**

PTAs are devices that consist of cylindrical columns that treat air and water flowing in a countercurrent mode. These towers are packed with inert solid shapes called tower packing that provide large interfacial areas for the transfer of chemicals between the phases. PTAs can have different types of packing which include random packing, stacked packing and structured and ordered packing. Random packings are those that are dumped randomly in the tower and their sizes go usually up to 3 in. Stacked packings, which can have sizes between 2 and 8 in., have to be placed in the tower by hand. Similarly, structured packings consist of entire ordered units that are placed inside the tower. The most common type of packing in PTAs is random packing. They tend to be more inexpensive, and they have high interpacking as well as intrapacking porosity. Higher porosity corresponds to lower pressure drops through the tower, thus decreasing the overall cost of the PTA (McCabe et al., 2005).

The equations used to design PTAs, Equations 2-39 to 2-42, were derived under the assumptions that the influent gas stream is free of the contaminant of concern and the flow in the

tower is plug flow for both gas and liquid streams so that there is a flat velocity profile across the tower and similar residence time. The plug flow assumption might not be valid for towers experiencing a lot of channeling, which could be a consequence of non-uniformity or maldistribution of the packing. Similarly, the assumption does not hold true everywhere in the tower since there are different gas flow resistances at the walls or relatively dry packing as compared to the internal body of the tower. Possible axial dispersion can cause the molecules to move at different speeds as well as the back mixing caused by other flow flowing in opposite direction, resulting in deviations from the assumptions (Treybal, 1980). It is well established that the height of packed towers determines the mass transfer efficiency while the tower's cross section determines the capacity of the tower, i.e. the amount of gas that can be treated by the system (Sherwood et al., 1938). Accordingly, PTAs design involves the calculation of two main terms, the height of transfer units (*HTU*) and the number of transfer units (*NTU*). *NTU* is dependent upon the driving force, i.e. the influent ( $C_o$ ) and effluent ( $C_e$ ) concentrations of the contaminant of concern in the aqueous phase, as well as the stripping factor ( $R$ ). *NTU* represents the number of hypothetical stages required for treatment, and corresponds to the difficulty in removing the solute from the liquid phase. The *HTU* value, dependent on the liquid flowrate ( $Q_L$ ), the cross sectional area of the tower ( $A$ ) and  $K_L a_w$ , characterizes the mass transfer efficiency from the liquid to the gas phase.

$$Z = HTU \times NTU \quad (2-39)$$

$$HTU = Q_L / (A \times K_L \times a_w) \quad (2-40)$$

$$R = (Q_G \times H) / Q_L \quad (2-41)$$

$$NTU = \frac{R}{R-1} \ln \left( \frac{\frac{C_0/C_e(R-1)+1}{R}}{R} \right) \quad (2-42)$$

When the influent air stream is contaminated with the contaminant of concern, the design equations cannot be simplified so the complete expression (Equation 2-43) to determine the height of the packing ( $Z$ ) in the tower has to be used.

$$Z = \frac{L_m(C_0 - C_e)}{K_L a(DF_{lm})} \quad (2-43)$$

The term  $L_m$  is the liquid velocity and  $DF_{lm}$  refers to the log mean of the driving force of the reaction which is the difference in concentration at some time  $t$  and at equilibrium ( $C_t - C_s$ ). This value is constantly changing with depth because the bulk liquid concentration at time  $t$  ( $C_t$ ) is changing. The log mean of the driving force is then given by Equation 2-44, where the subscripts  $o$ ,  $s$  and  $e$  represent the influent, equilibrium (as calculated from the Henry's Law) and effluent concentrations of the contaminant of concern in the aqueous phase.

$$DF_{lm} = \frac{DF_0 - DF_e}{\ln\left(\frac{DF_0}{DF_e}\right)} = \frac{(C_0 - C_s) - (C_e - C_s)}{\ln\left(\frac{(C_0 - C_s)}{(C_e - C_s)}\right)} \quad (2-44)$$

Mass transfer coefficients used for the design of PTAs are obtained from pilot studies when available (Kavanaugh and Trussell, 1980). However correlations can be helpful to extrapolate real data to other conditions that are different from the experimental conditions.  $K_L a_w$  depends on fluid properties, flow rates and the type of packing. Therefore, experimental pilot results can be applicable to full-scale results only under the same packing, chemicals and flowrate conditions (Treybal, 1980). When  $K_L a_w$  is obtained experimentally, errors are more likely to occur for low stripping factors. The sensitivity of  $K_L a_w$  measurements decreases as the stripping factor increases. This effect is speculated to occur due to the uncertainty on the values of  $H$ , which has a lower effect in the stripping factor equation ( $R = (Q_G \times H) / Q_L$ ) as the air to water ratio increases (Lamarche and Droste, 1989). Furthermore, the tower height calculated for

a full-scale system based on the  $K_{La_w}$  obtained from a pilot-scale tends to be a conservative value, meaning that the actual tower usually operates at higher efficiencies. A full-scale system will usually have a larger tower diameter, so the ratio of tower diameter to nominal packing diameter will be greater. An optimum value for this ratio is 12 or greater. Increasing this ratio decreases the channeling or short circuiting of the water down the tower which results in higher removal (Hand et al., 1999).

There are some factors that can produce errors in the determination of mass transfer coefficients. One of those factors is the end effect of the tower. End effects refer to the removal of volatile chemicals above and below the packing as a result of the air contacting the contaminated water but without the assistance of the packing. Since  $K_{La_w}$  represents the mass transfer due to the packing section of the tower, significant end effects can cause errors in experimental estimates of the mass transfer coefficients. Conventionally, mass transfer inside and outside the tower is assumed to be additive. Therefore, end effects are usually calculated by plotting NTU versus packing height ( $Z$ ). A positive y-intercept of the plot is considered as the number of transfer units equivalent to the end effects. This value can be then subtracted from the measured  $NTU$  to calculate the actual  $K_{La_w}$  (Hand et al., 1999). Roberts et al., however, showed that the mass transfer due to the packing and the one attributed to the end effects occurred under different flow condition; therefore, the  $NTU$  values for both cases should not be additive. They explained that a more reliable way to correct the value of  $K_{La_w}$  due to end effects was to measure the  $NTU$  in a tower without packing (Roberts et al. 1985).

When pilot studies are not available, there are correlations in the literature that allow calculations of mass transfer coefficients. There are 3 well known models for estimating the mass transfer coefficients in air stripping operations: the Sherwood and Holloway model which

assumes that the gas phase resistance is negligible, the Shulman et al. and Onda et al. models which account for both, the liquid and gas phase resistances (Lamarche and Droste, 1989). The Onda et al. (1968) correlation is the most widely used for PTA design. Additionally, this correlation has been validated by many pilot and full-scale studies (Roberts et al., 1985 and Hand et al., 1986). According to Lamarche and Droste, the Onda et al. correlation gives a better estimate of the mass transfer coefficients as compared to the Sherwood and Holloway and the Shulman et al. correlations. In their study, they found that the Sherwood and Holloway correlation seemed to overpredict the experimental  $K_{La_w}$  values probably because it neglects the gas phase resistance while the Shulman et al. model, in general, overpredicted high  $K_{La_w}$  values while it underpredicted low  $K_{La_w}$  values.

The Onda correlation is given in Equations 2-45 through 2-47.. This correlation estimates the wetted area available for mass transfer and uses that value to determine the local mass transfer coefficients for the gas and liquid phases.

$$a_w = a_t \left\{ 1 - \exp \left[ -1.45 \left( \frac{\sigma_c}{\sigma} \right)^{0.75} \left( \frac{L_m}{a_t \mu_L} \right)^{0.1} \left( \frac{L_m^2 a_t}{\rho_L^2 g} \right)^{-0.05} \left( \frac{L_m^2}{\rho_L a_t \sigma} \right)^{0.2} \right] \right\} \quad (2-45)$$

$$k_L = 0.0051 \left( \frac{L_m}{a_w \mu_L} \right)^{\frac{2}{3}} \left( \frac{\mu_L}{\rho_L D_L} \right)^{-0.5} \left( a_t d_p \right)^{0.4} \left( \frac{\rho_L}{\mu_L g} \right)^{-\frac{1}{3}} \quad (2-46)$$

$$k_g = 5.23 \left( a_t D_g \right) \left( \frac{G_m}{a_t \mu_g} \right)^{0.7} \left( \frac{\mu_g}{\rho_g D_g} \right)^{\frac{1}{3}} \left( a_t d_p \right)^{-2} \quad (2-47)$$

Based on this correlation, the wetted area is dependent on the total area of the packing ( $a_t$ ) and the liquid loading rate ( $L_m$ ) while the local mass transfer coefficients incorporate the nominal packing diameter ( $d_p$ ) and the air loading rate ( $G_m$ ). The values of  $L_m$  and  $G_m$  depend on the operating conditions of the system, i.e. the air and water flowrates and the chemical being

stripped. Values of  $d_p$  and  $a_t$  are characteristics of the packing material. Therefore, an important part of the optimization design for PTAs involves the selection of flowrates as well as the packing material (Nirmalakhandan et al., 1987).

The Onda et al. correlation is valid for  $L_m$  values between 0.8 and 43 kg/m<sup>2</sup>/s (1.1 to 63 gpm/ft<sup>2</sup>) and  $G_m$  values between 0.014 and 1.7 kg/m<sup>2</sup>/s (2.206 and 267.9 cfm/ft<sup>2</sup>). Equations 2-46 and 2-47 were correlated for Raschig rings, Berl saddles, spheres and rods made of ceramic, glass, and polyvinylchloride with nominal packing diameters between 3/8 and 2 in. The coefficient 5.23 shown in the gas side mass transfer coefficient (Equation 2-47) is valid for nominal packing diameters greater than 15 mm; packing with smaller diameters were best fit using a coefficient of 2.0 (Onda et al., 1968). Deviations from the experimental range of values are not advisable when using the Onda correlation, though Lamarche and Droste found good agreement between experimental and calculated values for other packing materials.

Table 2-1. Oxidation power of various species commonly used in treatment applications  
(Adapted from Three Bond, 2004).

| Reactive Species        | Oxidation Potential (V) |
|-------------------------|-------------------------|
| Fluorine                | 3.03                    |
| Hydroxyl radical        | 2.80                    |
| Atomic oxygen (singlet) | 2.42                    |
| Ozone                   | 2.07                    |
| Hydrogen peroxide       | 1.77                    |
| Perhydroxyl radical     | 1.70                    |
| Permanganate            | 1.69                    |
| Hypobromous acid        | 1.60                    |
| Chlorine dioxide        | 1.56                    |
| Hypochlorous acid       | 1.49                    |
| Hypoiodous acid         | 1.46                    |
| Chlorine                | 1.36                    |
| Bromine                 | 1.09                    |
| Iodine                  | 0.73                    |

Table 2-2. Properties of Degussa P25 (Degussa Technical Bulletin, 1990)

| Degussa P25 Properties                     | Value      |
|--|------------|
| BET surface area ( $\text{m}^2/\text{g}$ ) | 50         |
| Average primary particle size (nm)         | 21         |
| Band gap: anatase, rutile (eV)             | 3.29, 3.05 |
| Point of zero charge                       | pH = 6.0   |

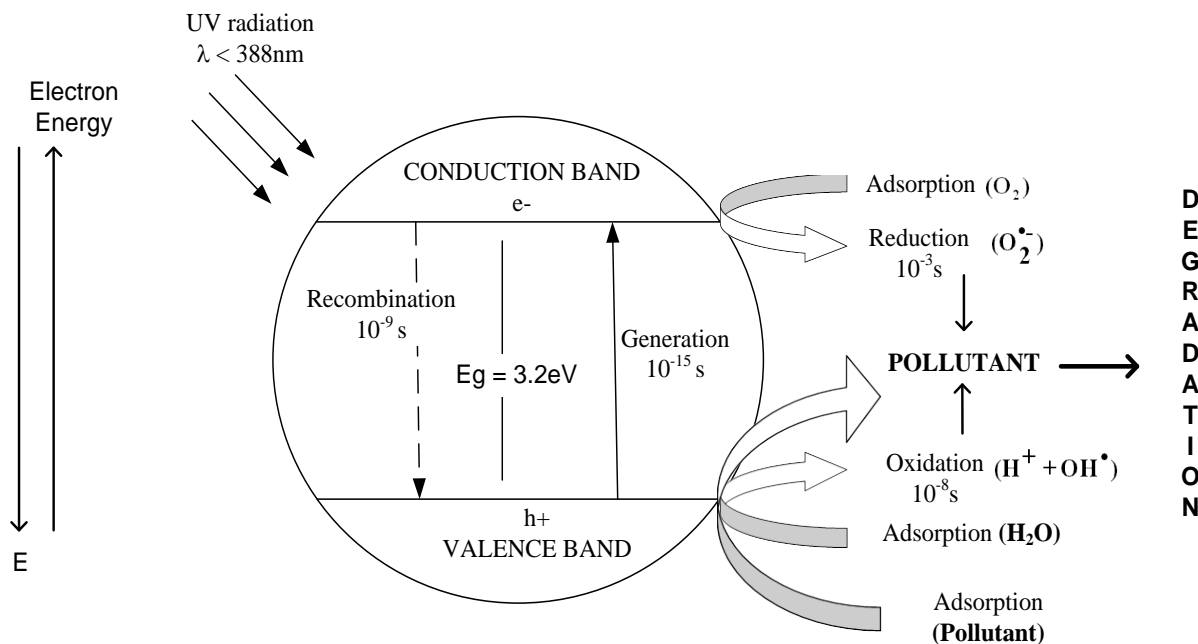


Figure 2-1. Energy band diagram of a spherical titania particle showing the basic reaction mechanism of  $\text{TiO}_2$  photocatalysis (Adapted from Herrmann, 2005).

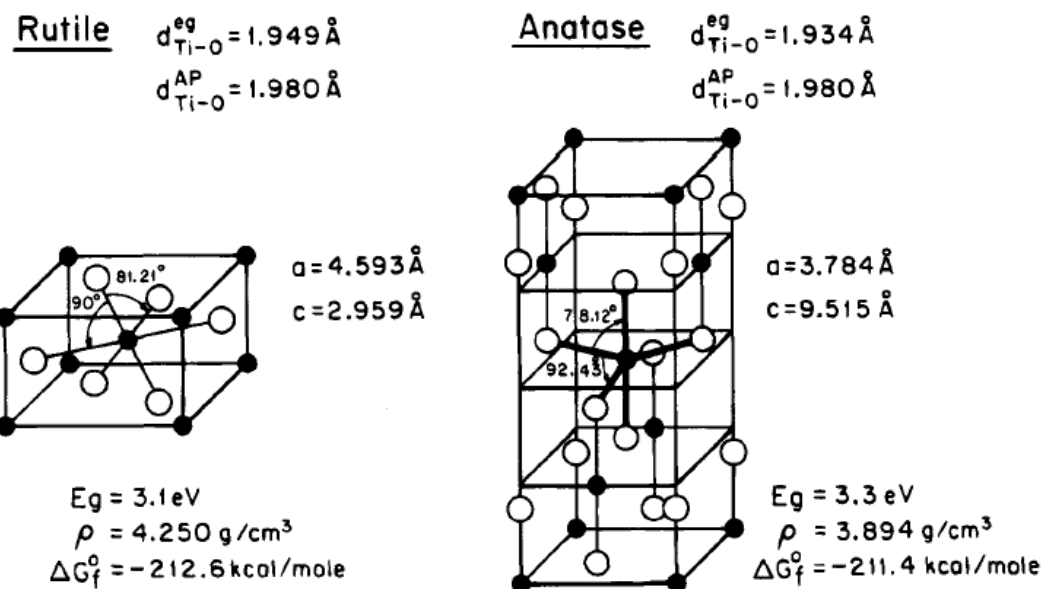


Figure 2-2. Structures and properties of rutile and anatase titanium dioxide (Obtained from Linsebigler et al., 1995).

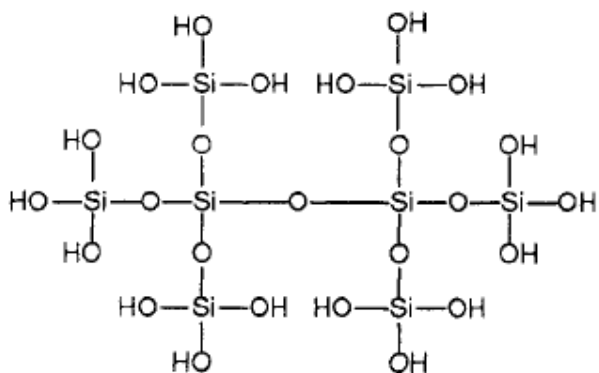


Figure 2-3. Linkages of  $\text{SiO}_2$  tetrahedras (Obtained from Hench and West, 1990)

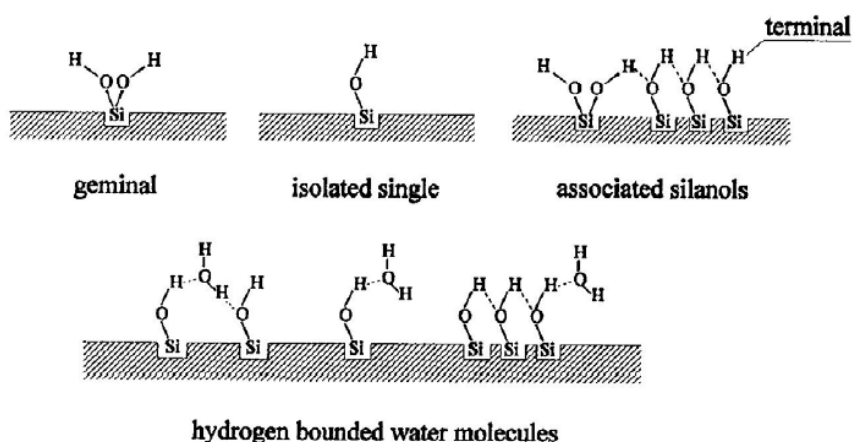


Figure 2-4. Silanol groups on the silica surface (Obtained from Legrand, 1998).

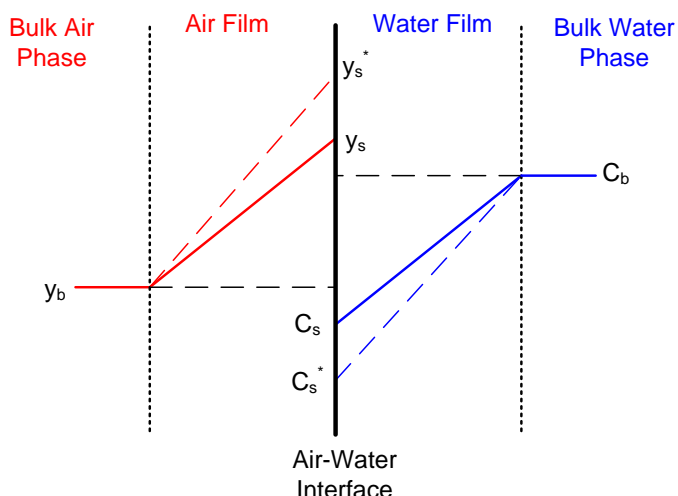


Figure 2-5. Diagram describing the equilibrium partitioning of a contaminant between the air and water phases using the two film theory.

## CHAPTER 3

### MATERIALS AND METHODS

#### **Pilot-Scale Reactor: Two-Phase Photocatalytic Oxidation Tower (TPOT)**

The two-phase photocatalytic tower (TPOT) was designed to simultaneously treat both air and water contaminated with VOCs, namely toluene. In some cases, however, the TPOT was used to test the removal of toluene in the gas or aqueous phases individually. The countercurrent flow reactor, built by Analytical Research Services (ARS), consisted of a clear PVC cylindrical column of 20.3 cm in diameter and 1.8 m in length. The tower was equipped with a liquid inlet and distributor in the form of a spray nozzle at the top; a gas inlet and distributor in the form of a perforated plate at the bottom; liquid and gas outlets at the bottom and top, respectively; three gas sampling ports vertically aligned 30.5 cm apart on the wall of the column; five 75W UV lamps emitting UV-C radiation (Phillips, TUV 64T5 4P SE UNP) covered by quartz envelopes; and packing occupying 1.2 m of the total height of the tower. The packing material was supported by the bottom perforated plate. CAD drawings of the reactor as well as its dimensions are shown in Figures 3-1 and 3-2, respectively. The colored fluid connections illustrated in Figure 3-1 represent the inlets and outlets for the liquid phase (in blue) and gas phase (in red).

The reactor design was based on criteria for the design of typical packed towers used as air strippers or absorbers. It is well established that the height of packed towers determines the mass transfer efficiency while the tower's cross section determines the capacity of the tower. Since the reactor was designed to improve and maximize the mass transfer between air and water phases as well as the diffusion from the bulk to the external surface and pores of the catalyst, the desired height had to be long to provide enough contact time and significant changes over reasonable sampling periods. The main factor controlling the diameter of the reactor was the diameter of the packing material. In order to minimize channeling or short circuiting of the water down the wall

of the tower, the ratio of tower diameter to nominal packing diameter should be greater than 12 (Treybal, 1980). Based on this criterion, a small packing material was desirable to minimize the diameter of the tower. The smallest commercially available tower packing found was plastic high flow rings with a nominal packing diameter of 15 mm (Rauschert Industries Inc.), which was used to compute the preferred minimum tower diameter.

The reactor packing consisted of silica-titania composites (STCs) commingled with the 15 mm nominal diameter plastic high flow rings shown in Figure 3-3. The composites were made of titanium dioxide embedded in a silica matrix which served as the  $\text{TiO}_2$  catalyst support which could be casted in any desired cylindrical pellets size. The commingled packing was chosen over the only STCs packing in order to decrease the pressure drop across the reactor, increase the interfacial area available for mass transfer and increase the penetration of UV irradiance. The packed section consisted of about 16% by bulk volume of STCs. The remaining volume was filled with plastic high flow rings, which had a void fraction of 91% and a specific surface area of  $313 \text{ m}^2/\text{m}^3$ . The porosity of the tower, determined by dividing the volume of water required to completely fill the packed section of the tower by the empty volume of the same section was 0.76. The mass percentages were 55% and 45% of the total mass in the reactor for STCs and high flow rings, respectively. A picture of the actual reactor packed with the palls rings and STCs during a typical experimental run is presented in Figure 3-4.

The lamps selected for the reactor emit short-wave UV radiation with a peak at 253.7 nm. Unlike most UV lamps emitting UV-C radiation, these lamps do not generate ozone because the lamp glass filters out the 185 nm ozone forming line (See Figure 3-5).

As shown by Equations 3-1 and 3-2, when an oxygen molecule absorbs light with energy at 185 nm, two oxygen atoms are produced. These atoms react with another oxygen molecule to

yield ozone, which is a strong oxidizing species. For the purpose of understanding the mechanisms involved in the degradation of toluene using TiO<sub>2</sub> photocatalysis, other extraneous factors that might contribute to toluene oxidation needed to be controlled, as is the case of ozone forming potential.



The reactor setup is shown in Figure 3-6. During a typical experimental run, aqueous phase toluene (Fisher, Certified ACS grade, >99.5% purity) at concentrations ranging from 150 ppb to 2500 ppb entered the reactor at the top inlet. The water was pumped from a 200 L feed tank to the top of the reactor by a centrifugal pump (AMPCO, Model KC2). Gas phase toluene entered the reactor at the bottom inlet of the tower. Concentrated toluene (100-1000 ppm<sub>v</sub>) from a compressed cylinder (Airgas) was diluted to approximately 1 to 10 ppm<sub>v</sub> by mixing it with air from an air compressor (Coleparmer, Model 07047) before entering the reactor. Samples were taken from the inlets ( $Y_o$ ,  $C_o$ ) and outlets ( $Y_e$ ,  $C_e$ ) for air and water as well as the 3 gas sampling ports on the tower wall.

Preliminary studies performed using the reactor packed with high flow rings only and single phase contaminant, showed that there were no significant losses of toluene in either the gas or aqueous phase due to piping, volatilization or photolysis. Additionally, the reactor showed high efficiency as an air stripper and absorber. The experimental results for these preliminary studies are shown in Appendix A

### Bench-Scale Reactor for Gas Phase Studies

Several studies on the degradation of gas phase toluene were carried out at the bench-scale. The reactor and setup used for these experiments, shown in Figure 3-7, consisted of a Pyrex annular reactor of 25 mm annulus with a 25 mm quartz envelope placed at the center of the

reactor packed with known masses of STCs to produce heights of approximately 4 to 8 cm. A porous glass frit at the bottom of the cylindrical reactor served as bed and envelope support. The STCs were packed on top of glass beads to improve gas distribution before reaching the catalyst. The porosity of the packed bed, determined by dividing the volume of the voids in the packed section by the empty volume of the same section was about 0.40. The same type of lamp used in the pilot reactor (Phillips, TUV 64T5 4P SE UNP) was used for the bench-scale studies. The intensity was measured using a digital UVX radiometer (UVP) connected to a 254 nm sensor (UVP, Model UVX-25). The intensity measured at the outside wall of the envelope was 15 mW/cm<sup>2</sup> while the intensities measured through the packing were 91 µW/cm<sup>2</sup> at 12.5 mm and 1.7 µW/cm<sup>2</sup> at 25 mm away from the outside wall of the envelope.

The gas stream flowed continuously through the reactor in a single pass configuration. During a typical run, toluene from a compressed cylinder (Airgas 100 ppmv) was diluted by mixing with breathing air from another compressed cylinder to a concentration of about 8 ppmv (30 mg/m<sup>3</sup>). The desired relative humidity (RH) was achieved by bubbling the air through a flask containing deionized water (DI) before mixing with toluene. The investigated range of RH at room temperatures of  $23 \pm 2^\circ\text{C}$  varied from 13%, obtained by bypassing the water bubbler, to 90%. The inlet and outlet RH and temperatures were measured using a Hygro-thermometer (EXTECH Instruments, 45320) and the temperatures inside the reactor and at the lamp envelope were monitored with thermocouples. Adsorption only experiments were performed at room temperature with the UV lamp turned off. For PCO experiments, no adsorption was allowed to take place before turning the lamp on, so the results show the combined effects of adsorption and PCO. For these experiments, the lamp and reactor were allowed to warm up for at least 1 h before starting the gas feed until they reached steady state temperatures corresponding to  $50 \pm$

3°C and  $83 \pm 2^\circ\text{C}$  for the reactor and lamp envelope, respectively. The gas volumetric flowrates ( $Q_G$ ) were varied from 12.5 to 26.7  $\text{cm}^3/\text{s}$  which produced superficial gas velocities ( $U_G$ ), defined as the volumetric flowrate divided by the cross-sectional area of the reactor normal to the flow ( $A$ ), across the annulus of 0.32 to 0.68  $\text{cm}/\text{s}$ . The experiments were run until steady state conditions were achieved. Influent and effluent samples were collected at different time intervals using 1 L teflon bags (SKC Inc.) and analyzed the same day. Control experiments were performed in the absence of the catalyst to ensure that toluene did not undergo photolysis or other losses due to adsorption to the systems' appurtenances.

### **UV Irradiance Distribution in the Reactor**

Providing a uniform ultraviolet (UV) radiation throughout the reactor is of great importance because the energy emitted by the photons activates the catalyst, which is the first step required for the degradation of toluene. The silica – titania composites (STCs) were commingled with the plastic high flow rings to allow further UV light penetration in the reactor and reach as many catalyst sites as possible. To demonstrate the advantage of the commingled packing compared to only STCs and to determine the UV distribution in the reactor, the UV-C irradiance ( $\lambda = 254 \text{ nm}$ ) was measured at different distances from the UV lamp and through different types of packing. The irradiance was measured using a digital UVX radiometer (UVP, Part No. 97-0015-0) implemented with a 254 nm sensor (UVP, Model UVX-25). Initially, the irradiance was measured as a function of lamp length to ensure that the output of the lamp was constant throughout its length. Figure 3-8 shows the UV irradiance as a function of lamp length averaged for measurements taken using two different lamps. The lamps were allowed to warm up for 15 minutes before the measurements were taken to ensure that the temperature would not influence the intensity measurements. The UV irradiance was measured at 2 different distances

from the lamp ( $X$ ), 0.95 cm and 6.25 cm. The results show that the irradiance is constant throughout the length of the lamp, except for the first 10 cm close to each end of the lamp, which showed lower irradiance. The average UV intensities measured were  $13.6 \text{ mW/cm}^2$  and  $3.9 \text{ mW/cm}^2$  for the distances of 0.95 and 6.25cm, respectively. The intensities were averaged for lamp lengths between 20 cm to 130 cm, so that the lower end intensities were not included. The irradiance greatly decreased when the detector is placed further from the lamp.

After verifying that the irradiance did not significantly change throughout the lamp length, the UV intensity was measured using different packing materials. The test setup is shown in Figure 3-9. The packing materials that were tested included: (a) air (as the blank), (b) high flow rings, (c) high flow rings commingled with STCs, and (d) STCs. The UV irradiance through air was determined using a cardboard box in several configurations: (1) the cardboard box, (2) the same box with the walls covered by aluminum foil but uncovered at the top, and (3) the aluminum foil covered box also covered at the top. The results for the irradiance as a function of distance to the lamp through air are shown in Figure 3-10. As observed in Figure 3-10, the UV intensity decreases exponentially with the increase of the distance from the lamp when there is no packing between the UV-C sensor and the lamp. Additionally, the irradiance is higher when the box is covered by aluminum foil due to increase in reflection of the light in the presence of the foil. Generally, the intensity should decrease as a function of the inverse square of the distance. This is not the case for the results shown above for air. This can be explained by the errors produced by the radiometer readings. The number that the radiometer reads out is a function of the spectral response of the radiometer, coupled with the spectral output of the emitter and taking into account the radiometer spatial response. The spectral response and output were calibrated for the 254 nm lamp used, but the spatial response becomes important when

measuring the irradiance at a surface near an extended emitter, such as the long 147 cm lamp used in the tower and these experiments. The sensor gives accurate measurements for point sources that are small in comparison with distance, and they produce lower measurements when used to measure extended light sources at relative small distances (UVP Inc.).

Experiments through the other packing styles were performed by using the cardboard box without covering the walls with foil to better model the surface of the actual reactor which is PVC and thus non-reflective. The results for these experiments are shown in Figure 3-12. The results presented in this figure include data for “small STCs” which refers to STCs of 3 mm in diameter by 5 mm in length that have been used in other studies. The results for these STCs were obtained from the work of Stokke (2008).

Placing any type of packing between the UV lamp and the sensor decreased the UV irradiance dramatically, as shown in Figure 3-11 by the large differences between the irradiances obtained through air and through different packing materials. The high flow rings allowed the highest UV penetration through the packing while the small STCs allowed the lowest penetration. UV penetration of the commingled packing was lower than for the packing of high flow rings only; however, the commingled packing allowed the UV to penetrate up to a distance of approximately 6 cm which is significantly greater than the 2.5 cm permitted by either type of STCs. Not only was the UV penetration greater for the commingled packing, but also the intensity measured at a given distance was orders of magnitude larger up to about 3 cm from the lamp. These results show that packing the reactor with the commingled high flow rings and STCs provides an advantage since the UV lamps can be further spaced as compared to only STCs, and a better UV radiation distribution can be achieved. These results are very important since the number of lamps in the reactor relates directly to energy costs and temperature increase

in the reactor, two factors that are of high importance in large scale applications. The actual placement of the UV lamps in the TPOT is shown in Figure 3-13.

The UV irradiance distribution in the reactor was calculated based on the results shown in Figure 3-12. The trend observed for the UV irradiance as a function of distance to the lamp for the commingled packing was fit using two models for different sections of the curve, as shown in Figure 3-14. The UV irradiance for distances between 1.3 and 2.5 cm was fit using a linear regression between those two points, given by Equation 3-3. The rest of the graph, i.e. distances to the lamp between 2.5 and 6.3 cm was fit with a third degree polynomial presented in Equation 3-4, where  $X$  is the distance to the UV lamp in cm and the UV irradiance ( $I$ ) is given in  $\mu\text{W}/\text{cm}^2$ .

$$I = 1490.03 \times X + 4092.33 \quad (3-3)$$

$$I = -4.847 \times X^3 + 96.534 \times X^2 - 634.020 \times X + 1374.7 \quad (3-4)$$

By integrating the regression equations and dividing the integral by the difference between the integral bounds (Equation 3-5), the average UV intensity was determined for annuli of about 1.3 cm from the lamp increasing up to 6.3 cm as shown in Table 3-1.

$$\text{Average} = \frac{\int_a^b f(x)dx}{b-a} \quad (3-5)$$

Any packing placed at a distance greater than 6.3 cm. was considered to receive no UV irradiation. The UV intensity from 0 and 1.3 cm. from the lamp was considered to be the intensity at 1.3 cm since no other smaller distances were measured. The intensity at distances closer than 1.3 cm to the lamps is expected to be greater than the assumed intensity, but this value was used to obtain a conservative estimate of the irradiance. Using the results in Table 2, the graph in Figure 3-15 was developed showing the UV intensity distribution in the tower for any cross-section of the reactor. This figure shows that 70% of the cross-sectional area of the

tower receives some UV radiation while the rest of the area does not seem to receive any irradiation. Using the intensities calculated in Table 3-1 and the areas determined for each 1.3 cm annulus around the UV lamp, the total intensity in each annulus was calculated. For the sections where annuli overlapped, the sum of the intensities of the overlapping annuli was used. The average intensity for the section of the surface that is irradiated was then multiplied by the length of the lamp and this value was divided by the total mass of irradiated STCs inside the reactor (70% of the total STCs mass). The average intensity in the reactor was found to be about 65  $\mu\text{W}$  per gram of irradiated STC or 220  $\mu\text{W}$  per gram of irradiated  $\text{TiO}_2$ .

### **Synthesis of the Silica-Titania Composites (STCs)**

The silica-titania composites (STCs) were prepared by a sol-gel method initially developed by Powers (1998), which used nitric acid and hydrofluoric acid as catalysts to decrease the gelation time by increasing the hydrolysis and condensation rates. The actual formula used to prepare STCs was obtained from Londeree (2002), who adapted Powers (1998) formula to use tetraethylorthosilicate (TEOS) as the silica precursor instead of tetramethylorthosilicate (TMOS) and incorporated the  $\text{TiO}_2$  catalyst in the silica matrix. For this research, the formulation was further modified to decrease the volume of ethanol by 50%. By this formulation, nanopure water, ethanol (Fisher, 200 proof), TEOS, 1M nitric acid (diluted from Fisher, Certified ACS) and 3%<sub>v</sub> hydrofluoric acid (diluted from 49% Fisher Certified ACS) were mixed in volume ratios of 12:6.25:9.25:1:1, respectively. While mixing, 115 mg of  $\text{TiO}_2$  (Degussa P25) were added to the mixture per mL of TEOS to obtain STCs containing about 30%<sub>wt</sub>  $\text{TiO}_2$ . The volumes of the chemicals used in the formulation to prepare one batch of STC are shown in Table 3-3; the components were added in the same order as presented in the table. The titanium dioxide used for all synthesis and experiments had a measured surface area of  $49 \text{ m}^2/\text{g}$ , as measured by a Quantachrome Autosorb 1C-MS gas sorption analyzer (NOVA 2200e).

The content of each batch was stirred in a Nalgene container and mixed for 20 minutes to allow gelation to occur. The resulting solution was pipetted into Costar polystyrene 24 well assay plates. Since the pellets in the reactor are bigger than those originally prepared by Londeree (2002), the drying schedule was also modified. The complete drying schedule is presented in Figure 3-16. The assay plates were covered with tightly sealed plastic bags to prevent premature evaporation. The aging process included 3 stages: sealed STC drying at room temperature for 3 days followed by 3 days in the oven at 73°C, and continued by another 3 days at 73°C but with the trays uncovered to allow some evaporation. Higher aging temperatures than 73°C would decrease the aging time, but since the casting molds are made of polystyrene, the maximum recommended temperature was 80°C. The maximum temperature (80°C) was not used because it was found that using such temperature quickly damaged the assay plates.

After aging, the pellets were placed in high temperature resistant trays and exposed to a series of heat treatments using a programmable oven. Initially the temperature was ramped from 25°C to 103°C at a rate of 2°C/min and held constant for 18 hrs. Next, the temperature was increased to 180°C and held for 6 hrs and slowly decreased to room temperature at 2°C/min. The last heat treatment in the process was curing at 450°C for about 2 hrs.

### **Characterization of the STCs**

Several representative samples (about 20) of multiple batches prepared to make STCs were obtained and analyzed to characterize the composites for their surface area, average pore size and pore volume. Nitrogen adsorption-desorption analyses were conducted using a Quantachrome Autosorb 1C-MS gas sorption analyzer (NOVA 2200e). During the analyses, mortar and pestel crushed STC samples were outgassed for 24 hours at 180 °C. The Brunauer, Emmett, and Teller (BET) model was used to determine the specific surface area of the STCs for the nitrogen adsorption/desorption data obtained from the isotherms ( $P/P_0 = 0.1$  to  $0.3$ ). The total pore

volume was determined by nitrogen adsorption at a relative pressure of  $P/P_0 = 0.99$ . The average pore size of the composites was calculated using Equation 3-6.

$$d = 4 * V_p / S \quad (3-6)$$

where  $d$  is average pore diameter,  $V_p$  is total pore volume, and  $S$  is specific surface area.

The pore size distribution (PSD) was computed using the method proposed by Barret, Joyner and Halenda (BJH), which assumes cylindrical pore geometry (Barret, 1951). For PSD calculations, desorption isotherms were used since they are generally accepted to be more appropriate than adsorption isotherms for PSD analysis.

A major concern about using silica embedded composites and casting them in a pellet shape was the loss of activity related to the loss of accessible catalyst surface area due to the potential entrapment of the  $TiO_2$  molecules when supported by silica. To determine if the activity of the STCs would remain unchanged in the mixed oxide and the pellet form, the  $TiO_2$  surface area accessible in the composite was analyzed using the functionalization procedure proposed by Marugan et al. (2007). This method measures the amount of phenylphosphonic acid ( $C_6H_7O_3P$ , PPA) that is reacted with titania to determine the surface area by assuming that the phosphorus (P) atoms incorporated in the composite during reaction are proportional to the  $TiO_2$  accessible surface area. PPA is used in the procedure because it can selectively react with titania in the presence of both silica and titania when the PPA solution is aqueous (Mutin et al., 2004). The method used consisted of mixing 200 mg of the STCs (or Degussa P25) with 200 mL of a 4 mM PPA solution prepared with a 4:1  $CH_3OH:H_2O$  (v/v) mixture. The PPA solution was allowed to mix with the composite material for at least 24 h under vigorous stirring to ensure enough time for the PPA molecules to bond with all the accessible  $TiO_2$  likely through Ti – O – P bonds as proposed by Mutin et al. (2004). The solids were then separated by filtering with a  $0.45 \mu m$

nylon filter and rinsed with at least two times the volume of the sample to ensure complete removal of PPA molecules that were not attached to the surface. The solids were finally dried for 24 h at 110°C. The catalyst was then dissolved by hydrofluoric acid attack. The catalyst digestion procedure was carried out by mixing about 42 mg of the dried sample in a digestion vessel per liter of a solution containing aqua regia (3:1 solution of 12 M HCl and 15 M HNO<sub>3</sub>) and 29 M HF in volume ratios of 1:5. After 24 hrs of digestion, 8.3 mL and 7.1 mL of H<sub>3</sub>BO<sub>3</sub> and nanopure water, respectively, were added per mL of digested solution. The resulting solution was analyzed for P using a Perkin-Elmer Plasma 3200 Inductively Coupled Plasma – Atomic Emission Spectroscopy (ICP-AES) system at a wavelength of 214.914 nm. The P content was correlated to the accessible TiO<sub>2</sub> surface area of the composite using the following two formulas.

$$\text{P atoms/nm}^2 \text{ TiO}_2 = [(\text{P concentration}) (\text{mg P/L})] \times [(\text{TiO}_2 \text{ loading})^{-1} (\text{L/mg TiO}_2)] \times [(\text{BET SA}_{\text{TiO}_2})^{-1} (\text{g TiO}_2/\text{m}^2)] \times [(10^{-18}) (\text{m}^2/\text{nm}^2)] \times [(30,973.76)^{-1} (\text{mol P/mg P})] \times [(6.022 \times 10^{23}) (\text{atoms P/mol P})]$$

$$\text{m}^2 \text{ TiO}_2 / \text{ g STC} = [(\text{P concentration}) (\text{mg P/L})] \times [(\text{STC loading})^{-1} (\text{L/mg STC})] \times [(\text{P surface coverage})^{-1} (\text{nm}^2 \text{ TiO}_2 / \text{atoms P})] \times [(6.022 \times 10^{23}) (\text{atoms P/mol P})] \times [(30,973.76)^{-1} (\text{mol P/mg P})] \times [(10^{-18}) (\text{m}^2/\text{nm}^2)]$$

The first formula determines the surface concentration of P atoms in the surface of pure TiO<sub>2</sub> Degussa P25 (no silica present) from the P concentration obtained by the ICP and the measured BET surface area of Degussa P25 (49 m<sup>2</sup>/g). The resulting value, in atoms of P per nm<sup>2</sup>, was used in the second equation to find the accessible TiO<sub>2</sub> surface area of the STCs.

### **Analytical Methods for Toluene and Oxidation Byproducts**

Since two phases of toluene, gas and aqueous phases, were investigated in this research, the analytical methods were developed such that minimum changes would have to be incorporated when analyzing either phase of the compound. Both phases of toluene were

analyzed using USEPA Method 524.2: Measurement of Purgeable Organic Compounds in Water by Capillary Column Gas Chromatography/ Mass Spectrometry. A ThermoQuest Trace GC/MS with a Tekmar 3100 Purge & Trap extraction system was used in this research. This GC/MS was implemented with a Rtx – VMS capillary column (Restek, cat # 19919). The Purge & Trap apparatus used a Vocarb 3000 trap to capture VOCs.

Aqueous phase toluene samples were collected in 40 mL vials with no headspace and stored at 4°C for no longer than 2 weeks to maintain the sample's integrity, based on the guidelines provided by USEPA Method 524.2. When analyzing these samples, 5 mL of the sample were introduced in the Purge & Trap where the sample was purged and the contaminants captured by the trap using the conditions presented in Table 3-3, to be finally desorbed to the GC/MS for separation and detection. Since minimum changes were desired in the analytical system configuration, the extraction of gas samples was very similar to the extraction of aqueous samples.

The gas phase samples were collected in tedlar bags and analyzed in a timely manner since studies have shown that the recovery of samples stored in tedlar bags decreases significantly with time (Andino and Butler, 1995; McGarvey and Shorten, 2000). For this research, it was determined that the samples should be analyzed within four days from collection because keeping the samples for any longer caused significant losses of the samples due to possible adsorption to the bags. Additionally, cleaning the bag immediately after use was also of utmost importance to keep the bags free of contamination. The cleaning procedure developed that worked best consisted of flushing the bags 10 times with air followed by 10 times of nitrogen flushing. The typical process for analyzing gas phase samples consisted of initially injecting 5 mL of DI water in the P&T apparatus. The purpose of the water was to provide the same

humidity conditions for all samples. Then, 5 mL of the gas sample stored in the teflar bag were extracted with a gas tight syringe (Hamilton SampleLock, Series 1705). At this point, the purge schedule in the P&T was initiated. While purging, the injection valve in the P&T was opened and the gas sample in the syringe was injected in the apparatus slowly to avoid overloading the trap since the optimal trap efficiency of VOCs was about 60 mL/min, and the purging gas (helium) was constantly flowing at 35 mL/min. Hence, an injection rate of about 5 mL/min was found to provide satisfactory results. After the gas injection, the valve is closed and the sample continued purging. After purging, the captured sample was desorbed to the GC/MS for analysis following the same oven temperature schedule as for aqueous phase samples shown in Table 3-3.

For all samples analyzed, the response factors (RF) were determined using an internal standard calibration, with fluorobenzene as the internal standard. The reliability of the GC/MS analysis was verified using the percent relative standard deviation (*RSD*), which is based on the *RF* of a chemical. The *RF* and *RSD* were calculated using Equations 3-7 and 3-8, respectively.

$$RF = (A_X \times C_{IS}) / (A_{IS} \times C_X) \quad (3-7)$$

$$RSD = 100 \times (S_{RF} / M_{RF}) \quad (3-8)$$

where  $A_X$  is the GC peak area of the target analyte,  $A_{IS}$  is the area of the internal standard,  $C_X$  and  $C_{IS}$  are the concentration of the target analyte and internal standard, respectively,  $S_{RF}$  is the standard deviation of the response factors and  $M_{RF}$  is the average response factor. The USEPA method required RSD below 20%. For all analyses, the RSD was always below 10%. The minimum detection limit (*MDL*) for each phase of toluene was also determined by analyzing 7 samples at the same low concentration and using Equation 3-9.

$$MDL = SD \times t_{a=99\%, n-1} \quad (3-9)$$

where  $SD$  is the standard deviation of the replicate analyses,  $t$  is the student's t-value for 99% confidence level with  $n-1$  degrees of freedom ( $t = 3.143$ ), and  $n$  is the number of replicates ( $n = 7$ ). The  $MDL$  for the gas phase was  $0.5 \mu\text{g/L}$  or  $0.13 \text{ ppm}_v$  while for the aqueous phase was about  $1 \mu\text{g/L}$ .

The oxidation byproducts monitored during some of the experimental runs were benzene, benzaldehyde, benzyl alcohol, benzoic acid and phenol. The method used to detect toluene, USEPA Method 524.2, also detected benzene. The other potential oxidation byproducts were expected to be found mostly adsorbed to the catalyst surface, so an extraction procedure was used in the cases where catalyst deactivation was encountered. The extraction consisted of placing the crushed STCs in acetonitrile for 2 h. The suspension was separated using  $0.45 \mu\text{m}$  cellulose acetate filters and the solution was analyzed using a High Performance Liquid Chromatography (Hitachi, D-7000).

Table 3-1. Calculated average UV intensity through the commingled packing at different annuli distances from the UV lamps.

| $X$ (cm)  | Avg. $I$ ( $\mu\text{W}/\text{cm}^2$ ) |
|-----------|--|
| 0 - 1.3   | 2200                                   |
| 1.3 - 2.5 | 1254                                   |
| 2.5 - 3.8 | 187                                    |
| 3.8 - 5.1 | 43                                     |
| 5.1 - 6.3 | 1.4                                    |

Table 3-2. Chemicals used in the STC formulation to produce one batch of  $140\text{\AA}$  STC with 30% by mass titania loading.

| Chemical                               | Amount |
|--|--------|
| Nanopure water (DI) (mL)               | 96.0   |
| Ethanol (mL)                           | 50.0   |
| TEOS (mL)                              | 74.0   |
| 1N Nitric Acid (mL)                    | 8.0    |
| 3% <sub>v</sub> Hydrofluoric Acid (mL) | 8.0    |
| Titanium dioxide (g)                   | 8.5    |

Table 3-3. Conditions of the GC/MS and Purge & Trap used for the analysis of gas and aqueous phase toluene.

| Tekmar 3100 Purge and Trap Conditions |  |           |
|---------------------------------------|--|-----------|
|                                       | Aqueous Phase  | Gas Phase |
| MCS Line temperature                  | 40°C   | 40°C      |
| Purge time                            | 10 min   | 5 min     |
| Dry purge time                        | 2 min  | 0 min     |
| Trap type                             | Carbopack B, Carboxen 1000 and Carboxen 1001                     |           |
| Desorption preheat temperature        | 220°C  | 220°C     |
| Desorption time                       | 6 min  | 6 min     |
| Bake temperature                      | 270°C  | 270°C     |
| Bake time                             | 10 min   | 10 min    |
| ThermoQuest Trace GC/MS Conditions    |  |           |
| Column                                | Restek, Rtx – VMS (fused silica)<br>30 m x 0.32 mm x 1.8 $\mu$ m |           |
| Program                               | 40°C (4 min) to 180°C at 10°C/min (2 min) to 200<br>at 20°C/min  |           |
| Carrier                               | Helium   |           |
| Detector                              | Ion trap, MS, m/z = 45-260 (0.6sec/scan)                         |           |

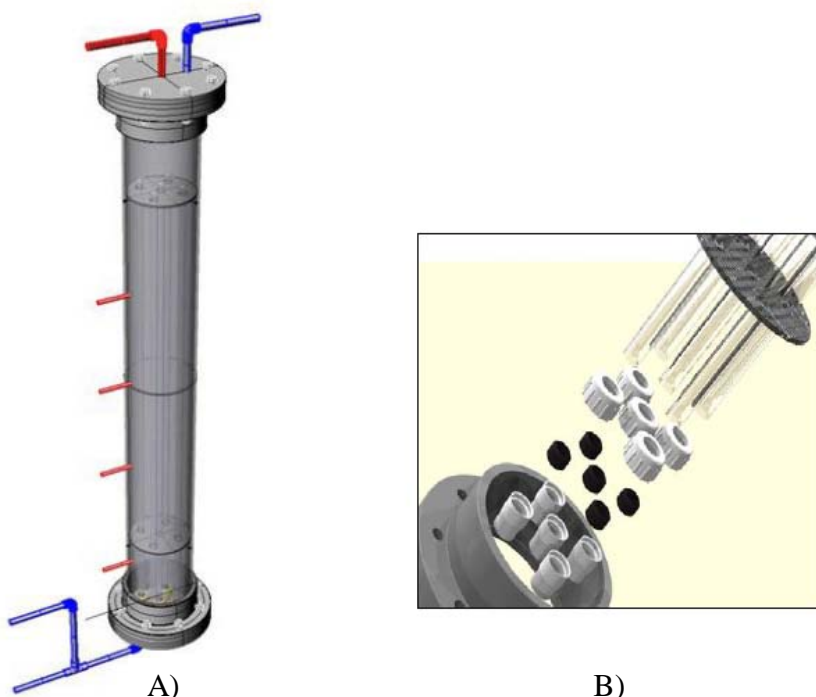


Figure 3-1. CAD drawings of the reactor. A) Figure depicting the final reactor design. B) Illustration of the UV lamp connections at the bottom section of the reactor (ARS, 2005)

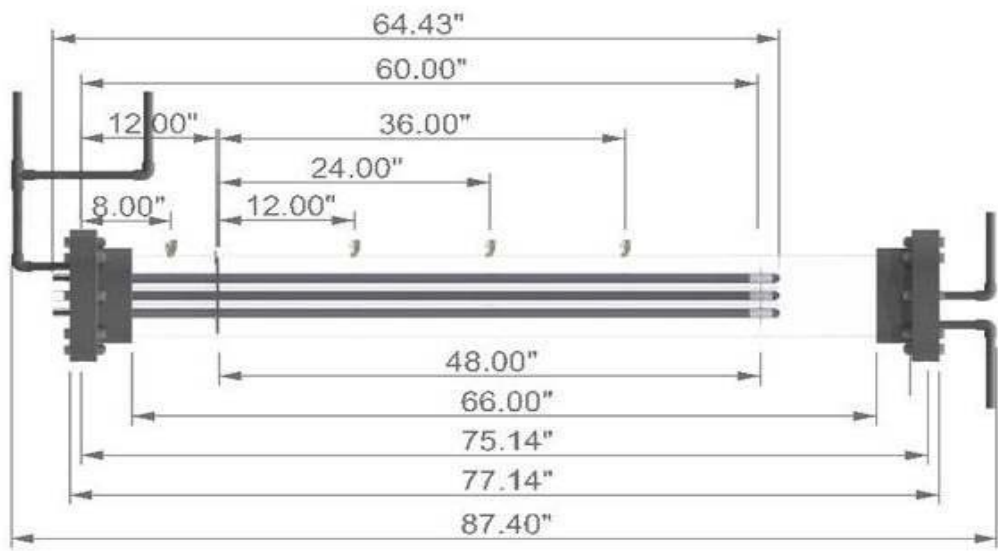


Figure 3-2. Dimensions of the TPOT reactor shown in horizontal configuration. (ARS, 2005).

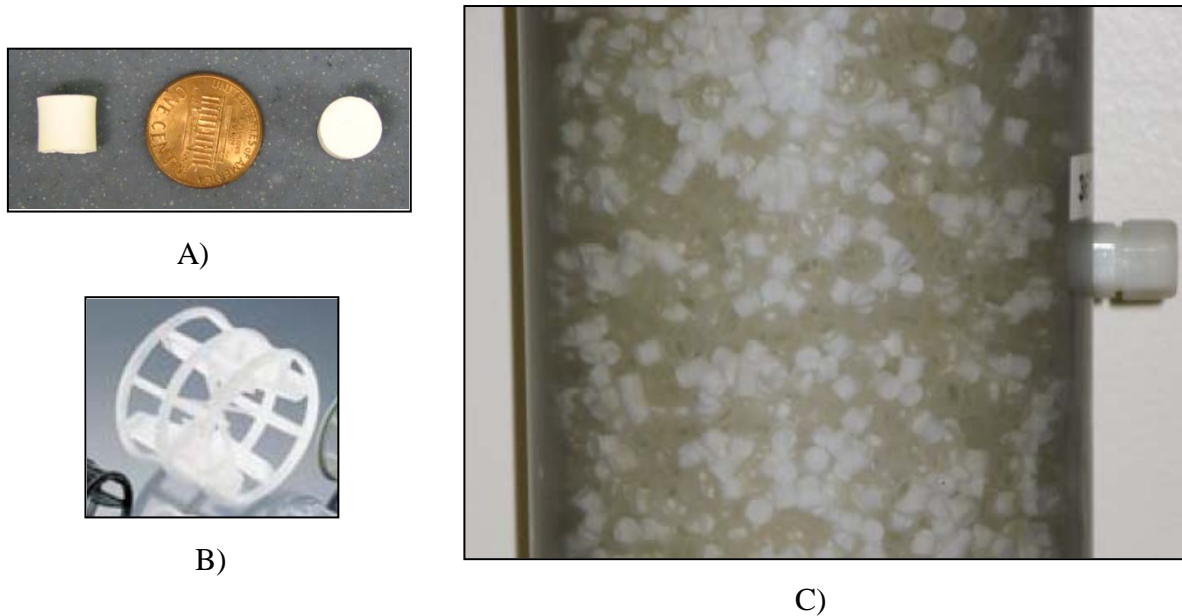


Figure 3-3. Picture of the two different packing materials that make up the commingled packing in the TPOT. A) STCs. B) High flow rings. C) Commingled packing: STCs and high flow rings.



Figure 3-4. Photograph of the reactor (TPOT) during a typical experimental run.

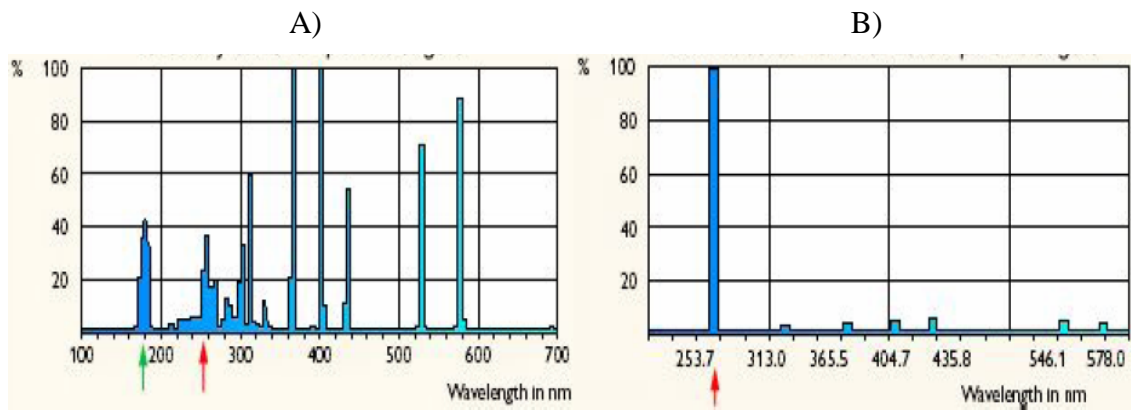


Figure 3-5. Emission spectrum of UV-C lamps: A) ordinary and B) non-ozone producing UV-C lamps.

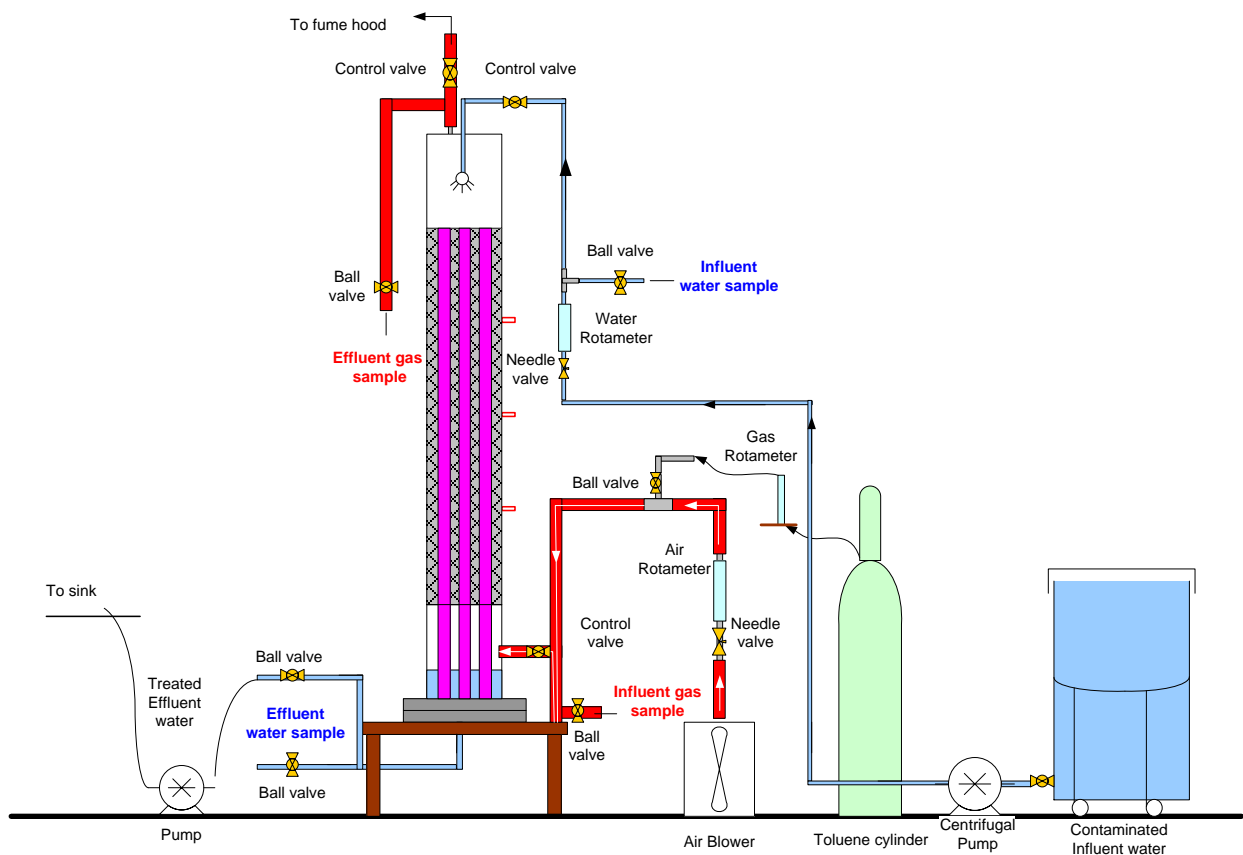


Figure 3-6. Reactor setup for a typical experimental run

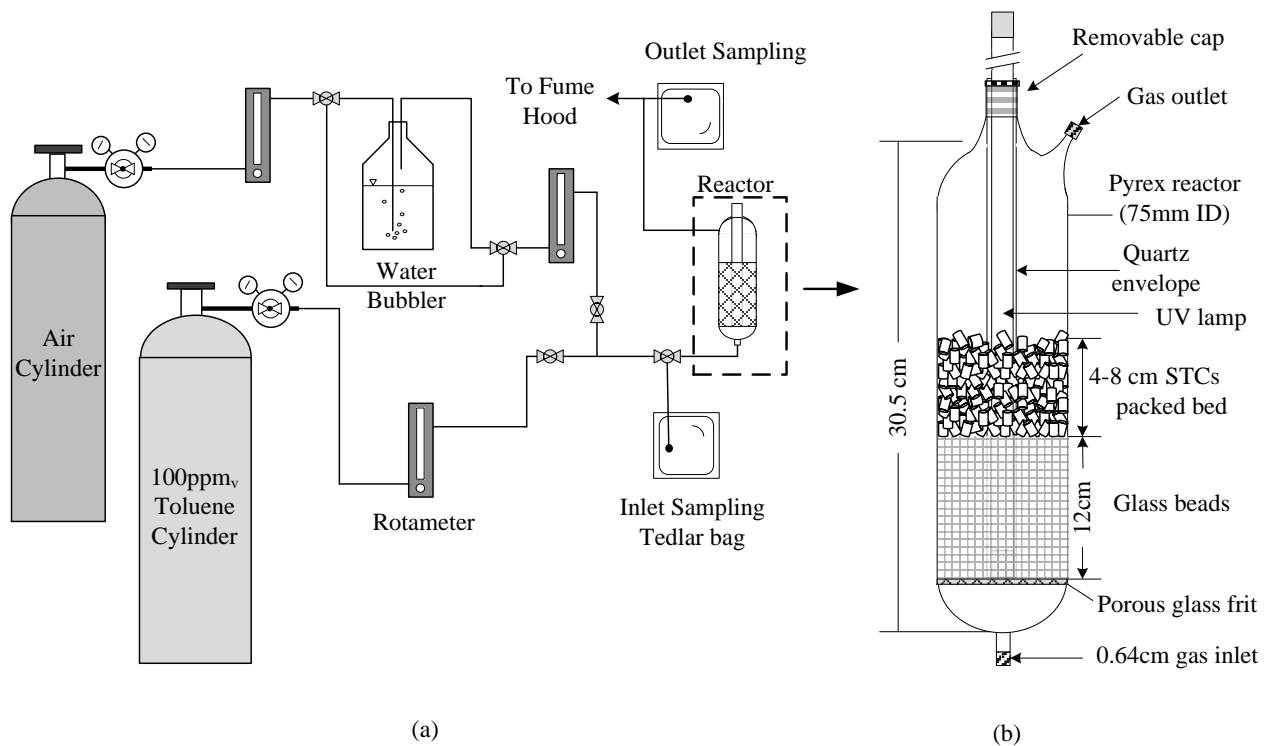


Figure 3-7. Gas phase experimental setup and reactor. (a) Schematic of the experimental setup. (b) Photocatalytic packed bed reactor.

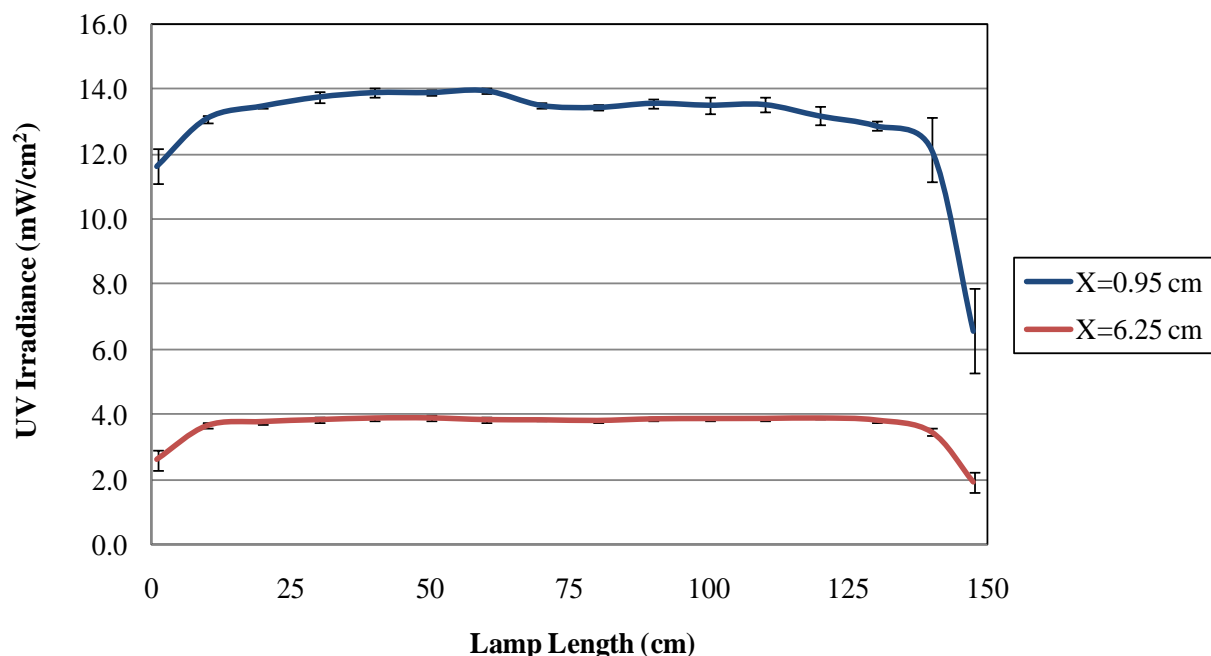


Figure 3-8. UV irradiance as a function of lamp length measured in ambient air with the UV radiometer sensor placed at 0.95cm and 6.25 cm from the lamp.

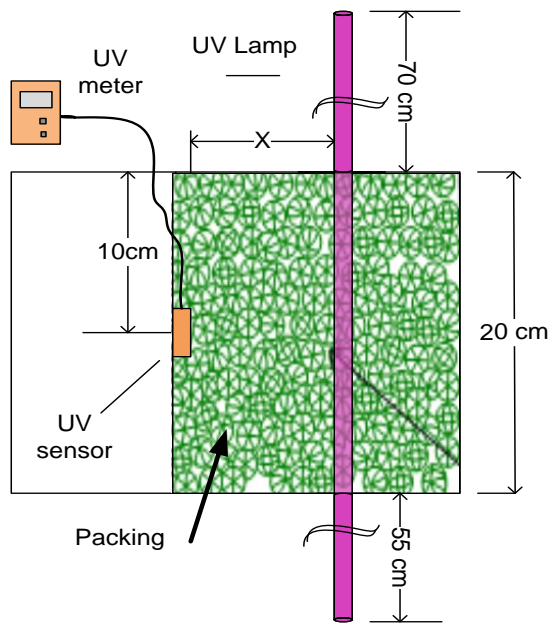


Figure 3-9. Top view of the box setup used to measure the UV intensity as a function of different packing materials at different “X” distances from the lamp.

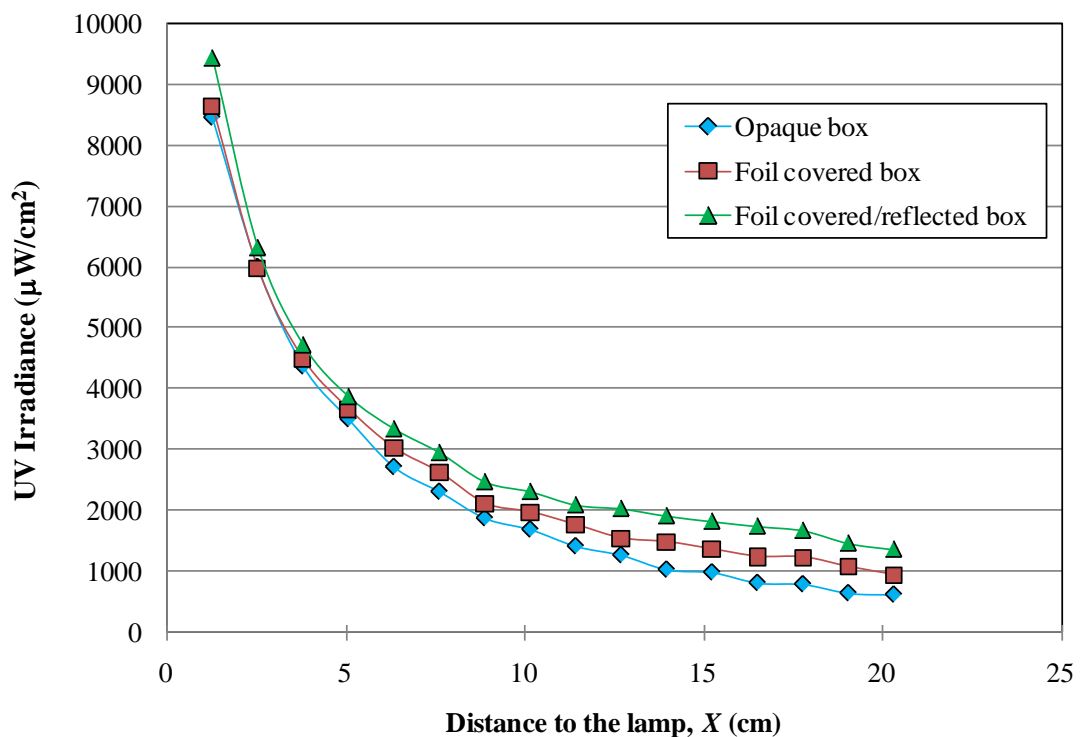


Figure 3-10. UV irradiance as a function of distance to the lamp through ambient air using the set up of Figure 3-9 for different extents of reflective surfaces.

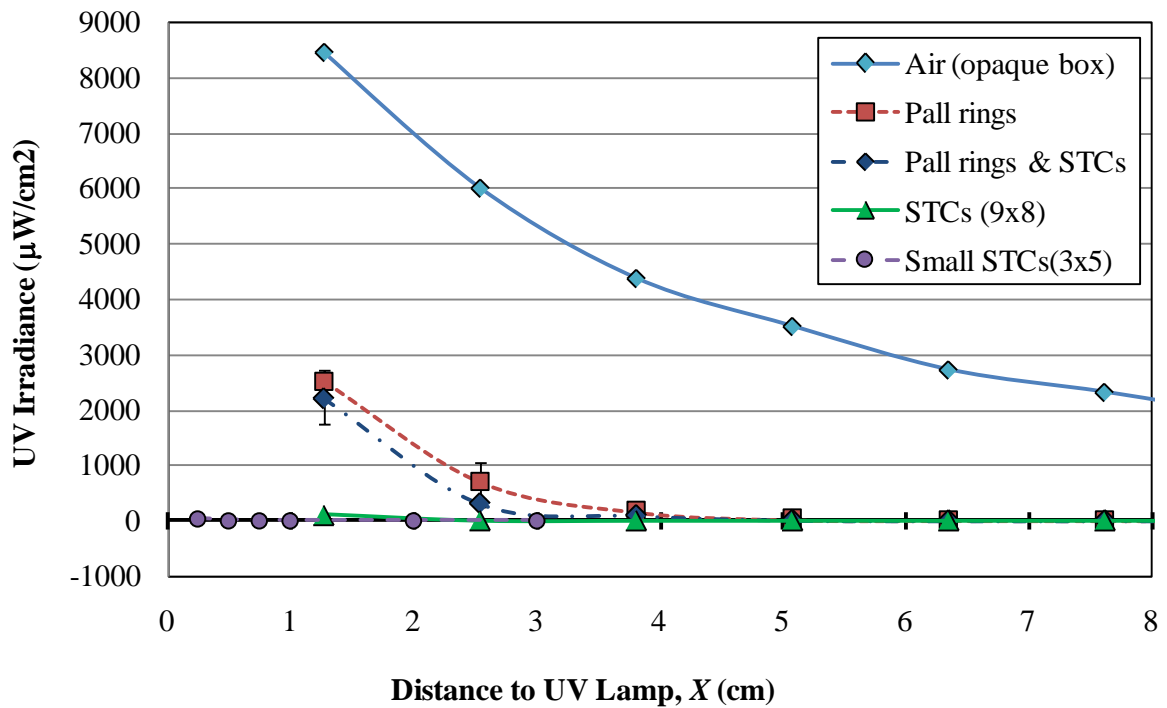


Figure 3-11. UV intensity as a function of the distance from the UV lamp through different packing materials.

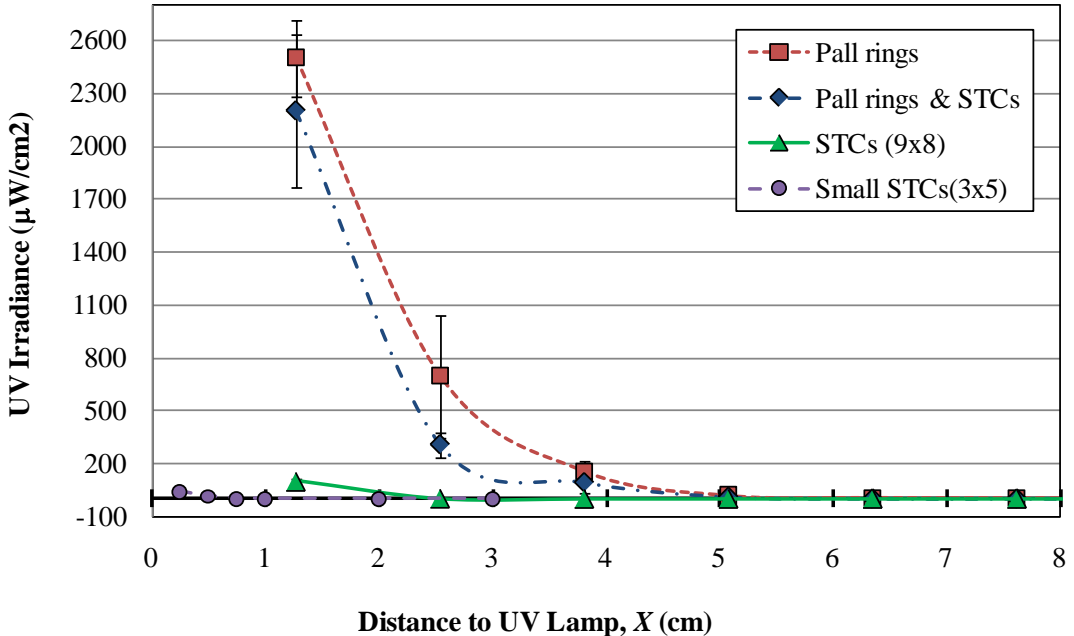


Figure 3-12. Enlarged version of Figure 3-11

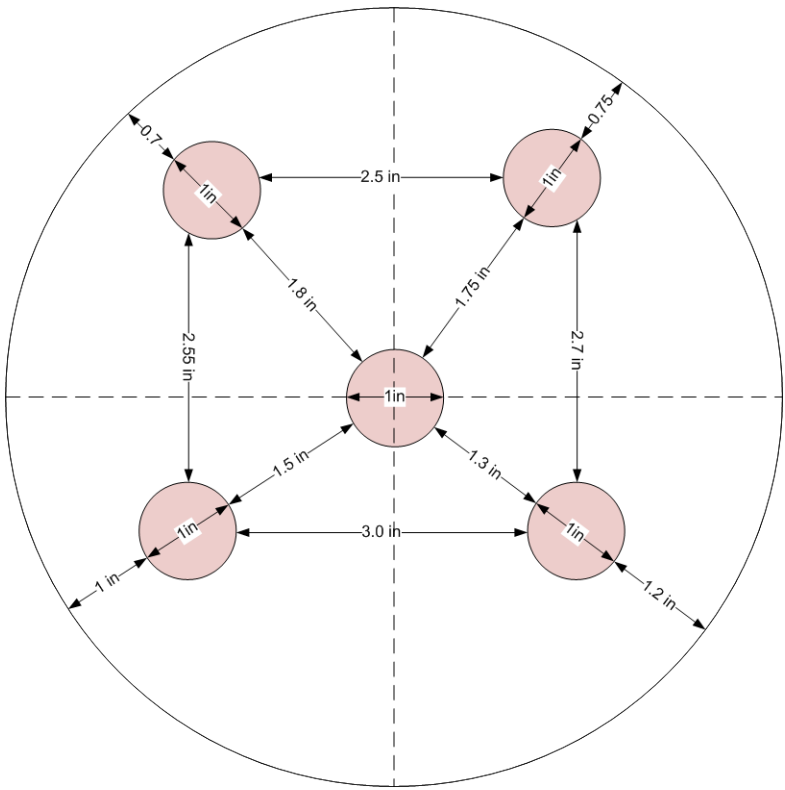


Figure 3-13. Actual placement of the five UV lamps inside the TPOT measured after packing the reactor with the commingled packing.

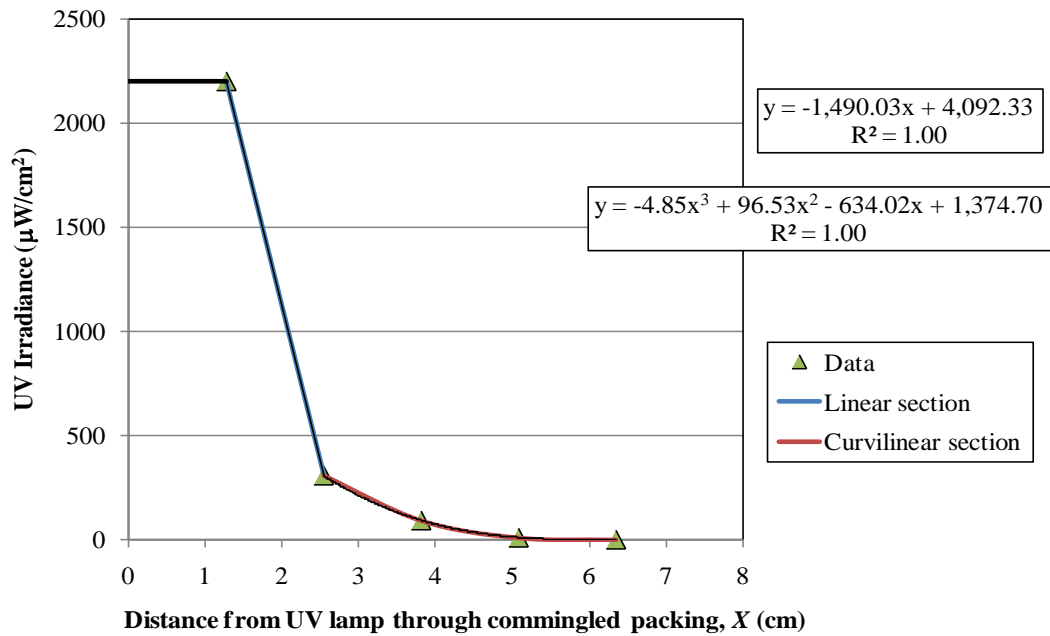


Figure 3-14. Fit of the data obtained for UV intensity through the commingled packing.

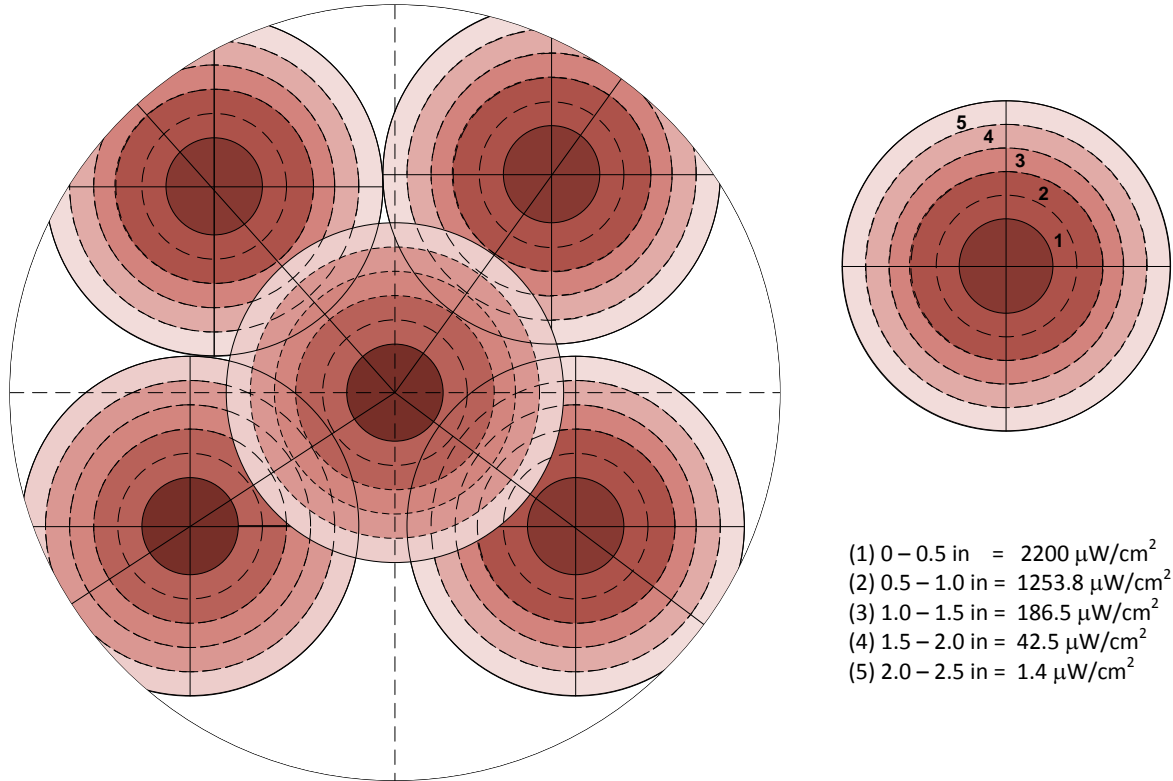


Figure 3-15. UV irradiance distribution inside the reactor. Inner most (darkest) circles represent the UV lamps. The concentric circles around the lamps show the UV intensity for every 1.3 cm annuli, corresponding to the intensities in Table 3-1. Note intensities from each lamp are not added in this figure.

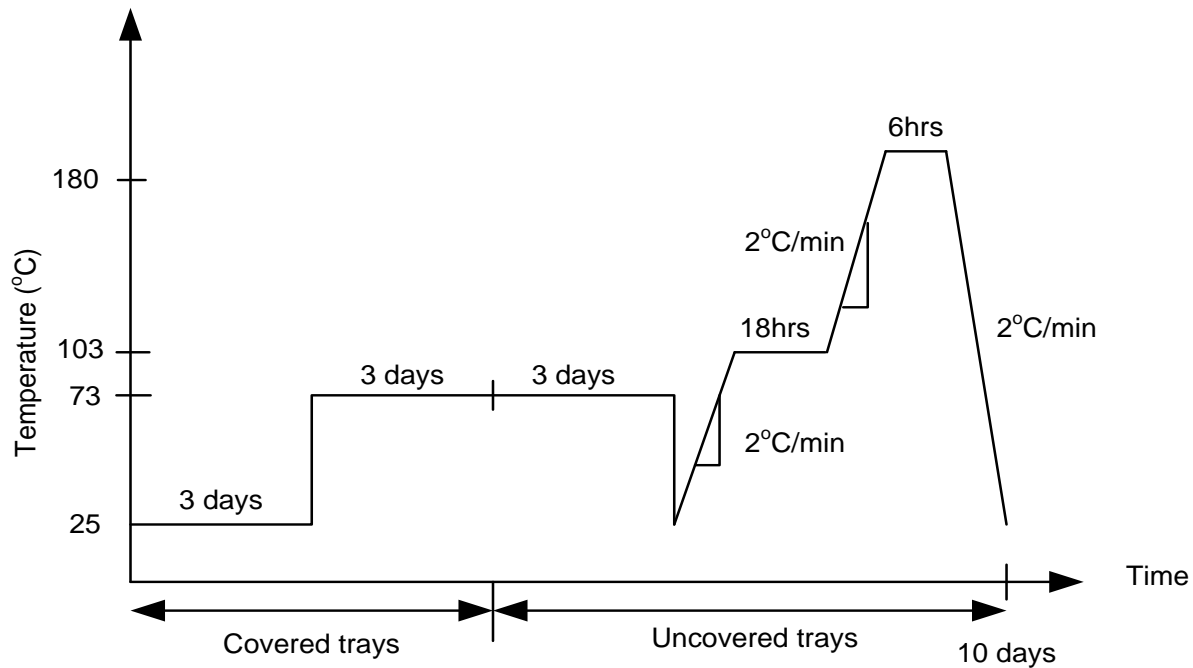


Figure 3-16. Drying schedule for cylindrical STCs of 9 mm in diameter by 8 mm in height used to pack the TPOT (Figure not drawn to scale).

## CHAPTER 4

### CHARACTERIZATION OF SILICA-TITANIA COMPOSITES

The properties of the STCs used for packing the pilot-scale reactor are shown in Table 4-1.

The STCs have an average pore diameter of about 152 Å, a BET surface area of 250 m<sup>2</sup>/g and a pore volume of 0.94 cc/g. A typical nitrogen adsorption-desorption isotherm is shown in Figure 4-1. The STCs exhibited a Type IV isotherm with a H1 hysteresis loop (as defined by the IUPAC (Sing et al., 1985)). These isotherms are characteristic of mesoporous materials with uniform spheroid particles that tend to be nonporous or possess a narrow pore size range. The narrow pore size distribution (PSD) was confirmed by the PSD analysis shown in Figure 4-2 several for different batches of the same STCs formulation, plotted as the differential pore volume as a function of pore diameter. The PSD is an important characteristic of the composite catalyst material since it can affect the diffusion of toluene in the STCs during adsorption and surface reaction and also the desorption of byproducts after oxidation. The STCs showed a unimodal distribution of pore diameters with more than 90% of the pore volume attributed to pore diameters in the range of 70 and 200 Å. The peaks of the PSDs shown in Figure 4-2 do not correspond to the hydraulic pore diameter determined for the batches presented in Figure 4-2 as determined by equation 3-6. The BJH method for determining the PSDs of the STCs assumes the ideality of perfectly cylindrical pores, and this ideality did not apply to the STCs. In addition there is also the possibility of the presence of networks within the pellets that are not accounted for by the BJH method. Accordingly, the hydraulic pore radius was used as the characteristic pore diameter.

Another important characteristic of the STCs that was analyzed was the accessible area of TiO<sub>2</sub> in the composite material. As discussed in Chapter 3, the method used for this analysis uses PPA to determine the available area. Since the size of PPA molecules is greater than toluene

molecules (*ca.*  $11 \times 16$  Å versus  $4 \times 8$  Å), the area measured by using this method should also be accessible to toluene molecules. Additionally, the PSD analysis showed that most of the pores in the STCs have a diameter greater than 50 Å, which is well above the size of PPA molecules, so potential resistances due to intraparticle diffusion were expected to be insignificant during the procedure.

The TiO<sub>2</sub> accessible surface area analysis was performed using the composites in the form of powder (pellets crushed with mortar and pestle), cylindrical pellets as used in the pilot reactor (9mm x 8mm), and as pellets without any titania loading (silica only). The P content in each of the materials analyzed and the TiO<sub>2</sub> available surface area, presented in Table 4-2, were calculated using the formula shown in Chapter 3.

The P surface coverage found for Degussa P25 was 2.97 atoms P/nm<sup>2</sup>. This value is comparable to the results found by other researches that have used the same procedure (Marugan et al. 2007; Mutin et al., 2004). Based on the measured BET surface area of Degussa P25 TiO<sub>2</sub> (49 m<sup>2</sup>/g) used in the synthesis of the STCs, the theoretical TiO<sub>2</sub> surface area expected in each STC is about 30% of that value or 14.7 m<sup>2</sup>/g STC (since STC is about 30%<sub>wt</sub> TiO<sub>2</sub>). The results for the accessible surface area of the STCs analyzed per gram of STC are presented in Table 4-2 and the comparison of this area per gram of TiO<sub>2</sub> is shown in Figure 4-3. The results indicate that there was about 20% loss of active TiO<sub>2</sub> surface area accessible for reaction by using silica as the titania support. The decrease in surface area can be attributed to possible clumping or coating of the titania particles by silica during the synthesis of the STCs. There were no considerable differences, however, in the available area between the composites in powder and pellet form. This shows that the surface area of titania available for reaction is not affected by the casting of the STCs as the cylindrical pellets. The low available surface area of TiO<sub>2</sub> found for the silica

only composites confirms that the method measures the functionality of titania only so that the contribution of silica to the total active surface area can be neglected. The available surface area measured for the powdered STDs is in agreement with the areas found by Byrne et al., where approximately 70% of the titania surface area was found to be accessible for reaction in STCs prepared using a similar formulation as the one used in this research.

Table 4-1. Properties of STCs

| Property                 | Units             | Value ± STD  |
|--------------------------|-------------------|--------------|
| Diameter                 | mm                | 9.1 ± 0.4    |
| Length                   | mm                | 8.1 ± 1.1    |
| TiO <sub>2</sub> loading | % wt              | 29.6 ± 1.4   |
| BET surface area         | m <sup>2</sup> /g | 250.0 ± 43.0 |
| Pore diameter            | Å                 | 152.0 ± 23.0 |
| Total pore volume        | cc/g              | 0.94 ± 0.06  |

\*STD – Standard deviation for at least 20 samples.

Table 4-2. Phosphorus content from ICP – AES results and accessible TiO<sub>2</sub> surface area

|             | P Content<br>(mg P/g STC) | P Surface<br>Coverage<br>(atoms P/nm <sup>2</sup> ) | Available<br>TiO <sub>2</sub> SA<br>(m <sup>2</sup> /g STC) | Inaccessible TiO <sub>2</sub><br>(%) |
|-------------|---------------------------|---|---|--------------------------------------|
| Degussa P25 | 7.49 (2)                  | 2.97  | 14.7  |                                      |
| Powder.B1   | 1.82 (3)                  |   | 11.9  | 19.1                                 |
| Powder.B2   | 1.97 (1)                  |   | 12.9  | 12.3                                 |
| Pellet.B1   | 1.74 (2)                  |   | 11.4  | 22.4                                 |
| Silica Only | 0.23 (2)                  |   | 1.5   | NA                                   |

\*NA – Not applicable. (#) # of samples analyzed.

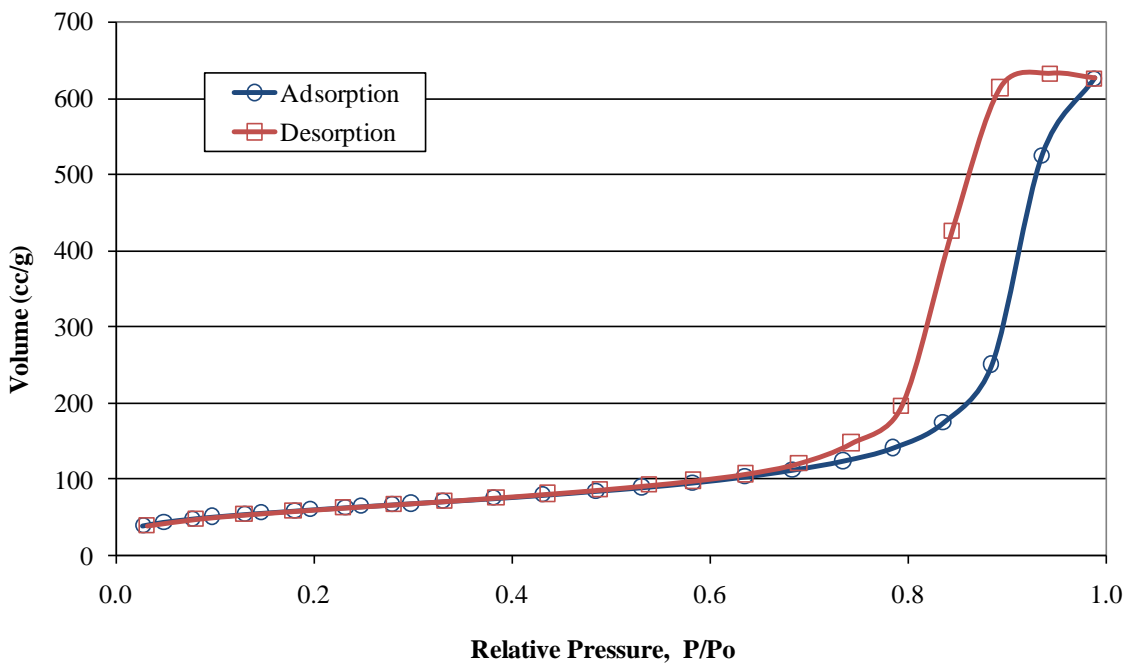


Figure 4-1. Typical nitrogen adsorption/desorption isotherm for the STCs used to pack the pilot-scale reactor.

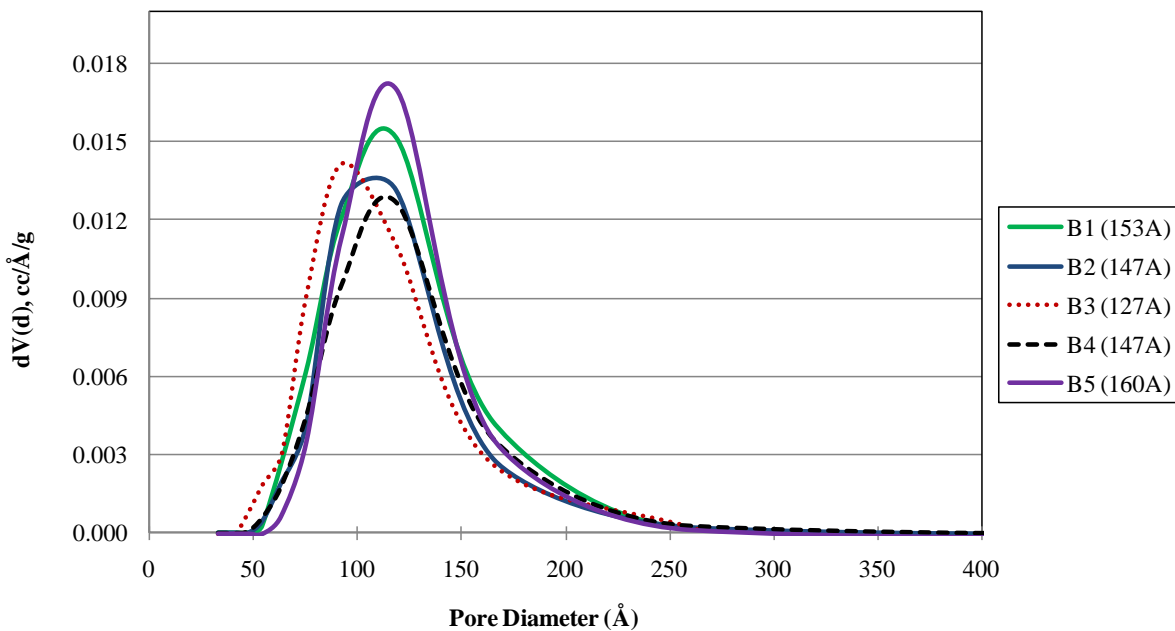


Figure 4-2. Typical pore size distributions of the STCs used to pack the pilot-scale reactor. The legend indicates the batch number (B1 to B5) and the number in parenthesis refers to the measured hydraulic radius in Angstroms for the specific batch.

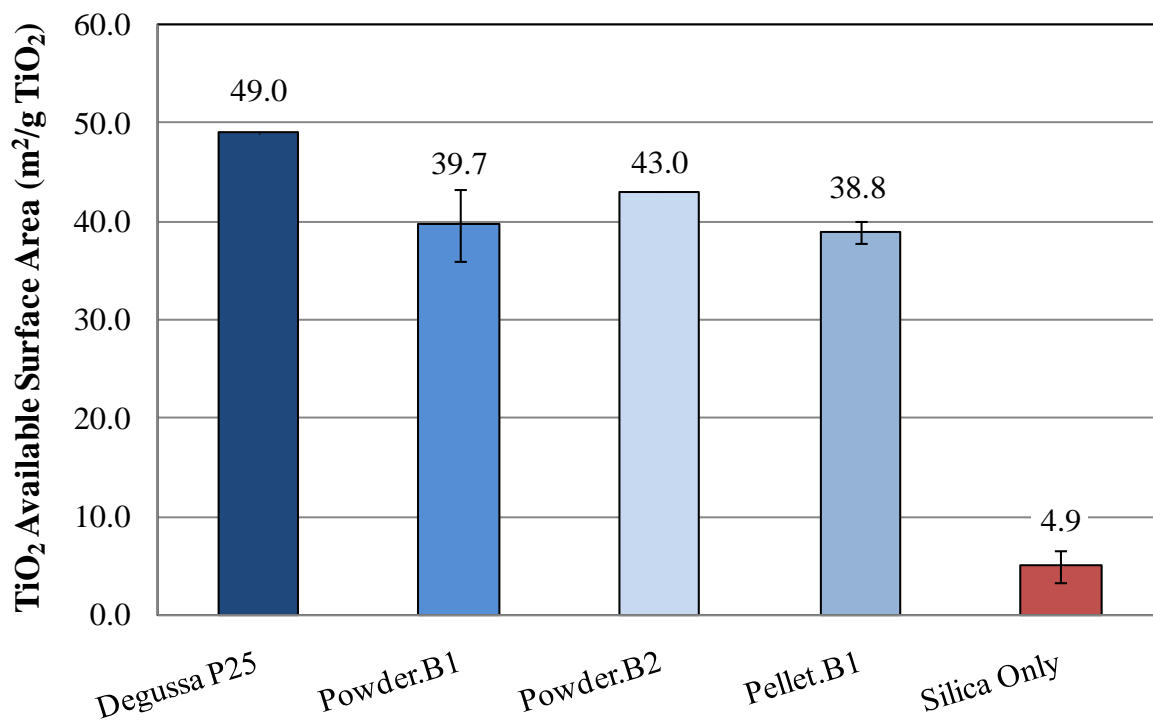


Figure 4-3. Comparison of the accessible titanium dioxide surface area for different STC shapes.  
B1 and B2 refer to two different batches of STC pellets.

## CHAPTER 5

### GAS PHASE TOLUENE DEGRADATION STUDIES

#### **Bench-Scale Studies**

The objective of the work presented in this chapter was to investigate the oxidation of toluene using the STCs in the gas phase only. Several conditions considered to affect the oxidation of toluene, especially when present simultaneously with the aqueous phase, were investigated. Some of these conditions include the effects of adsorption in PCO, the effect of relative humidity, the degree of wetting of the STCs, and the residence time of the gas phase in the reactor. Many of the results presented in this section were also used to predict the performance of the gas phase end polishing section for the overall proposed treatment system.

#### **Gas Phase Toluene Studies Using Dry STCs**

##### **Adsorption of toluene in a packed bed reactor**

The adsorption capacity of the dry STCs for toluene was studied using the bench-scale annular reactor with a 25 mm annulus. The adsorption experiment was conducted by running toluene through the reactor in the dark until the STCs were completely saturated. Based on the large surface area of the composites; adsorption was expected to play an important role during photocatalysis. During this run, no water vapor was added to the system; so, the measured RH was about 13%. The toluene inlet concentration was kept relatively constant at  $90 \pm 10 \text{ mg/m}^3$ . Once the STCs reached exhaustion, the UV lamps were turned on to allow photocatalysis to take place. The results presented in Figure 5-1, show that the STCs have a large adsorption capacity for toluene. For the given conditions, it took about 45 h of continuous flow for the STCs to reach exhaustion. The adsorption capacity of the STCs for toluene, calculated by integration of the adsorption breakthrough curve, was about 2.5 mg toluene/g STC. Following adsorption, there was significant desorption of toluene when the lamps were turned on. Some desorption was

expected to occur due the increase in the reactor temperature from approximately 23°C to 50°C and the high loading of toluene already in the STCs. After about 14 h of desorption, significant conversion of toluene was observed, but this conversion became insignificant after about 35 h of PCO. The loss of activity of the catalyst was attributed to deactivation of the STCs under dry conditions since a yellowish coloration of the STCs was observed at the end of the run. Many other studies of toluene PCO using Degussa P25 TiO<sub>2</sub> have correlated this yellow coloration with catalyst deactivation (Alberci and Jardim, 1997; Einaga et al., 2001). Note that no change in STC color was observed for adsorption only, so deactivation was attributed to the reactions occurring during photocatalysis.

### **PCO of toluene: Effect of water vapor**

Due to the large desorption effect shown in Figure 5-1, the rest of the PCO experiments did not include an adsorption step prior to PCO, so the combined effects of adsorption and PCO are reported. The effect of water vapor on the removal of toluene by PCO was investigated by increasing the RH from 13% to 90%, which corresponds to water vapor concentrations of *ca.* 3,600 ppm<sub>v</sub> (2,600 mg/m<sup>3</sup>) and 24,500 ppm<sub>v</sub> (18,500 mg/m<sup>3</sup>), respectively. The inlet toluene concentration ( $Y_o$ ), flowrate ( $Q_G$ ), and packed depth ( $Z$ ) were kept constant during both experiments. The results are shown in Figure 5-2. Initially, the conversion of toluene is large under both dry and high RH conditions, likely due to the combined effect of adsorption and PCO. However, under dry conditions, the outlet effluent concentration continuously increased to achieve a pseudo steady state corresponding to about 10% removal after 50 h of experimental run. For high RH, the increase in outlet concentrations was significantly smaller. At 90% RH, steady state conditions were achieved after only 20 h and the toluene removal obtained for the following 55 h of the run remained constant at approximately 67%. These results confirmed the importance of water vapor in the system to prevent the loss of catalyst activity. It is important to

note however, that the yellowish coloration of the STCs after the runs was still observed for both low and high RH, suggesting that there is some deactivation effect still taking place.

### **PCO of toluene: Effect of space time ( $\tau$ )**

The effect of space time was determined by increasing the flowrate of the packed bed or changing the packed bed depth ( $Z$ ). For all runs, the toluene inlet concentration and RH were kept constant at 30 mg/m<sup>3</sup> and 90%, respectively. By increasing the flowrate, the superficial velocity ( $U_G$ ) was correspondingly increased. Similarly, the toluene and water vapor loadings were also modified as a result in the change in flowrate. The experimental conditions used for the runs showing the effect of space time are shown in Table 5-1.

The effects of space time on the oxidation of toluene are shown in Figure 5-3. The increase in space time resulted in an increase in toluene removal. Initially, the removal was high for all space times, but it decreased to a lower steady state value with time. The decreased in removal is faster for the shorter residence time likely due to the larger toluene and water vapor loadings. For the longest space time of 25.0 seconds, pseudo steady state was reached after about 60 h of operation. The steady state removals achieved were about 31%, 67% and 93% for the space times of 5.9 s, 12.5 s and 25.0 s, respectively. These removals are higher than many of the results reported in the literature for similar residence times. For example Maira et al. (2001a) and Belver et al. (2003), who used an annular reactor with TiO<sub>2</sub> coated in the walls, found initial removals of 55% and steady state removals of about 5% after 150 min for space times of approximately 5 s. Similarly, Boulamanti et al. (2008) reported about 55% removal for 25 s residence time, and they were able to achieve removals greater than 95% only after about 75 s of residence time.

By using high water vapor concentrations and longer residence times, deactivation was expected to be minimized. However, the yellowish coloration of the STCs was observed in all runs, suggesting that catalyst poisoning was still taking place. No byproducts were detected in

the effluent flow. However, by analyzing the catalyst surface, benzaldehyde and benzoic acid were the species found to be adsorbed to the catalyst. The results showed that despite the catalyst deactivation observed, high toluene removals (>90%) can be achieved and maintained for prolonged periods of time using the STCs.

### Kinetic analysis

The kinetic analysis for PCO of toluene using dry STCs was performed using the pseudo steady state results from the experiments described in Table 5-1. Analysis of kinetic data free of mass transfer influences is preferred over such an analysis complicated by mass transfer limitations. Resistance to mass transfer can be either external, from the bulk phase to the catalyst pellet, or internal, which refers to the diffusion through the pores. External mass transfer influences are usually assessed by increasing the flowrate in the reactor since it is well established that in the presence of external mass transfer influences, the reaction rate increases with fluid velocity. If the system is free of external mass transfer influences the oxidation rate will be the same despite the increase in superficial velocity. The average rate of reaction ( $r$ ) used to determine the influence of external mass transfer on toluene oxidation was calculated by

Equation 5-1:

$$r = -dY/dt = (Y_o - Y_e)/\tau \quad (5-1)$$

where  $Y_o$  is the influent toluene concentration and  $Y_e$  is the effluent toluene concentration determined at pseudo steady state. These reaction rates are shown in Table 5-2. For the two cases where the superficial velocity was increased by increasing the flowrate and keeping the same packed volume, the reaction rates were very similar,  $1.72 \times 10^{-5}$  and  $1.69 \times 10^{-5}$  mol/m<sup>3</sup>/s. Based on these values, it is expected that external mass transfer influences are not significant. However, when the reactor used to make this comparison is not a differential reactor, such is the case in

this study, the intrinsic rate of reaction might also be affected by the increase in flowrate due to the larger differences between inlet and outlet concentrations, making it difficult to differentiate the two effects, unless the studies are performed using two different catalyst beds with the same space time and different velocities (Satterfield, 1970). This case was not investigated in this work. Therefore, to further determine if the external mass transfer resistance was significant, the Mear's criterion ( $C_M$ ) was used (Fogler, 1999). This criterion uses the measured rate of reaction ( $r$ ) to determine if the external mass transfer can be neglected. The Mears criterion ( $C_M$ ) states that when the inequality shown in Equation 5-2 is satisfied, external mass transfer is negligible. The variables in  $C_M$  include  $R$ , which is the characteristic pellet radius (radius/2 for cylindrical pellets),  $n$  is the reaction order (assumed to be 1 for toluene),  $k_c$  is the mass transfer coefficient, which was determined using the Thoenes – Kramers's correlation shown in Equation 5-3, and  $Y_b$ , which is the bulk concentration (Folger, 1999). Since  $Y_b$  was unknown and could not be assumed to be the same as  $Y_o$ , both the influent ( $Y_o$ ) and effluent ( $Y_e$ ) concentrations were tested to ensure the results would apply to both extreme cases of concentration present in the system.

$$C_M = (r \times R \times n) / (k_c \times Y_b) < 0.15 \text{ for negligible external mass transfer} \quad (5-2)$$

$$Sh' = 1.0(Re')^{1/2}(Sc)^{1/3}$$

$$\left[ \frac{k_c d_p}{D_G} \left( \frac{\phi}{1-\phi} \right) \frac{1}{\gamma} \right] = \left( \frac{U_G d_p \rho_G}{\mu_G (1-\phi) \gamma} \right)^{1/2} \left( \frac{\mu_G}{\rho_G D_G} \right)^{1/3} \quad (5-3)$$

The variables used in the Thoenes – Kramer's correlation include  $Re' = Re / [(1 - \phi) \times \gamma]$ ,  $Sh' = Sh / [(1 - \phi) \times \gamma]$ ,  $d_p$  is the equivalent diameter of a sphere of the same volume,  $\phi$  is the void fraction of the packed bed,  $\gamma$  is the shape factor (external SA/  $\pi d_p^2$ ),  $\mu_G$  is the gas dynamic viscosity,  $\rho_G$  is the gas density, and  $D_G$  is the gas phase diffusivity ( $D_G = 7.42 \times 10^{-6} \text{ m}^2/\text{s}$ , used for toluene diffusivity in air).

The calculation results for the Mears' criterion, shown in Table 5-2, indicated the criterion is satisfied ( $C_M < 0.15$  for no external mass transfer resistance) for all flow conditions investigated, thus it was possible to assume that there were no concentration gradients between the bulk and the external surface of the catalyst pellets. Similarly, the influences of internal mass transfer in the kinetics of the reaction were assessed by using the Weisz – Prater Criterion ( $C_{WP}$ ). When the inequality for the Weisz – Prater criterion described by Equation 5-4 holds, it means that pore diffusion is not important in the system and can be neglected. This criterion is also a function of the measured rate of reaction and the characteristic pellet radius ( $R$ ) in addition to the contaminant surface concentration (in this case assumed to be the same as the bulk concentration,  $Y_o$ , due to the lack of external mass transfer limitations found above), and the effective diffusivity ( $D_e$ ) (Fogler, 1999).

$$C_{WP} = (-r \times R^2) / (Y_o \times D_e) < 1.0 \quad \text{for negligible internal mass transfer} \quad (5-4)$$

The effective diffusivity, which is defined by Equation 5-5, is a function of the diffusivity ( $D_G$ ) of the contaminant in the gas phase, the catalyst grain porosity ( $\varepsilon$ ), determined to be 0.7 for the STCs used in this study, and the tortuosity factor for the STCs ( $\tau_c$ ), which was assumed to be 3 as it usually is for many mesoporous materials (Satterfield, 1970).

$$D_e = (D \times \varepsilon) / \tau_c \quad (5-5)$$

The values obtained from the Weisz-Prater expression for the different flow conditions used in the experimental runs are shown in Table 5-2. All these values are less than 1, meaning that there are no diffusion limitations inside the pellets and consequently no concentration gradients within the pellets.

Based on the Mears and Weisz-Prater criteria, the measured rates of reaction at steady state can be considered free of mass transfer influences, so they are expected to be the result of the

intrinsic photochemical kinetics only. Consequently, the steady state removals at various space times shown in Figure 5-3 were used to determine the reaction rate constant for toluene oxidation using the STCs. The Langmuir-Hinshelwood (L-H) model, described by Equation 5-6, has been successfully used by many researchers to describe and model the degradation rates of toluene PCO using Degussa P25 TiO<sub>2</sub> (Obree and Brown, 1995; Bouzaza et al., 2006; Boulamanti et al., 2008):

$$r = dC/dt = (kKY)/(1 + KY) \quad (5-6)$$

where  $k$  is the rate constant,  $K$  is the adsorption equilibrium constant, and  $Y$  is the bulk contaminant concentration. For low inlet contaminant concentrations ( $KY \ll 1$ ), the L-H kinetic equation can be reduced to a pseudo-first order rate equation, with an overall rate constant  $k'$  equal to  $kK$ , shown by Equation 5-7:

$$\ln(Y_e/Y_o) = -k'\tau \quad (5-7)$$

The experimental results and the L-H model are presented in Figure 5-4. The L-H model resulted in a good fit of the data ( $R^2 > 0.99$ ), indicating that the first order reaction simplification is valid. The rate constant calculated from the slope of the linear regression equation fit in Figure 5-4 was equal to 0.12 s<sup>-1</sup>. Bouzaza and Laplanche (2002), who used an annular reactor configuration for the PCO of toluene with Degussa P25 TiO<sub>2</sub>, followed a similar approach for their kinetics analysis and their calculated rate constant was 0.066 s<sup>-1</sup>. Other pseudo first order kinetic rate constants derived from the L-H model reported in the literature are even lower, in the 7.3x10<sup>-4</sup> s<sup>-1</sup> range. Compared to the values reported in the literature for TiO<sub>2</sub> only, the rate constant for toluene using the STCs is greater than many of those cases, suggesting the STCs enhanced performance over using TiO<sub>2</sub> alone.

Stokke and Mazyck (2008), who used the same STCs formulation for the removal of methanol, found in their kinetics analysis a rate constant of  $0.40\text{ s}^{-1}$  for methanol. This  $k'$  is larger than the rate constant found for toluene in this study. Similarly, other researchers investigating the PCO of various VOCs have also found rate constants for alcohols that are higher than those of aromatics under the same operating conditions (Kim et al., 2002; Bouzaza et al., 2006). This can be expected given the structure of the molecules. Aromatic compounds have a benzene ring which tends to be more difficult to break down during oxidation. Alcohols, on the other hand, tend to be smaller molecules with an OH terminal group that is usually very reactive.

### **Gas Phase Toluene Studies Using Wetted STCs**

#### **Toluene adsorption in a batch reactor**

The adsorption of toluene on STCs was shown to be significant in the presence of both low and high water vapor concentrations when the STCs were dry. During the simultaneous treatment of gas and aqueous phases, the pellets were expected to be wetted at all times. Accordingly, the assessment of gas phase toluene adsorption and PCO under wet STCs conditions was of interest.

Adsorption of toluene was initially compared using dry and pre-wetted STCs in batch reactors. The batch experiments were performed by suspending about 3 g of STCs (10 STCs) in a bottle containing 50 mL of pure liquid toluene. The pellets were not in direct contact with the liquid toluene. They were placed in an aluminum container suspended above the liquid, so that they were only in contact with gas phase toluene resulting from volatilization (vapor pressure 30.6 mmHg at  $T = 26.5^\circ\text{C}$ ). The gas phase concentration of toluene inside the bottles was not measured, but it was determined by the vapor pressure of toluene to be approximately 139 mg/L. The experimental setup is shown in Figure 5-5 for the four different wetting scenarios investigated. The first reactor contained water vapor as the gas phase and dry STCs as the

sorbent; the other three reactors contained toluene vapor as the gas phase and dry STCs (for reactor 2), STCs pre-wetted with DI water (for reactor 3) or STCs pre-wetted in a 1 ppm toluene solution (for reactor 4). The STCs were pre-wetted by soaking them in the respective solutions for at least 24 hrs before the experiment. During the experiments, the weight of the STCs was monitored over time. The samples were weighted at the beginning of the experiment and at different time intervals. The uptake was observed for several hours (up to 50 hours) and it was assumed that the increase of the weight of the STCs was due to the adsorption of the compound present in the gas-phase. The STCs used in these experiments had an average pore diameter of 147 Å, a BET SA of 248 m<sup>2</sup>/g, a pore volume of 0.91 cc/g and a TiO<sub>2</sub> loading of 29%<sub>wt</sub>. The results showing the mass of either water vapor or toluene gas adsorbed per gram of STC as a function of time are shown in Figure 5-6.

The results in Figure 5-6 show that when the STCs were dry, they had a large adsorption capacity for water vapor and toluene. The adsorption capacity of the STCs for water vapor increased linearly at a rate of approximately 0.3 mg/min and equilibrium was not reached even after 50 h of adsorption. The amount of water vapor found to be adsorbed at the end of the run was about 0.3 g of water vapor per g of STC, but it appeared from the adsorption trend that there was still higher capacity for water vapor adsorption under dry conditions. The adsorption of toluene to the dry STCs reached equilibrium after about 24 h with an adsorption capacity of approximately 0.8 g of toluene/ g STC, which corresponds to about 21 toluene molecules adsorbed per nm<sup>2</sup>. This capacity is greater than the one found for the continuous flow experiments. These results suggest that multilayer adsorption might be occurring under batch conditions, which is not the case for continuous flow conditions.

Pre-wetting the STCs resulted in decreased adsorption. Unlike dry STCs, the STCs that were pre-wetted in either DI water or 1 mg/L toluene solution did not show significant adsorption during the 50 h of experimental run. These results showed that the wetting of the STCs completely inhibited adsorption of gas-phase toluene. The inhibition of adsorption was not completely unexpected in the batch experiments because water or an aqueous solution was pre-adsorbed to the STCs, which are known to have a high affinity for water, thus ensuring that all available adsorption sites became occupied by the wetting solution. Water molecules were adsorbed to the STCs likely by hydrogen bonding, and these strong bonds could not be outcompeted by the toluene molecules present in the gas phase.

### **Toluene adsorption in a continuous flow packed-bed reactor**

Although toluene adsorption was inhibited during batch experiments due to the pre-wetting of the packing, the performance of the wetted STCs was also assessed using a continuous flow packed bed reactor. For these experiments, a small vertical cylindrical reactor with an outside diameter of 4.2 cm packed with the STCs was used. The reactor was similar to the previously described annular reactor but the lamp envelope at the center of the reactor was removed. The flow rate used in the small reactor was about 1,300 mL/min, which translated to an empty bed contact time (EBCT) of approximately 7 s. The toluene concentration used for all runs was  $14 \pm 3$  ppm<sub>v</sub>. For each run, the reactor was packed with glass beads near the gas inlet and 100 pellets (about 34 g STCs) on top of the beads. The beads were used to provide a more uniform distribution of the gas flow before reaching the STCs. The same experiment was performed using three different wetting conditions. During the first run, dry STCs were used. For the second and third run, pellets pre-soaked in DI water or 1 mg/L aqueous toluene solution were used. Similar to the batch experiments, the STCs were wetted by pre-soaking them in the desired

solutions. The STCs used in these experiments had an average pore size of 168 Å, a BET SA of 213 m<sup>2</sup>/g, a pore volume of 0.90 cc/g, and TiO<sub>2</sub> loading of 29.0%<sub>wt</sub>.

The results for all wetting conditions of the continuous flow experiments are presented in Figure 5-7. Similar to the results obtained in the batch reactor, the adsorption of gas phase toluene was drastically affected by the presoaking of the STCs with either DI water or 1 ppm toluene solution. When dry pellets were used, the removal of toluene by adsorption was initially 85%, decreasing to about 70% after 6 h of adsorption. Conversely, when the pellets were presoaked in solution, no significant adsorption of toluene was observed. This means that water remained adsorbed to the STCs despite the reactor configuration, preventing significant toluene adsorption to the pellets.

### Pilot-Scale Studies

On the one hand, when trying to determine the photocatalytic oxidation of toluene using the STCs, excluding adsorption effects is preferred so that the removal can be only attributed to PCO; thus inhibiting the adsorption of toluene by pre-wetting of the STCs was a potential alternative for those purposes. However, many of the mechanisms proposed for the oxidation of toluene using TiO<sub>2</sub> involve an adsorption step before reaction, so that the reaction could occur between the adsorbed contaminant and the OH radical or the hole in the titania surface. There is no consensus in the literature as to whether the reaction occurs right at the surface, in the bulk gas phase or a combination of both. For the case of toluene, it was shown earlier that the presence of water vapor plays an important role for the complete conversion of toluene to CO<sub>2</sub> and water and at decreasing catalyst deactivation. However, the effect of completely wetting the catalyst during gas phase toluene PCO has not been previously investigated. Consequently, it was important to determine the extent of toluene photocatalysis when the STCs were wetted to help elucidate potential reaction mechanisms. PCO experiments could not be performed at the

bench scale due to the large increase in temperature inside the reactor (from 25°C to over 50°C), which caused the adsorbed pre-wetting solution to dry within the first 10 min of the experimental run. Therefore, the effects of STC wetting was only assessed at the pilot-scale.

### **Toluene Adsorption Using TPOT**

The effect of wetting on gas phase toluene adsorption was investigated in the TPOT before assessing its effect on PCO to ensure that the same effects were observed at the pilot-scale as those found at the bench-scale.

#### **Adsorption of toluene using dry STCs**

Initially, the extent of toluene gas phase adsorption on the dry STCs in the pilot-scale reactor was determined. During these experiments, the commingled packing, high flow rings and STCs, were dry and the only flowing phase through the reactor was the gas phase contaminated with toluene. The effects of mass loading and superficial velocity on adsorption were investigated by varying the influent toluene concentration ( $Y_o$ ) and the gas volumetric flowrate ( $Q_G$ ), respectively. The RH was that of the ambient air, since that was the air mixed with the toluene to produce the dilute gas influent. The humidity remained constant at about 45% at 22.3°C. The experimental conditions for the adsorption experiments performed are given in Table 5-3. The results showing the adsorption breakthrough curves for the dry STCs are presented in Figure 5-8.

Different from the results found at the bench-scale, the adsorption of toluene in the TPOT using dry STCs did not show the large adsorption capacity expected given the large number of STCs used to pack the reactor (*ca.* 7,500 STCs). Initially, the removal of toluene was high, but it became negligible after only 4 h of continuous flow for all conditions tested. The total amounts of toluene adsorbed were 156, 93 and 177 µg/g of STC for runs 1, 2 and 3, respectively. These

values were lower than the amount of toluene adsorbed to the STCs in the bench-scale packed bed reactor (2.5 mg/g STC).

Increasing the mass loading rate from 309 to 586  $\mu\text{g}/\text{min}$  did not significantly affect the removal of toluene by adsorption, as shown by the breakthrough curves for runs 1 and 2. However, decreasing the superficial velocity resulted in higher toluene removal (runs 2 and 3), likely due to the increase in residence time which allowed more time for adsorption. The difference in adsorption trends between the bench-scale and pilot-scale experiments indicated a possible effect of the commingled packing on the flow patterns of the pilot-scale reactor.

Another possible reason to the lower amounts of toluene adsorbed in the TPOT compared to the bench-scale annular reactor was competition with water vapor which was not as significant at the bench-scale. During the adsorption experiment at the bench-scale, the water vapor concentration was about  $2.6 \text{ g/m}^3$ . This concentration was about 3.5 times higher at the pilot-scale. The effluent water vapor concentration normalized by the influent water vapor is shown in Figure 5-9 as a function of run time. These results were very similar to the toluene adsorption breakthrough curves in Figure 5-8. As the superficial velocity was decreased, higher amounts of water vapor were adsorbed as it occurred for toluene, but less water vapor was applied at the lower flowrates. Despite the lower amounts of toluene adsorbed using the TPOT, adsorption of gas phase toluene was found to be significant up to about 4 h of continuous operation for the dry STCs.

### **Adsorption of toluene using wetted STCs**

The effect of wetting of the STCs on gas phase toluene adsorption was assessed in the TPOT. The wetting of the STCs in the TPOT was performed by completely filling and draining the reactor with tap water, followed by a continuous flow of water at about  $6 \text{ L/min}$  for 15 to 20 minutes to ensure complete wetting of the STCs. The same experimental conditions as the one

shown in Table 5-3 for run 2 were used to perform the test using the wetted STCs. The results showing the adsorption of toluene in the TPOT under dry versus wet STCs conditions are shown in Figure 5-10. Similar to the bench-scale findings, wetting the STCs completely prevented adsorption from taking place even after 3 h of experimental run, suggesting that no significant drying of the pre-wetted packing occurred.

### **Toluene PCO Using TPOT**

#### **PCO of toluene using dry STCs**

The photocatalytic oxidation of toluene under dry conditions was investigated in the TPOT. Similar to the results found at the bench-scale, it was shown that pre-adsorbing toluene before PCO resulted in large desorption of toluene after the lamps were turned on due to the high increase in the temperature in the reactor caused by the lamp operation (Figure 5-11), and no significant removal due to PCO could be observed during the length of the experimental run. Consequently, all the subsequent experiments performed using dry STCs, showed the combined effects of adsorption and photocatalysis.

The results for the combined adsorption/PCO gas phase experiments using dry STCs are shown by the conversion ( $X_A$ ) or removal of toluene defined by Equation 5-8 as a function of the run time.

$$X_A = (Y_o - Y_e)/Y_o \quad (5-8)$$

Since the tower had been previously used with water, the STCs were dried by running ambient air through the reactor for prolonged periods of time, and turning the UV lamps on and off periodically for about 1 h intervals to allow the system to dry faster. The packing of the tower was considered to be dried by visual inspection, measurements of influent and effluent RH and also by inspecting a few samples of the STCs obtained from inside the reactor.

Initially, toluene PCO in the TPOT was tested by running 3 experiments under the same initial conditions to determine the performance of the tower for consecutive runs. The initial conditions were:  $Y_o = 65 \pm 10 \text{ mg/m}^3$ ,  $Q_G = 142 \text{ L/min}$ , influent RH = 44% and influent gas temperature = 23°C. The results for these experiments are shown in Figure 5-12. Based on the bench-scale experiments, the removal of toluene by PCO using dry STCs was expected to be high in the TPOT since the space time for the experiments was about 15 s, which corresponded to steady state removals higher than 70% at the bench-scale. However, the removal of toluene observed at the pilot-scale was initially high, as high as 50% conversion, but it rapidly decreased to zero after about 4 h of continuous operation. Furthermore, the TPOT performance at removing toluene decreased after every run. This behavior suggested deactivation of the STCs, likely due to poisoning of the catalyst by strongly adsorbed intermediates. The lower conversion might be also attributed to the lower adsorption of gas phase toluene found earlier, which was likely decreased even further by the large temperature increase in the reactor as a result of the UV lamps.

To verify if the catalyst was losing activity due to poisoning, the packing was regenerated by flushing ambient air through the reactor for several hours, followed by 1h of UV while flushing air, and repeating the sequence at least 3 times. The conversion of toluene in the TPOT improved after every regeneration, as shown in Figure 5-13. The initial removals increased to about 57% and 70% for the first and second regenerations, respectively. These removals also decreased with time but they did not go to zero. After the first regeneration, the steady state conversion was about 12% while this value improved to about 23% for the second regeneration. Regenerating the tower by flushing air and turning the UV on in the absence of the contaminant likely allowed the adsorbed intermediates in the catalyst to be destroyed due to the excess

number of photons and electron scavenger (air). Additionally, the water vapor in the clean air used to regenerate the tower, likely provided more water molecules to regenerate the hydroxyl radicals at the surface of the TiO<sub>2</sub>.

As shown by the bench-scale results, the presence of water vapor in the influent gas is an important parameter to decrease catalyst deactivation by increasing conversion of toluene to CO<sub>2</sub> and water instead of more persistent intermediates, and also to maintain the catalyst activity. During the PCO experiments, the initial RH was not varied but, but it was measured throughout the length of the tower at the 3 sampling ports on the wall of the tower placed 1 ft apart. The water vapor concentrations as a function of tower height at various run times for the experiment corresponding to the 2<sup>nd</sup> regeneration study are shown in Figure 5-14.

The water vapor entering the reactor decreased as a function of both reactor length and run time. These results suggest that water vapor is being consumed during the PCO of toluene. After about 90 min of continuous operation, the water vapor in the reactor is around 3 g/m<sup>3</sup>, which is similar to the lower water vapor concentration used in the bench-scale experiment that resulted in steady state removals of only 10%. The decrease in toluene removal as a function of time (Figure 5-13), follows the same trend as the decrease in water vapor concentration as a function of time; indicating that water vapor is a requirement for toluene PCO to take place.

In addition to the water vapor concentration, another important factor that can influence the photocatalytic process is the lamp's temperature. The expected output of the UV lamps can be greatly influenced by the temperature; consequently, different types of lamps have an optimum temperature range that produces the highest irradiation output. Figure 5-15 shows the relative output of the lamps as a function of temperature for the lamps used in this research. From the figure, it can be observed that the maximum output occurs at a temperature of 42.2 °C, and it

decreases for higher or lower temperatures. The temperature of the lamps, as measured at the lamp envelope, during the PCO experiments, increased to about 125°C as shown in Figure 5-13. This temperature is well above the optimum operating temperature of the lamps; so, it is expected that the lamps performance is not at its maximum.

### **PCO of toluene using wetted STCs**

Investigating the wetting of the packing on gas phase toluene PCO was very important due to its implications in the treatment of toluene present in the gas and aqueous phases simultaneously. Accordingly, gas phase toluene PCO was studied under different wetting conditions using the TPOT. Two approaches were used for testing the effect of packing wetting. First, toluene PCO was tested by pre-wetting the packing with tap water. The pre-wetting procedure consisted of flowing water through the tower at a rate of 7.5 L/min for about 10 minutes before the run. The other wetting approach was to keep the tower continuously wetted by flowing tap water free of toluene simultaneously with the contaminated gas phase toluene. For the latter approach, some absorption of toluene from the gas phase to the aqueous phase was anticipated, so conversion was calculated by performing a mass balance on toluene in the reactor including both phases. For this experiment, toluene conversion was calculated using Equation 5-9.

$$X_A = 1 - (Y_e \times Q_G + C_e \times Q_L) / (Y_o \times Q_G) \quad (5-9)$$

The results showing the conversion of toluene for the different wetting conditions of the packing are shown in Figure 5-16. When the packing was either pre-wetted or continuously wetted, the net removal of toluene was zero, meaning that wetting the packing completely hindered photocatalysis. The results for the pre-wetted packing showed an increase in toluene removal from zero to almost 30% after about 1 h of the run time. The increased removal after some time can be explained by the drying of the packing due to the heat produced by the UV

lamps and evaporation of water as a result of air flow through the packed bed. Having the UV lamps turned on at all times increased the temperature inside the reactor; thus, drying the commingled packing that was wetted before the experiment was started. The drying of the packing was confirmed by the water condensation observed at the gas effluent.

By keeping the packing wetted at all times, no net removal was found during the 3 h run. These results were surprising because although adsorption was shown to be inhibited by wetting of the packing, the photocatalysis of toluene was not anticipated to become negligible in the absence of adsorption given the requirement of water vapor for large toluene removals to occur. Creating a water film around the STCs prevented direct contact of the titania embedded in the pellets and the toluene present in the gas phase. These results suggest that the mechanism involved in toluene PCO using STCs requires an adsorption step of the contaminant for the reaction to occur. Despite having the hydroxyl radical forming potential (i.e. water) pre-adsorbed, it is evident that the reaction does not occur in the bulk gas phase since no removal was observed under any wetting conditions.

Table 5-1. Summary of experimental conditions for the bench-scale gas phase PCO experiments using dry STCs

| $\tau$<br>s | Z<br>cm | $Q_G$<br>cm <sup>3</sup> /s | $U_G$<br>cm/s |
|-------------|---------|-----------------------------|---------------|
| 5.9         | 4       | 26.7                        | 0.68          |
| 12.5        | 4       | 12.5                        | 0.32          |
| 25.0        | 8       | 12.5                        | 0.32          |

Table 5-2. Mears ( $C_M$ ) and Weisz-Prater ( $C_{WP}$ ) criteria for the determination of mass transfer influences.  $C_M < 0.15$  indicates no significant external mass transfer resistance.  $C_{WP} < 1$  indicates no significant internal mass transfer resistance.

| $\tau$<br>(s) | $r \times 10^5$<br>(mol/m <sup>3</sup> /s) | $r$<br>( $\mu$ g/L/s) | $k_c \times 10^2$<br>(m/s) | $C_M < 0.15$<br>$Y_b = Y_o$ | $C_M < 0.15$<br>$Y_b = Y_e$ | $C_{WP} < 1$ |
|---------------|--|-----------------------|----------------------------|-----------------------------|-----------------------------|--------------|
| 5.9           | 1.72                                       | 1.59                  | 3.11                       | 0.0038                      | 0.0056                      | 0.159        |
| 12.5          | 1.69                                       | 1.55                  | 2.11                       | 0.0057                      | 0.0171                      | 0.159        |
| 25.0          | 1.18                                       | 1.09                  | 2.21                       | 0.0038                      | 0.0511                      | 0.113        |

Table 5-3. Experimental conditions for the adsorption experiments using dry STCs in the TPOT

| Run # | $C_o$ mg/m <sup>3</sup> | $Q_G$ L/min | $\tau$ s | $U_G$ cm/s | Mass Loading $\mu\text{g}/\text{min}$ | Influent Water Vapor g/m <sup>3</sup> |
|-------|-------------------------|-------------|----------|------------|---------------------------------------|---------------------------------------|
| 1     | $74 \pm 4$              | 142         | 15.4     | 7.9        | 585.8                                 | $8.69 \pm 0.12$                       |
| 2     | $39 \pm 3$              | 142         | 15.4     | 7.9        | 308.7                                 | $8.74 \pm 0.08$                       |
| 3     | $76 \pm 5$              | 85          | 25.7     | 4.7        | 360.1                                 | $9.10 \pm 0.14$                       |

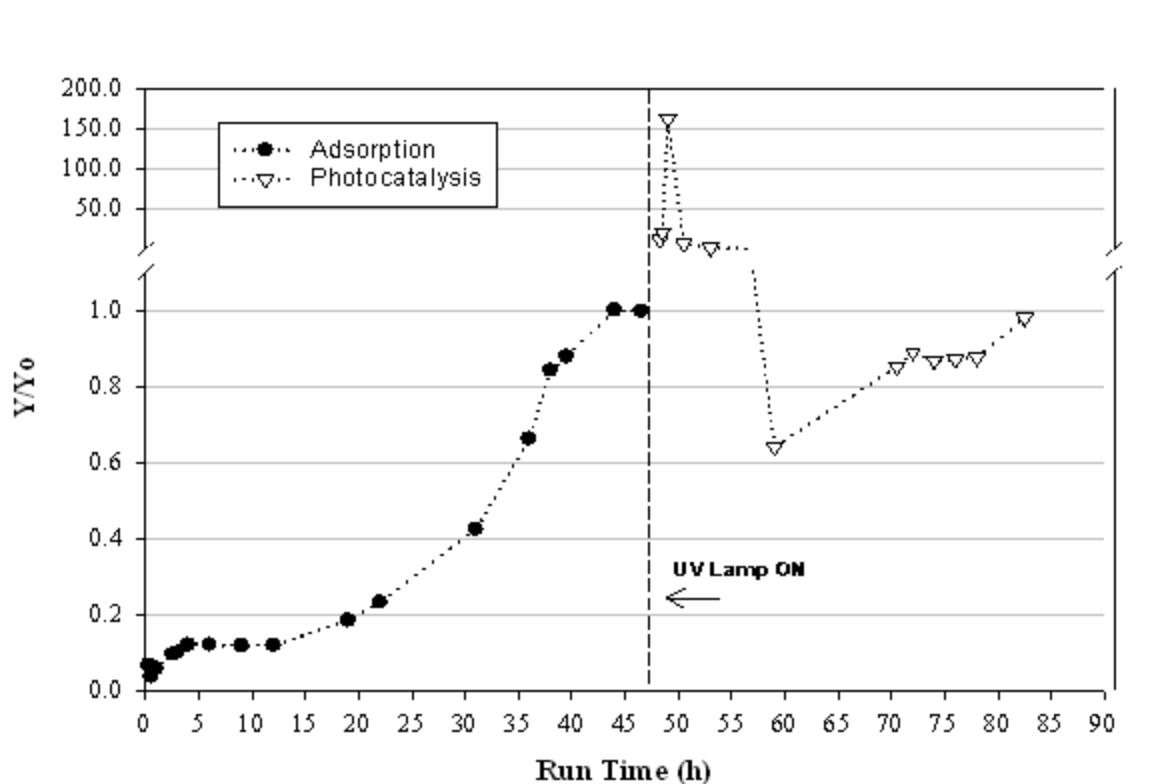


Figure 5-1. Gas phase adsorption of toluene followed by PCO using dry STCs and low relative humidity conditions in the bench scale reactor:  $\text{RH} = 13\%$ ,  $Y_o = 90 \pm 10 \text{ mg/m}^3$ ,  $Q_G = 3.3 \text{ cm}^3/\text{s}$ . Bed Volume =  $42 \text{ cm}^3$ .  $Y$  is the effluent concentration of toluene in the gas phase.

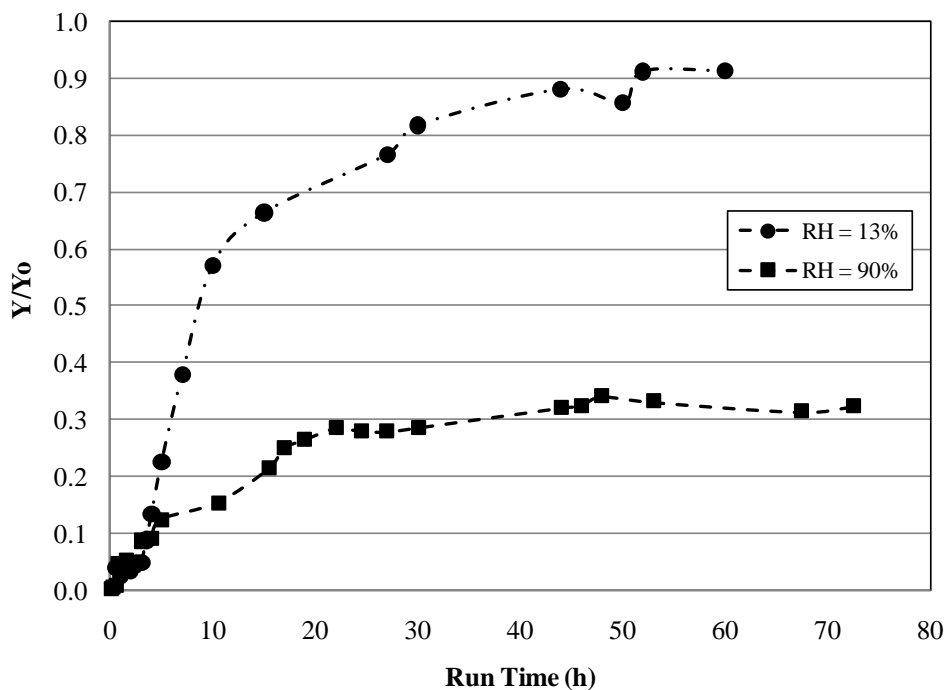


Figure 5-2. Normalized effluent toluene concentration during simultaneous adsorption and PCO experiments at different water vapor concentrations as a function of run time.  $Y_o = 30 \text{ mg/m}^3$ .  $Q_G = 12.5 \text{ cm}^3/\text{s}$ . Bed Volume =  $157 \text{ cm}^3$ .

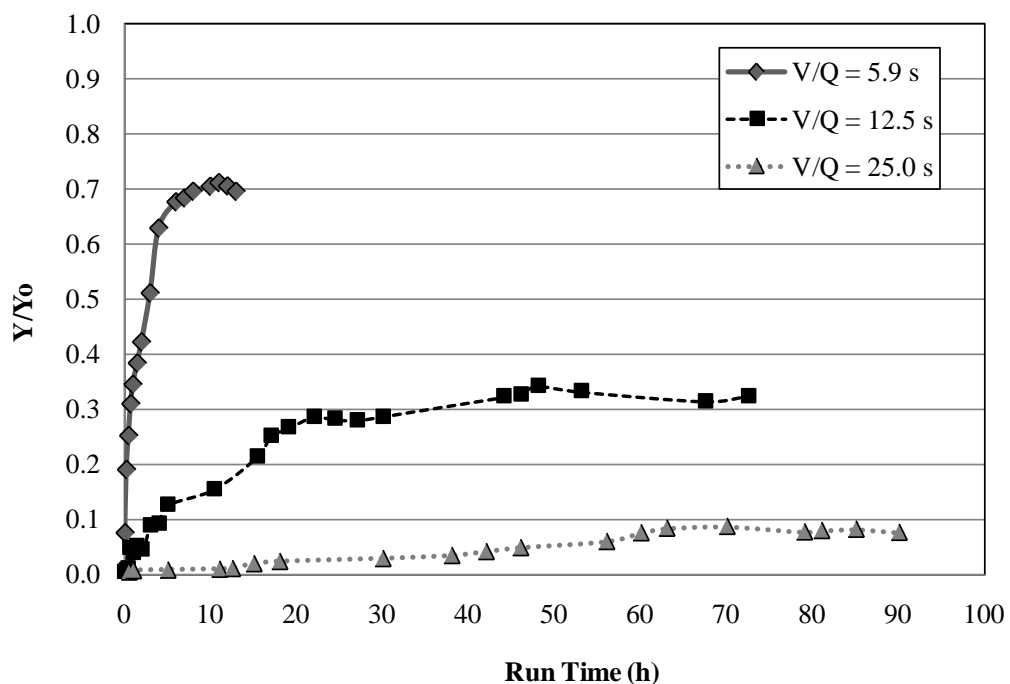


Figure 5-3. Normalized effluent toluene concentrations as a function of run time at various space times.  $Y_o = 30 \text{ mg/m}^3$ ,  $RH = 90\%$ .

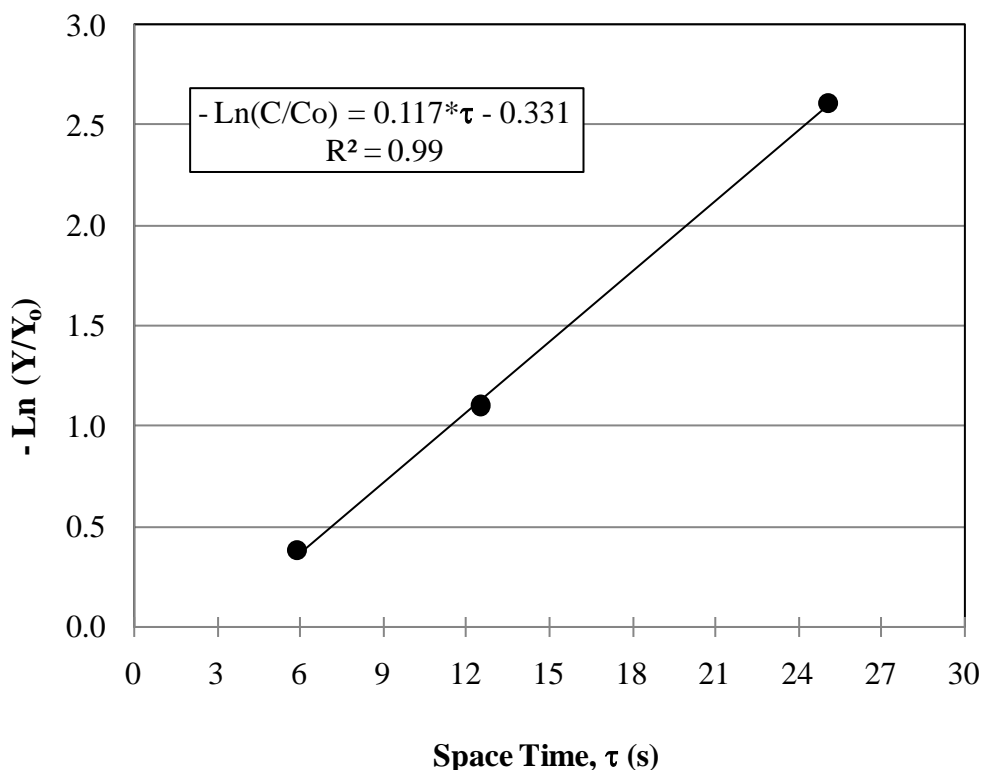


Figure 5-4. Linear regression of the Langmuir-Hinshelwood model

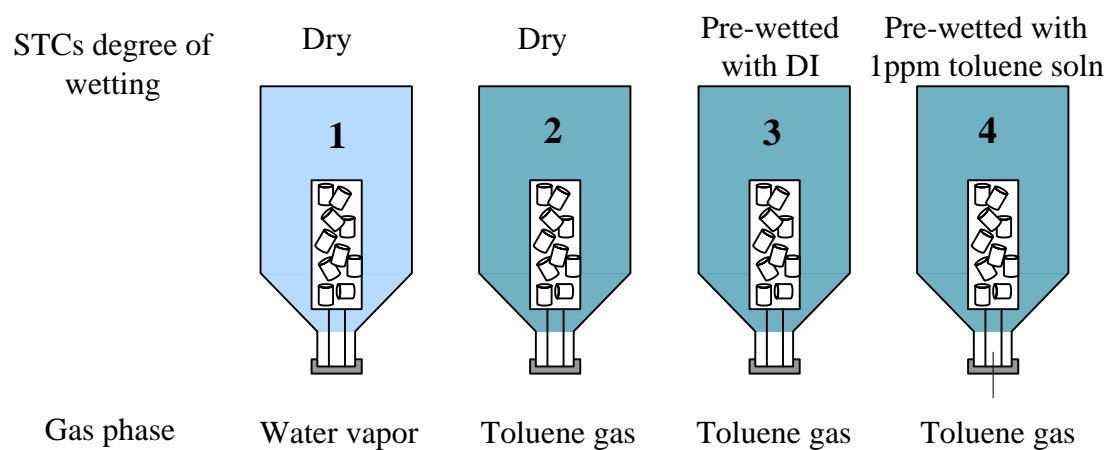


Figure 5-5. Plan view of the experimental setup of the batch experiments to assess adsorption under different STCs wetting conditions.

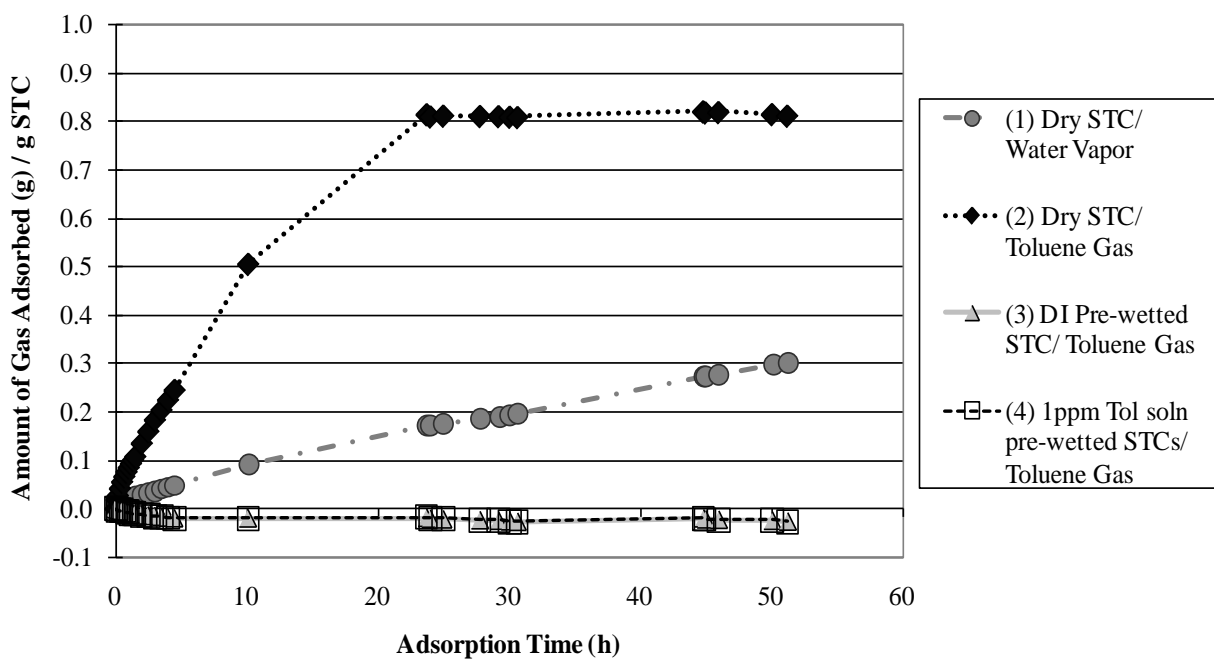


Figure 5-6. Gas phase adsorption of water vapor and toluene to STCs under different wetting conditions.

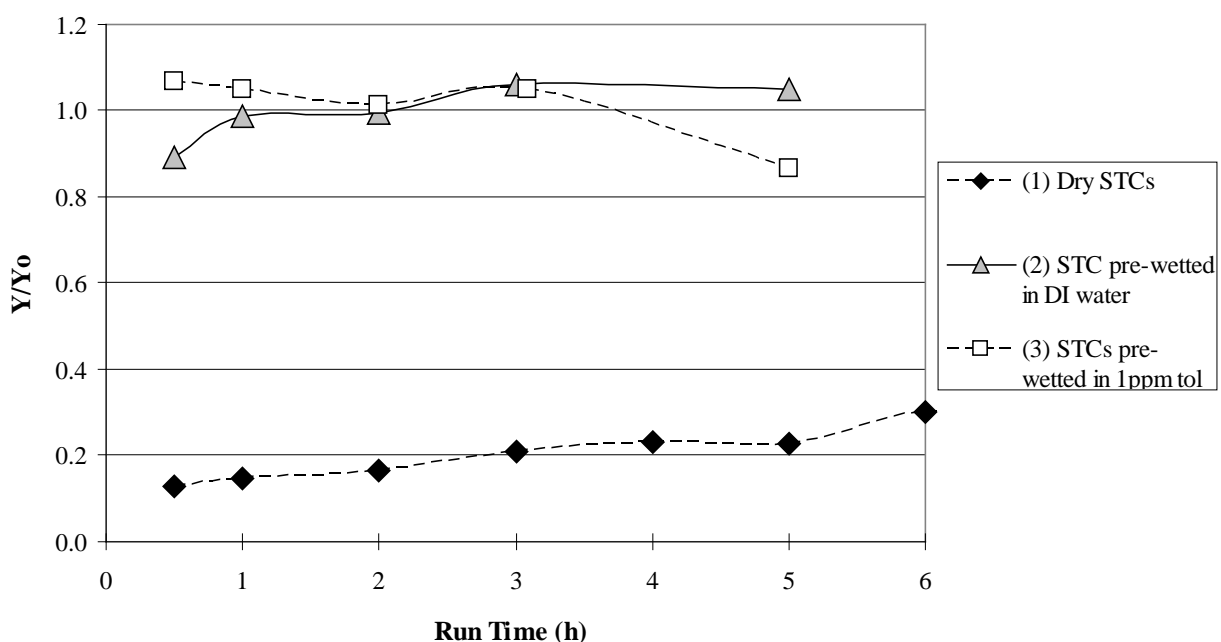


Figure 5-7. Adsorption of gas phase toluene to STCs under different wetting conditions in a continuous flow reactor.

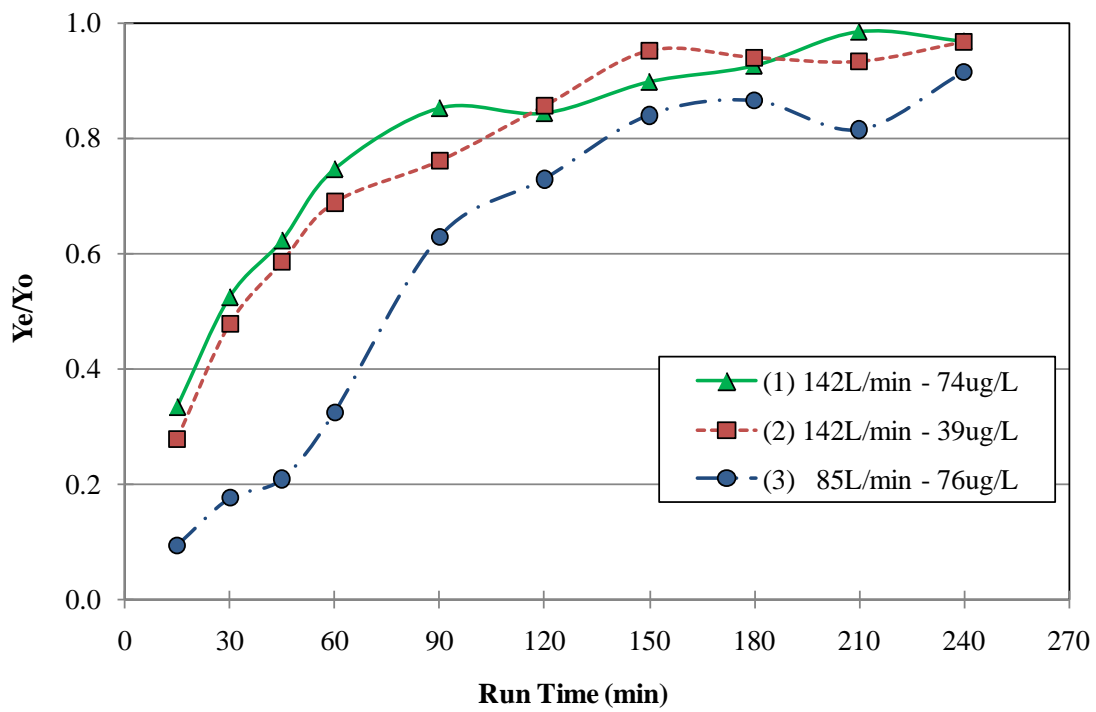


Figure 5-8. Adsorption breakthrough curves for toluene on the dry STCs in the commingled packing of the pilot-scale reactor.

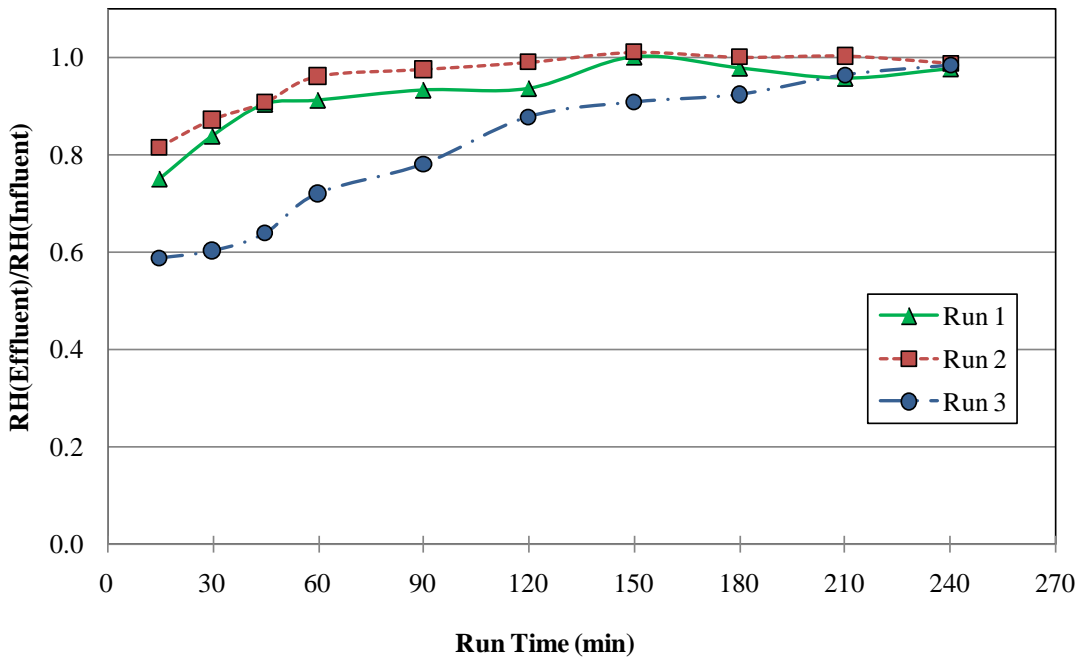


Figure 5-9. Adsorption breakthrough curves for water vapor on the dry STCs in the commingled packing of the pilot-scale reactor.

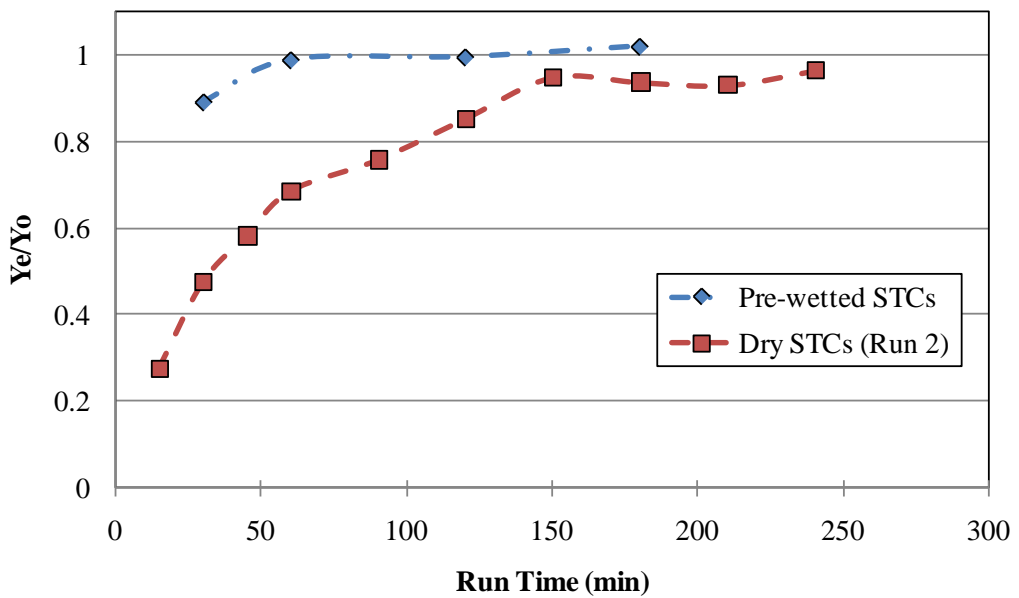


Figure 5-10. Comparison of gas phase toluene adsorption using the TPOT with dry versus pre-wetted STCs.

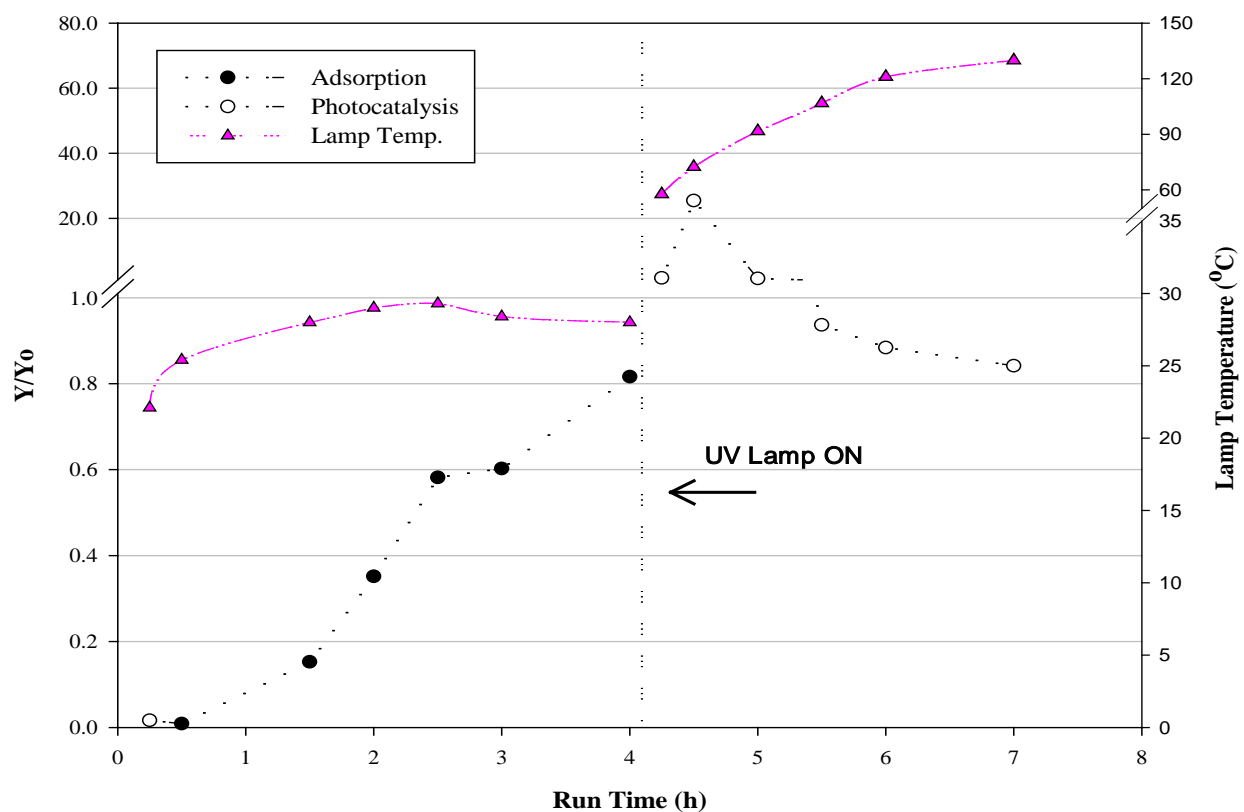


Figure 5-11. Adsorption of gas phase toluene followed by PCO in the TPOT using dry STCs and ambient relative humidity.  $Y_o = 85 \text{ mg/m}^3$ ,  $Q_G = 142 \text{ L/min}$ .

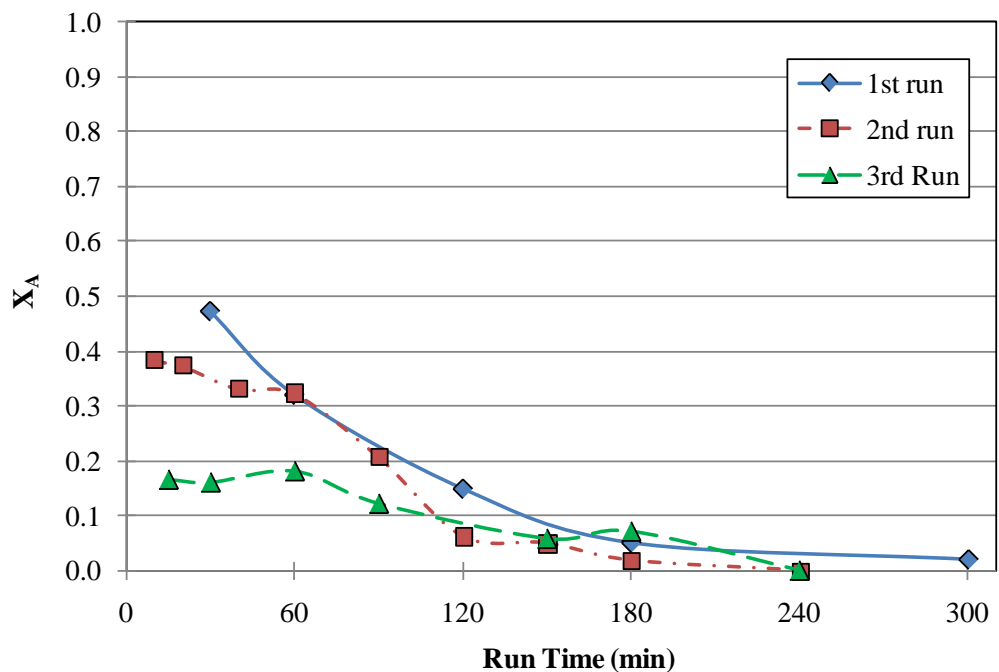


Figure 5-12. Conversion of toluene by PCO in TPOT for 3 studies performed using the same initial conditions:  $Y_o = 65 \pm 10 \text{ mg/m}^3$ ,  $Q_G = 142 \text{ L/min}$ ,  $\text{RH}_{\text{avg}} = 44\%$ ,  $T_{\text{avg}} = 23^\circ\text{C}$

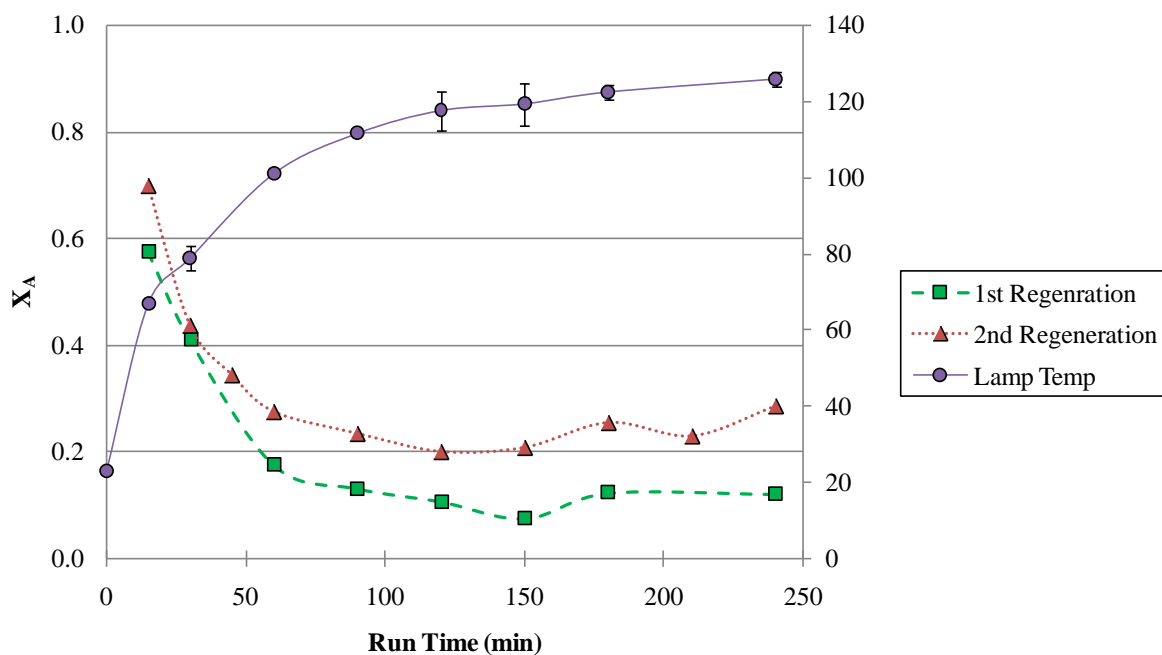


Figure 5-13. Conversion of gas phase toluene by PCO in the TPOT after catalyst regeneration.  $Y_o = 60 \pm 10 \text{ mg/m}^3$ ,  $Q_G = 142 \text{ L/min}$ ,  $\text{RH}_{\text{IN,avg}} = 44\%$ ,  $T_{\text{IN,avg}} = 23^\circ\text{C}$ .

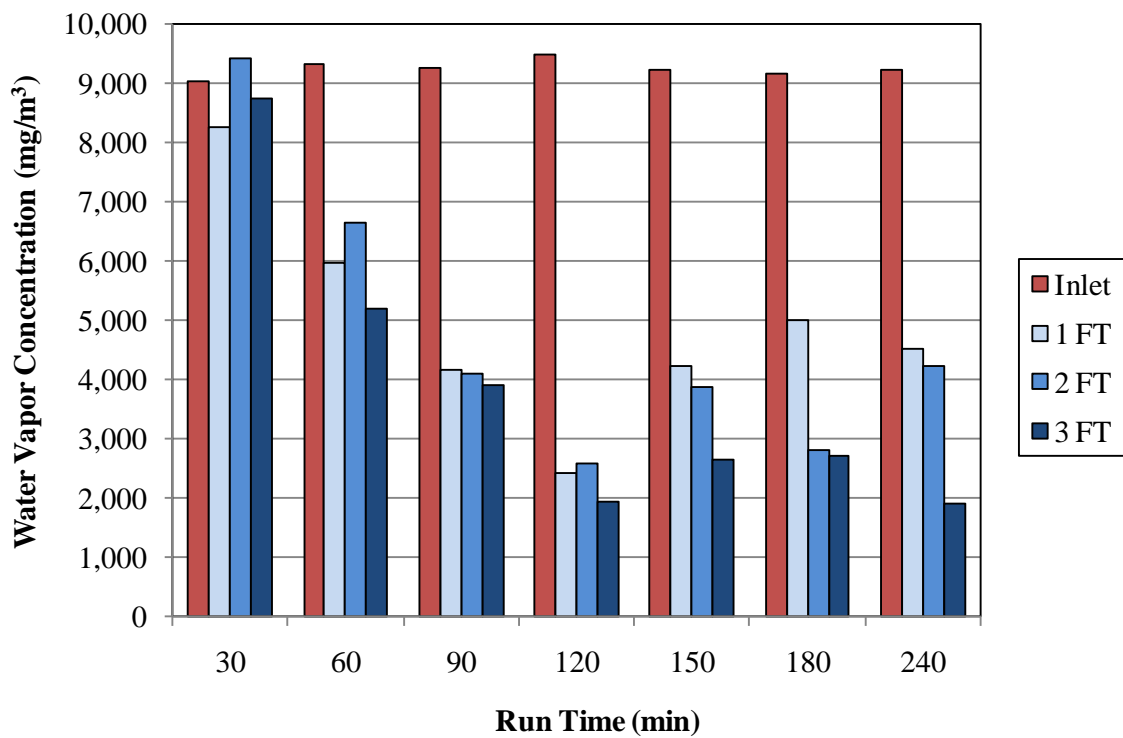


Figure 5-14. Water vapor concentration profile in the TPOT at various run times for the experiment corresponding to the 2<sup>nd</sup> regeneration study. Samples were collected from the influent and at packing depths of 1, 2, and 3 feet.

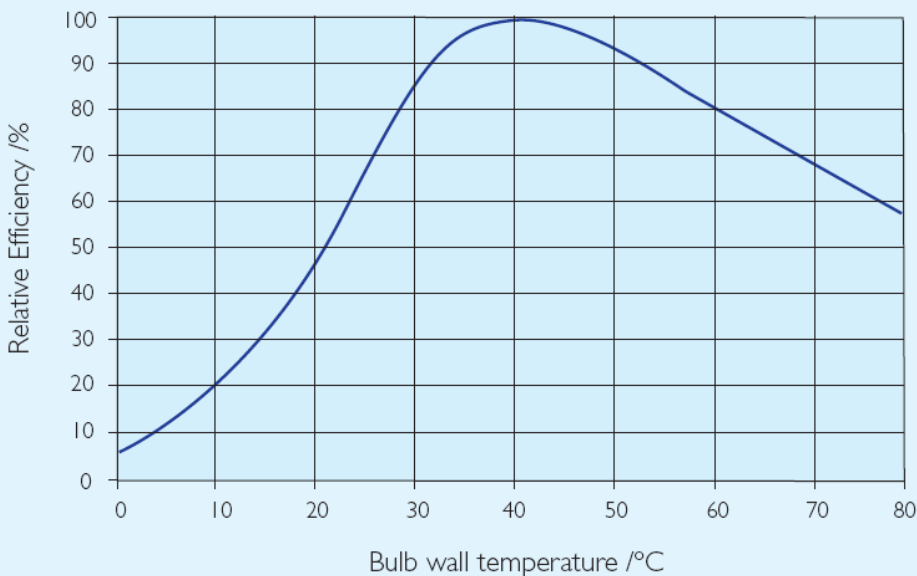


Figure 5-15. Relative output of the UV-C lamps used in this research as a function of temperature (Obtained from Philips, 2004).

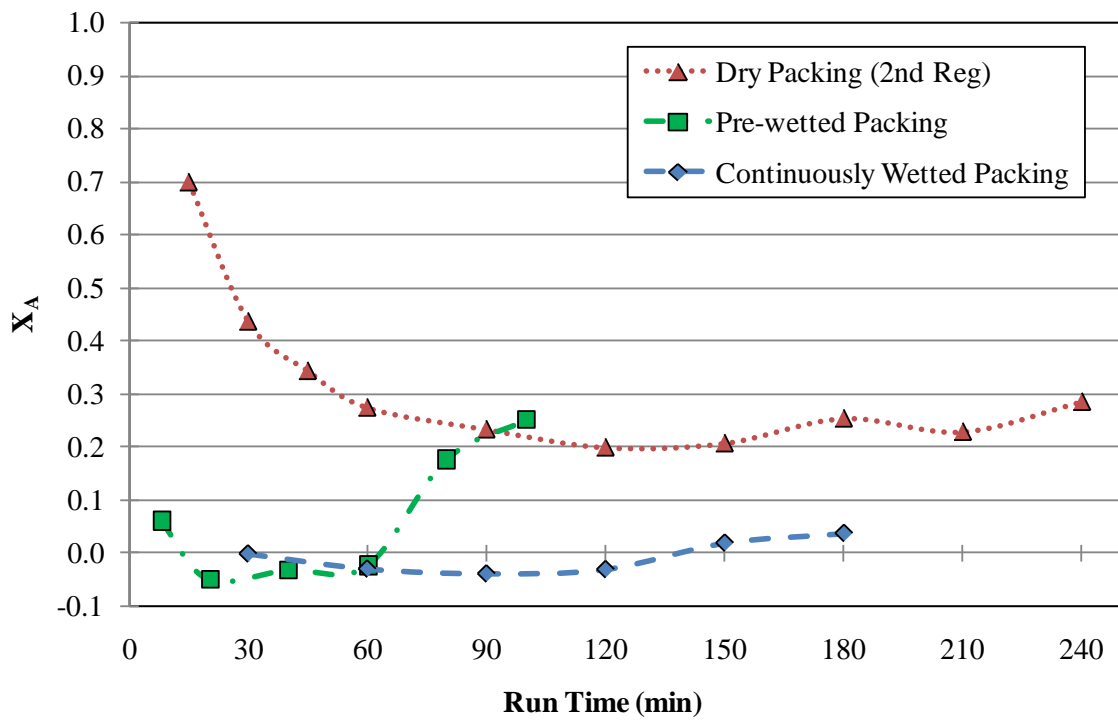


Figure 5-16. Effect of wetting of the packing on gas phase toluene removal by PCO in the TPOT.  
 $Y_o = 60 \pm 10 \text{ mg/m}^3$ ,  $Q_G = 142 \text{ L/min}$ ,  $Q_L = 3.8 \text{ L/min}$ ,  $\text{RH}_{\text{IN,avg}} = 44\%$ ,  $T_{\text{IN,avg}} = 23^\circ\text{C}$ .

## CHAPTER 6

### AQUEOUS PHASE TOLUENE DEGRADATION STUDIES

#### **Bench-Scale Studies**

**Adsorption of Toluene in a Batch Reactor:** The extent of aqueous phase toluene adsorption to the STCs was determined by performing batch adsorption equilibrium experiments. During these experiments, either the initial concentration of toluene or the mass of STCs was kept constant while the other parameter was changed. The systems were expected to be at equilibrium since adsorption times of at least 24 h were used. When the STCs are placed in any solution, some outgassing of the air present in the pore matrix is observed due to the large internal pore volume of the STCs. To prevent losses of toluene by volatilization when placing the STCs in the aqueous toluene solution, the STCs were soaked in DI water for about 24 hrs before placing them in the batch reactors. The removal of toluene as a function of STC mass is shown in Figure 6-1 for initial toluene concentrations of about 190 µg/L and 1000 µg/L. Increasing the mass of STCs increased the removal of toluene because of the larger available area present for adsorption. However, the initial concentration did not seem to have a noticeable impact on the removal of toluene since both removal curves followed the same trend as a function of STC mass. The slope of the removal curve decreased with increasing STC mass. The maximum concentration removal achieved for the mass of STCs tested was about 75% which corresponded to approximately 6 g STCs (about 16 STCs pellets).

The adsorption results were compared to the two most commonly used single component adsorption isotherms to describe the adsorption of organic contaminants: Langmuir and Freundlich isotherms. The models describing the adsorption density ( $q$ ) as a function of contaminant concentration ( $[A]$ ) are given by equations 6-1 and 6-2 for Langmuir and Freundlich isotherms, respectively. A linearization method was used for each isotherm to find the two fitting

parameters for the models that best matched the data. The linear forms of the models are shown in Equations 6-3 to 6-5 for the Langmuir type 1 (L1), Langmuir type 2 (L2) and Freundlich isotherms, respectively. The fitting parameters, shown in Table 6-1, were calculated from the slope and y-intercept found by the linear regression of the plots:  $1/[A]$  vs.  $1/q$  (for L1),  $[A]$  vs.  $[A]/q$  (for L2) and  $\log [A]$  vs.  $\log q$  (for Freundlich).

$$q_{Langmuir} = K_{ads} \times q_{max} \times [A] / (1 + K_{ads} \times [A]) \quad (6-1)$$

$$q_{Freundlich} = K_f [A]^n \quad (6-2)$$

$$1/q_{L1} = 1 / (K_{ads} \times q_{max}) \times 1/[A] + 1/q_{max} \quad (6-3)$$

$$[A]/q_{L2} = 1/q_{max} \times 1/[A] + 1/(K_{ads} \times q_{max}) \quad (6-4)$$

$$\log q = n \times \log [A] + \log K_f \quad (6-5)$$

The results showing the adsorption density in  $\mu\text{g}$  of toluene/g of STC as a function of toluene concentration are presented in Figure 6-2 together with the fits for the isotherms evaluated. The adsorption isotherm seems to follow a fairly linear trend for the concentration range investigated (48 to 888  $\mu\text{g}/\text{L}$ ). The adsorption density was not very large for this aqueous phase toluene – STC system since only about 6  $\mu\text{g}$  of toluene were adsorbed per gram of STC for the highest concentration included (or about 446 molecules of toluene/  $\mu\text{m}^2$  based on a  $250 \text{ m}^2/\text{g}$  surface area of the STCs). The best fit, determined by comparing the sum of squared differences between the data and the model (SSqD), was obtained by the Freundlich isotherm (SSqD = 0.36), followed by L2 (SSqD = 1.4) and L1 (SSqD = 5.3). The exponent found for the Freundlich isotherm was close to 1 ( $n = 0.87$ ), which agrees with the linearity of the adsorption isotherm shown by the data. However, it is important to notice that the isotherm fit does not necessarily imply that the underlying assumptions used to derive the isotherms (eg. monolayer vs. multilayer

adsorption) are valid for the aqueous toluene – STC system. These isotherms provide a mathematical tool to describe the trends shown by the data.

### Pilot-Scale Studies

#### Adsorption of Toluene Using TPOT

Given the large internal surface area of the STCs and the results observed at the bench-scale, some adsorption of toluene was expected to occur in the aqueous phase. Therefore, aqueous phase adsorption was tested in the TPOT at different liquid loading rates. Higher loading rates were expected to increase the surface area available for adsorption since they result in larger wetted packing areas. As shown in Figure 6-3, despite the increase of liquid loading rate, no significant removal by adsorption was observed.

Previously presented batch scale experiments showed significant adsorption of toluene, which was not surprising given the adsorption time used of 24 h. Similarly, Holmes et al. (2004) found significant toluene adsorption using the same material of a smaller pellet size in a continuous flow reactor. In their reactor system, they achieved equilibrium after 5 h. The lack of adsorption in the TPOT is probably due to the short average residence time of the water in the reactor of less than 60 seconds. Although the STCs have a large surface area for adsorption, it seems that they require long contact times for significant adsorption to be observed. The time for adsorption available in the TPOT (less than 60 s) was not enough to show significant differences in influent and effluent concentrations for the mass loading rates (1.5 – 3.6 mg/min) used during the experiments. Adsorption is expected to occur until equilibrium is achieved in the STCs in the TPOT, but it does not affect the concentration of the effluent because the removal for a single pass of fluid is small due to the small residence time

## **PCO of Toluene Using TPOT**

The photocatalytic oxidation of toluene in the aqueous phase was tested as a function of two important parameters expected to have a significant effect on PCO: the initial concentration of toluene and the liquid loading rate. The removal of toluene as a function of initial concentration for a flowrate of 3.8 L/min (loading of 3.1 gpm/ft<sup>2</sup>), shown in Figure 6-4, indicates that increasing the toluene inlet concentration resulted in a higher removal, likely due to the increase in driving force for the transfer of toluene across the liquid-solid film, which resulted in higher concentrations at the catalyst surface and thus higher removal.

The effect of liquid loading rate in the conversion of toluene can be observed in Figure 6-5. All the results shown in Figure 6-5 were obtained at an initial toluene concentration of approximately  $495 \pm 37 \mu\text{g/L}$ . The conversion of toluene decreased as the liquid loading rate was increased. Increasing the liquid loading rate affects three important factors for aqueous PCO: the wetted surface area and the liquid film thickness both increase while the mean residence time decreases. Increasing the area of the catalyst that is wetted with the contaminated solution should result in higher removals since more of the toluene in the aqueous phase would have the opportunity to be in contact with the catalyst surface; however, by increasing the film thickness, the liquid-solid resistance is increased, so the driving force is adversely affected. Similarly, the lower residence time in the reactor at higher flowrates provides less reaction time and reduces the removal of toluene by PCO.

## **TPOT Hydrodynamics**

A basic understanding of the hydrodynamic behavior and mass transfer in the trickled bed reactor used in this research is essential for design, scale-up, scale-down, and performance prediction purposes. It was of interest to analyze the hydrodynamic behavior of the reactor to

obtain estimates of the dispersion coefficients since these are needed to determine the liquid-solid mass transfer coefficients used for modeling the reactor.

The hydrodynamic behavior of trickle packed bed reactors is usually characterized by the axial dispersion and/or the liquid holdup. The axial dispersion is generally specified by an axial dispersion coefficient ( $D_{AX}$ ) which provides information about the extent of the deviation of the flow from the ideal plug (or piston) flow (de Andrade Lima, 2006).

Tracer studies have long been used to characterize the hydraulic behavior of real reactors. TPOT is not a reactor that is completely saturated with water; on the contrary, the water is introduced by a spray nozzle so that the molecules trickle over and through the packing. A tracer test in a trickle bed provides an estimate of the average time it takes the water molecules to make its way through the packing of the tower. The type of tracer test used in the TPOT was the step input tracer test. This method entails the introduction of tracer at a constant dosage or concentration until the effluent concentration reaches a steady-state value. While continuously feeding the reactor with the tracer, the effluent concentrations are measured and the resulting data provide the cumulative residence time distribution function,  $F(t)$ . Once the cumulative residence time distribution (RTD) function is constructed the residence time density function ( $E(t)$ ) for the data is easily obtained as the first derivative of the distribution function with respect to time (Equation 6-6)

$$E(t) = dF(t)/dt \quad (6-6)$$

Generation of the residence time density function allows calculation of the mean residence time,  $t_m$ . The mean value of the residence time of the water molecules in the reactor is given by the first moment of the centroid of the RTD curve, shown in Equation 6-7.

$$t_m = \frac{\int_0^\infty tE(t)dt}{\int_0^\infty E(t)dt} = \frac{\int_0^\infty tE(t)dt}{\int_0^\infty E(t)dt} \approx \sum_0^\infty tE\Delta t \quad (6-7)$$

Since analytical methods of integration are not adequate to use in discrete data sets such as the collected data from tracer tests, numerical integration is required in order to calculate  $t_m$ . The method used for all numerical integrations in this analysis was the trapezoid rule, described by Equation 6-8:

$$Area = \frac{1}{2}(f_i + f_{i-1}) * (t_i - t_{i-1}) \quad (6-8)$$

where  $f$  represents the function to be integrated over time, and the final result is the sum of all the areas calculated between the points.

The axial dispersion coefficient can be calculated by fitting the RTD obtained from the tracer test to an RTD model that incorporates the coefficient as one of the fitting parameters. Several models have been proposed from which an axial coefficient can be identified. Most of these methods are modifications of the most ubiquitous model used in the literature, the one dimensional piston – dispersion (PD) model (or ideal plug flow with dispersion, or advection-dispersion model) described by Equation 6-9 for a non-reactive tracer (Piche et al., 2002).

$$D_{AX} \frac{d^2C}{dz^2} - U_L \frac{dC}{dz} = \frac{dc}{dt} \quad (6-9)$$

The dispersion component in this model is simply a hypothetical term that has the form of Fick's second law added to the plug flow model. The model has no particular mechanistic significance because the use of this model requires empirical evaluation of the dispersion term, i.e. the measured dispersion characteristics need to be correlated with other system properties. Nevertheless, it provides some measure of the back-mixing in the reactor. The closed form

mathematical solution for a step input of tracer, which is the method used for the tracer tests in this work, can be obtained by treating the stimulus as an injection of the tracer to an open tube which extends from the point of injection to infinity in both directions, so that the initial and boundary conditions are (Weber and DiGiano, 1996):

$$C = 0 \text{ for } x > 0 \text{ at } t = 0$$

$$C = C_{IN} \text{ for } x < 0 \text{ at } t = 0$$

$$C = 0 \text{ at } x = \infty \text{ for } t \geq 0$$

$$C = C_{IN} \text{ at } x = -\infty \text{ for } t \geq 0$$

where  $C_{IN}$  is the step concentration of the tracer. For this particular instance, the length of the dispersion is unbounded, and the solution for the concentration as a function of position and time is given by the error function. The solution for a specific bed length is shown by Equation 6-10. This equation shows that the  $F(t)$  curve will broaden as the dispersion coefficient increases. The dispersion number  $N_d$ , shown in Equation 6-10 is defined as the dispersive mass transport over the advective mass transport or  $D_{AX}/(U \times Z)$ , which is also the inverse of the reactor Peclet number ( $Pe$ ). The relationship indicates that as the dispersion number increases, the transport by dispersion increases relative to the transport by advection.

$$\frac{C_{out}}{C_{in}} = F(t) = 0.5 \left\{ 1 - erf \left[ 0.5(N_d)^{-0.5} \frac{1 - \left( \frac{t}{t_m} \right)}{\left( \frac{t}{t_m} \right)^{0.5}} \right] \right\} \quad (6-10)$$

The tracer of choice for the experiments was sodium chloride (NaCl) because it can be easily measured using a conductivity meter and it does not adsorb to the plastic packing in the reactor or to the STCs. However, when STCs are washed with water, the solution's conductivity tends to increase due to the residual fluoride present in the pellets, thus influencing the conductivity measurements attributed to NaCl. Although the STCs were expected to leach fluoride during continuous flow operation and confounding results were anticipated by using NaCl as the tracer, it was determined that after 10 min of wetting of the packing with tap water,

an steady state conductivity was achieved. Additionally, high concentrations of tracer were used to decrease the effect of the potential leaching of fluoride that could increase the conductivity measurements.

Tracer tests were performed using high flow rings only packing as well as the commingled packing. The cumulative RTDs measured during the tracer test and the RTDs calculated from the  $F(t)$  data are presented in Figure 6-6 for both packing configurations. Based on the tracer test results, the mean residence time was calculated by numerically deriving the cumulative RTD for each type of packing and flowrate to obtain  $E(t)$  and then using Equations 6-7 and 6-8. The dispersion coefficient was determined by minimizing the squared sum of the difference between the modeled values for  $F(t)$  obtained from Equation 6-10 and the measured results. All these calculated values for the mean residence time and dispersion coefficients for the different liquid loading rates investigated are shown in Table 6-2.

The results illustrated in Figure 6-6 for the high flow rings only packing showed that the residence time distributions of the water molecules in the TPOT are very similar despite the flowrate. For the case of the commingled packing (Figure 6-6B), the RTDs showed higher dispersion or wider RTDs for the lower flowrates indicating that the system is approaching plug flow as the flow rate is increased. The dispersion coefficients in the reactor for the commingled packing compared to the high flow rings only packing seemed to be slightly higher. This is not unexpected because the dispersion in a reactor tends to increase when the heterogeneity of the packing increases.

The dispersion coefficients obtained from the analysis, presented in Table 6-2, ranged from about 4 to 9 cm<sup>2</sup>/s. These values followed a linearly increasing trend with increasing flowrate as shown in Figure 6-7. For the lowest flow used, 1.9 L/min, the dispersion coefficient was about

4.0 cm<sup>2</sup>/s. This value increased to 6.3 cm<sup>2</sup>/s when the flow was doubled and to 8.8 cm<sup>2</sup>/s by increasing the flowrate from 3.8 to 5.7 L/min. The dispersion coefficients calculated from the tracer test analysis were similar to the values obtained from correlations found in the literature for trickle bed reactors. For example, well known correlations such as those proposed by Otake and Kunugita (1958), Sater and Levenspiel (1966) and Michell and Furzer (1972) and many others summarized by de Andrade Lima (2006) resulted in dispersion coefficients in the range of 1 to 12 cm<sup>2</sup>/s, which are comparable to the values found for this system. Many of these correlations available in the literature are functions of the Reynolds (Re) and Galileo (Ga) numbers. The calculation of these numbers requires the particle diameter of the packing as one of the known parameters. For the case of the TPOT, the commingled packing makes it difficult to determine one value for this parameter since there are two types of packing both with different diameters (9 mm for STCs, 15 mm for PR). The value used in the correlations was the average diameter obtained as a weighted average in terms of the bulk volume occupied by each type of packing, which resulted in an average particle diameter of 14.8 mm.

An empirical correlation, shown in Figure 6-7, was determined from the data to predict the dispersion coefficients in the TPOT packed with the commingled packing for purposes of modeling. This correlation is given in Equation 6-11. The two parameters used for the correlation were Re ( $= d_p U_L \rho_w / \mu_L$ ) and Ga ( $= d_p^3 \rho_w^2 g / \mu_L^2$ ) as most of the other correlations in the literature (de Andrade Lima, 2006). The exponent fitted for Ga was - 0.10 which is similar to the values found in other correlations. The coefficient for Re, however, was 0.84, which is slightly higher than the values used in the literature which are in the range of 0.5 to 0.7.

$$D_{AX} = 1.98 \times Re^{0.84} Ga^{-0.10} \quad (6-11)$$

The mean residence time decreased with flowrate for both types of packing, but it was higher for the commingled packing compared to the high flow rings only. Mixing the STCs with the pall ring packing decreased the porosity of the tower from about 0.9 for the high flow rings only to 0.76 for the commingled packing. Lower porosity is an indication of more packing present in the tower and increased tortuosity in the system. This means that there are more tortuous paths for the water to flow through, which will tend to increase the holdup in the reactor resulting in higher residence times of the water molecules. This will also tend to increase the tailing effect. The mean residence time for the reactor packed with the mixed high flow rings and STCs followed a linear trend with respect to the liquid loading rate as shown in Figure 6-8 for the loadings investigated in this work.

### **Liquid-Solid Mass Transfer Coefficient ( $K_{LSaC}$ )**

By knowing the dispersion coefficients in the TPOT as a function of liquid loading rate, the liquid-solid mass transfer coefficients ( $K_{LSaC}$ ) can be more easily investigated, as shown in this section. Mass transfer coefficients from the liquid to the solid catalyst were determined by performing a mass balance on the reactor for the liquid phase and numerically solving the resulting second order differential equation using the finite difference method. By this method, finite differences are substituted by the derivatives of the original equation and also the boundary conditions. The reactor was modeled using the plug flow with dispersion model (PFD) given in Equation 6-12 and solved at steady state. The corresponding boundary conditions used to solve the model are shown in Equations 6-13 and 6-14. For the analysis, the central differences shown in Equations 6-15 and 6-16 were used for the second and first order derivatives, respectively. By performing such substitution, a linear differential equation is transformed into a set of simultaneous algebraic equations that can be solved using traditional methods which use some type of matrix multiplication, such as the LU decomposition method. Before using the model for

the conditions evaluated in this research, it was tested using parameters from examples from Chapra and Canale (2003) to determine if the solutions were correct and ensure that the model was working properly.

$$D_{AX} \frac{d^2C}{dz^2} - U_L \frac{dC}{dz} - (K_{LS} a_c)(C - C_s) = \frac{dC}{dt} = 0 \quad (6-12)$$

$$-D_{AX} \frac{dC_0}{dz} = U_L (C_{IN} - C_0) \quad \text{at } z = 0 \quad (6-13)$$

$$\frac{dC_Z}{dz} = 0 \quad \text{at } z = Z \quad (6-14)$$

$$\frac{d^2C}{dz^2} = \frac{C_{i+1} - 2C_i + C_{i-1}}{\Delta z^2} \quad (6-15)$$

$$\frac{dC}{dz} = \frac{C_{i+1} - C_{i-1}}{2\Delta z} \quad (6-16)$$

The boundary condition at the reactors' inlet (Equation 6-13) indicates that at  $t < 0$ , the reactor is devoid of contaminant and at  $t = 0$ , the chemical is injected in the reactor at a constant level of  $C_{IN}$  (the flux is constant). The second condition (Equation 6-14) assumes that the dispersion in the reactor does not affect the exit rate; so, the contaminant leaves the reactor purely as a function of the flow through the outlet.

Continuity of flux requires that:  $r = K_{LS} a_C * (C - C_s) = -k * C_s^n$ . The surface concentration,  $C_s$ , shown in Equation 6-13, then can be solved for if the reaction kinetics at the surface are known. However, the intrinsic kinetics for the system are not known in this case, so  $C_s$  was assumed to be equal to zero, implying that the contaminant does not accumulate at the surface of the catalyst. This also implies that the system is mass transfer limited as compared to surface reaction limited because by assuming that the external resistance controls ( $K_{LS} a_C \ll k$ ), so  $(C - C_s)$  becomes a large value suggesting that  $C_s \ll C$ . This assumption is not unrealistic if the reaction

occurring at the catalyst surface is considered to be instantaneous. For the case of photocatalytic reactions, it is expected that the contaminant will react as soon as it reaches the surface of the catalyst given that there is sufficient hydroxyl radicals and UV intensity.

To determine if the system was mass transfer limited the rates were determined as a function of the loading rates (or superficial velocities) using Equation 6-17 since it is well established that in the absence of external mass transfer limitations these rates will remain unchanged.

$$r = -dC/dt = (C_o - C_e)/t_m \quad (6-17)$$

The results for the reaction rates, presented in Table 6-3, indicate that the system appears to be limited by external mass transfer at the lower velocities, but the rates remained similar for velocities greater than 0.22 cm/s. However, as explained for the gas phase results of the bench scale kinetic analysis, this is true only for a differential reactor, which is not the case of the TPOT. Therefore, similar to the analysis performed in Chapter 5, the Mears criterion was determined to assess the importance of external mass transfer in the system. The same criterion used for the gas phase (Equation 5-2) was used for the aqueous phase, but for this analysis all the parameters in Equations 5-2 and 5-3, such as the density, viscosity, and diffusivity referred to the aqueous phase. The aqueous phase diffusivity ( $D_L \sim 8 \times 10^{-10} \text{ m}^2/\text{s}$ ) was calculated using the correlation shown in Equation 6-18 (Hand et al., 1999).

$$D_L = 13.26 \times 10^{-5} / (\mu_w^{1.14} \times V_b^{0.589}) \quad (6-18)$$

where  $\mu_w$  is the viscosity of water in centipoises and  $V_b$  is the molar volume for toluene (118.3  $\text{cm}^3/\text{mol}$ ). The results obtained for the Mears criterion are shown in Table 6-3 for both the inlet and outlet concentrations since the bulk phase concentration was unknown. All the results found were greater than 0.15, indicating that the system is severely limited by mass transfer. Showing

that the system is mass transfer limited supports the validity of the assumption made about  $C_S$ .

By eliminating  $C_S$  from Equation 6-13, the calculation of  $K_{LSaC}$  is greatly simplified since it becomes the only unknown in the differential equation. The dispersion coefficient in the model was determined using the correlation obtained in the previous section shown in Equation 6-11.

Data on the removal of toluene were available as a function of inlet concentration and liquid loading rate. The initial experimental conditions and results for these data are shown in Table 6-4. By using the known effluent concentrations (at  $Z = 122$  cm) from the experiments corresponding to a set of given initial operating conditions,  $K_{LSaC}$  was determined by minimizing the sum of squared differences (SSqD) of the actual effluent concentrations and those found with the model by using Solver in Microsoft Excel. The concentration profiles predicted by the model using the fitted  $K_{LSaC}$  values are shown in Figures 6-9 and 6-10 for the experiments where either the liquid loading rate or the initial concentrations were changed, respectively. Figures 6-9 and 6-10 also show the measured effluent concentrations for each experiment used, which are given in Table 6-4.

The results for the fitted  $K_{LSaC}$  values, were individually correlated as a function of Reynolds (Re) number (Figure 6-11) and concentration (Figure 6-12) using a power law model. The coefficients obtained for each individual model were then used as first guesses to fit the liquid-solid mass transfer coefficients in terms of both parameters, Re and  $C_{IN}$ . The resulting correlation is presented in Equation 6-19.

$$K_{LS}a_C(s^{-1}) = 1.2 \times 10^{-3} \times Re^{-0.50} \times C_{IN}^{0.25} \quad (6-19)$$

The exponent for each term is very similar in the single and multiple parameters correlations. The Re number in the correlation is dimensionless while  $C_{IN}$  is given in units of  $\mu\text{g/L}$ . The  $K_{LSaC}$  calculated from this correlation is in units of  $\text{s}^{-1}$ . The comparison of the mass

transfer coefficients fitted to the aqueous phase data (data) and those obtained from the correlation developed as a function of Reynolds number and concentration, shown in Figure 6-13, indicates that there is little deviation between the data and the values obtained by the correlation, so the correlation given in Equation 6-19 can be used to determine the liquid-solid mass transfer coefficient for the range of conditions used in the experiments.

The correlations for the dispersion coefficient and the liquid-solid mass transfer coefficient were developed in this chapter with the purpose of using them in the modeling of the reactor when the two phases are flowing simultaneously. Most authors that have investigated the dispersion in trickled bed reactors agree that the dispersion coefficients are not significantly affected by the gas flowrate (Piche et al. 2002). Therefore, the coefficients developed for the aqueous phase only flow, should still be valid for the two-phase flow.

Table 6-1. Langmuir and Freundlich isotherms fitting parameters for the aqueous phase toluene adsorption data obtained in batch experiments.

| Isotherm Model | $K_{ads} (\times 10^4)$<br>L/ $\mu$ g toluene | $q_{max}$<br>$\mu$ g toluene/g STC | $K_f$<br>( $\mu$ g/g STC)(L/ $\mu$ g) <sup>n</sup> | n    |
|----------------|---|------------------------------------|--|------|
| L1             | 7.11  | 39.1                               |  |      |
| L2             | 5.25  | 51.5                               |  |      |
| Freundlich     |   |                                    | 0.045  | 0.87 |

Table 6-2. Mean residence time and dispersion coefficients for the high flow rings only packing and commingled packing obtained from the tracer tests.

|                   | High flow rings Only |                                | STCs & High flow rings |                                |
|-------------------|----------------------|--------------------------------|------------------------|--------------------------------|
| Flowrate<br>L/min | $t_m$<br>s           | $D_{AX}$<br>cm <sup>2</sup> /s | $t_m$<br>s             | $D_{AX}$<br>cm <sup>2</sup> /s |
| 1.89              |                      |                                | 50.27                  | 3.97                           |
| 3.78              | 34.50                | 6.25                           | 40.42                  | 6.29                           |
| 5.68              |                      |                                | 31.70                  | 8.82                           |
| 7.57              | 29.40                | 7.21                           |                        |                                |

Table 6-3. Rate constants and Mears ( $C_M$ ) criterion for the determination of external mass transfer influences in the aqueous phase.  $C_M < 0.15$  indicates no significant external mass transfer resistance.

| $U_L$<br>(cm/s) | Liquid Loading<br>(gpm/ft <sup>2</sup> ) | $r$<br>( $\mu\text{g}/\text{L}/\text{s}$ ) | $k_c \times 10^5$<br>(m/s) | $C_M < 0.15$<br>$C_b = C_o$ | $C_M < 0.15$<br>$C_b = C_e$ |
|-----------------|--|--|----------------------------|-----------------------------|-----------------------------|
| 0.12            | 1.7                                      | 7.3  | 1.53                       | 2.06                        | 6.74                        |
| 0.22            | 3.3                                      | 4.2  | 2.11                       | 1.02                        | 1.64                        |
| 0.32            | 4.7                                      | 3.9  | 2.53                       | 0.72                        | 0.97                        |
| 0.38            | 5.6                                      | 4.4  | 2.76                       | 0.71                        | 0.92                        |

Table 6-4. Experimental conditions for the aqueous phase PCO experiments in the TPOT.

| Exp.<br># | $U_L$<br>cm/s | $Re$ | $C_{IN}$<br>$\mu\text{g}/\text{L}$ | $C_{out}$<br>$\mu\text{g}/\text{L}$ | Actual $K_{LSAC}$<br>$\text{s}^{-1} \times 10^3$ | Predicted $K_{LSAC}$<br>$\text{s}^{-1} \times 10^3$ |
|-----------|---------------|------|------------------------------------|-------------------------------------|--|---|
| 1         | 0.12          | 16.7 | 532                                | 163                                 | 1.39   | 1.41  |
| 2         | 0.22          | 31.8 | 445                                | 275                                 | 0.94   | 0.98  |
| 3         | 0.32          | 46.1 | 491                                | 367                                 | 0.80   | 0.83  |
| 4         | 0.38          | 54.3 | 514                                | 398                                 | 0.82   | 0.78  |
| 5         | 0.22          | 31.8 | 160                                | 108                                 | 0.77   | 0.76  |
| 6         | 0.22          | 31.8 | 250                                | 159                                 | 0.89   | 0.85  |
| 7         | 0.22          | 31.8 | 908                                | 512                                 | 1.14   | 1.17  |
| 8         | 0.22          | 31.8 | 1404                               | 716                                 | 1.37   | 1.30  |

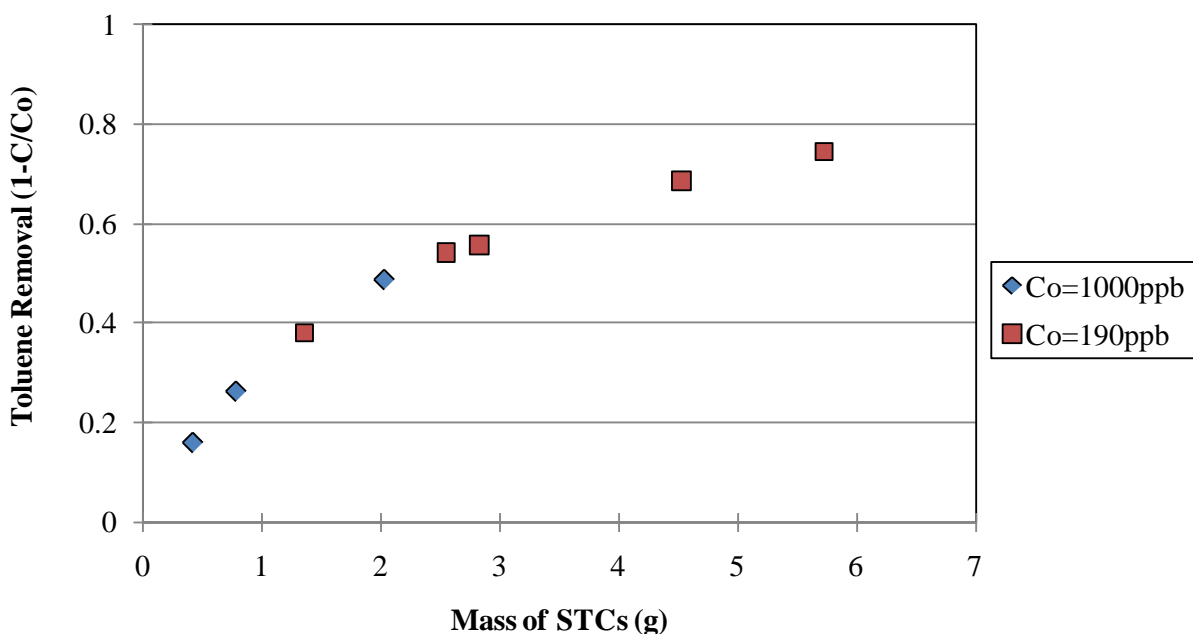


Figure 6-1. Removal of toluene due to adsorption in batch experiments as a function of STCs mass for different initial aqueous phase toluene concentrations. Data measured at equilibrium (adsorption time of 24 h).

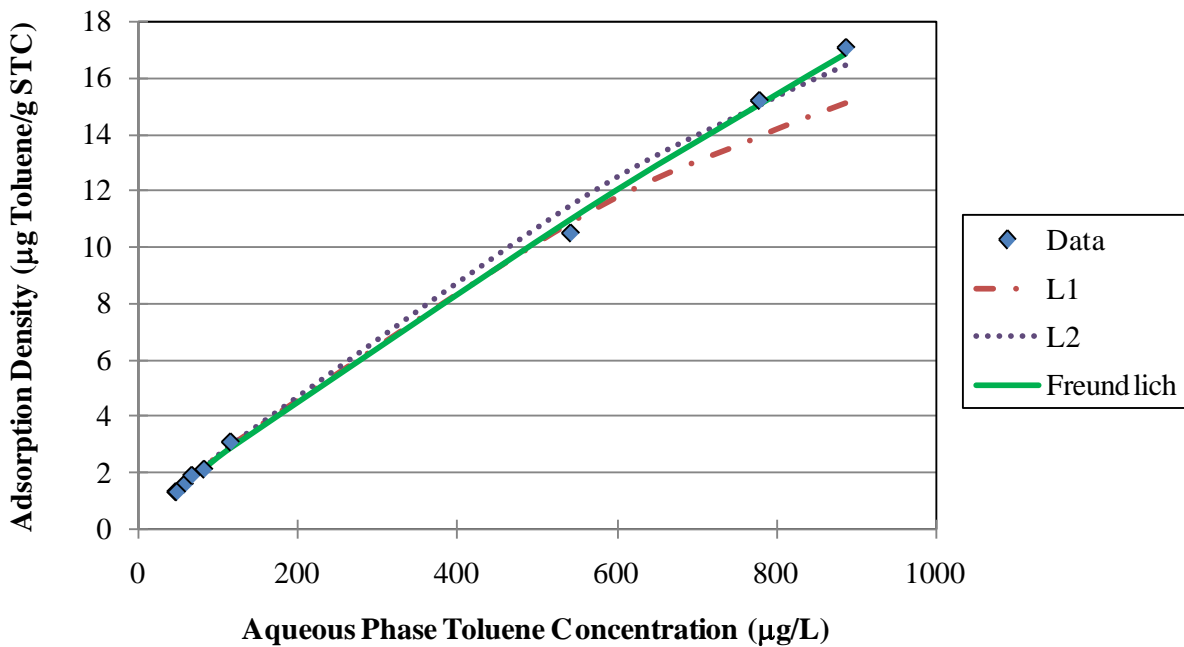


Figure 6-2. Adsorption isotherm for the aqueous phase toluene – STCs system. Comparison between the data and isotherm models.

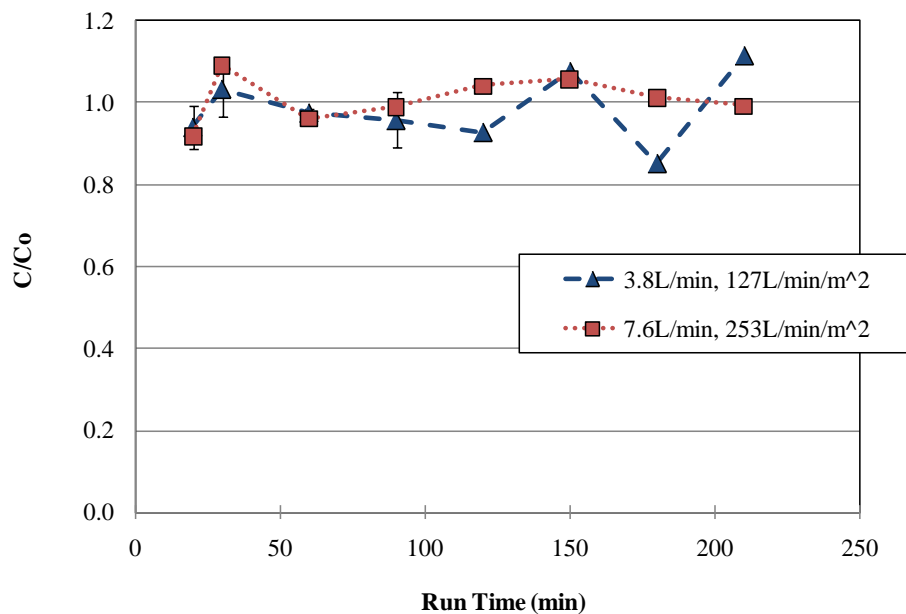


Figure 6-3. Aqueous phase toluene adsorption for different liquid loading rates. Average  $C_0 = 388 \mu\text{g/L}$  for  $127 \text{ L/min/m}^2$  and  $481 \mu\text{g/L}$  for  $253 \text{ L/min/m}^2$ .

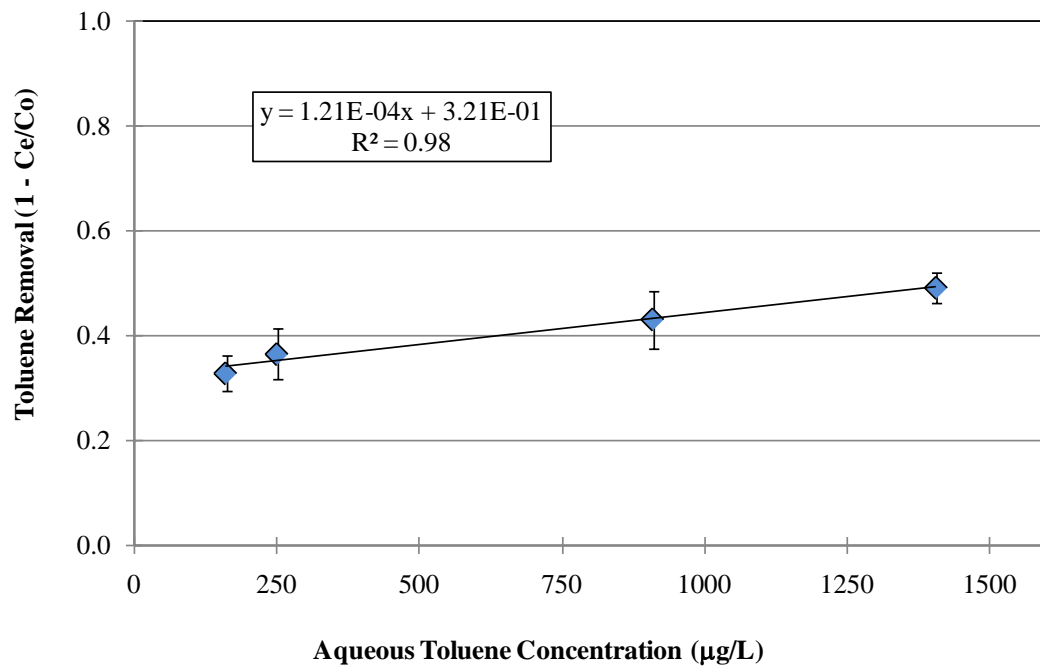


Figure 6-4. Toluene removal as a function of inlet toluene concentration in the TPOT at a flowrate of 3.8 L/min.

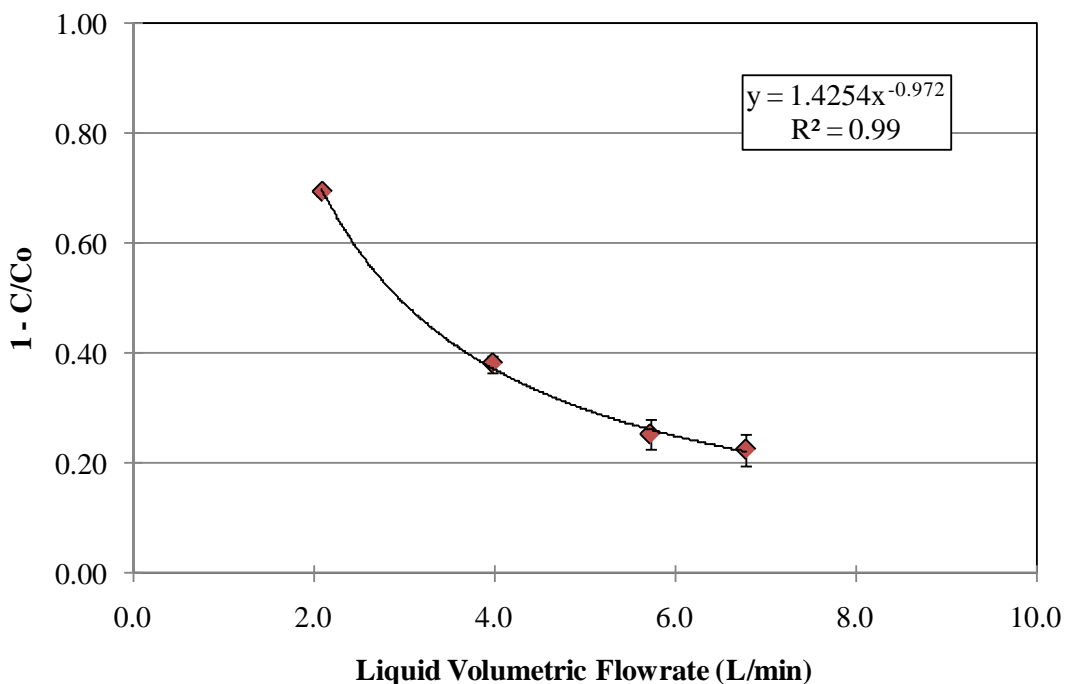


Figure 6-5. Aqueous phase toluene removal in the TPOT as a function of flowrate.  $C_o = 495 \pm 37 \mu\text{g/L}$ .

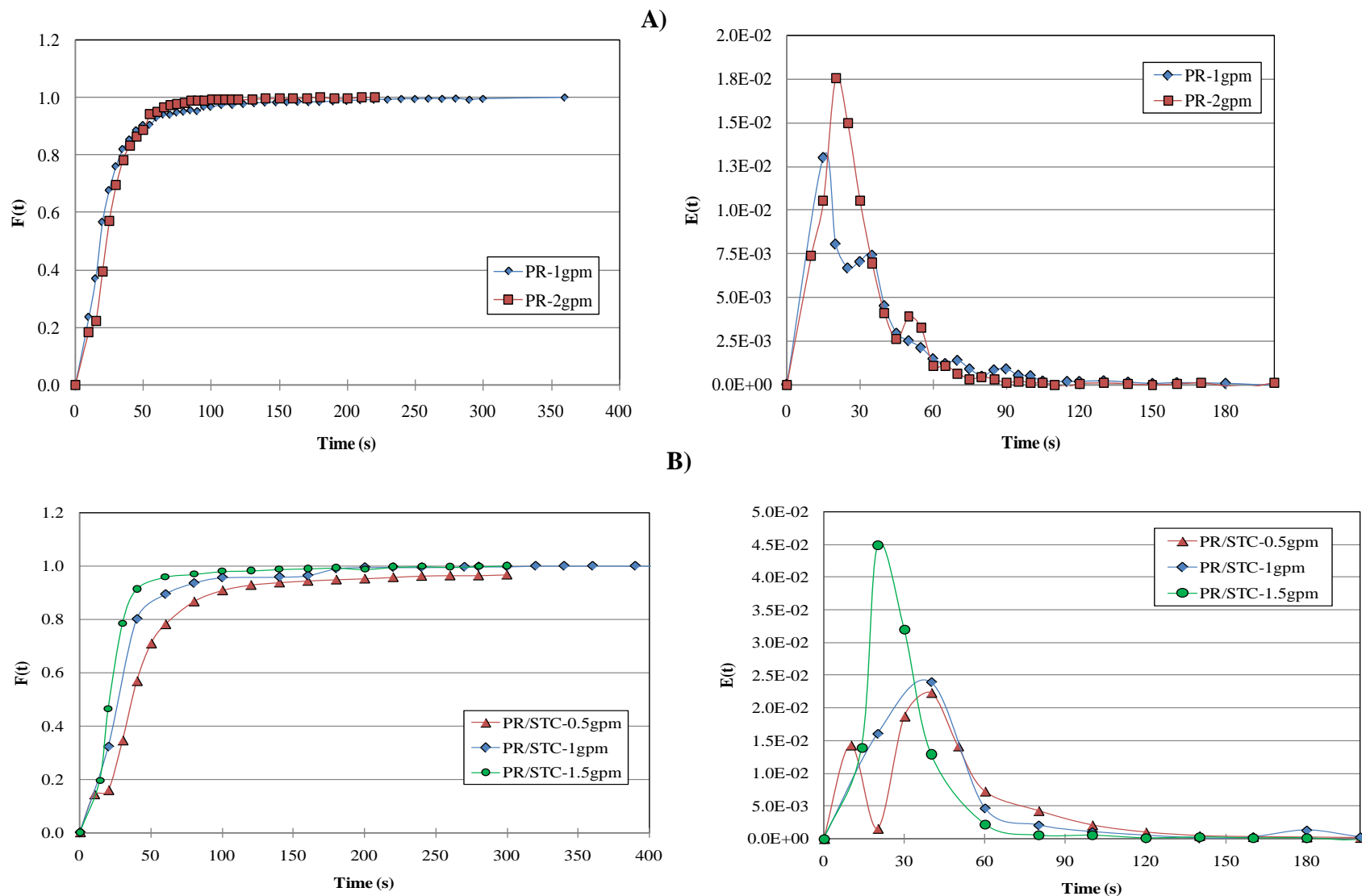


Figure 6-6. Cumulative RTD ( $F(t)$ ) and RTD ( $E(t)$ ) functions obtained from the tracer test analysis for the TPOT at different flowrates and packed with different packing styles: A) high flow rings only (PR) and B) commingled packing (PR/STC).

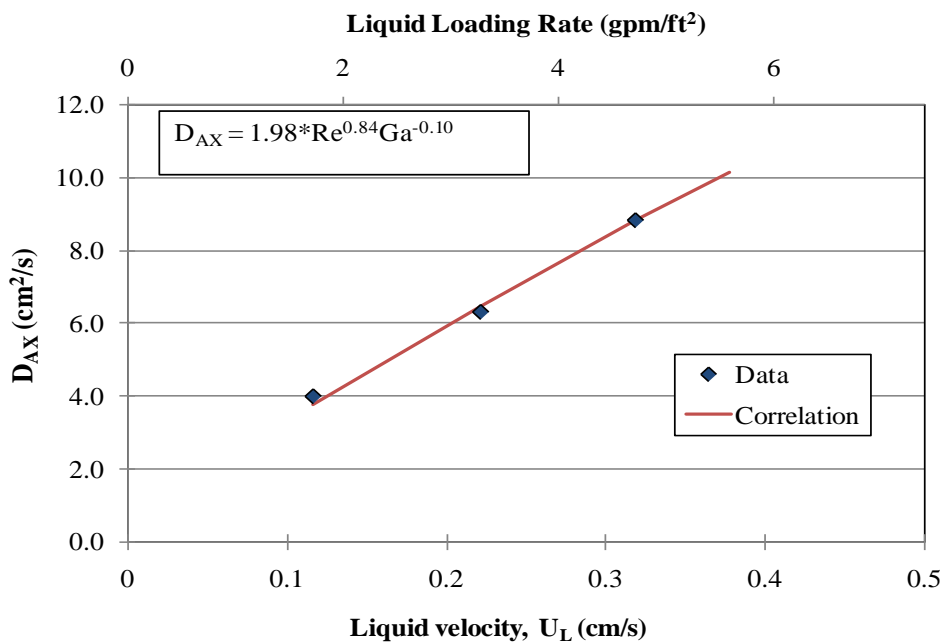


Figure 6-7. Dispersion coefficients for the TPOT with commingled packing obtained from the tracer tests (data) and determined by the empirical correlation fitted to the data.

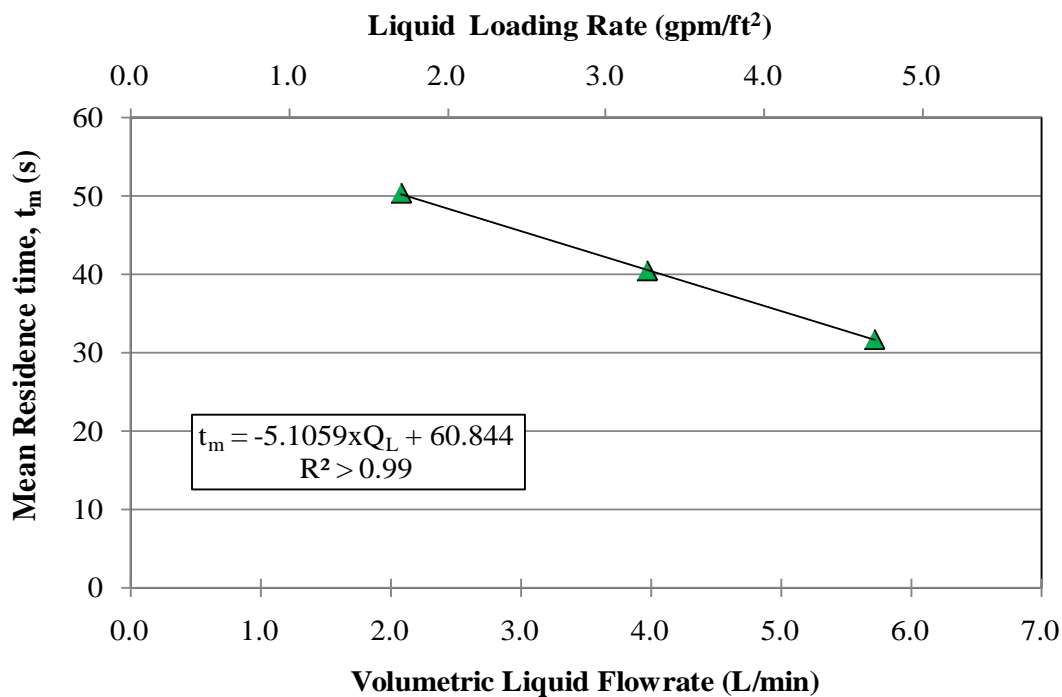


Figure 6-8. Mean residence time as a function of liquid loading rate for the TPOT packed with the commingled packing.

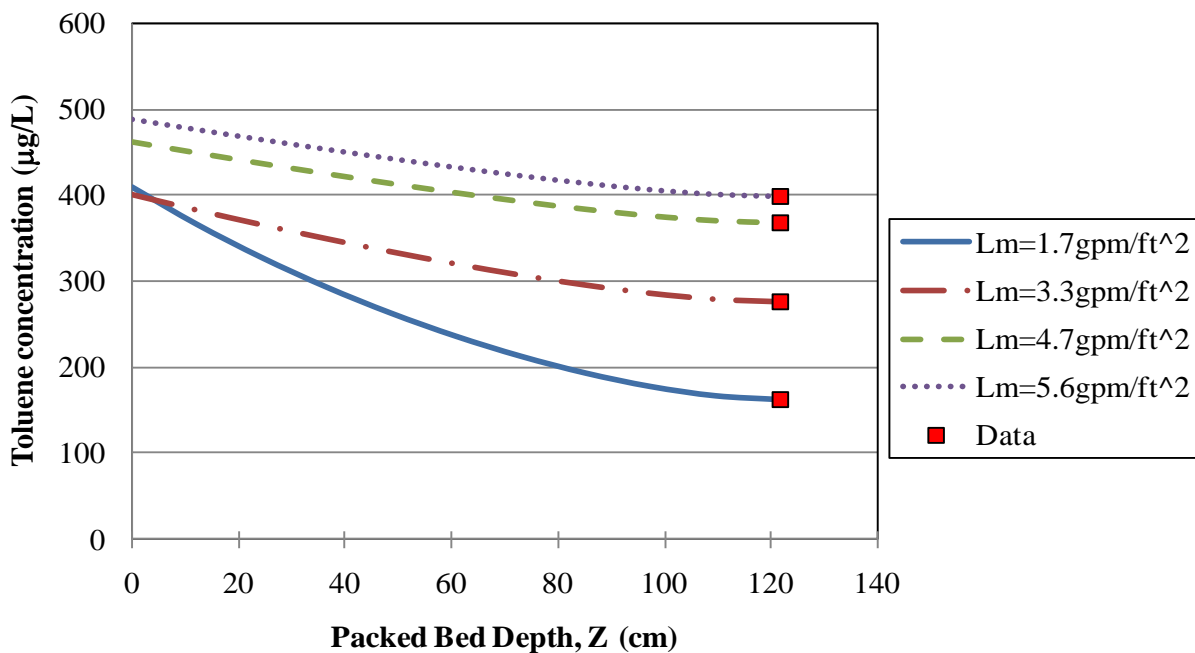


Figure 6-9. Aqueous phase toluene concentrations predicted using the PFD model as a function of the depth of the packing for different liquid loading rates ( $L_m$ ).  $C_o = 495 \pm 37 \mu\text{g/L}$  for all loading rates.

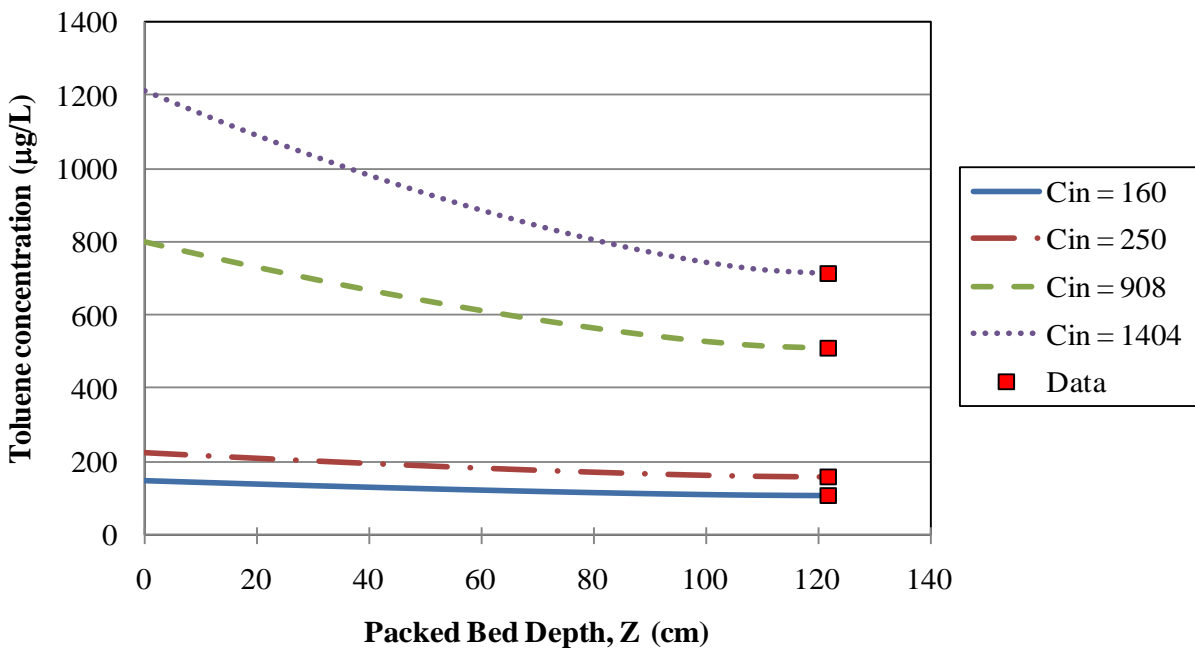


Figure 6-10. Aqueous phase toluene concentrations predicted using the PFD model as a function of the depth of the packed tower for different initial toluene concentrations ( $C_{in}$ ).  $Q_L = 3.8 \text{ L/min}$  for all concentrations.

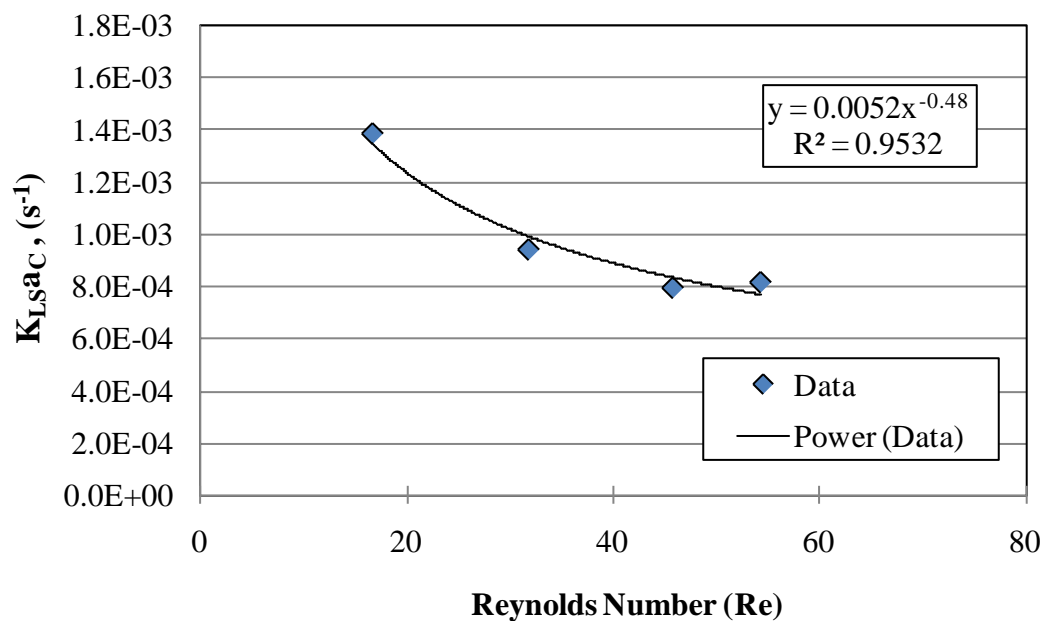


Figure 6-11. Liquid-solid mass transfer coefficient as a function of the Reynolds number.

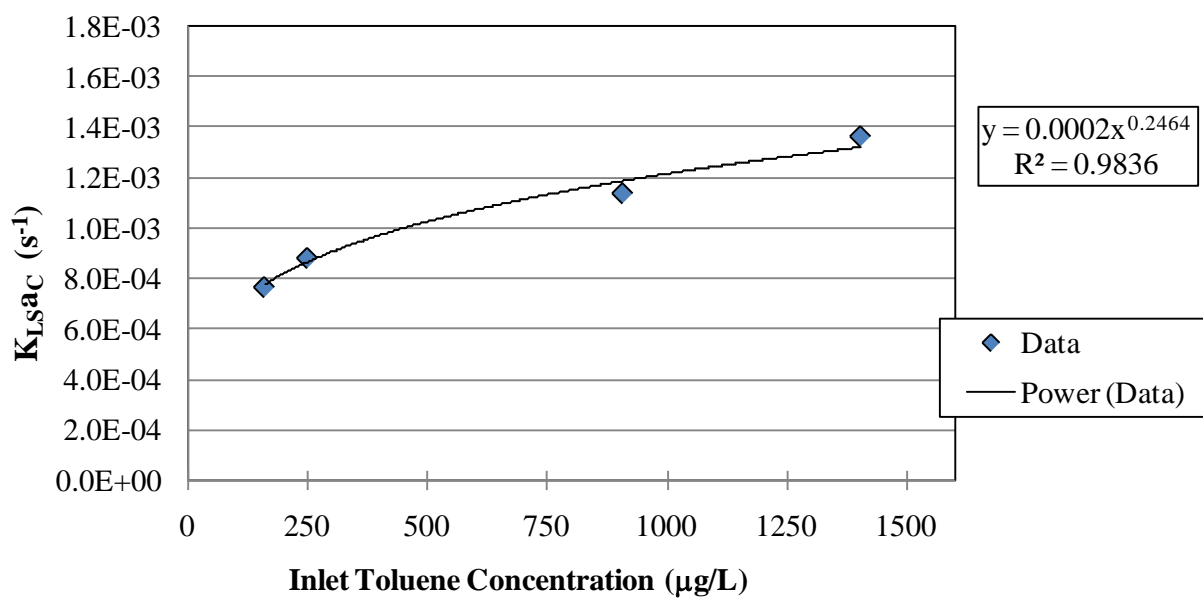


Figure 6-12. Liquid-solid mass transfer coefficient as a function of the inlet toluene concentration.

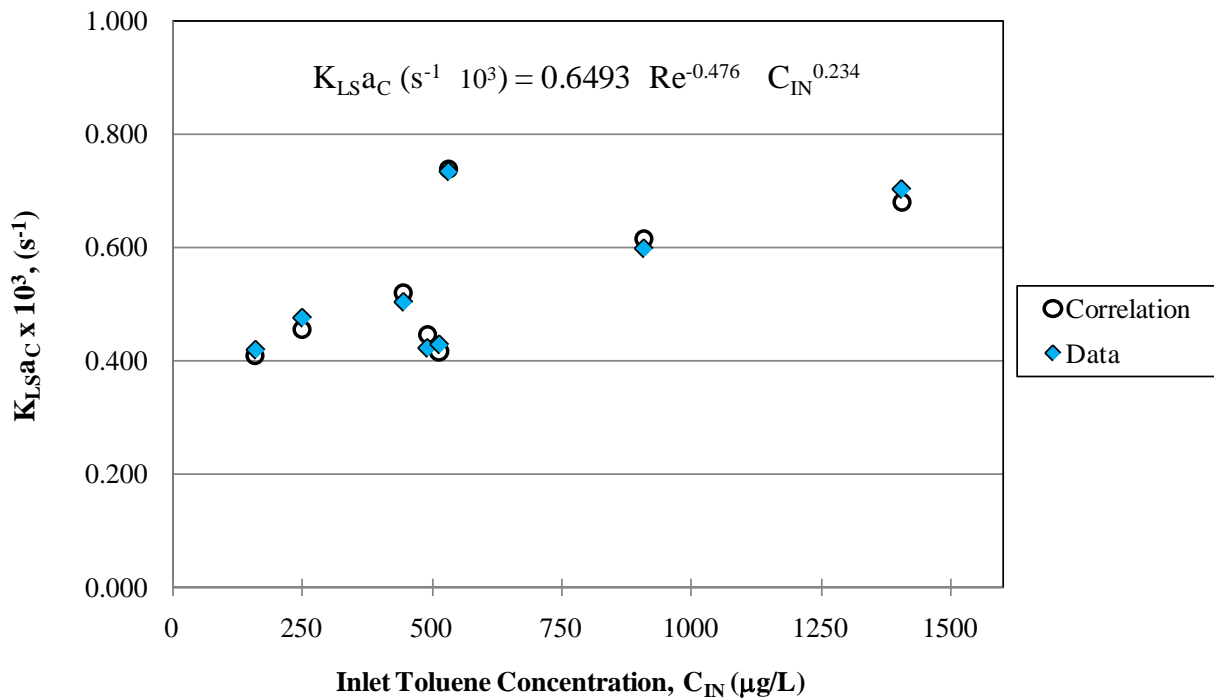


Figure 6-13. Actual versus liquid-solid mass transfer coefficients calculated from the correlation in Equation 6-19 as a function of Re and  $C_{IN}$ .

CHAPTER 7  
SIMULTANEOUS GAS AND AQUEOUS PHASE TOLUENE DEGRADATION USING THE  
PILOT-SCALE REACTOR

**Gas-Liquid Mass Transfer Coefficient ( $K_{GLa_w}$ )**

The gas –liquid mass transfer coefficient is an important parameter in the modeling of the two-phase reactor. Consequently, the overall gas-liquid mass transfer coefficients were determined for both packing configurations used in the large scale reactor: high flow rings only and palls rings commingled with STCs. These coefficients were obtained for different air to water ratios by holding the water flowrate constant and changing the air flowrate in a setup similar to a stripping experiment, where the aqueous phase is contaminated and the gas phase is free of contaminants. The air flowrate was kept constant only long enough to reach steady state (at least 5 min). Once steady state was achieved, the air flowrate was increased to reach the next steady state, at which point influent and effluent water phase concentrations were measured. During both experiments, the water flowrate was kept constant. The effect of liquid loading rate was determined by performing the experiment at different water flowrates. Similar to other experiments performed in the TPOT, the packing was wetted in the way described in the experimental section. Based on the single phase experiments, adsorption was not a concern for these experiments since it was shown to be insignificant under wetted packing conditions.

The overall gas-liquid mass transfer coefficients were calculated from the measured influent and effluent aqueous phase concentrations using Equations 2-39 through 2-44, which are repeated here for convenience. The results were compared to  $K_{GLa_w}$  values predicted by the Onda correlation, presented in Chapter 2. The Onda correlation, given by Equations 2-45 through 2-47 and repeated here for convenience, uses certain packing characteristics usually obtained from the packing manufacturer such as the nominal packing diameter ( $d_p$ ), the critical surface tension ( $\sigma_c$ ) and the specific surface area ( $a_t$ ). These characteristics were determined for the STCs in the

laboratory. Therefore, the properties used for the calculations when using the commingled packing were based on weighted average of the individual properties available or calculated for both types of packing. The properties were weighted by the bulk volume that each type of packing occupies in the reactor because this weighting method resulted in better fits than using a surface area weighting. The properties for high flow rings were obtained from the manufacturer; however, for the STCs, they had to be either calculated, such as the specific surface area (area of cylinder/ volume of cylinder) or found in the literature (e.g. critical surface tension). The packing characteristics used for  $K_{LSA_w}$  calculations are shown in Table 7-1.

$$Z = HTU \times NTU \quad (2-39)$$

$$HTU = Q_L / (A \times K_L \times a_w) \quad (2-40)$$

$$R = (Q_G \times H) / Q_L \quad (2-41)$$

$$NTU = \frac{R}{R-1} \ln \left( \frac{\frac{C_0 - C_e}{C_e} (R-1) + 1}{R} \right) \quad (2-42)$$

$$Z = \frac{L_m (C_0 - C_e)}{K_L a (DF_{lm})} \quad (2-43)$$

$$DF_{lm} = \frac{DF_0 - DF_e}{\ln \left( \frac{DF_0}{DF_e} \right)} = \frac{(C_0 - C_s) - (C_e - C_s)}{\ln \left( \frac{(C_0 - C_s)}{(C_e - C_s)} \right)} \quad (2-44)$$

$$a_w = a_t \left\{ 1 - \exp \left[ -1.45 \left( \frac{\sigma_c}{\sigma} \right)^{0.75} \left( \frac{L_m}{a_t \mu_L} \right)^{0.1} \left( \frac{L_m^2 a_t}{\rho_L^2 g} \right)^{-0.05} \left( \frac{L_m^2}{\rho_L a_t \sigma} \right)^{0.2} \right] \right\} \quad (2-45)$$

$$k_L = 0.0051 \left( \frac{L_m}{a_w \mu_L} \right)^{\frac{2}{3}} \left( \frac{\mu_L}{\rho_L D_L} \right)^{-0.5} \left( a_t d_p \right)^{0.4} \left( \frac{\rho_L}{\mu_L g} \right)^{-\frac{1}{3}} \quad (2-46)$$

$$k_g = 5.23 \left( a_t D_g \right) \left( \frac{G_m}{a_t \mu_g} \right)^{0.7} \left( \frac{\mu_g}{\rho_g D_g} \right)^{\frac{1}{3}} \left( a_t d_p \right)^{-2} \quad (2-47)$$

The results, presented in Figure 7-8, show that the Onda correlation underestimates the actual mass transfer coefficient for all liquid loading rates used and for both types of packing. Although the Onda correlation has shown good agreement for many packing styles used in different towers operating at a wide variety of conditions, it has not been validated for the high flow rings used in this work. For the case of the commingled packing, the disagreement with the correlation is expected given that the mixed packing is not a conventional packing, and therefore many of the parameters were arbitrarily estimated.

Interestingly, however, it was found that by increasing the wetted surface area proposed by Onda et al. (1968), the mass transfer coefficients could be closely predicted using Equations 2-46 and 2-47. The equation predicting the wetted surface area (Equation 2-45) for the Onda correlation, resulted in low wetted areas for the TPOT under the operating conditions studied. Therefore, an approach to improve the predictions using the Onda correlation was to increase the wetted surface area prediction for the reactor, since visual assessment of this parameter during the tower's operation seemed to indicate that a greater percent of the total area was actually being wetted. Accordingly, the equation to predict the wetted area was modified by changing the exponential coefficient used for the ratio of the critical surface tension to the liquid surface tension ( $\sigma_c / \sigma$ ) from 0.75 to 0.075, thereby minimizing the effects of the surface tension in the wetting process. This change in coefficient resulted in the best fit of the predicted  $K_{GL}a_w$  by the Onda correlation to the measured values. The modified equation used to predict the wetted area is shown in Equation 7-1.

$$a_w = a_t \left\{ 1 - \exp \left[ -1.45 \left( \frac{\sigma_c}{\sigma} \right)^{0.075} \left( \frac{L_m}{a_t \mu_L} \right)^{0.1} \left( \frac{L_m^2 a_t}{\rho_L^2 g} \right)^{-0.05} \left( \frac{L_m^2}{\rho_L a_t \sigma} \right)^{0.2} \right] \right\} \quad (7-1)$$

The effect of the modified wetted area equation in the predicted wetted areas for the case of the commingled packing compared to the values obtained by the Onda equation are shown as a function of the liquid flowrate in Figure 7-2. The comparison between the wetted area calculated from the Onda versus the modified Onda equation show that the increase in wetted area is large, between 10 and 20 percent for the range of flowrates plotted.

Using the modified wetted area, new values for  $K_{GLa_w}$  were obtained (called modified Onda), and these can be observed in Figure 7-1 in relation to the data and the Onda predictions. There is an excellent agreement between the data and the Modified Onda predictions for all liquid loading rates tested and for both types of packing used in the tower. This good agreement suggests that the actual wetted area in the reactor is likely higher than the area predicted by the Onda correlation.

The mass transfer coefficients measured for the commingled packing were higher than those measured for the high flow rings only (Figure 7-3). The increase in  $K_{GLa_w}$  by using the commingled packing can be explained by the larger overall surface area for mass transfer provided by the mixed packing as well as the smaller effective diameter of the packing.

As shown in Figures 7-1 and 7-4, the overall mass transfer coefficients for both types of packing increased as the air to water ratio increased. As observed in Equation 2-47, increasing the gas flowrate results in an increase of the local gas - side mass transfer coefficient ( $k_g$ ). Consequently, the gas phase resistance decreases, meaning that the overall mass transfer coefficient is increased by lowering the mass transfer resistance through the film (Equation 2-37).

The effect of the liquid loading rate on  $K_{GLa_w}$  was also investigated by increasing the liquid flowrate during the experiments. The results, presented in Figure 7-5, show that the coefficients

increase linearly as a function of liquid flowrate. The main factor affecting the increase in mass transfer coefficient is the increase in wetted area as a result of the higher liquid loading rate, which increased from about  $97 \text{ m}^2/\text{m}^3$  for 2 L/min to about  $140 \text{ m}^2/\text{m}^3$  for 5.7 L/min (Figure 7-2).

### **Simultaneous Two-Phase Degradation Studies**

These experiments tested the main hypothesis of this research: can a counter flow reactor packed with STCs efficiently enable the simultaneous treatment of gas and aqueous phase toluene?. During these experiments, both streams were contaminated with toluene, and they were allowed to flow simultaneously through the packed bed. Inlet and outlet concentrations in both phases were recorded to determine the overall removal efficiency achieved by the photocatalytic tower. The water flowrate during these experiments was kept constant at 3.8 L/min (liquid loading of  $3.1 \text{ gpm}/\text{ft}^2$ ) while the air flowrate varied from run to run.

When considering the two-phase countercurrent flow of a compound in a packed tower, the direction of transfer of the compound from the gas phase to the aqueous phase or vice versa will be determined by concentrations of toluene in the aqueous and gas phases relative to equilibrium concentrations, as determined by Henry's law, in the tower. These concepts were explained and reviewed in Chapter 2. Two saturation conditions of toluene can exist in the reactor:

- The aqueous phase is supersaturated with respect to the gas phase, meaning that the toluene present in the aqueous phase will tend to transfer to the gas phase. This condition is referred to as stripping.
- The aqueous phase is undersaturated with respect to the gas phase, meaning that the toluene in the gas phase will tend to transfer to the aqueous phase. This condition is referred to as absorption.

In the countercurrent flow reactor, the saturation conditions were determined for the top and bottom sections of the reactor. The conditions at the top of the reactor are represented by the influent aqueous phase ( $C_o$ ) and the effluent gas phase ( $Y_e$ ) concentrations while the bottom of

the reactor is represented by the effluent aqueous phase ( $C_e$ ) and influent gas phase concentrations ( $Y_o$ ). These concentrations were plotted in a graph with respect to the equilibrium conditions predicted by the Henry's law in order to determine the tendency of mass transfer in the reactor for the different experiments performed. All the following references to supersaturated and undersaturated are used with respect to the aqueous phase.

The actual saturation conditions given at the top and bottom of the tower during each of the six two-phase experimental runs (labeled from a to f) and the predicted equilibrium conditions are shown in Figure 7-6. Based on the points representing the conditions occurring at the top of the tower (illustrated by squares), one of the experiments was performed with the solution unsaturated with respect to the gas phase at the water inlet at the top of the reactor (i.e. above the equilibrium line) while the rest of the experiments were performed under supersaturated solution conditions (i.e. points are below the equilibrium line). The experiments performed under supersaturated conditions were analyzed in terms of the driving force and the air to water ratio. Interestingly, the conditions at the bottom of the reactor (represented by the triangles) are very close to the equilibrium line predicted by the Henry's law. These results show that, similar to a stripping/absorption tower, the system tends to move towards equilibrium

The letter shown in the legend of Figure 7-6 refers to the name given to the experiment; "top" and "bot" refer to the conditions at the top and bottom of the reactor, respectively, and the number that follows is the gas flowrate. The results for each one of the two-phase experimental runs are shown in Figures 7-7 through Figure 7-12. The format for each figure is the same for the different runs. Each figure shows 4 different graphs that can be described as follows:

- Graphs (A) and (B) show the change of the aqueous phase and gas phase concentrations, respectively, as a function of run time ( $t = 0$  when UV lamps were turned on). These plots also include the expected concentrations that would be obtained in both, the aqueous and gas phases, if no toluene oxidation occurred, and there was only mass transfer in the

reactor ( $C_e$  if no PCO). These expected concentrations were determined using  $K_{GLa_w}$  values calculated with the modified Onda correlation previously determined.

- Graph (C) shows the toluene mass balance, i.e. the actual overall mass flow into and out of the reactor as calculated using Equation 7-2.
- Graph (D) shows the summary of the removal of toluene (decrease in toluene concentration represented by positive removal or increase in concentration represented by a negative removal) for the gas phase ( $1 - Y_e/Y_o$ ) and the aqueous phase ( $1 - C_e/C_o$ ). The overall mass flow removal ( $1 - M_e/M_o$ ) is also shown.

$$Q_G \times Y_o + Q_L \times C_o = Q_G \times Y_e + Q_L \times C_e \quad (7-2)$$

All the experimental conditions for runs (a) through (f) are summarized Table 7-2, where

$Q_G$  refers to the volumetric gas flowrate and is given in units of L/min. The volumetric liquid flowrate,  $Q_L$ , used for all runs shown in Table 7-2 was 3.8 L/min. The toluene removal in the aqueous phase was calculated as  $(1 - C_e/C_o)$ . The gas phase removal was determined by  $(1 - Y_e/Y_o)$ . The actual percent toluene removal refers to the net removal in the tower due to mineralization of toluene, and it was calculated by determining the mass flowrates at top and bottom of the reactor.

Figure 7-13 illustrates the results for the two-phase experiments plotted as the overall removal of toluene in the two phases as a function of the aqueous phase concentration. Additionally, the expected removal of toluene in the aqueous phase as predicted by the correlation shown in Figure 6-4 for the single phase experiments is also plotted as a function of concentration in the same figure. Notice that the linear correlation for the aqueous phase included concentrations up to about 1400  $\mu\text{g/L}$ . Since higher concentrations were used in the two-phase experiments, the line obtained by the correlation was extrapolated to the highest concentration observed in the two-phase experiments. The results shown in Figure 7-13 and Table 7-2 indicate that for all the experiments considered as supersaturated at the top of the reactor, i.e. experiments (a) to (e) (See Figure 7-13), the tendency was to strip toluene from the

aqueous to the gas phase. All the supersaturated experiments showed a large removal of toluene from the aqueous phase (>90%). The gas phase, on the other hand, showed an increase in concentration, and thus negative percent removals. This increase was the result of stripping, i.e. the transfer of toluene from the aqueous phase to the gas phase. Although the gas phase concentration increased significantly, toluene was accumulated in the gas phase at a lower rate than if photocatalysis did not occur as shown by graph B in Figures 7-14 to 7-18, meaning that toluene was oxidized in the tower. For the experiment considered undersaturated, absorption of toluene from the gas phase to the aqueous phase occurred and no significant removal was achieved in either phase.

Based on Figure 7-13, it is evident that the removal of toluene occurs in the aqueous phase and that for the most part, higher removals can be achieved when the aqueous phase is the only flowing phase. With the exception of experiments b and c, which achieved removals higher than predicted by aqueous phase photocatalysis only, having the two phases flowing simultaneously results in a lower net toluene removal.

The main factors that influence the overall removal of toluene during the two-phase PCO include those parameters that will tend to affect the aqueous phase concentration in the reactor since the removal occurs mostly in the aqueous phase. Factors that decrease the driving force in the aqueous phase, and thus the overall toluene removal, can be compared from the results presented in Table 7-2:

Air to water ratio: The supersaturated experiments showed a net removal of toluene between 37% and 68%, except for experiment (d), which did not show a substantial mass removal (only 6.2%). The major operational difference associated with experiment (d) was the higher gas flowrate. In general, it was observed that by increasing the gas flowrate, the net

toluene removal significantly decreased. By increasing the gas flowrate (or air to water ratio), the stripping of toluene to the gas phase is expected to be greater. Based on the single phase experiments; however, toluene is not photocatalyzed in the gas phase, but in the aqueous phase. Therefore, increasing the stripping of toluene decreases the aqueous phase concentration which is the driving force for photocatalysis, and hence the overall removal is adversely affected.

Aqueous phase concentration: The influent aqueous phase concentration for experiment (b) is about twice that of experiment (a). The net toluene removal at the higher aqueous concentration was 62.5% compared to 36.6% for experiment (a). The results confirm that the aqueous phase concentration is one of the main driving forces for phototcatalysis in the reactor.

Gas phase concentration: Lower influent gas phase concentrations can adversely influence the removal of toluene in the system because it increases the driving force for toluene transfer to the gas phase by stripping, but the toluene present in this phase will not be oxidized. This tendency can be observed by comparing experiments (b) and (e), which have the same gas flowrate, comparable initial aqueous phase concentrations and water temperatures, but the influent gas phase concentration for experiment (b) is about 6 times larger than for experiment (e). The gas phase concentration difference results in an increased water phase removal and an overall decrease in toluene mass removal of 15% for experiment (e) as compared to (b).

Temperature: This parameter was not intentionally varied in this study to determine its effect in the process. However as a result of heat discharged by the UV lamps, small temperature differences were noted. It is well established that, on one hand, higher temperatures increase the volatility of toluene and thus its stripping tendency, so increasing the temperature in the system can have adverse effects on the net removal of toluene. On the other hand, higher temperatures usually increase oxidation rates, thus favoring toluene removal in the system. The dominant

effect cannot be inferred from the experimental runs since the temperature differences were so small.

For the case of undersaturated conditions at the water inlet, the toluene concentration in the aqueous phase increased while it decreased in the gas phase, i.e. there was toluene absorption in the tower. These results are consistent with the undersaturated nature of the system leading to toluene absorption from the gas to the aqueous phase. However, there was no net destruction of toluene in the system. Again, photocatalysis in the gas phase seems to be inhibited when the packing was wetted. For undersaturated conditions, most of the toluene was present in the gas phase, so these toluene molecules did not undergo oxidation. The fewer molecules that were transferred to the aqueous phase could potentially undergo photocatalysis. However, the rate of transfer between the phases, the time the molecules need to be in contact with the catalyst once toluene is transferred to the aqueous phase, and the rate of toluene oxidation in the aqueous phase would need to be examined in detail in order to predict the conditions under which toluene removal would occur for undersaturated conditions.

By adjusting the conditions to favor the aqueous phase concentration to increase, the overall removal of toluene can be improved in the two-phase system as compared to the single phase. Although most of the removal in the two-phase photocatalytic tower seems to be occurring in the aqueous phase, the complete two-phase system proposed in this study, consisting of the two-phase photocatalytic oxidation tower and the two end “polishing” sections for each phase, has many advantages compared to other systems used to remove VOCs. The main advantage of the TPOT is its versatility due to the stripping/ absorption potential of the in the reactor.

Table 7-1. Individual and averaged properties for the two different packing materials used to pack the TPOT.

| Property                 | STC                 | High flow rings |       | Commingled |
|--------------------------|---------------------|-----------------|-------|------------|
|                          |                     |                 |       |            |
| Nominal diameter         | $d_p$ (mm)          | 9.1             | 15.9  | 14.8       |
| Specific surface area    | $a_t$ ( $m^2/m^3$ ) | 452.1           | 313.0 | 334.5      |
| Critical surface tension | $\sigma_c$ (N/m)    | 0.027*          | 0.033 | 0.0321     |
| Bulk Volume              | V (L)               | 6.0             | 32.8  |            |

\*Value obtained from Gould and Irene (1988).

Table 7-2. Summary of operational conditions and toluene removals for the simultaneous two-phase experiments.

| Exp.                             | $Q_G$<br>(L/min) | Co<br>( $\mu g/L$ ) | Yo<br>( $\mu g/L$ ) | Avg.<br>$T_{water}$<br>( $^{\circ}C$ ) | Aqueous<br>Removal<br>(%) | Gas<br>Removal<br>(%) | Net %<br>Toluene<br>Removal | Predicted %<br>Aqueous<br>Removal |
|----------------------------------|------------------|---------------------|---------------------|--|---------------------------|-----------------------|-----------------------------|-----------------------------------|
| <b>Supersaturated Conditions</b> |                  |                     |                     |  |                           |                       |                             |                                   |
| a                                | 142              | 1288                | 23                  | 23.5                                   | 95.3                      | -52.1                 | 36.6                        | 47.8                              |
| b                                | 142              | 2419                | 11                  | 24.4                                   | 90.2                      | -95.5                 | 62.5                        | 61.5                              |
| c                                | 116              | 2506                | 6                   | 25.7                                   | 95.1                      | -340.4                | 68.0                        | 62.5                              |
| d                                | 202              | 1258                | 8                   | 25.1                                   | 90.7                      | -246.6                | 6.2                         | 47.4                              |
| e                                | 142              | 2642                | 2                   | 24.6                                   | 94.7                      | -1953.2               | 47.2                        | 64.2                              |
| <b>Undersaturated Conditions</b> |                  |                     |                     |  |                           |                       |                             |                                   |
| f                                | 142              | 424                 | 161                 | 24.4                                   | -99.2                     | 0.12                  | 5.0                         | 37.3                              |

†ΣI

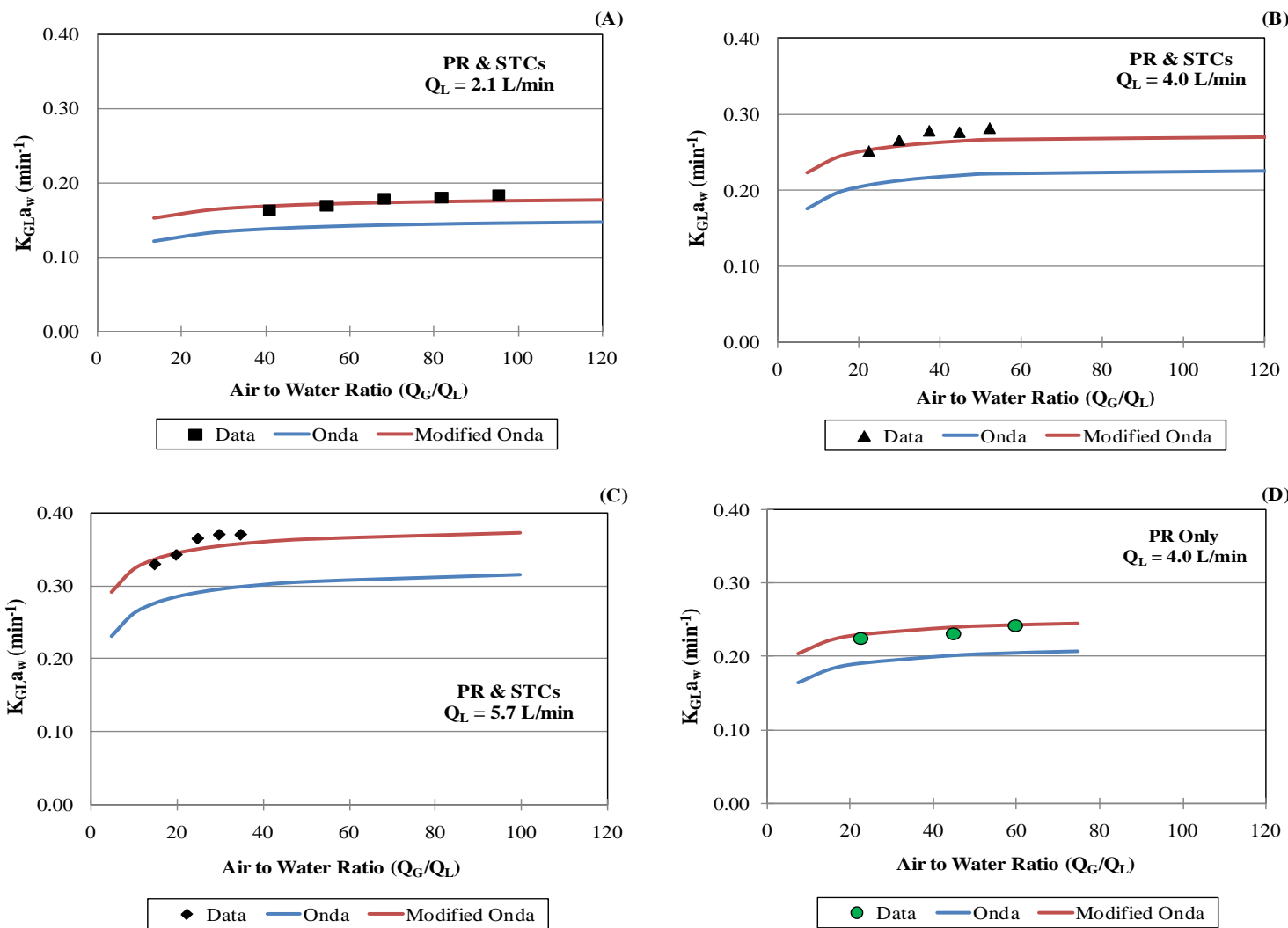


Figure 7-1. Comparison of the measured overall gas-liquid mass transfer coefficients to the coefficients predicted by the Onda correlation and by the Modified Onda correlation for different liquid flowrates and packing styles as a function of air to water ratio. A) to C) show results for the commingled packing while D) refers to the high flow rings only.

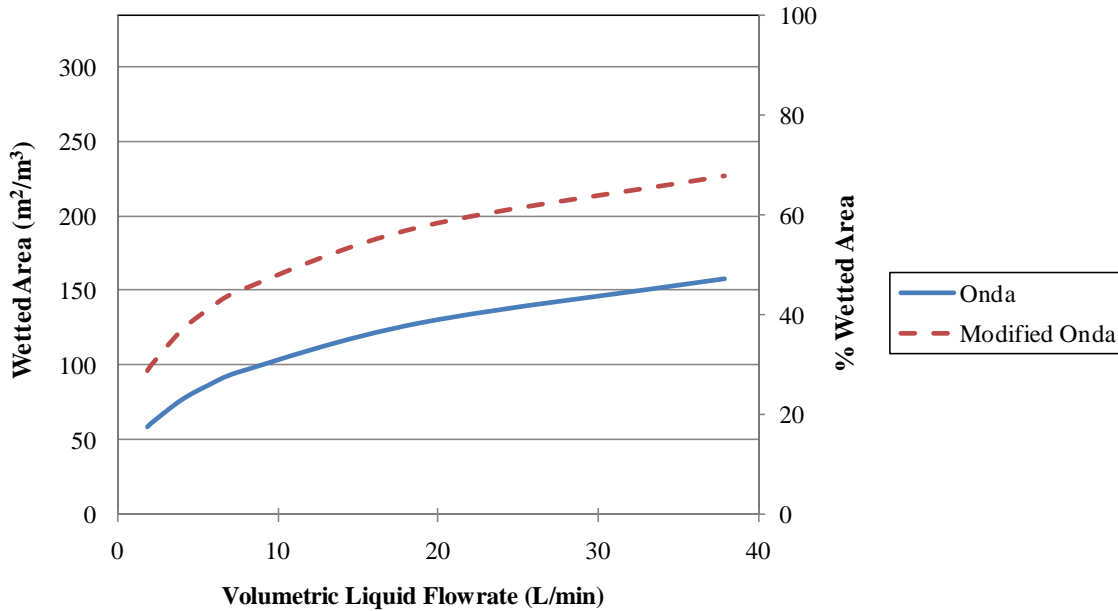


Figure 7-2. Comparison of the predicted wetted surface area of the packing calculated using the Onda correlation and the Modified Onda correlation as a function of liquid flowrate for the tower packed with the commingled packing.

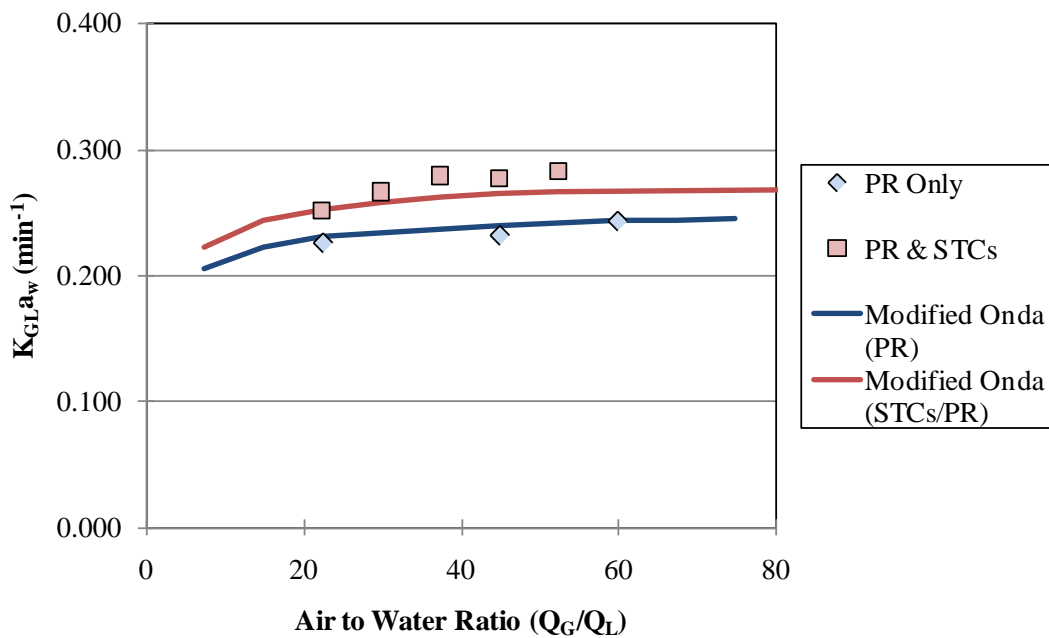


Figure 7-3. Comparison of overall gas-liquid mass transfer coefficients for the tower packed with high flow rings only and the commingled packing as a function of air to water ratio for a liquid flowrate of 4.0 L/min.

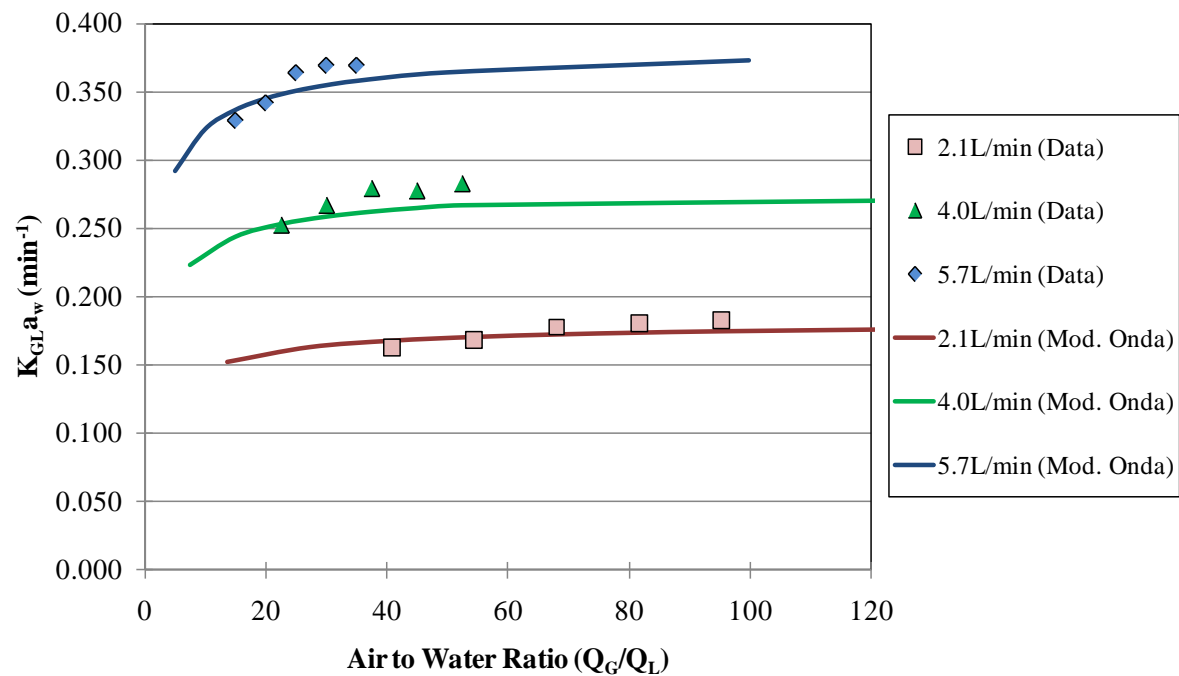


Figure 7-4. Overall gas-liquid mass transfer coefficients as a function of air to water ratio for different liquid flowrates for the tower packed with commingled packing.

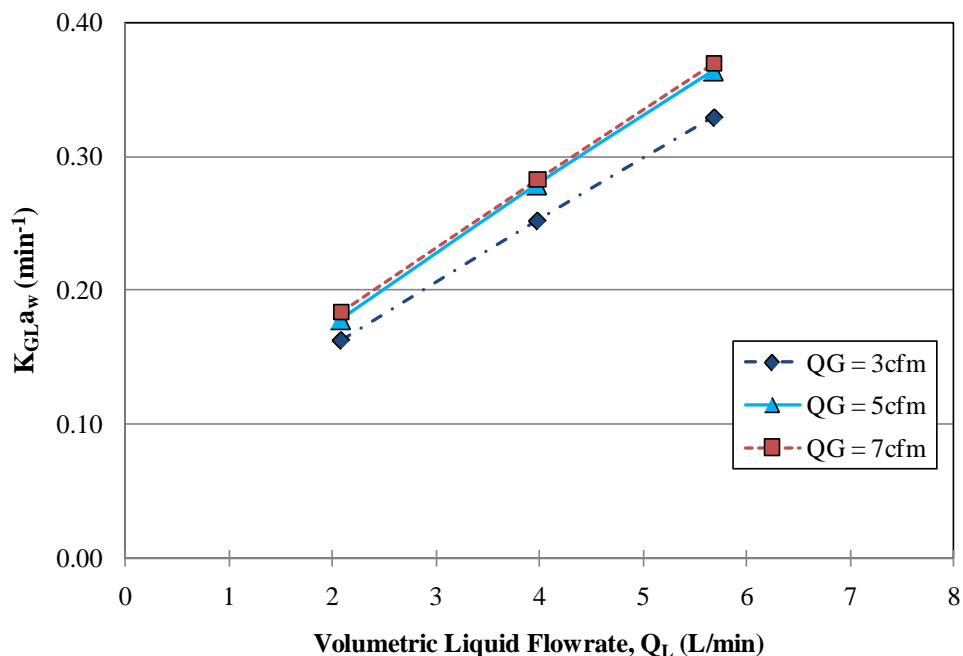


Figure 7-5. Effect of the liquid flowrate on  $K_{GLa_w}$  for different gas flowrates for the tower packed with the commingled packing.

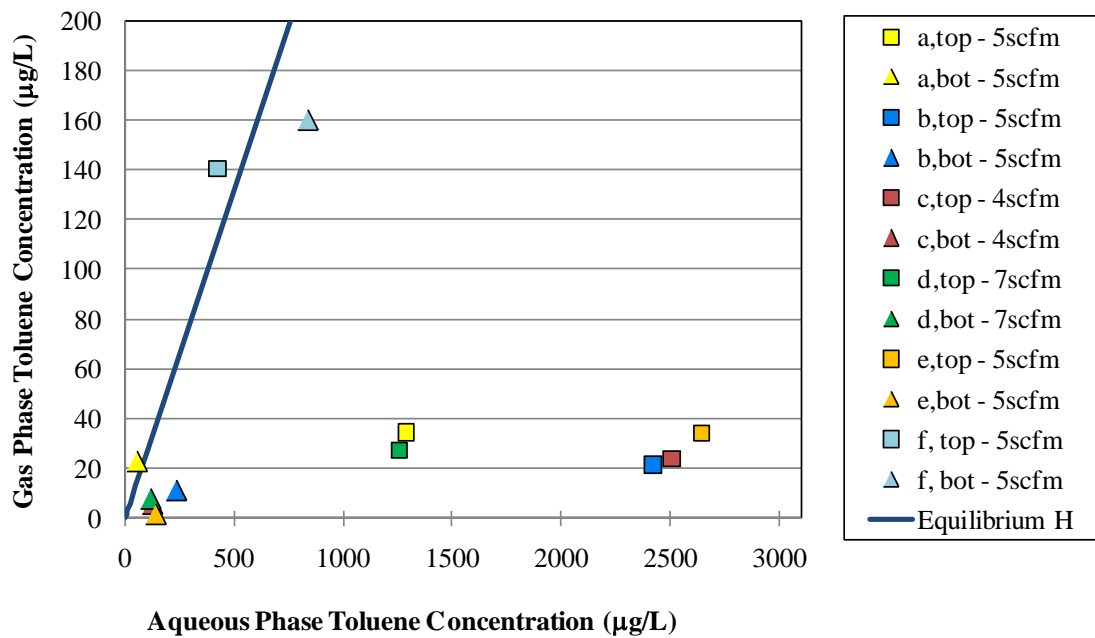


Figure 7-6. Comparison of actual saturation conditions in the reactor for the different experimental runs and the equilibrium concentrations predicted by the Henry's law.

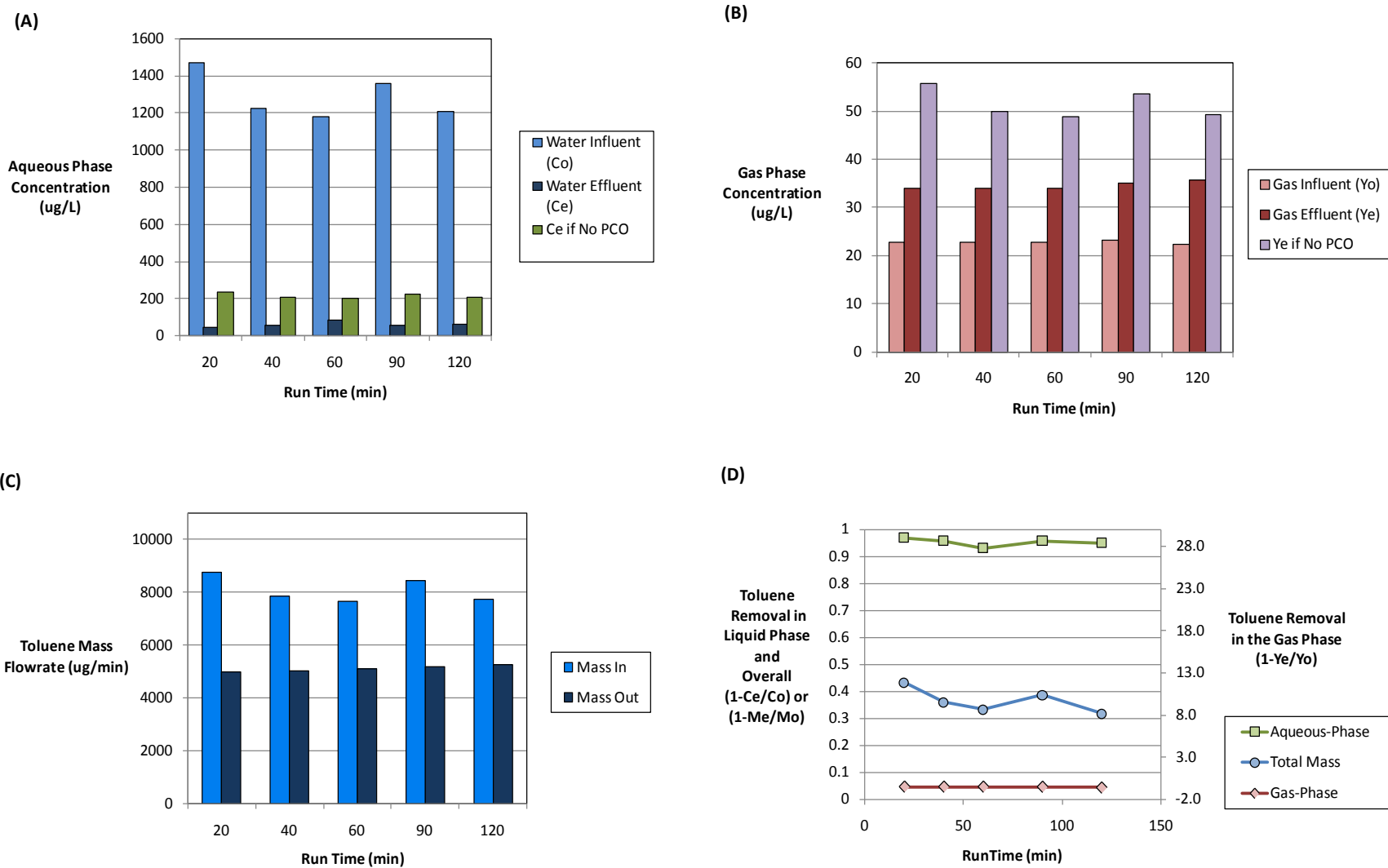


Figure 7-7. Results for two-phase experiments using saturated conditions : Experiment (a) conditions:  $Q_L=3.8\text{L/min}$ ,  $Q_G=142\text{L/min}$ ,  $T_{\text{water}} = 23.5^\circ\text{C}$ . (A) Aqueous phase (B) Gas phase (C) Toluene mass balance (D) Summary of removals.

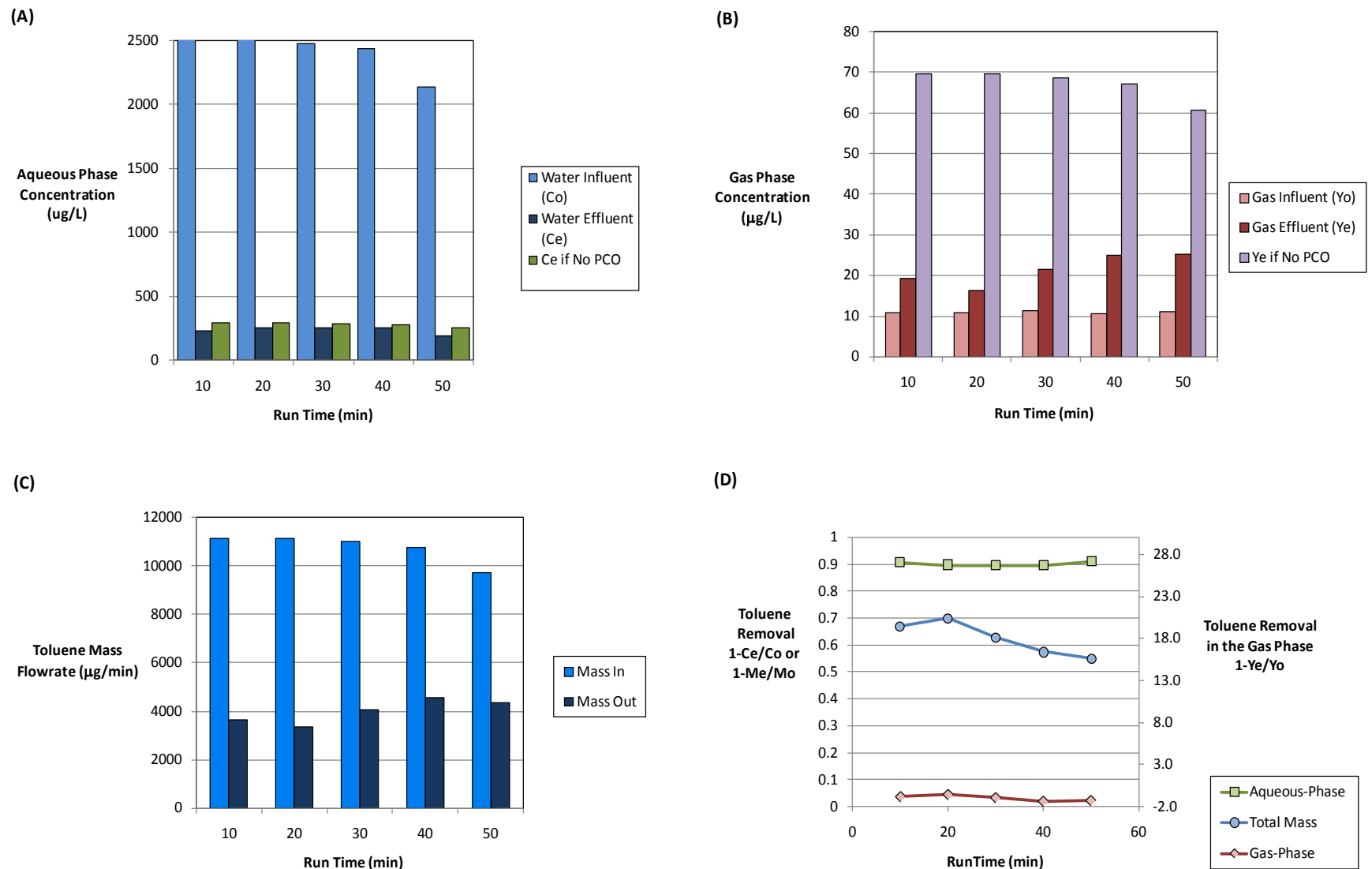


Figure 7-8. Results for two-phase experiments using saturated conditions : Experiment (b) conditions:  $Q_L = 3.8 \text{ L/min}$ ,  $Q_G = 142 \text{ L/min}$ ,  $T_{\text{water}} = 24.4^\circ\text{C}$ . (A) Aqueous phase (B) Gas phase (C) Toluene mass balance (D) Summary of removals.

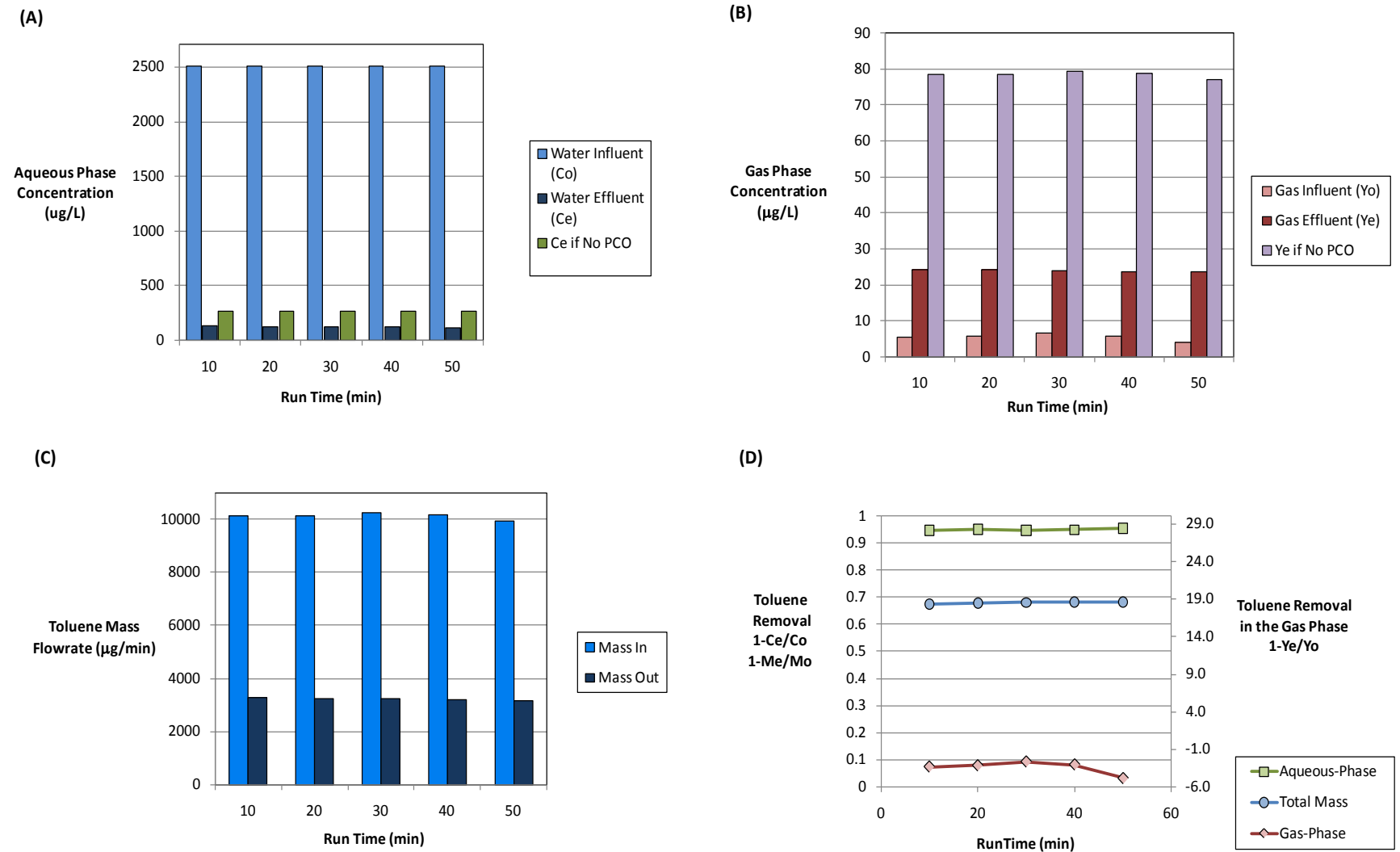


Figure 7-9. Results for two-phase experiments using saturated conditions : Experiment (c) conditions:  $Q_L = 3.8 \text{ L/min}$ ,  $Q_G = 116 \text{ L/min}$ ,  $T_{\text{water}} = 25.7^\circ\text{C}$  A) Aqueous phase (B) Gas phase (C) Toluene mass balance (D) Summary of removals.

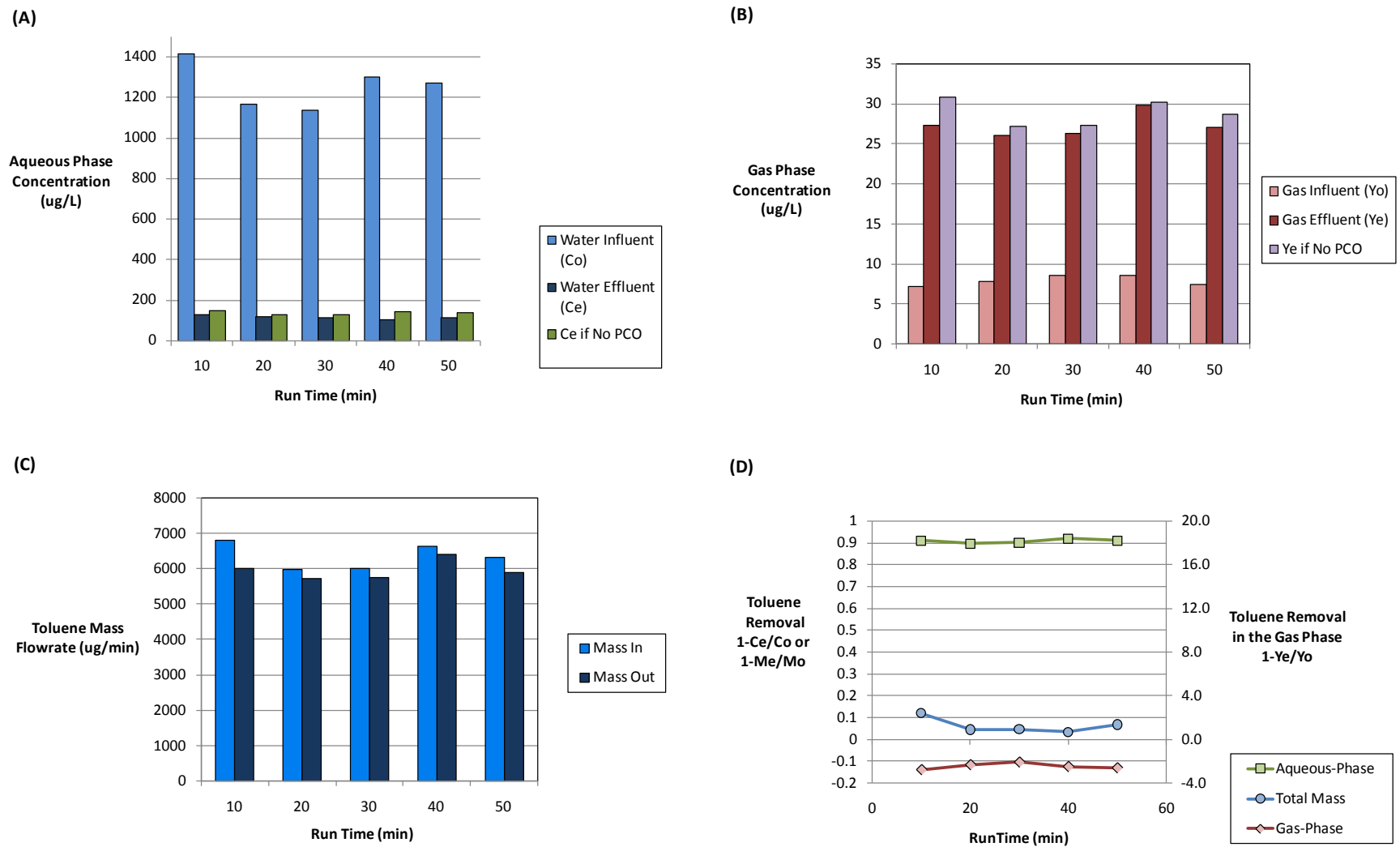


Figure 7-10. Results for two-phase experiments using saturated conditions : Experiment (d) conditions:  $Q_L = 3.8 \text{ L/min}$ ,  $Q_G = 202 \text{ L/min}$ ,  $T_{\text{water}} = 25.1^\circ\text{C}$  (A) Aqueous phase (B) Gas phase (C) Toluene mass balance (D) Summary of removals.

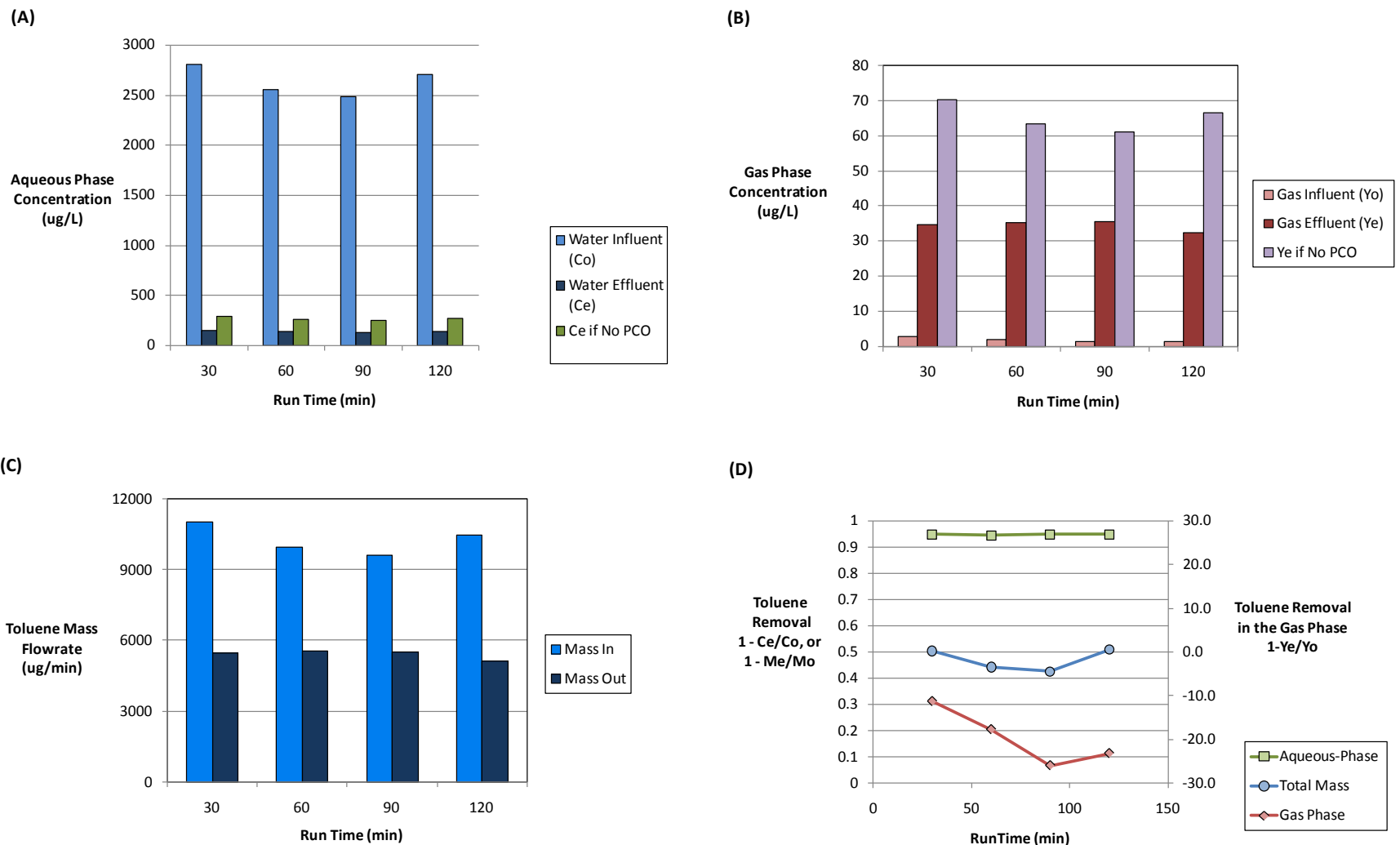
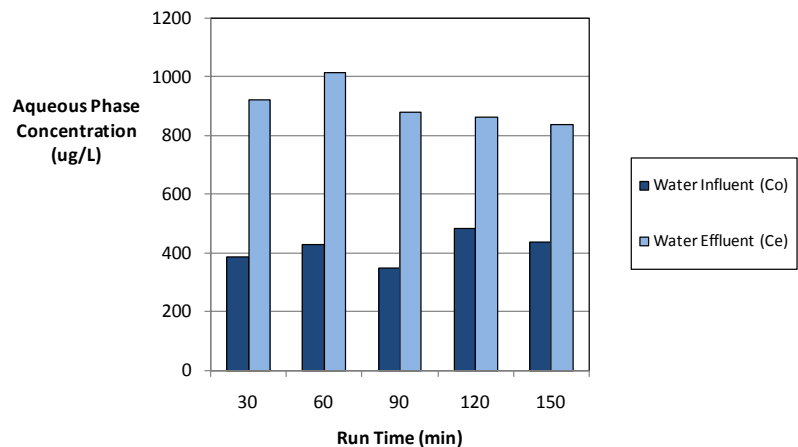
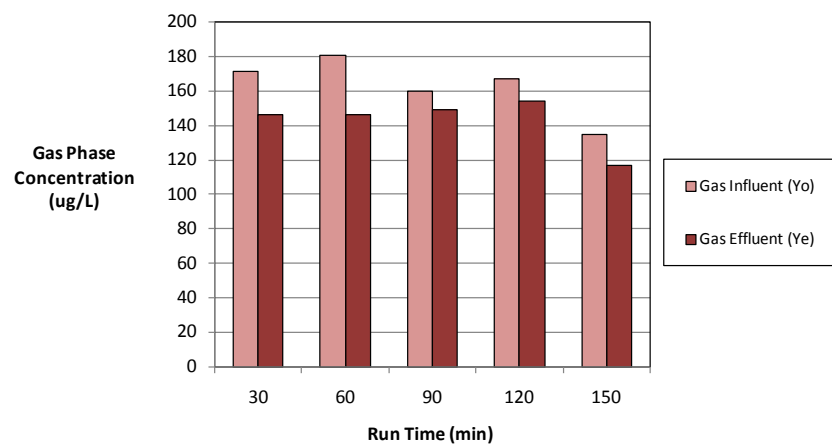


Figure 7-11. Results for two-phase experiments using saturated conditions : Experiment (e) conditions:  $Q_L = 3.8 \text{ L/min}$ ,  $Q_G = 142 \text{ L/min}$ ,  $T_{water} = 24.6^\circ\text{C}$  (A) Aqueous phase (B) Gas phase (C) Toluene mass balance (D) Summary of removals.

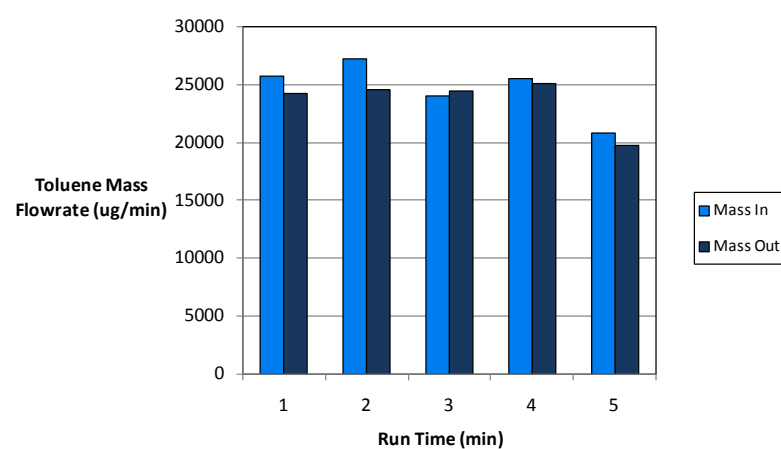
(A)



(B)



(C)



(D)

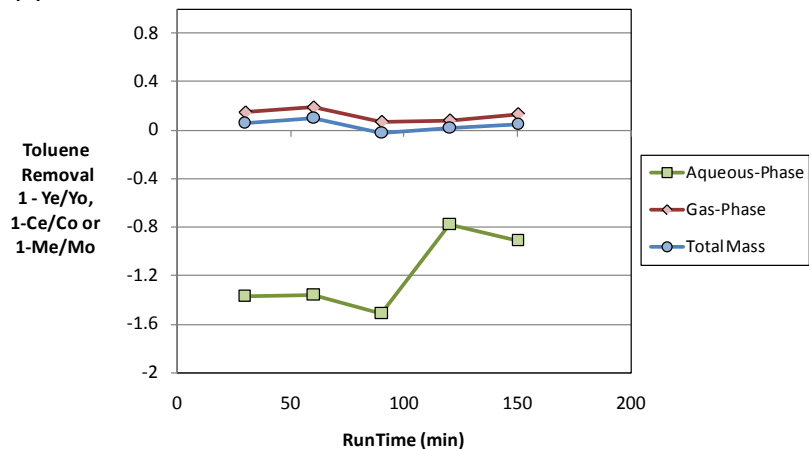


Figure 7-12. Results for two-phase experiments using undersaturated conditions : Experiment (f) conditions:  $Q_L = 3.8 \text{ L/min}$ ,  $Q_G = 142 \text{ L/min}$ ,  $T_{\text{water}} = 24.4^\circ\text{C}$  (A) Aqueous phase (B) Gas phase (C) Toluene mass balance (D) Summary of removals.

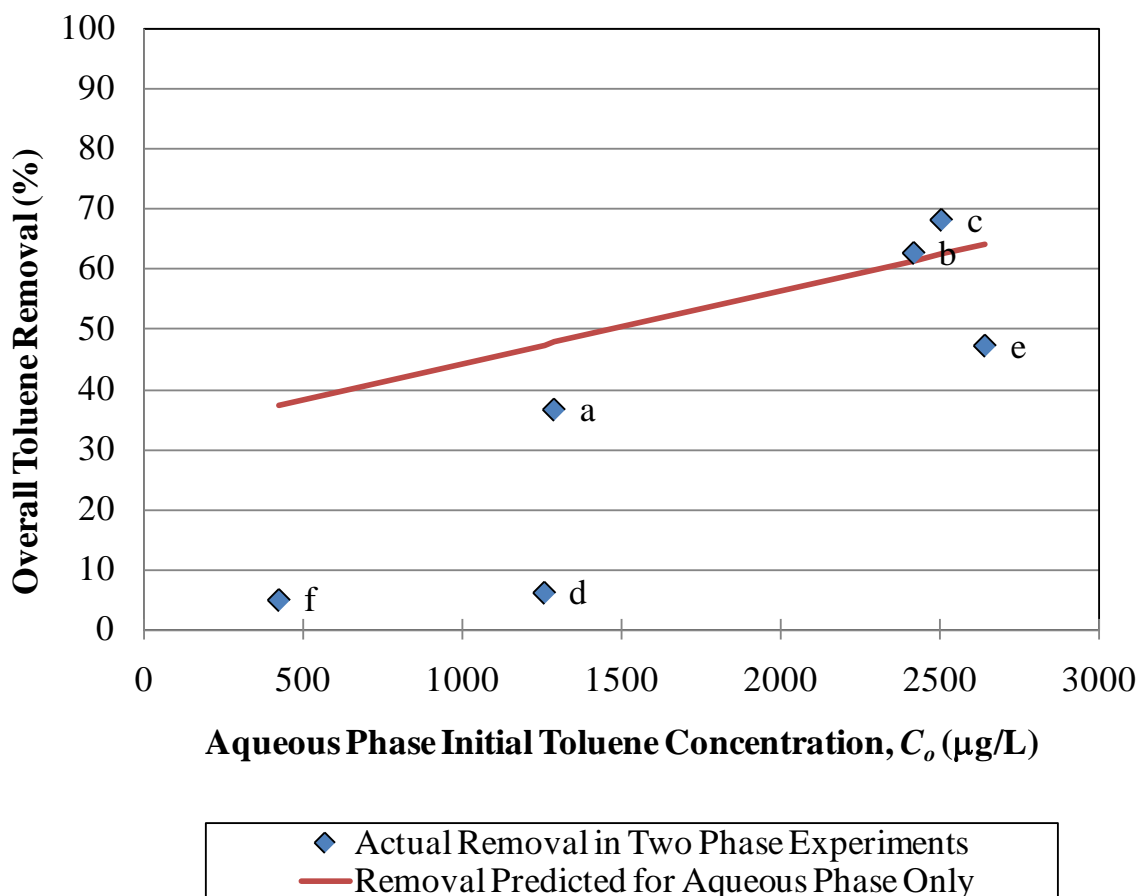


Figure 7-13. Comparison of the removal of toluene in the two-phase experiments to the expected removal in the aqueous phase only (i.e. in the absence of the gas flow)

## CHAPTER 8

### MATHEMATICAL MODELING AND SIMULATION OF THE TPOT

#### **Model Development**

The two-phase oxidation tower used in this research was mathematically modeled with the purpose of predicting its performance for any specified set of conditions and tracking the concentration profile throughout the length of the reactor. The temperature differences in the reactor when both phases were simultaneously flowing were considered to be small (less than 3°C difference), so isothermal models were appropriate for the simulation of the system investigated. Given that the ratio of the tower diameter to the packing diameter was between 12 and 22, the conditions in the radial direction were considered to be uniform, i.e. that the axial velocity over the cross section of the bed is constant (Sater and Levenspiel, 1966). Accordingly, the conversion of toluene was predicted by using one-dimensional models. Given that the gas phase velocities were high, a plug flow with dispersion model was used for toluene in the gas phase as it is usually for many stripping towers (Sater and Levenspiel, 1966). For aqueous phase toluene, however, a plug flow with dispersion model was considered. To describe the flow through the tower mathematically and solve the models, some simplifying assumptions were made:

- The axial dispersion is negligible for the gas phase.
- Adsorption of toluene for either phase is negligible.
- Gas and liquid phase concentration profiles are a function of the packing bed length only.
- The area for mass transfer between gas and liquid is the wetted area determined using the total surface area of comingled packing that is available in the reactor
- The area for the mass transfer between liquid and solid is only the wetted area determined using the catalyst surface area available in the reactor.

Schematics of the reactor showing the inflows and outflows for the contaminant as well as the differential reactor volume used to write the mass balances on toluene are shown in Figure 8-

1. Additionally, Figure 8-2 shows the mass transfer resistances for the gas, liquid and solid phases included in the modeling of the reactor.

Applying the selected models, the mass conservation equations written for each phase, with their respective boundary conditions are shown in Equations 8-1 to 8-3 for the aqueous phase and 8-4 to 8-5 for the gas phase. The solid phase mass balance is also shown in Equation 8-6.

Toluene in the aqueous phase:

$$D_{AX} \frac{d^2C}{dz^2} - U_L \frac{dC}{dz} + (K_{GL} a_w) \left( \frac{Y}{H} - C \right) - (K_{LS} a_c) (C - C_s) = 0 \quad (8-1)$$

Boundary conditions

$$\begin{aligned} \text{At } z = 0 & \quad -D_{AX} \frac{dC}{dz} = U_L (C_{IN} - C) \\ \text{At } z = Z & \quad \frac{dC}{dz} = 0 \end{aligned} \quad (8-2) \quad (8-3)$$

Toluene in the gas phase:

$$-U_G \frac{dY}{dz} - (K_{GL} a_w) \left( \frac{Y}{H} - C \right) = 0 \quad (8-4)$$

Boundary conditions

$$\begin{aligned} \text{At } z = 0 & \quad \frac{dC}{dz} = 0 \\ \text{At } z = Z & \quad C = C_s \end{aligned} \quad (8-5)$$

The equality of mass transfer and reaction rate is given by:

$$-r_{net} = (K_{LS} a_c) (C - C_s) \quad (8-6)$$

Similar to the aqueous phase solution, the above equations were solved numerically to obtain the axial profiles for the concentrations of toluene in the gas and aqueous phases. Both models were solved using the finite difference approximation methods. Spatial derivatives as well as boundary conditions were expressed by central differences approximations shown by Equations 6-15 and 6-16. The resulting set of algebraic equations was solved using typical methods to solve linear sets of algebraic equations such as the LU decomposition method. The dispersion coefficient and mass transfer coefficients were estimated using the correlations developed in Chapter 7 for the aqueous phase. The dispersion coefficient found for the aqueous phase was used in the two-phase system since many other researchers have found that this coefficient is only marginally affected by the gas flowrate (Piche et al. 2002). The surface concentration,  $C_s$ , was assumed to be zero by using the same assumptions as in the aqueous phase model. A summary of all these correlations is given in Table 8-1.

The model was initially solved for the concentration of toluene as a function of the packed bed depth using the correlations given in Table 8-1. The initial conditions entered in the model were those used for the two-phase experiments (a through e) performed in the TPOT, which are summarized in Tables 7-3 and 8-2. The concentration profiles using these correlations are presented in Figure 8-3 and can be identified by the number 1 in the legend. The results in Figure 8-3 show that the effluent concentrations obtained from the model predictions were higher than the actual effluent concentrations measured for the aqueous and the gas phases during the actual experiments (shown by the single markers in Figure 8-3). Accordingly, the net toluene conversions predicted by the model were much lower than the conversions obtained during the experimental runs, as shown in Table 8-2.

The model includes three main coefficients estimated in this research: the dispersion coefficient, the gas-liquid mass transfer and the liquid-solid mass transfer coefficients. In order to improve the model predictions, the effects of these coefficients were investigated. The dispersion coefficients were not modified because they were found to mostly influence the initial removal of toluene compared to the removal at the end of the packed section. As shown in Figure 8-4, increasing the dispersion coefficient resulted in most of the liquid phase removal of toluene to occur in the first few centimeters of the packed section, which did not appear to be very realistic.

The mass transfer coefficients, however, had a larger effect on the removal of toluene throughout the entire length of the packing. Varying the gas-liquid mass transfer coefficients resulted in better fits to the gas phase data. Similarly, the liquid-solid mass transfer coefficients influenced mostly the aqueous phase concentrations. Trying to calibrate the model with either coefficient individually did not result in good predictions for both phases. Consequently the model was calibrated by fitting both, the gas-liquid and the liquid-solid mass transfer coefficients to each set of data individually. The data available for the two-phase experiments only includes the concentrations measured at the inlet and the outlet of the reactor, so the fitting was performed to match the effluent concentration for both phases. Since the reactor flows in a countercurrent mode, the effluent gas phase concentration is given at  $z = 0$  while the aqueous phase concentration at the outlet occurs at  $z = Z$ , as shown in Figure 8-3. The calibration was performed by changing both mass transfer coefficients to minimize the SSqD at the effluent concentrations.

The concentration profiles obtained after calibrating the model with the mass transfer coefficients are shown in Figure 8-3, and these profiles can be identified by the number 2 in the

legend. Using the fitted liquid-solid mass transfer coefficients resulted in a better fit as compared to the results obtained from the correlation suggesting that there are other phenomena occurring in the reactor when both phases are present that are not being accounted for by the model or cannot be lumped in the  $K_{LSa_c}$  estimates for just the aqueous phase. Fitting the  $K_{LSa_c}$  and  $K_{GLa_w}$  resulted in good agreement for both the gas and aqueous phase concentrations; so, the net conversions were very closely approximated with the new values of the mass transfer coefficients (Figure 8-5 and Table 8-2.).

As presented in Table 8-3, results for the liquid-solid mass transfer coefficients used for the calibrated model were larger than the ones predicted from the correlations whereas the gas-liquid mass transfer coefficients did not follow a specific overall tendency compared to the values predicted by the Modified Onda correlation. The mass transfer coefficients predicted by the correlations given in Table 8-1 were very similar for all the experimental conditions investigated. This is because all the experiments were performed at the same liquid loading rate, and this is the parameter that seems to have the most effect on the determination of both coefficients using these correlations. However, the calibrated coefficients suggest that these coefficients might be also significantly dependent on the gas phase loading rate because larger differences for both mass transfer coefficients were observed for the cases where the gas loading rate was changed. The gas loading rate appears to have a large positive impact on the values of  $K_{GLa_w}$  and the opposite impact on  $K_{LSa_c}$ . Although the influence of the gas loading rate seems to be important for the determination of both coefficients, a specific trend was not observed for either case as a function of gas loading rate.

### **Model Simulation**

The main objective of modeling the reactor is to be able to make predictions about its performance given a set of operating conditions. Therefore, in this section, the performance of

the complete proposed system, TPOT and the end polishing sections is illustrated. The initial set of operating conditions is given in Table 8-3. These conditions are similar to the ones used for the two-phase experiments. Also, the reactor used for the simulation is the TPOT, meaning that its dimensions and packing characteristics have not changed. Although the dimensions of the system have been already set for the middle two-phase section, the model can be solved for the length of this section if the desired outlet aqueous phase concentration is specified. The final target effluent concentrations, i.e. the concentrations desired at the end of the polishing sections were chosen to be the inhalation chronic reference exposure level for toluene and the MCL for benzene in drinking water, which are equal to 0.30 µg/L and 5 µg/L, respectively. These values were chosen for this section of the study, although other values could be chosen to meet other required air and water concentrations. The MCL for benzene was chosen instead of toluene because toluene's MCL is 1 mg/L, which is rather high for the inlet concentrations used in the simulation, so a polishing section for the aqueous phase would not be required to meet that MCL, and for the purposes of this simulation, it was desired to have large enough aqueous concentrations at the effluent of the TPOT relative to the MCL, so that a liquid phase polishing section would be required to meet the target effluent contaminant level.

The two-phase model used the correlations specified in Table 8-1, but the liquid-solid mass transfer coefficient was multiplied by a factor of 3.5 since it was found that these values were likely underestimated by the correlation when used in the model of the two-phase system for most conditions studied. The concentration profile for the operating conditions specified is shown in Figure 8-6. Furthermore, the concentration profile for the same system operated in the absence of photocatalysis (i.e. with the UV lamps off, so that the only process taking place is mass transfer) were also plotted in the same graph. The net removal of toluene from the tower,

shown in Figure 8-7, indicates that about 42% of the contaminant's mass is removed in this reactor for the operating conditions specified.

Based on the simulation for the middle section of the system, the concentrations leaving the TPOT and thus entering the polishing sections were 31.2  $\mu\text{g/L}$  and 111.8  $\mu\text{g/L}$  for the gas and aqueous phases, respectively. The gas phase reactor was sized based on the pseudo first order reaction rate constant found during the small scale gas phase experiments in Chapter 5, which was  $0.12 \text{ s}^{-1}$ . Since the effluent gas from the TPOT is expected to be highly humidified due to its contact with the liquid phase, no significant deactivation of the catalyst is expected to occur in the gas phase polishing section. The liquid phase polishing section was designed using the pseudo first order rate constant found by Holmes et al. (2004), who used a bench-scale reactor packed with the small STCs (3 mm x 5 mm). The concentration range in their experiments was 100 to 200  $\mu\text{g/L}$ , which is similar to the concentrations expected to be leaving the two-phase reactor. Different from the middle section, the end polishing sections are saturated systems, meaning the water is completely filling the reactor instead of just flowing in a trickled mode. The gas phase end polishing section was designed to maintain a minimum superficial velocity requirement of 1 cm/s to diminish the influence of mass transfer effects, as determined by the bench-scale experiments. The polishing sections characteristics are shown in Table 8-5. The diameters ( $D$ ) for both sections are larger than those used during the bench-scale experiments; so, multiple lamps will need to be included in the reactors to achieve the necessary irradiation and comparable reaction rates. The complete treatment system showing the conversion of toluene at the different stages is illustrated in Figure 8-8.

### **Effects of Operating Parameters on the TPOT Performance**

The effects of the several operating parameters that can be adjusted in the TPOT during a typical run were investigated. An individual parameter's effect on toluene conversion was

determined by doubling the value of such parameters compared to a base scenario selected. The base scenario had the same initial operating conditions as the one used for the system simulation ( $Q_L = 3.785 \text{ L/min}$ ,  $Q_G = 113.5 \text{ L/min}$ ,  $C_{in} = 1500 \text{ mg/L}$ ,  $Y_{in} = 10 \text{ mg/L}$ ,  $T_w = 24^\circ\text{C}$ ). The concentration profiles and removals were determined by solving the two-phase model developed earlier using the correlations given in Table 8-1 for all required coefficients, since based on previous results, these coefficients seem to be a conservative approximation of the actual mass transfer coefficients in the two-phase reactor. The parameters investigated included the gas and liquid flowrates, the gas and liquid inlet concentrations and the temperature. The aqueous and gas phase concentration profiles are shown in Figures 8-9 and 8-10, respectively. The net conversion of toluene as a function of packed bed depth is presented in Figure 8-11 for the different parameters investigated.

For the aqueous phase, doubling the initial gas phase concentration, gas flowrate and decreasing the temperature did not have a significant effect on the concentration profile compared to the base scenario. Doubling the liquid loading rate, however, adversely affected the removal of toluene in the aqueous phase. The lower residence time and the thicker liquid film formed as a result of the higher flowrate negatively affects the conversion of toluene to a greater extent than the increase in wetted surface area (~ 20% increase) which improves the conversion of toluene in the aqueous phase. The other factor that influenced the concentration profile in the TPOT was increase in initial liquid phase concentration. Even though the concentration was doubled, the concentration sharply decreased with packed bed depth achieving almost the same removal in the aqueous phase as the base scenario, suggesting that the concentration is an important driving force for the conversion of toluene in the liquid phase.

Starting at a concentration of 10 µg/L (at  $Z = 122$  cm), the gas phase concentration increased for all conditions studied as it moved through the length of the bed. Factors improving the removal in the gas phase were the water temperature and gas flowrate. Doubling the other parameters resulted in higher gas phase concentration; the liquid flowrate had the highest adverse impact followed by the aqueous inlet concentration and the gas inlet concentration. Increasing either the gas or liquid phase concentrations resulted in higher mass of toluene in the reactor, thus it was expected that these concentrations would be higher than the base scenario. Similarly, doubling the liquid flowrate increases the mass loading, thus compared to the base scenario, the concentrations should be higher if similar removals are expected. However, the results for the doubled gas flowrate were unexpected since increasing the gas flow should result in higher stripping and thus, higher gas phase concentrations, as occurred during the experimental runs. Decreasing the temperature results in lower  $H$  values that decrease the stripping potential, but this parameter does not take into account its effect on reaction rates.

The trends in the profiles shown for the individual phases might not be the same as those showing the net conversion of toluene due to the large difference in flowrates for the gas and aqueous phases. Surprisingly, the parameter that resulted in the highest removal compared to the base scenario was the decreased temperature. By lowering the temperature from 25°C to 10°C, the gas –liquid mass transfer coefficient is decreased by a factor of about 2 compared to the base scenario, so stripping is significantly affected. However, the effects of temperature on reaction kinetics were not included in the model, so its overall effect cannot be impartially assessed. The increased inlet concentration also resulted in greater removals, and the reasons for this have been previously stated. Doubling either the gas flow or concentration resulted in lower net conversions since they adversely impact the liquid phase removal. Finally, doubling the liquid flowrate

resulted in the lowest removal, and the adverse effects of this parameter on removal have been explained above. All the effects of the investigated parameters on removal based on the model solution agree with the observed effects obtained from the two-phase experiments.

Table 8-1. Summary of correlations used to determine the parameters involved in the solution to the differential equations developed to model the TPOT.

*Axial Dispersion Coefficient,  $D_{AX}$*

$$D_{AX} = 1.98 \times Re^{0.84} Ga^{0.10} \quad (6-11)$$

*Overall gas-liquid mass transfer coefficient,  $K_{GL}a_w$*

$$\frac{1}{K_L a_w} = \frac{1}{k_l a_w} + \frac{1}{H k_g a_w} \quad (2-37)$$

$$a_w = a_t \left\{ 1 - \exp \left[ -1.45 \left( \frac{\sigma_c}{\sigma} \right)^{0.075} \left( \frac{L_m}{a_t \mu_L} \right)^{0.1} \left( \frac{L_m^2 a_t}{\rho_L^2 g} \right)^{-0.05} \left( \frac{L_m^2}{\rho_L a_t \sigma} \right)^{0.2} \right] \right\} \quad (7-1)$$

$$k_L = 0.0051 \left( \frac{L_m}{a_w \mu_L} \right)^{2/3} \left( \frac{\mu_L}{\rho_L D_L} \right)^{-0.5} \left( a_t d_p \right)^{0.4} \left( \frac{\rho_L}{\mu_L g} \right)^{-1/3} \quad (2-46)$$

$$k_g = 5.23 \left( a_t D_g \right) \left( \frac{G_m}{a_t \mu_g} \right)^{0.7} \left( \frac{\mu_g}{\rho_g D_g} \right)^{1/3} \left( a_t d_p \right)^{-2} \quad (2-47)$$

*Overall liquid-solid mass transfer coefficient,  $K_{LS}a_c$*

$$K_{LS}a_c (s^{-1}) = 1.2 \times 10^{-3} \times Re^{-0.50} \times C_{IN}^{0.25} \quad (6-19)$$

Table 8-2. Comparison of the actual net toluene removal to the net removal predicted by the two-phase model using different calibration methods. (1)K's calculated from correlations in Table 8-1, (2) Both  $K_{LSa_c}$  &  $K_{GLa_w}$  were modified to calibrate the model.

| Exp | $Q_G$<br>(L/min) | $C_o$<br>( $\mu\text{g/L}$ ) | $Y_o$<br>( $\mu\text{g/L}$ ) | Net Toluene Removal using different K's |                           |                                      |
|-----|------------------|------------------------------|------------------------------|---|---------------------------|--------------------------------------|
|     |                  |                              |                              | Actual                                  | (1) K's from correlations | (2) $K_{LSa_c}$ & $K_{GLa_w}$ fitted |
| a   | 142              | 1288                         | 23                           | 0.38                                    | 0.19                      | 0.37                                 |
| b   | 142              | 2419                         | 11                           | 0.63                                    | 0.29                      | 0.63                                 |
| c   | 116              | 2506                         | 6                            | 0.69                                    | 0.30                      | 0.68                                 |
| d   | 202              | 1258                         | 8                            | 0.08                                    | 0.23                      | 0.06                                 |
| e   | 142              | 2642                         | 2                            | 0.49                                    | 0.32                      | 0.47                                 |

Table 8-3. Comparison of the mass transfer coefficients calculated using the correlations developed for the aqueous phase and those found by calibrating the model.

| Exp | (1) K's from correlations               |   | (2) $K_{LSa_c}$ & $K_{GLa_w}$ fitted    |   |
|-----|---|---|---|---|
|     | $K_{GLa_w}$<br>( $s^{-1} \times 10^3$ ) | $K_{LSa_c}$<br>( $s^{-1} \times 10^3$ ) | $K_{GLa_w}$<br>( $s^{-1} \times 10^3$ ) | $K_{LSa_c}$<br>( $s^{-1} \times 10^3$ ) |
| a   | 4.19                                    | 1.30                                    | 4.09                                    | 4.68                                    |
| b   | 4.29                                    | 1.52                                    | 1.44                                    | 4.87                                    |
| c   | 4.37                                    | 1.54                                    | 2.21                                    | 6.89                                    |
| d   | 4.42                                    | 1.29                                    | 9.41                                    | 1.74                                    |
| e   | 4.30                                    | 1.56                                    | 4.79                                    | 5.35                                    |

Table 8-4. Operating conditions selected for the simulation of the system's performance.

| Parameter   | Units               | Value  |
|-------------|---------------------|--------|
| $Q_G/Q_L$   |                     | 30.0   |
| $Q_L$       | L/min               | 3.8    |
| $Q_G$       | L/min               | 113.5  |
| $L_m$       | gpm/ft <sup>2</sup> | 3.1    |
| $T_{water}$ | °C                  | 25.0   |
| $C_{in}$    | ug/L                | 1500.0 |
| $Y_{in}$    | ug/L                | 10.0   |

Table 8-5. Reactor characteristics for the end polishing sections of the treatment system.

|              | $\tau$<br>min | $Q$<br>L/min | Z<br>M | D<br>Cm | U<br>cm/s | Inlet<br>ug/L | Outlet<br>ug/L |
|--------------|---------------|--------------|--------|---------|-----------|---------------|----------------|
| Gas Phase    | 0.71          | 113.5        | 0.43   | 49.08   | 1.0       | 31.2          | 0.3            |
| Liquid Phase | 18.28         | 3.8          | 1.10   | 28.34   | 0.10      | 111.8         | 5.0            |

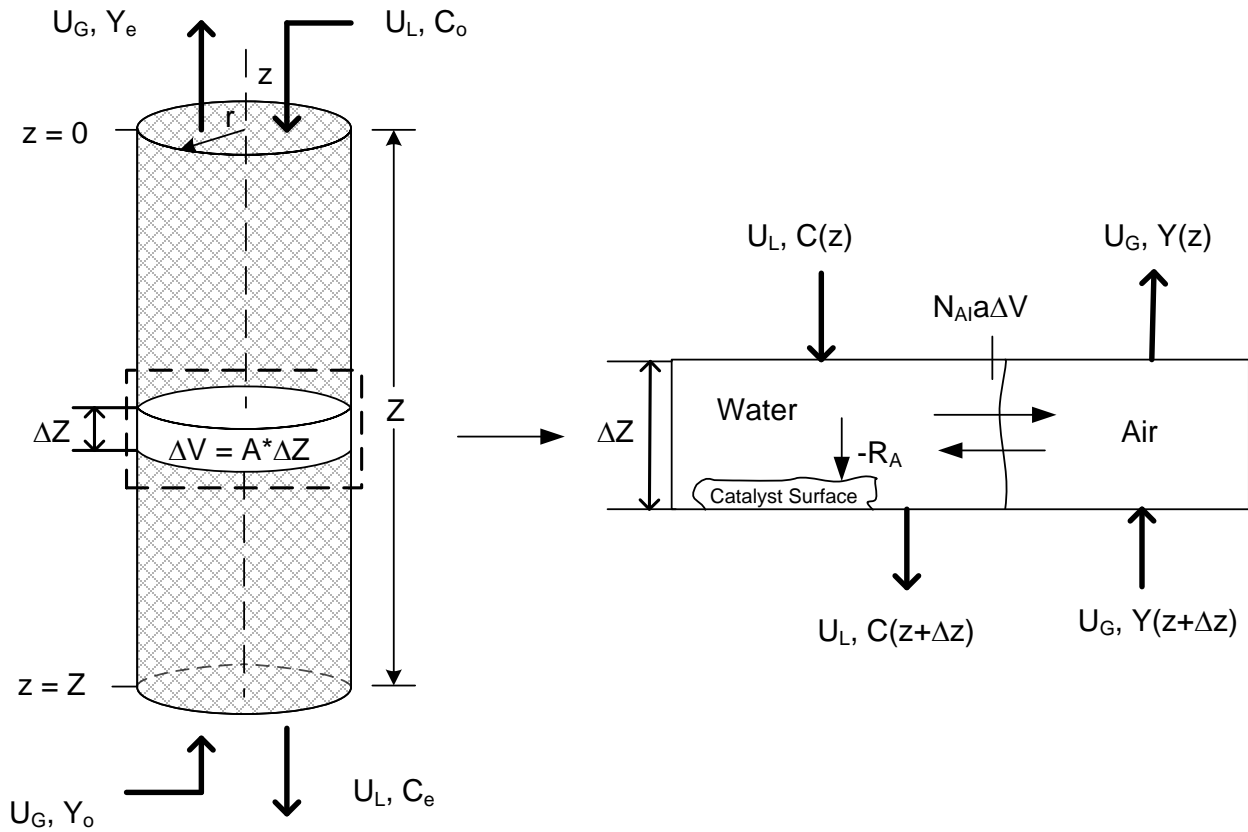


Figure 8-1. Schematics of the reactor and differential volume used to determine toluene's mass balance equations.

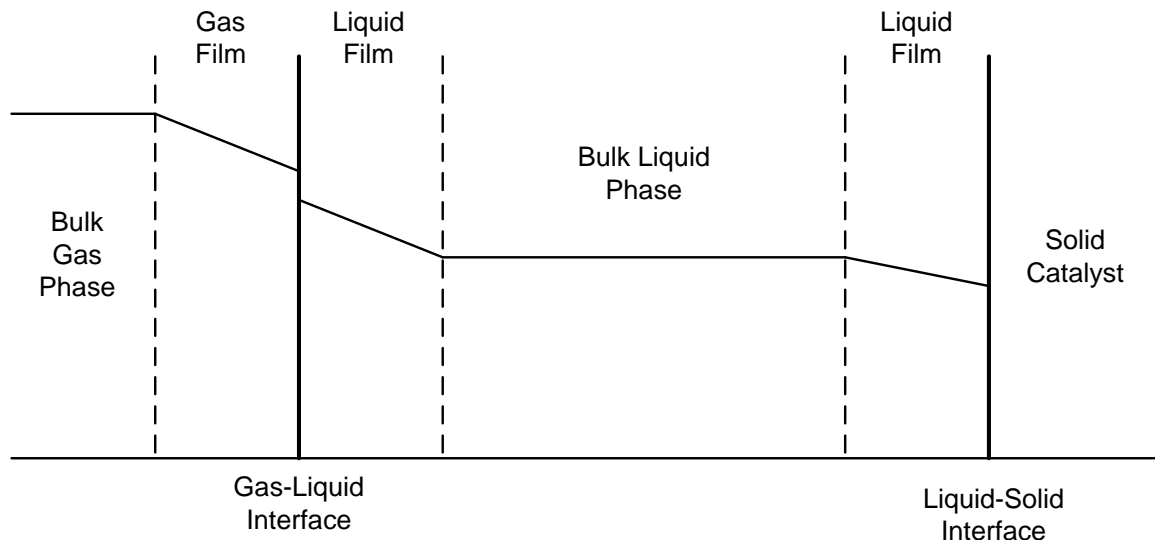


Figure 8-2. Gas, liquid and solid phases resistances and concentration profiles in the TPOT.

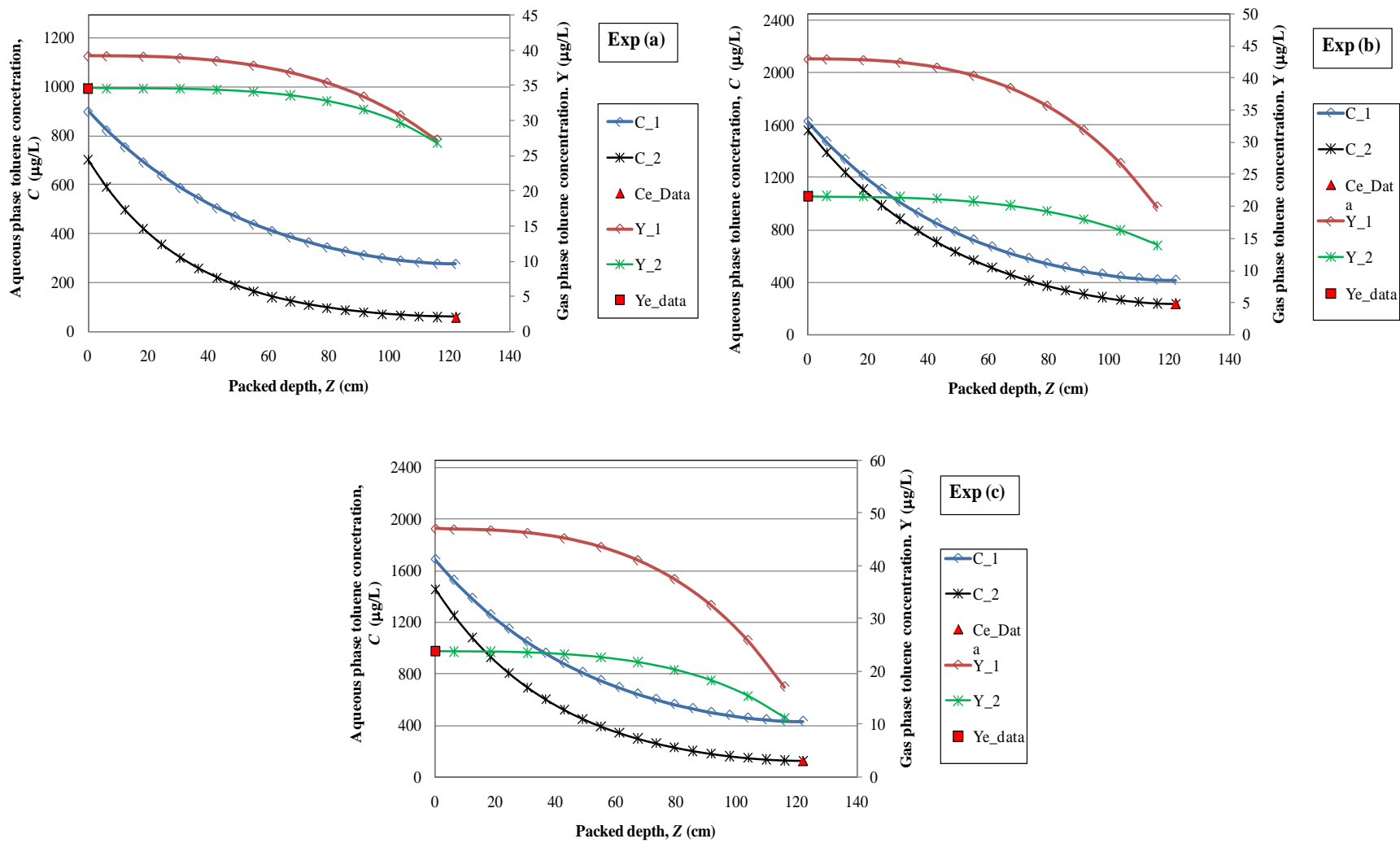


Figure 8-3. Comparison of concentration profiles obtained from the model using the correlation derived for the aqueous phase (1) and the one fitted to the two-phase data (2). Except for the ones identified in the legend as individual points, the markers on the curves do not represent measured data, but were included only to facilitate the identification of the curves..

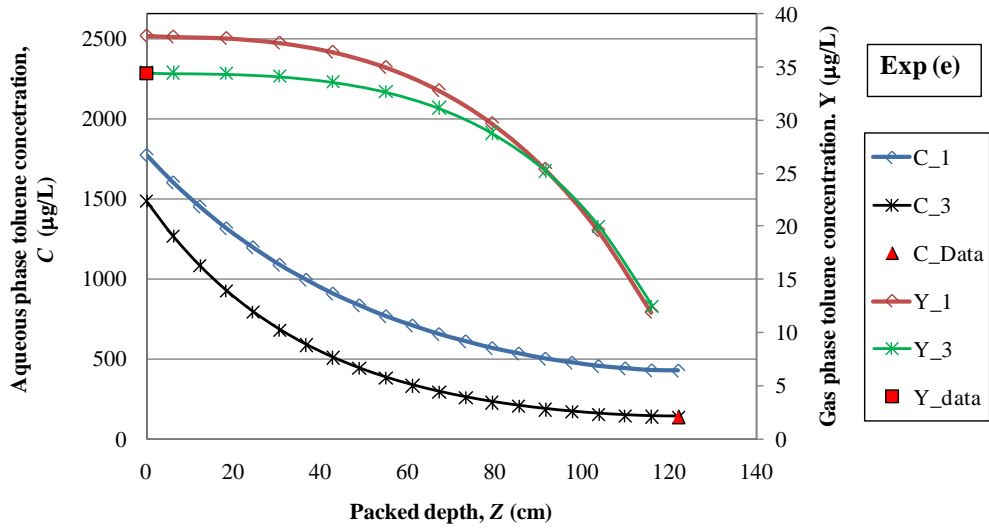
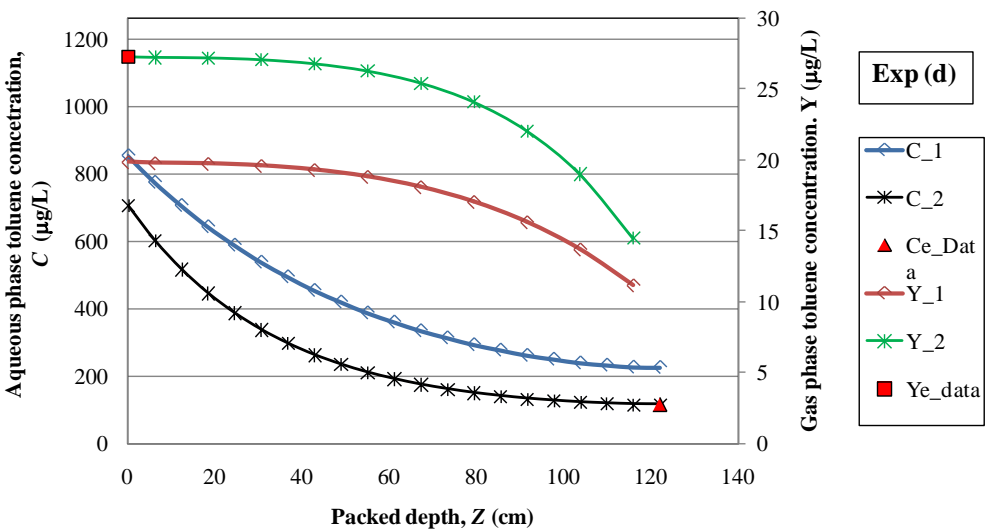


Figure 8-3. Continued

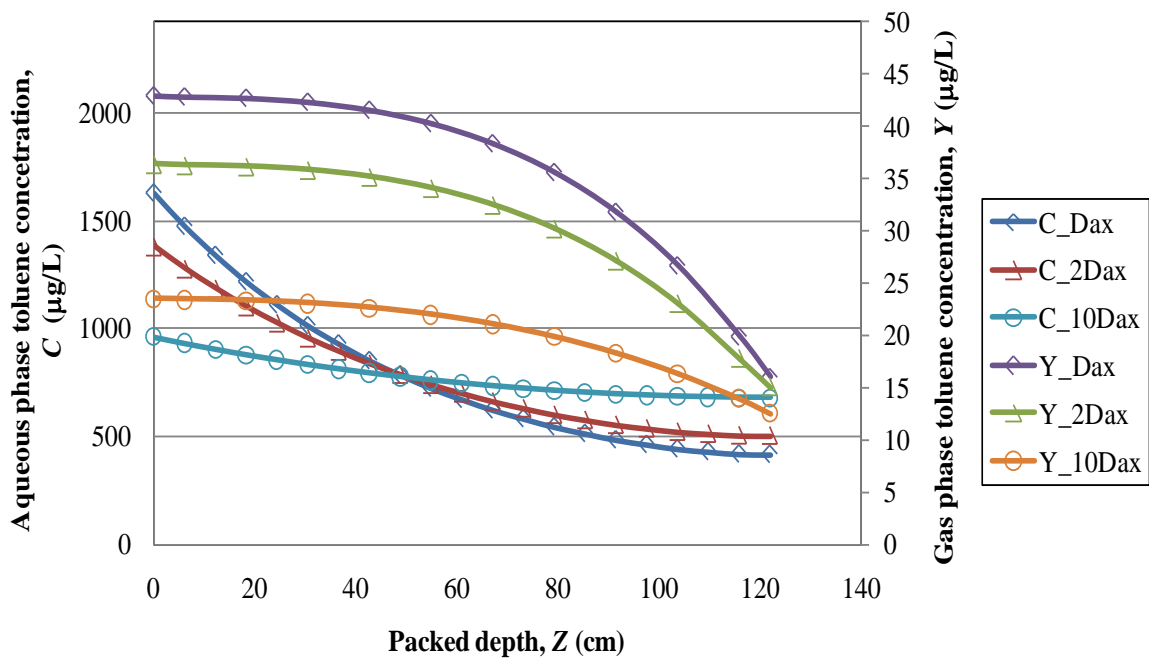


Figure 8-4. Effects of dispersion coefficient on the aqueous and gas phases profiles obtained from the models using the K's calculated from the correlations. The initial conditions are those for Experiment (b):  $QL = 3.8 \text{ L/min}$ ,  $QG = 142 \text{ L/min}$ ,  $T_{water} = 24.40^\circ\text{C}$ . The markers on the graph do not represent measured data; they are only used to facilitate identifying the respective curves.

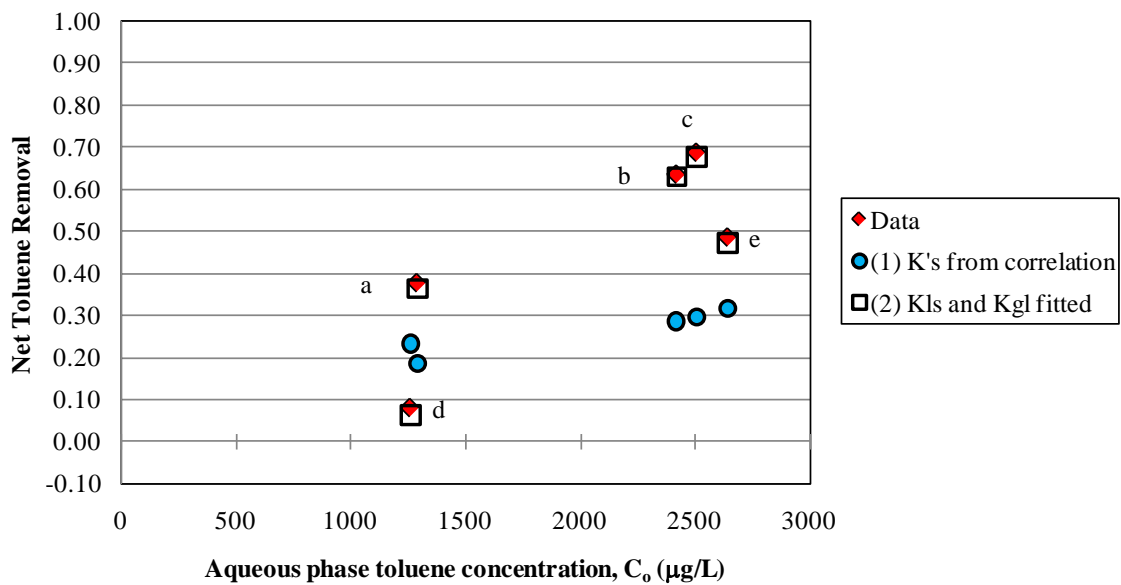


Figure 8-5. Actual net toluene removal versus the net removal predicted by the two-phase model using different mass transfer coefficients.

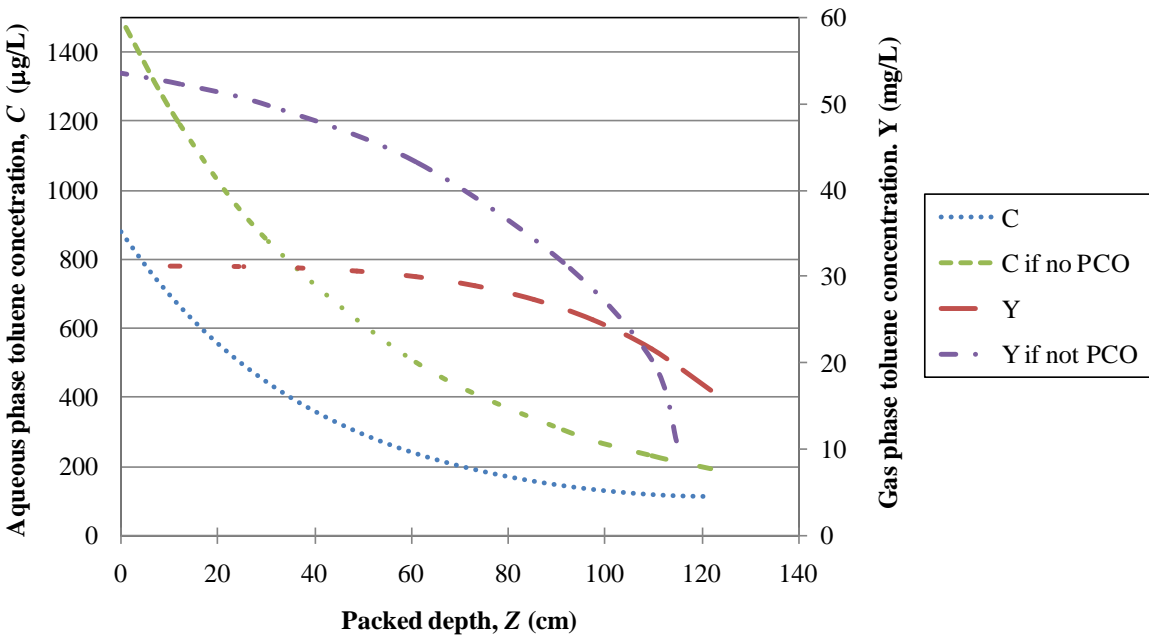


Figure 8-6. Concentration profile for toluene in the TPOT present in the gas and aqueous phases in the presence of PCO (UV lamps on) and due to mass transfer only (UV lamps off).

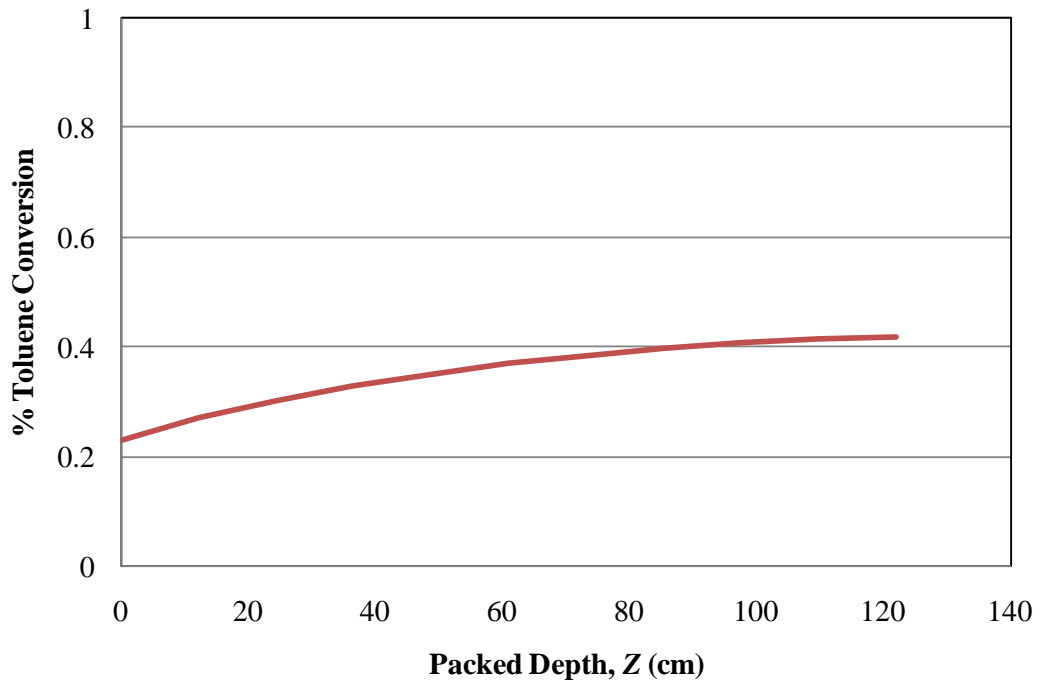


Figure 8-7. Net toluene removal in the TPOT as a function of packed bed depth

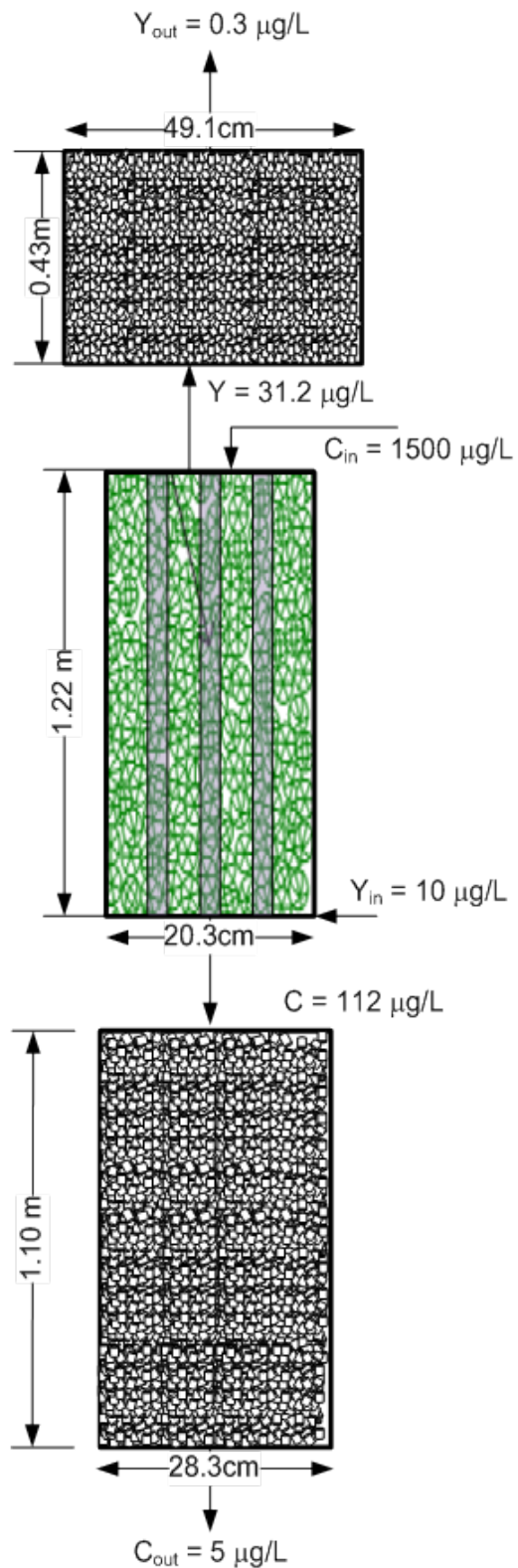


Figure 8-8. Complete treatment system showing the simulation results.

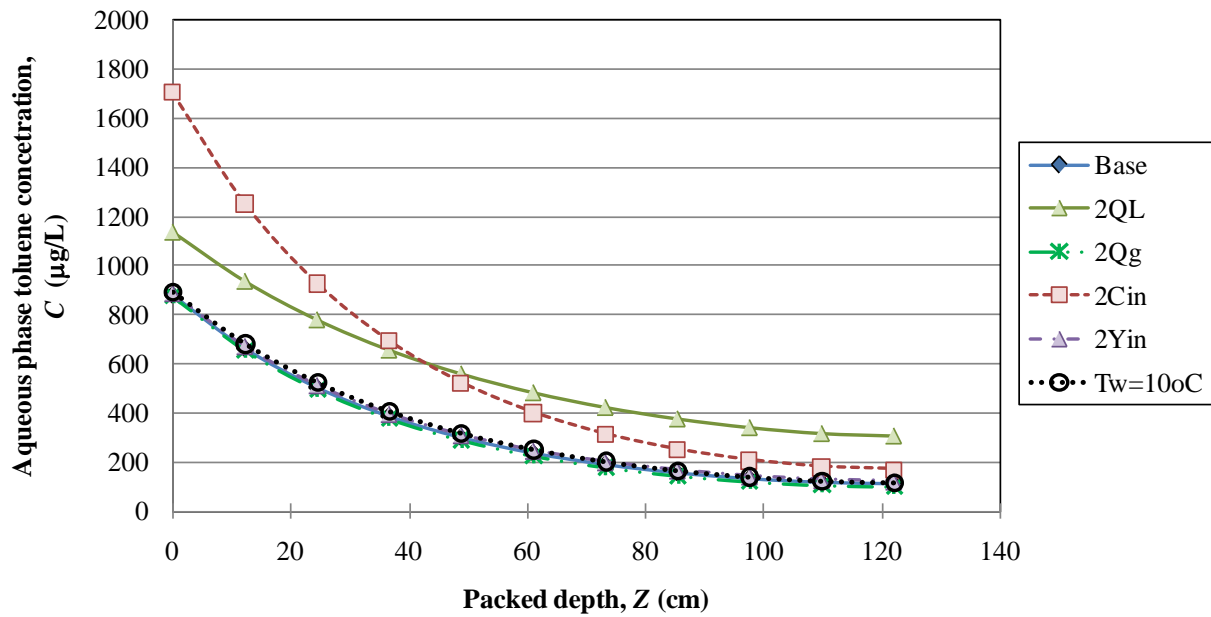


Figure 8-9. Effect of different operating parameters on the aqueous phase profile concentrations in the TPOT. Base profile:  $Q_L=3.785\text{L}/\text{min}$ ,  $Q_G=113.5\text{L}/\text{min}$ ,  $C_{in}=1500\text{mg/L}$ ,  $Y_{in}=10\text{mg/L}$ ,  $T_w=24^\circ\text{C}$ .

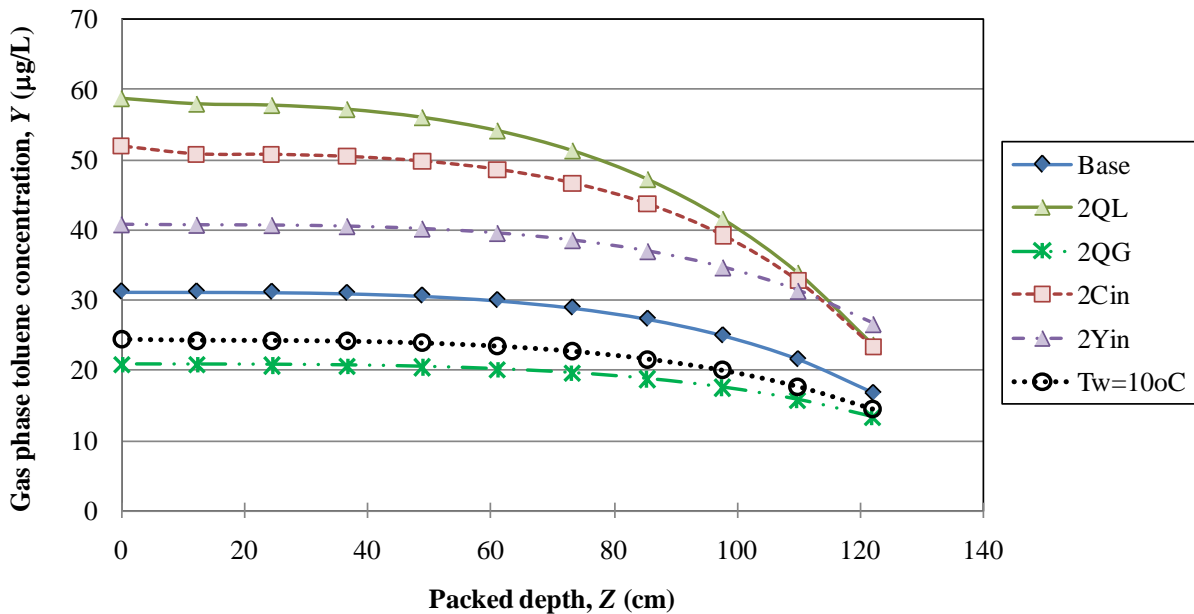


Figure 8-10. Effect of different operating parameters on the gas phase profile concentrations in the TPOT. Base profile:  $Q_L=3.785\text{L}/\text{min}$ ,  $Q_G=113.5\text{L}/\text{min}$ ,  $C_{in}=1500\text{mg/L}$ ,  $Y_{in}=10\text{mg/L}$ ,  $T_w=24^\circ\text{C}$ .

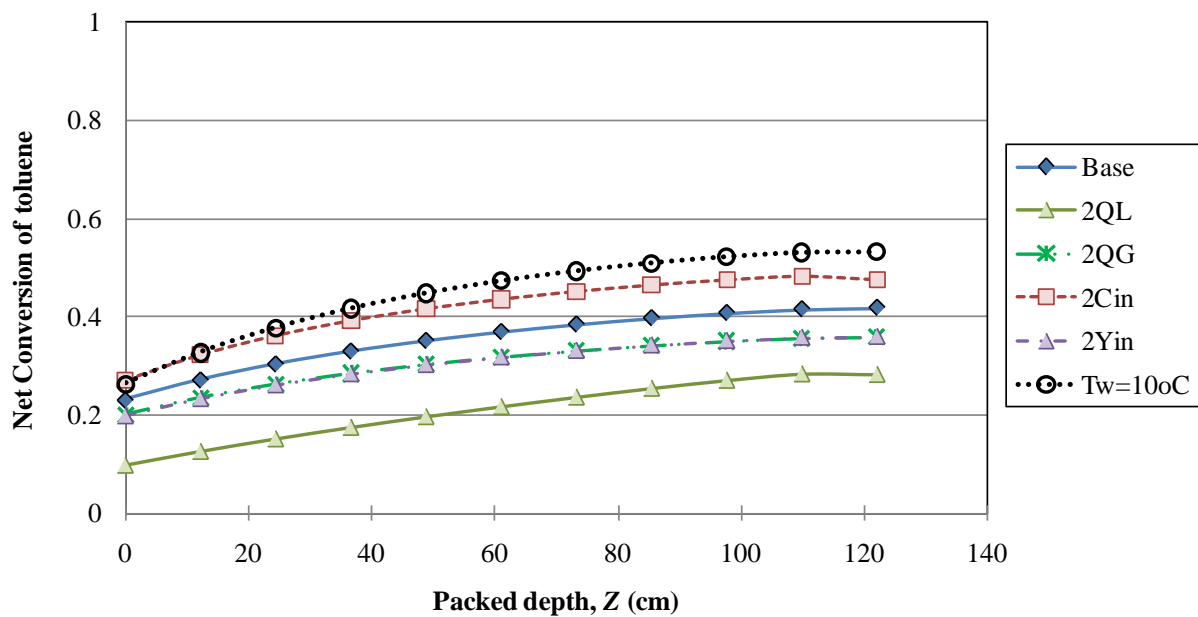


Figure 8-11. Effect of different operating parameters on the net toluene conversion in the TPOT as a function of packed bed depth. Base profile:  $Q_L = 3.785 \text{ L/min}$ ,  $Q_G = 113.5 \text{ L/min}$ ,  $C_{in} = 1500 \text{ mg/L}$ ,  $Y_{in} = 10 \text{ mg/L}$ ,  $T_w = 24^\circ\text{C}$ .

## CHAPTER 9 CONCLUSIONS

The photocatalytic oxidation of toluene was investigated using a novel countercurrent flow reactor designed to enable the treatment of toluene present in the gas phase and the aqueous phase simultaneously. The main conclusions formulated from the experimental results were the following:

1. The accessible surface area of titanium dioxide in the STCs developed for the photocatalytic reactor compared to pure Degussa P25  $\text{TiO}_2$  decreased by about 20%. However, no significant differences were found between the area available in the STCs when used as a powder or as a large pellet (9mm x 8mm) of cylindrical shape.
2. Gas phase adsorption of toluene was large during both bench and pilot-scale experiments in the absence of a water phase coating the pellets. The adsorption capacity decreased remarkably as temperature increased
3. Gas phase toluene conversions greater than 90% were achieved in bench-scale experiments using the STCs only when they were dry and there was sufficient water vapor concentration in the gas. Under the operating conditions investigated, the reaction kinetics were not limited by external or internal resistances to mass transfer. The removal of toluene in the gas phase using dry STCs exhibited pseudo-first order reaction kinetics with rate constant of  $0.12 \text{ s}^{-1}$ .
4. Deactivation of the catalyst was observed during gas phase PCO under all conditions investigated at the bench-scale. This deactivation was more pronounced, however, when the relative humidity was low. Accompanying deactivation was the presence of a yellowish coloration of the STCs.
5. During pilot-scale studies, the extent of PCO of toluene in the gas phase was found to be lower than during bench-scale studies. The decreased activity was attributed to the insufficient relative humidity during pilot-scale operations, the significant deactivation encountered in the pilot reactor, and the large increase in the lamps' temperature. Deactivation was confirmed because the reactor was able to achieve greater toluene conversions after catalyst regeneration. The increase in lamp temperature can affect gas phase PCO in two ways: it increases reactor temperature thus negatively affecting the adsorption of toluene to the catalyst, and it affects the UVC output of the lamps which is temperature sensitive.
6. PCO of toluene in the gas phase was completely inhibited by the wetting of the STCs, for batch, continuous flow and trickled flow operations.

7. Since wetting of the packing resulted in negligible PCO in the gas phase, likely due to the lack of adsorption of toluene to the catalyst, the reaction mechanism for PCO in the gas phase involves an adsorption step so the reactions do not occur at the bulk phase.
8. Adsorption of toluene in the aqueous phase was determined at the bench-scale and found to be significant during batch experiments. However, it was negligible during pilot-scale operations at different liquid loading rates most likely due to the much shorter residence times (< 60 s) encountered in the pilot reactor. Adsorption occurs until equilibrium is achieved, but it does not affect the concentration of the effluent because the removal for a single pass of fluid is small due to the small residence time.
9. PCO of toluene in the aqueous phase was found to linearly increase as a function of inlet concentration and decrease as function of liquid loading rate. Increasing the concentration increases the driving force for transfer between liquid and solid, thus improving toluene conversion. Increasing the loading rate results in opposing effects for PCO. On the one hand it increases the wetted surface area of the packing which should result in improved PCO; on the other hand it increases the thickness of the liquid film in the reactor which increases the resistance to mass transfer between the liquid-solid interface and it also decreases the residence time of toluene in the reactor, both of which produce an adverse effect on PCO.
10. The mean residence time of toluene in the aqueous phase was determined using a step input tracer test. The mean residence time was greater for the TPOT packed with the commingled packing compared to the only high flow rings packing due to the lower porosity which indicates increased tortuosity and holdup in the system. For the commingled packing, the mean residence time decreased linearly with flowrate.
11. The dispersion coefficients obtained from the tracer test increased with liquid superficial velocity, and they were correlated to the Reynolds and Galileo numbers
12. The reactor was modeled for the liquid phase only using a one dimensional plug flow with dispersion equation, which was numerically solved by the finite differences method. Using this model, overall liquid-solid mass transfer coefficients were obtained by minimizing the sum of squared differences between the model and the experimental results.  $K_{LSA_c}$  was found to be a function of flowrate and inlet concentration, thus it was correlated to the Reynolds number and the influent toluene concentration.
13. The UV distribution in the reactor was improved by using the commingled packing compared to just STCs, as confirmed by the increase in UV irradiance penetration from 2.5 cm to about 6 cm for the STCs only packing and the commingled packing, respectively.
14. It was determined that about 30% of the reactor did not receive any UV irradiance. The average UV intensity in the reactor was found to be about 220  $\mu\text{W/g}$  of irradiated  $\text{TiO}_2$ . Optimization of the lamp and packing placement in the reactor will provide more efficient use of the UV radiation generated and lower energy requirements.

15. Overall gas-liquid mass transfer coefficients, which includes the specific surface area, were found to be greater for the reactor packed with the commingled packing as compared to just STCs. Improved mass transfer coefficients were the result of the greater surface area available for transfer provided by the commingled packing
16. A modified version of the Onda correlation was found to produce excellent predictions for the overall gas-liquid mass transfer coefficients. The modified Onda correlation accounted by a greater wetted area than the one proposed by Onda et al., and the modification was performed by adjusting one of the coefficients of the equation for the wetted area provided by Onda et al. The modification decreased the effect of surface tension in the wetting process.
17. The gas-liquid mass transfer coefficients showed a moderate non-linear increase as a function of the air-to-water ratio, and they increased linearly with liquid flowrate. However,  $K_{GLa_w}$  is expected to achieve a maximum as a function of liquid loading rate, since most of the improvement is due to the increase in wetted area, which will achieve a maximum as a function of the liquid flowrate.
18. The two-phase experimental results indicated that compared to the conversions of toluene found for the aqueous phase only, the two-phase system usually resulted in lower conversions for the same aqueous phase concentrations, suggesting that most of the removal in the two-phase system occurs at the liquid solid interface.
19. The removal of toluene in the two-phase countercurrent tower can be adversely affected by:
- Decrease in the aqueous phase concentration → decreases the driving force for aqueous phase PCO.
  - Increase in air to water ratio → Increases stripping to the gas phase, thus decreasing the aqueous phase concentration.
  - Decrease in gas phase concentration → increases the gas phase capacity for toluene, which increases the stripping potential, thus decreasing the aqueous phase concentration.
20. The two-phase reactor was modeled using a plug flow with dispersion model for the aqueous phase and a plug flow model for the gas phase. The modeling effort with adjust of mass transfer coefficients was successful.
21. The liquid-solid mass transfer coefficients found by the two-phase model were between 1.3 to 6 times greater than the coefficients found for the single aqueous phase model. The gas phase flowrate and concentration, which were not part of the correlations, seem to affect these coefficients, although a specific trend was not found.
22. The mathematical model is a useful tool to simulate the reactor's performance for a given set of operating conditions. It also allows investigating the effects of the different variables on the net toluene conversion.

Due to the stripping capacity of the TPOT, this system can achieve aqueous phase removals that single phase photocatalytic systems would not be able to achieve given the residence time in the system. Other authors have achieved removals greater than 80% but using reaction times greater than 40 min (Holmes et al., 2004; Cao et al., 2000). For the average residence time of less than 60 seconds provided in the TPOT, the aqueous phase removal achieved is remarkable. The removals obtained were as high as or higher than those achieved by a stripping tower; however, due to the photocatalytic capacity of the system the gas phase concentration exiting the reactor is lower than for a stripping tower relying only on mass transfer. Therefore, if this reactor was used to treat VOCs in the aqueous phase, the treatment of the effluent gas in this system would be cheaper than for a stripping tower using granular activated carbon (GAC) to treat the effluent gas due to the lower toluene gas loading that the GAC system would need to treat. Although the initial capital cost of the photocatalytic system might be greater than the one for a conventional treatment system, such as a stripping tower treating the off gas using granular activated carbon (GAC), because of the UV lamps and catalyst that need to be incorporated in the stripping tower and in the end polishing sections, the long term cost is expected to be lower because of two reasons: (1) the catalyst is self – regenerated which is not the case for activated carbon which needs to be replaced several times during the lifetime of the system, and (2) the TPOT system completely destroys the contaminant, meaning that there are no disposal costs related to this systems, which is not the case for GAC treatment that requires the thermal oxidation of the carbon to completely destroy the contaminants.

Some recommendations for future work include:

- Model validation by testing the tower with different VOCs.
- Potential coating of the conventional tower packing to make better usage of the catalyst mass in the reactor and improve even further the UV penetration.

- The competitive effects of VOCs in a multi-component system employing the TPOT should be modeled since these systems will be more indicative of real world applications.
- Bench-scale studies to determine the reaction rate of toluene PCO in the aqueous phase for modeling of the polishing section.
- Energy requirement comparisons with conventional treatment systems for VOCs.
- In depth analysis of the oxidation byproducts in the gas phase to better determine the reasons for catalyst deactivation.

## APPENDIX A PRELIMINARY STUDIES

### **Studies on System's Integrity**

#### **System Losses**

The potential losses in the system due to piping, leaks or/and volatilization were assessed individually for the gas and aqueous phases using the TPOT reactor packed only with plastic high flow rings, i.e. in the absence of the catalyst. Either the gas or aqueous influent was spiked with toluene and passed through the packed tower at the desired flowrate. The UV lamps were turned off during all these experiments while the inlet and outlet concentrations were monitored. The gas and aqueous phase results presented in Figures A-1 and A-2, respectively, show the average of at least two replicates of the same experiment and their corresponding standard deviations shown by the error bars.

The results obtained from the gas phase experiments (Figure A-1) show that it takes about 20 min for the gas phase concentrations to reach steady state under the given conditions. After steady state is achieved, there are not significant losses in the system since inlet and outlet concentrations are very similar. Similar to the gas phase, steady state is reached after about 20 min for the aqueous phase. Most of the initial lower effluent concentrations might be attributed to the volatilization of toluene in the reactor. Once the tower volume is saturated with toluene that transferred to the gas phase, no other losses seem to be present since all the influent toluene is accounted for at the effluent.

#### **Losses Due to Photolysis**

Possible losses of toluene due to photolysis were investigated. Because the UV lamps used in the reactor are non-ozone producing, no oxidation of toluene was expected during exposure to UV radiation in the absence of the catalyst. However, photolysis experiments were still

performed to assure that the lamp glass filtered the correct wavelength and to confirm the absence of other extraneous factors that could be an issue in the presence of UV radiation. Each contaminant phase was analyzed individually, and during these experiments the UV lamps were kept on at all times. For the gas phase experiments, toluene was allowed to flow for 20 min in the dark to reach steady state. After that period elapsed, the UV lamps were turned on. One run for each phase was performed and the results are presented in Figures A-3 and A-4.

The results obtained for the gas phase and aqueous phase toluene photolysis experiments are similar to the results previously shown for the other losses in the system. The normalized concentrations are very close to 1, showing no significant differences between the inlet and outlet concentrations for either phase. As expected, there is no evidence to show that toluene undergoes photolysis under the given experimental conditions.

### **Stripping**

The stripping capacity of the tower was evaluated to compare its actual performance to typical strippers. During these experiments, air and water were simultaneously flowing through the reactor, but only the aqueous phase was contaminated with toluene. The objective of this setup was to determine the removal of toluene due to mass transfer from the aqueous phase to the gas phase as a function of different air to water ratios. Furthermore, the mass transfer coefficients were determined and compared to predictions by the Onda. The influence of temperature changes on the transfer of toluene when the UV lamps were on or off was also investigated.

Three different runs of stripping experiments were performed. Runs 1 and 2 were performed using different air to water ratios to determine their influence in the mass transfer coefficients. Run 2 and 3, used the same air to water ratio, but the UV lamps were turned on during the third run to investigate the influence of temperature changes due to heat produced by the high energy lamps. The results for the 3 runs are shown in Figure A-5.

The results for runs 1 and 2 indicate that changing the air to water ratio ( $V/Q$ ) from 18.7 to 45 affects the toluene transfer from the aqueous to the gas phase.  $V/Q$  was altered by changing both, the water and the gas flowrate. Furthermore, the water temperature was 1°C higher for run 1 than for run 2. As explained in the literature review, factors influencing the transfer of contaminants from the aqueous phase to the gas phase include the concentration gradient and the overall mass transfer coefficient. In turn, the mass transfer coefficient is influenced by the temperature and liquid loading rate ( $L_m$ ). Comparing runs 1 and 2, the main factor favoring mass transfer in the second run is the large increase in the air to water ratio. The factors opposing mass transfer are the decrease in temperature and liquid loading rate, which result in a decreased mass transfer coefficient. The combination of all these factors resulted in a higher mass transfer in the second run as compared to the first one (89.6% versus 82.5% toluene transfer to the gas phase). The overall mass transfer coefficients were calculated to be  $0.407 \text{ min}^{-1}$  for run 1 and  $0.248 \text{ min}^{-1}$  for run 2. The coefficients predicted the Onda correlation underestimated the actual coefficients. By using a modified Onda coefficient that predicts a larger wetted area, as described in Chapter 7, the predicted coefficients were closer to the measured  $K_{La_w}$ . As expected,  $K_{La_w}$  was smaller for run 2 because of the lower liquid loading rate and temperature.

Temperature effects due to the UV lamps were assessed by comparing runs 2 and 3. The water temperature for run 3 was about 5°C higher than for run 2. Increasing the temperature increases the removal efficiency of toluene from 89.6% (run 2) to 94.9% (run 3). Similarly, the overall mass transfer coefficient was increased to  $0.327 \text{ min}^{-1}$  for run 3, and the predicted coefficient using the Onda correlation was also smaller for this run. Although determining effects of the heat produced by turning on the UV lamps under the same experimental conditions was the main goal of run 3, the increase in removal cannot be solely attributed to temperature because

the initial toluene concentration was higher in run 3 than in run 2, which will increase the driving force for the stripping process; thus also contributing to the higher removal.

### Absorption

Similar to the stripping experiments, absorption experiments were conducted in the presence of both streams flowing through the reactor to determine the tendency of gas phase toluene to transfer to the aqueous phase if only the gas phase was contaminated with toluene. The transfer to the aqueous phase was monitored by sampling influent and effluent streams and these results are presented in Figure A-6.

The inlet and outlet concentrations of toluene in the gas phase in Figure A-5 seemed very similar, so no significant absorption can be observed from the gas phase results. However, the effluent aqueous concentrations show that some toluene is actually transferring to the aqueous phase despite the high volatility of toluene. Although the aqueous phase concentrations might seem large compared to the gas phase concentrations, the gas phase flowrate is greater than the aqueous phase flowrate, 37 times larger. Compared to the stripping capacity of this compound, its absorption potential is very small, though it cannot be neglected.

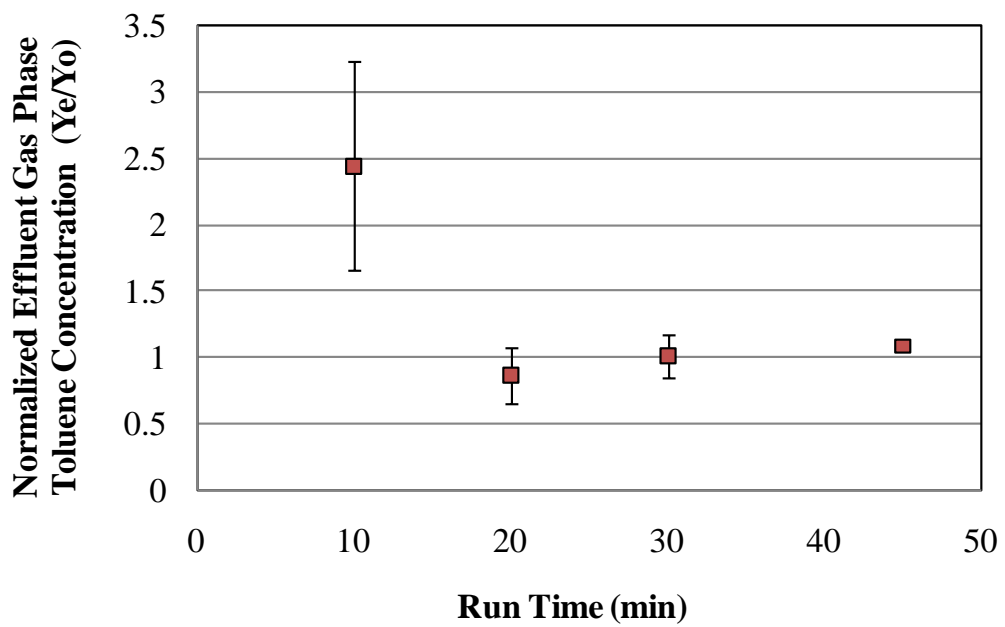


Figure A-1. System losses in the gas phase due to potential leaks. Packing: plastic high flow rings only. Average influent gas phase concentration,  $Y_0 = 2.3 \text{ ppm}_v$  for run 1 and  $10.4 \text{ ppm}_v$  for run 2. Gas flowrate,  $Q_G = 5 \text{ cfm}$  for all runs.

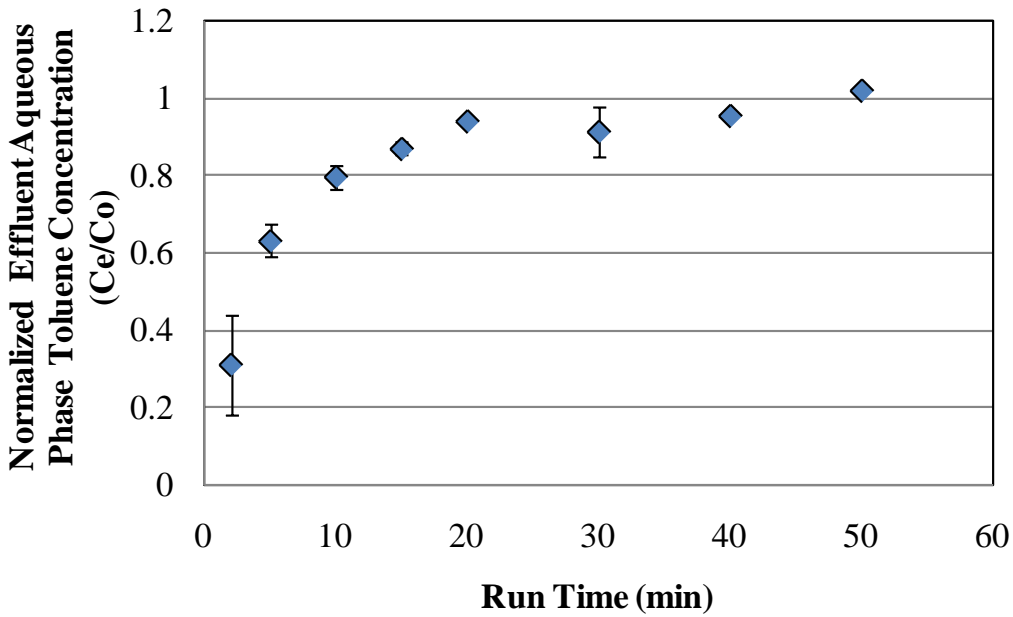


Figure A-2. System losses in the aqueous phase due to volatilization and/or leaks. Packing: plastic high flow rings.  $C_0 = 1.6 \text{ mg/L}$  (run 1),  $1.7 \text{ mg/L}$  (run 2), and  $1.9 \text{ mg/L}$  (run 3).  $Q_L = 3.8 \text{ L/min}$  for all runs.

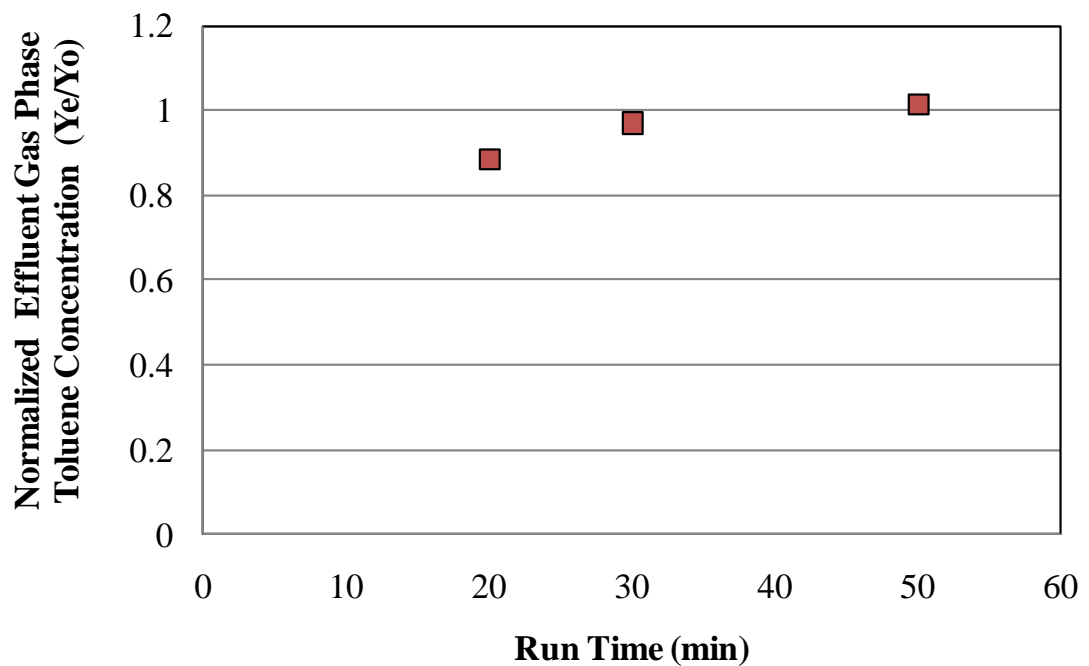


Figure A-3. Photolysis of toluene in the gas phase.  $Y_o = 10.8$  ppmv.  $Q_G = 5$  cfm.

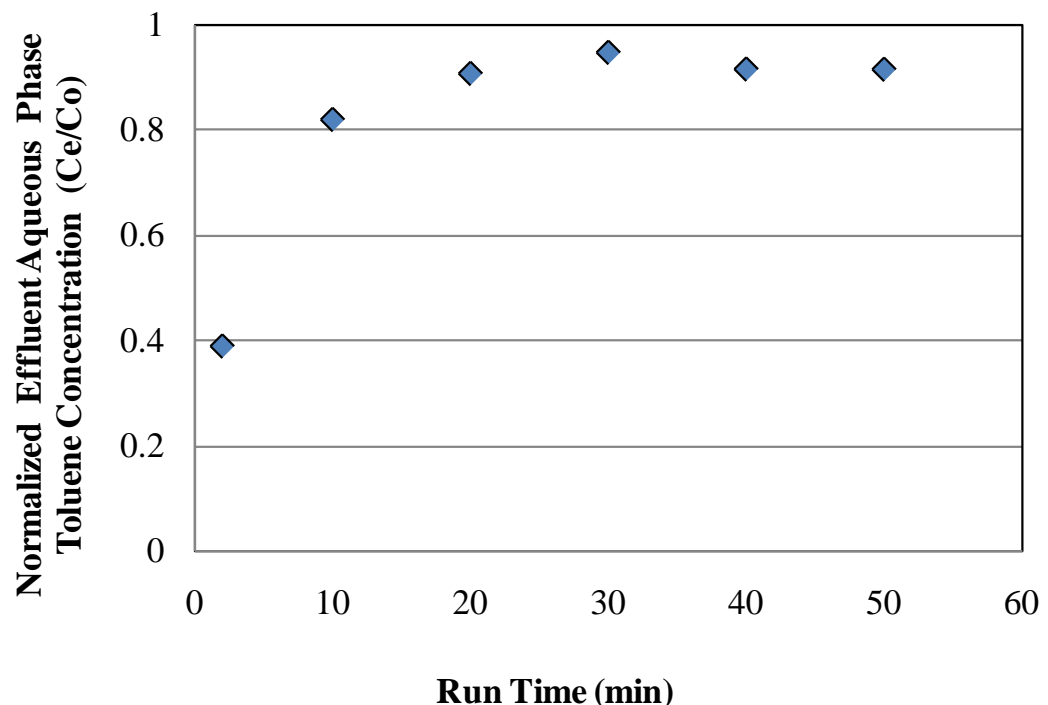


Figure A-4. Photolysis of toluene in the aqueous phase.  $C_o = 1.6$  mg/L (run 1),  $Q_L = 3.8$  L/min.

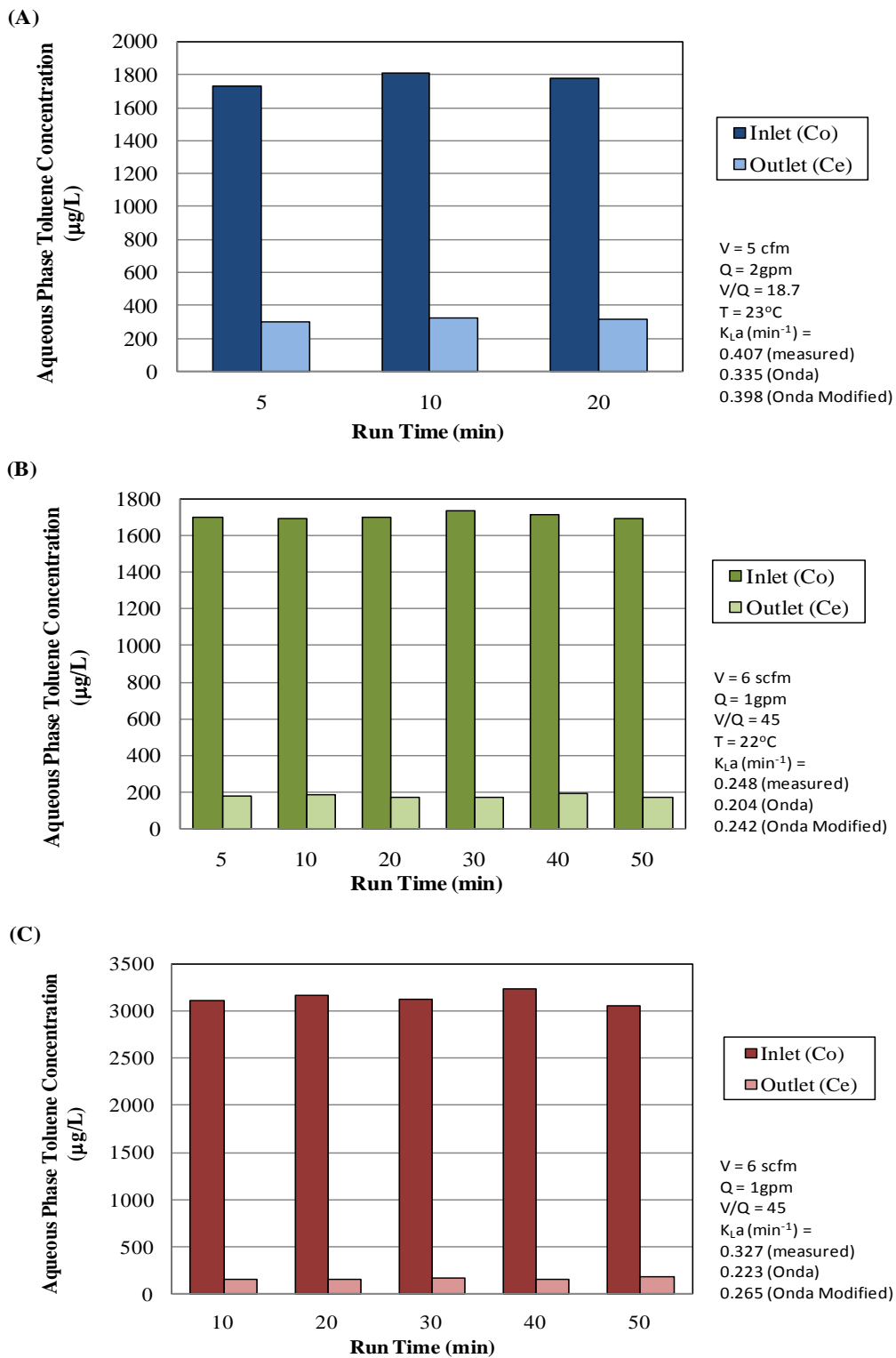


Figure A-5. Toluene stripping in the TPOT packed with high flow rings only using the UV lamps off and on and having the air flow free of contaminant. (A) Run 1. (B) Run 2. (C) Run 3. UV lamps off for (A) and (B). UV lamps on for (C)

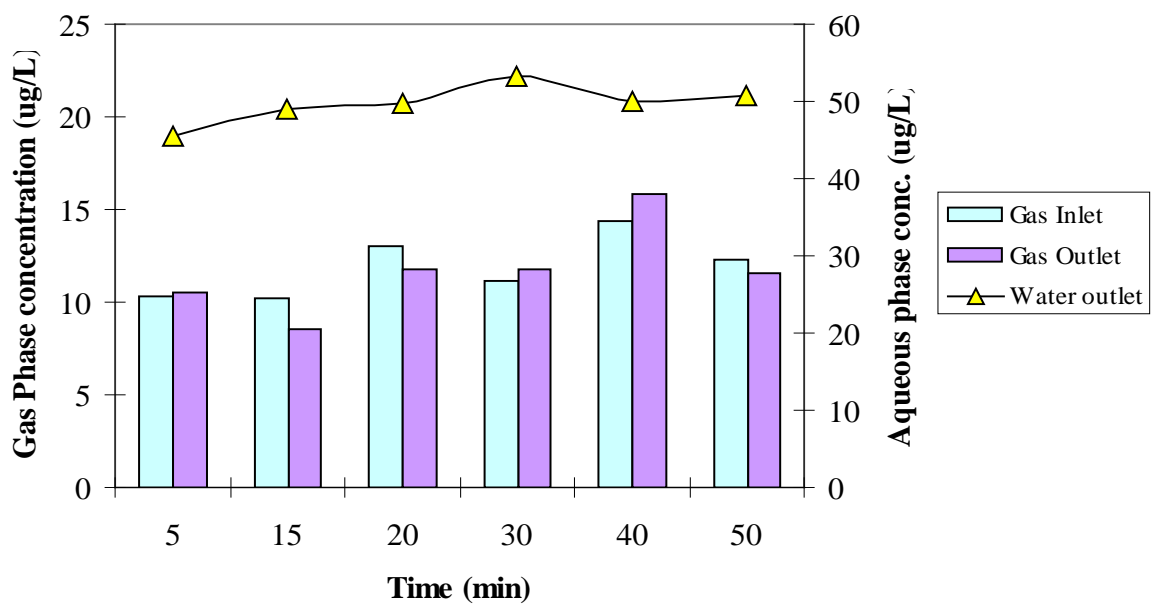


Figure A-6. Toluene absorption in the TPOT packed with plastic high flow rings only and the water flow free of contaminants.  $Q_L = 3.8 \text{ L/min}$ .  $Q_G = 5 \text{ cfm}$ .  $Q_G/Q_L = 37.4$ . UV lamps off.

## APPENDIX B ASSESSMENT OF LEACHING OF NANOMATERIALS

A fairly new concern about using heterogeneous photocatalysis with titanium dioxide for large scale applications, specially for applications that will result on the discharge of the effluents to aquatic environments or for drinking water purposes is the potential leaching of the nanomaterials during the system's operation. This is a concern since recent research studies have shown that even low concentrations of these materials can cause adverse effects on the health of living organisms. For example, Lovern and Kapler (2006) investigated the effects of nanosize  $\text{TiO}_2$  (30 nm average diameter) on *Daphnia magna*, a common filter feeder. They found that the lowest  $\text{TiO}_2$  concentration causing an observable effect was 2.0 mg/L while a concentration of 5.5 mg/L caused 50% mortality. The mortality rate continued to increase with increasing titanium dioxide concentration reaching 100% mortality at 10 mg/L. So far, a concentration of titanium dioxide that causes mortality or severe irreversible adverse health effects has not been determined for either humans or the ecosystem, but many studies suggest that concentrations above 2 mg/L might start producing some observable adverse health effects.

Accordingly, the effluents from the TPOT were measured for  $\text{TiO}_2$  and  $\text{SiO}_2$  concentrations. The effects of the UV radiation on the leaching of silica and titania were investigated by measuring effluents from adsorption and PCO experiment (Figure 9-1). The effects of flowrate on the leaching of materials was also investigated and presented in Figure 9-2. Finally the effects observed with time after multiple runs were also assessed by sampling effluents from many runs performed on different dates (Figure 9-3). In general, all the results showed no titania present at the influent stream whereas some titania was measured at the effluent. However, all the concentrations of titania detected were in the ppb range. No trends were observed for the effects of UV radiation and flowrate on the leaching of titania. For the case

of silica, the concentrations measured were much higher, in the ppm range, but these values were just barely higher for the effluent samples compared to the influent samples, meaning that most of the silica measured was already present in the tap water used for the experiments.

Furthermore, the leaching of both materials was relatively steady as a function of time, so it was not affected by the number of runs performed in the reactor. These results indicate that although some titania was observed at the effluent of the TPOT, the concentrations were well below those expected to produce adverse health effects on humans or the environment.

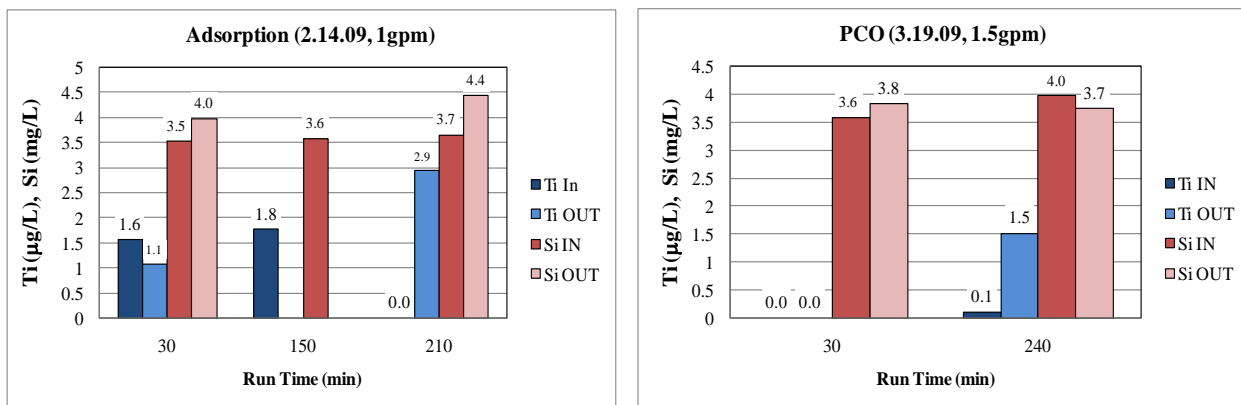


Figure B-1. Effects of the UV radiation on the leaching of silica and titania from the TPOT packing.

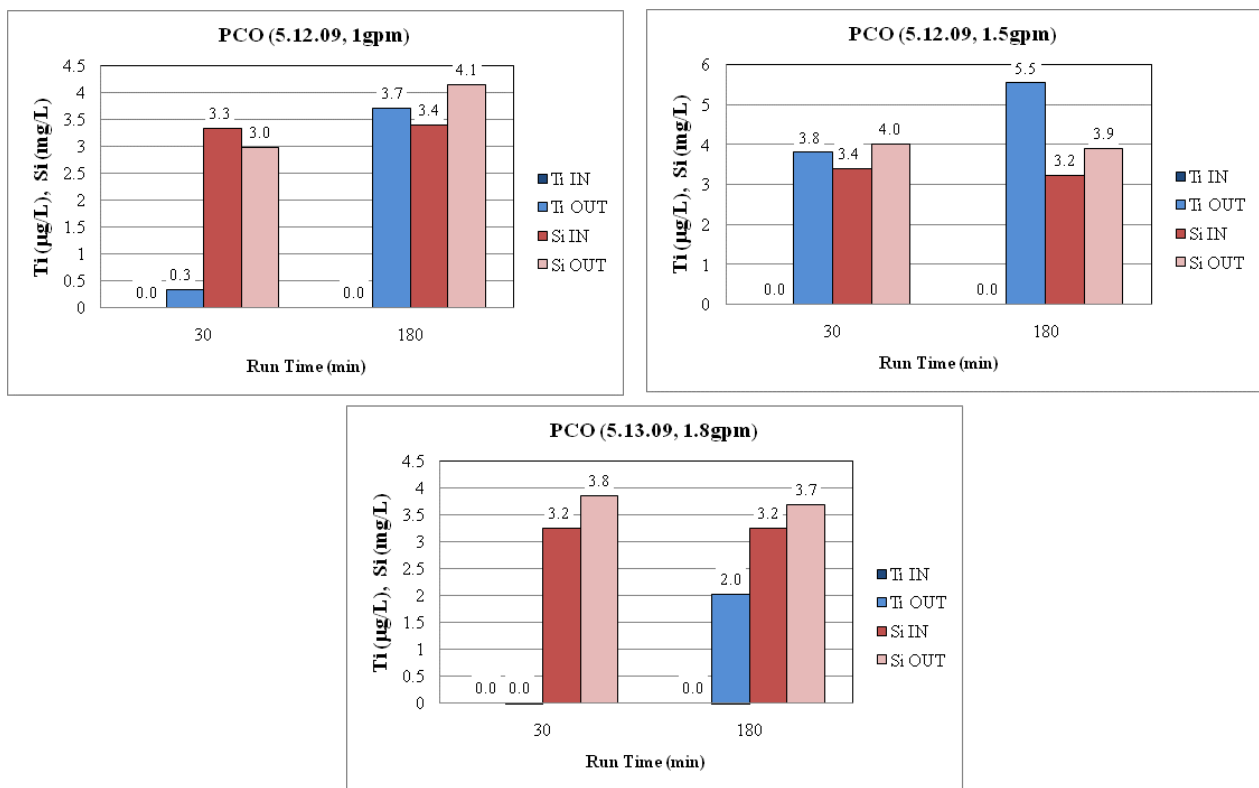


Figure B-2. Effect of the flowrate on the leaching of silica and titania from the packing on the TPOT.

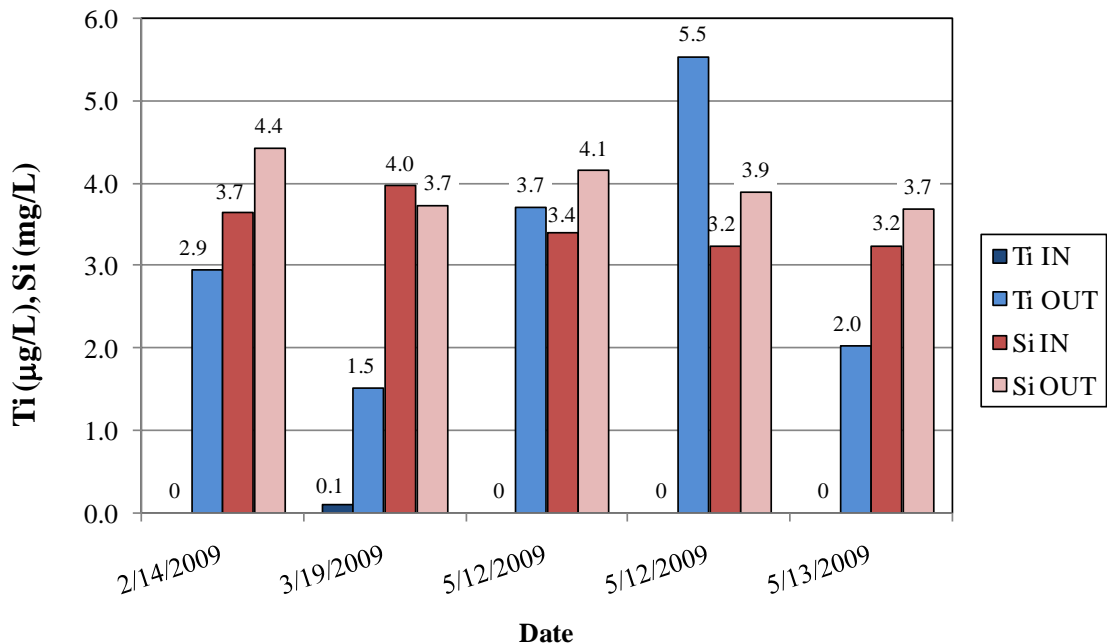


Figure B-3. Leaching of silica and titania from the packing in the TPOT for several experiments performed at various dates.

## LIST OF REFERENCES

- Alberci, R.M., Jardim, W.F., 1997. Photocatalytic destruction of VOCs in the gas-phase using titanium dioxide. *Appl. Catal. B: Environ.* 14, 55-68.
- Ameen, M.M., Raupp, G.B., 1999. Reversible catalyst deactivation in the photocatalytic oxidation of dilute o-xylene in air. *J. Catal.* 184, 112–122.
- Andino, J.M., Butler, J.W., 1991. A Study of the Stability of Methanol-Fueled Vehicle Emissions in Tedlar Bags .*Environ. Sci. Technol.* 25, 1644-1646.
- Anpo, M., Chiba, K., Tomonari, M., Coluccia, S., Che, M., Fox, M.A., 1991. Photocatalysis on native and platinum-loaded TiO<sub>2</sub> and ZnO catalysts: Origin of different reactivities on wet and dry metal oxides. *Bull. Chem. Soc. Jpn.* 64, 543-551.
- Arai, J., Tanaka, K., and Khlaifat, A.L., 2006. Photocatalysis of SiO<sub>2</sub>-loaded TiO<sub>2</sub>. *J. Mol. Catal. A: Chem.* 243, 85–88.
- Armor, J.N., 1992. Environmental Catalysis. *Appl. Catal. B: Environ.* 1, 221-256.
- Augugliario, V., Coluccia, S., Loddo, V., Marchese, L., Martra, G., Palmisano, L., Schiavello, M., 1990. Photocatalytic oxidation of gaseous toluene on anatase TiO<sub>2</sub> catalyst: mechanistic aspects and FT-IR investigation. *Appl. Catal. B: Environ.* 20, 15-27.
- Barrett, E. P., Joyner, L. G., Halenda, P. P., 1951. The determination of pore volume and area distributions in porous substances. I. Computations from nitrogen isotherms. *J. Amer. Chem. Soc.* 73, 373-380.
- Belhekar, A.A., Awate, S.V., Anand, R., 2002. Photocatalytic activity of titania modified mesoporous silica for pollution control. *Catal. Commun.* 3, 453-458.
- Blount, M.C., Kim, D.H., Falconer, J.L., 2001. Transparent thin-film TiO<sub>2</sub> photocatalysts with high activity. *Environ. Sci. Technol.* 35, 2988-2994.
- Blount, M.C., Falconer, J.L., 2002. Steady-state surface species during toluene photocatalysis. *Appl. Catal. B: Environ.* 39, 39-50.
- Boonamnuayvitaya, V., Tayamanon, C., Sae-ung, S., Tanthanapanichakoon, W., 2006. Synthesis and characterization of porous media produced by a sol-gel method. *Chem. Eng. Sci.* 61, 1686-1691.
- Boulamanti, A. K., Korologos, C. A., Philippopoulos, C. J., 2008. The rate of photocatalytic oxidation of aromatic volatile organic compounds in the gas-phase. *Atmos. Environ.* 42, 7844-7850.
- Bouzaza, A., Laplanche, A., 2002. Photocatalytic degradation of toluene in the gas phase: comparative study of some TiO<sub>2</sub> supports. *J. Photochem. Photobiol. A: Chem.* 150, 207-212.

- Bouzaza, A., Vallet, C., Laplanche, A., 2006. Photocatalytic degradation of some VOCs in the gas phase using an annular flow reactor. Determination of the contribution of mass transfer and chemical reaction steps in the photodegradation process. *J. Photochem. Photobiol. A: Chem.* 177, 212-217.
- Byrne, H.E., Kostedt IV, W.L., Stokke, J.M., Mazyck, D.W., 2009. Characterization of HFcatalyzed silica gels doped with Degussa P25 Titanium Dioxide. *J. Non-Cryst. Solids.* In Press.
- Cao, L., Gao, Z., Subi, S.L., Obee, T.N., Hay, S.O., Freihaut, J.D., 2000. Photocatalytic oxidation of toluene on nanoscale TiO<sub>2</sub> catalysts: studies of deactivation and regeneration. *J. Catal.* 196, 253–261.
- Chapra, S.C., Canale, R.P., 2002. Numerical methods for engineers. 4<sup>th</sup> Ed. McGraw-Hill, New York, NY.
- Cortese, A.D., 1990. Clearing the air. *Environ. Sci. Technol.* 24, 442-448.
- Crittenden J.C., Liu, J., Hand, D.W., Perram, D.L., 1997. Photocatalytic oxidation of chlorinated hydrocarbons in water. *Wat. Res.* 31, 429-438.
- de Andrade Lima, L. R. P., 2006. Liquid axial dispersion and holdup in column leaching. *Minerals Eng.* 19, 37-47.
- D’Oliveira, J.C., Ai-Sayyed, G., Pichat, P., 1990. Photodegradation of 2- and 3-chlorophenol in TiO<sub>2</sub> aqueous suspensions. *Environ. Sci. & Technol.* 24, 990-996.
- Degussa Technical Bulletin No. 56, 1990. Highly dispersed metallic oxides produced by the AEROSIL® process.
- Einaga, H., Futamura, S., Ibusuki,T., 2001. Heterogeneous photocatalytic oxidation of benzene, toluene, cyclohexene and cyclohexane in humidified air: comparison of decomposition behavior on photoirradiated TiO<sub>2</sub> catalyst. *Appl. Catal. B: Environ.* 38, 215-225.
- Emeline, A.V., Rudakova, A.V., Ryabchuk, V.K., Serpone, N. , 1998. Photostimulated reactions at the surface of wide band-gap metal oxides (ZrO<sub>2</sub> and TiO<sub>2</sub>): Interdependence of rates of reactions on pressure-concentration and on light intensity. *J. Phys. Chem. B.* 102, 10906-10916.
- Fan, J., Yates, J.T., 1996. Mechanism of photooxidation of trichloroethylene on TiO<sub>2</sub>: detection of intermediates by infrared spectroscopy. *J. Am. Chem. Soc.* 118, 4686-4692.
- Fogler, H. S., 1999. Elements of chemical reaction engineering; Prentice Hall PRT: Upper Saddle River, New Jersey.
- Fox, M.A., Dulay, M.T., 1993. Heterogeneous photocatalysis. *Chem. Rev.* 93, 341-357.

- Gould, G., Irene, E.A., 1988. An in situ study of aqueous HF treatment of silicon by contact angle measurement and ellipsometry. *J. Electrochem. Soc.* 135, 1535-1542.
- Hager, S., Bauer, R., 1999. Heterogeneous photocatalytic oxidation of organics for air purification by near UV irradiated titanium dioxide. *Chemosphere*. 38, 1549-1559.
- Hand, D.W., Crittenden, J.C., Gehin, J.L., Lykins, B.W., 1986. Design and evaluation of an air-stripping tower for removing VOCs from groundwater. *J. AWWA*. 78, 87-97.
- Hand, D.W., Hokanson, D.R., Crittenden, J.C., 1999. Air stripping and aeration, in: Letterman, R.D. (Ed), *Water Quality and Treatment: A Handbook of Community Water Supplies*. AWWA and McGraw-Hill, New York, pp. 5.1-5.68.
- Hench, L.L., West, J.K., 1990. The sol-gel process. *Chem. Rev.* 90, 33-72.
- Hennenzel, O., Pichat, P., Ollis, D.F., 1998. Benzene and toluene gas-phase photocatalytic degradation over H<sub>2</sub>O and HCl pretreated TiO<sub>2</sub>: by-products and mechanisms. *J. Photochem. Photobiol. A: Chem.* 118, 197-204.
- Herrmann, J.M., 2005. Heterogeneous photocatalysis: State of the art and present applications. *Topics Catal.* 34, 49-65.
- Hoffmann, M.R., Martin, S.T., Choi, W., Bahnemann, D.W., 1995. Environmental applications of semiconductor photocatalysis. *Chem. Rev.* 95, 69-96.
- Holmes, F.R., 2003. The performance of a reactor using photocatalysis to degrade a mixture of organic contaminants in aqueous solution. Masters Thesis, University of Florida.
- Holmes, F.R., Chadik, P.A., Mazyck, D.W., Wu, C.Y., Garton, M.J., Powers, K.W., Londeree, D.J., 2004. Photocatalytic Oxidation of Selected Organic Contaminants in a Continuous Flow Reactor Packed With Titania-Doped Silica. International Conference on Environmental Systems. Colorado Springs, CO, USA.
- Hopper J.R., Saleh J.M., Pike R., 2001. Design of multi-phase and catalytic chemical reactors: a simulation tool for pollution prevention. *Clean Prod. Proc.* 3, 92-103
- Japar, S.M.; Wallington, T.J., Rudy, S.J., Chang, T.Y., 1991. Ozone-forming potential of a series of oxygenated organic compounds. *Environ. Sci. Tech.* 25, 415-420.
- Kang, M., Hong, W.J., Park, M.S., 2004. Synthesis of high concentration titanium incorporated nanoporous silicates (Ti-NPS) and their photocatalytic performance for toluene oxidation. *Appl. Catal. B: Enviro.* 53, 195–205.
- Kavanaugh, M.C., Trussell, R.R., 1980. Design of aeration towers to strip volatile organic contaminants from drinking water. *J. AWWA*. 72, 12:684
- Kim, S. B., Hong, S. C., 2002. Kinetic study for photocatalytic degradation of volatile organic compounds in air using thin film TiO<sub>2</sub> photocatalyst. *Appl. Catal. B: Environ.* 35, 305-315.

- Kobayakawa, K., Sato, C., Sato, Y., Fujishima, A., 1998. Continuous-flow photoreactor packed with titanium dioxide immobilized on large silica gel beads to decompose oxalic acid in excess water. *J. Photochem. Photobiol. A: Chem.* 118, 65-69.
- Kresge, C.T., Leonowicz, M.E., Roth, W.J., Vartuli J.C., Beck J.S., 1992. Ordered mesoporous molecular sieves synthesized by a liquid-crystal template mechanism. *Nature* 359 (1992) 710-712.
- Lamarche, P., Droste, R.L., 1989. Air-stripping mass transfer correlations for volatile organics. *J. AWWA*. January, 78-89
- Larson, S.A., Falconer, J.L., 1997. Initial reaction steps in photocatalytic oxidation of aromatics. *Catal. Letters.* 44, 57-65.
- Legrand, P., 1998. On the silica edge. In: *The Surface Properties of Silicas*. John Wiley & Sons, Inc., New York, 130-200.
- Lewandowski, M., Ollis, D.F., 2003a. A Two-Site kinetic model simulating apparent deactivation during photocatalytic oxidation of aromatics on titanium dioxide ( $TiO_2$ ). *Appl. Catal. B: Environ.* 43, 309-327.
- Lewandowski, M., Ollis, D.F., 2003b. Extension of a Two-Site transient kinetic model of  $TiO_2$  deactivation during photocatalytic oxidation of aromatics: concentration variations and catalyst regeneration studies. *Appl. Catal. B: Environ.* 45, 223-238.
- Lichtin, N.N., Avudaithai, M., 1996.  $TiO_2$ -Photocatalyzed oxidative degradation of  $CH_3CN$ ,  $CH_3OH$ ,  $C_3HCl$ , and  $CH_2Cl_2$  supplied as vapors and in aqueous solution under similar conditions. *Environ. Sci. Technol.* 30, 2014-2020.
- Linsebigler, A.L, Lu, G., Yates, J.T., 1995. Photocatalysis on  $TiO_2$  surfaces: Principles, mechanisms and selected results. *Chem. Rev.* 95, 735-758.
- Londeree, DJ. 2002. Silica-titania composites for water treatment. Master thesis. University of Florida.
- Lovern, S.B., Klaper, R., 2006. Daphnia magna mortality when exposed to titanium dioxide and fullerene ( $C_{60}$ ) nanoparticles. *Environ. Toxicol. Chem.* 25, 1132-1137.
- Lou, Y., Ollis, D.F., 1996. Heterogeneous photocatalytic oxidation of trichloroethylene and toluene mixtures in air: Kinetic promotion and inhibition, time-dependent catalyst activity. *J. Catal.* 163, 1-11.
- Ludwing, C.Y., 2004. The performance of silica-titania composites in a packed-bed reactor for the photocatalytic destruction of gray water. Master thesis. University of Florida..
- Maira, A.J., Yeung, K.L., Soria, J., Coronado, J.M., Belver, C., Lee, C.Y., Augugliaro, V., 2001a. Gas-phase photo-oxidation of toluene using nanometer-size  $TiO_2$  catalysts. *Appl. Catal. B: Environ.* 29, 327-336.

- Maira, A.J., Coronado,J.M., Augugliaro,V., Yeung, K.L., Conesa, J.C., Soria, J., 2001b. Fourier transform infrared study of the performance of nanostructured TiO<sub>2</sub> particles for the photocatalytic oxidation of gaseous toluene. *J. of Catal.* 202, 413– 420.
- Marci, G., Addamo, M., Augugliaro, V., Coluccia, S., García-López, E., Loddo, V., Martra, G., Palmisano, L., Schiavello, M., 2003. Photocatalytic oxidation of toluene on irradiated TiO<sub>2</sub>: comparison of degradation performance in humidified air, in water and in water containing a zwitterionic surfactant. *J. Photochem. and Photobiol. A: Chem.* 160, 105–114.
- Marugán, J., López-Muñoz, M. J., Aguado, J., van Grieken, R., 2007. On the comparison of photocatalysts activity: A novel procedure for the measurement of titania surface in TiO<sub>2</sub>/SiO<sub>2</sub> materials. *Catal. Today.* 124, 103-109.
- Martra, G., Coluccia, S., Marchese, L., Augugliaro, V., Loddo, V., Palmisano, L., Schiavello, M., 1999. The role of H<sub>2</sub>O in the photocatalytic oxidation of toluene in vapour phase on anatase TiO<sub>2</sub> catalyst: A FTIR study. *Catal. Today* 53, 695–702.
- McCabe, L.M., Smith, J.C., Harriott, P., 2005. Unit operations of chemical engineering. 7th Ed. Chem. Eng. Series. New York: McGraw-Hill.
- McGarvey, L.J., Shorten, C.V., 2000. The effects of adsorption on the reusability of tedlar air sampling bags. *AIH AJ.* 61, 375–380.
- Mendez-Roman, R., Cardona-Martinez, N., 1998. Relationship between the formation of surface species and catalyst deactivation during the gas-phase photocatalytic oxidation of toluene. *Catal. Today.* 40, 353-365.
- Michell. R.W., Furzer, I.A., 1972. Mixing in trickle flow through packed beds, *Chem. Eng. J.* 4, 53–63
- Miyabe, K., Guiochon, G., 2004. Comparison of the characteristics of adsorption equilibrium and surface diffusion in liquid-solid and gas-solid adsorption on C18-silica gels. *J. Phys. Chem. B.* 108, 2987-2997.
- Mo, J., Zhang, Y., Xu, Q., Yang, R., 2009. Effect of TiO<sub>2</sub>/adsorbent hybrid photocatalysts for toluene decomposition in gas phase. *J. Hazardous Mat.* In Press, Corrected Proof.
- Mutin, P. H., Lafond, V., Popa, A. F., Granier, M., Markey, L., Dereux, A., 2004. Selective surface modification of SiO<sub>2</sub>-TiO<sub>2</sub> supports with phosphonic acids. *Chem. Materials.* 16, 5670-5675.
- Nirmalakhandan, N., Lee, Y.H., Speece, R.E., 1987. Designing a cost-efficient air-stripping process. *J. AWWA.* 79, 56-62.
- Obee, T.N., Brown, R.T., 1995. TiO<sub>2</sub> Photocatalysis for indoor air applications: Effects of humidity and trace contaminant levels on the oxidation rates of formaldehyde, toluene, and 1 ,3-butadiene. *Environ. Sci. Technol.* 29, 1223-1231.

Office of Environmental Health Hazard Assessment (OEHHA). 2002. Air toxics hot spots program risk assessment guidelines. Part II. Technical Support Document for Describing Available Cancer Potency Factors.

Ollis, D.F., Pelizzetti, E., Serpone, N., 1991. Destruction of water contaminants. Environ. Sci. Technol. 25, 1523-1529.

Ollis, D.F., 2005a. Kinetic disguises in heterogeneous photocatalysis. Topics Catal. 35, 217-223.

Ollis, D.F., 2005b. Kinetics of liquid phase photocatalyzed reactions: An illuminating approach. J. Phys. Chem. B. 109, 2439-2444.

Onda, K., Takeuchi, H., Okumoto, Y., 1968. Mass transfer coefficients between gas and liquid phases in packed columns. J. Chem. Eng. Jpn. 1, 56-62.

Otake, T., Kunugita, E., 1958. Mixing characteristics of irrigated packed towers. Kagaku Kogaku. 22, 144–150.

Pengyi, Z., Fuyan, L., Gang, Y., Qing, C., Wanpeng, Z., 2003. A comparative study on decomposition of gaseous toluene by O<sub>3</sub>/UV, TiO<sub>2</sub>/UV and O<sub>3</sub>/TiO<sub>2</sub>/UV. J. Photochem. Photobiol. A: Chem. 156, 189-194.

Peral, J., and Ollis, D.F., 1992. Heterogeneous photocatalytic oxidation of gas-phase organics for air purification - acetone, 1-butanol, butyraldehyde, formaldehyde, and meta-xylene oxidation. J. Catal. 136, 554-565.

Philips Lighting, 2004. UV Disinfection – Application Information. Document No. 3222 635 43401. Printed in The Netherlands.

Piché, S., Larachi, F., Iliuta, I., Grandjean, B.P.A., 2002. Improving predictions of liquid back-mixing in trickle-bed reactors using a neural network approach, J. Chem. Technol. Biotechnol. 77, 989-998.

Pintar, A., Bercic, G., Levec, J., 1997. Catalytic liquid-phase oxidation of aqueous phenol solutions in a trickle-bed reactor. Chem. Eng. Sci. 52, 4143-4153.

Pitoniak, E., Wu, C.Y., Londeree, D.J., Mazyck, D.W., Bonzongo, J. D., Powers, K.W., Sigmund, W., 2003. Nanostructured silica-gel doped with TiO<sub>2</sub> for Hg vapor control.” J. Nanoparticle Res. 5, 282-292.

Powers, K., 1998. The development and characterization of sol gel substrates for chemical and optical applications,” Ph.D. Dissertation, University of Florida.

Ray, A.K., 1999. Design, modeling and experimentation of a new large-scale photocatalytic reactor for water treatment. Chem. Eng. Sci. 54, 3113-3125.

- Roberts, P.V., Hopkins, G.D., Munz, C. and Riojas, A.H., 1985. Evaluating two- resistance models for air stripping of volatile organic compounds in a countercurrent, packed column. Environ. Sci. Technol. 19, 164-173.
- Sater, V.E, Levenspiel, O., 1966. Two-phase flow in packed beds. Evaluation of axial dispersion and holdup by moment analysis. I&EC Fundamentals. 5, 86–92
- Satterfield, C.N., 1969. Mass transfer in heterogeneous photocatalysis. M.I.T. Press. Cambridge, MA.
- Sauer, M.L., Hale M.A., Ollis, D.F., 1995. Heterogeneous photocatalytic oxidation of dilute toluene-chlorocarbon mixtures in air. J. Photochem. and Photobiol. A: Chem. 88, 169-178.
- Sauer, M.L., Ollis, D.F., 1996. Catalyst deactivation in gas-solid photocatalysis. J. Catal. 163, 215-217.
- Serpone, S., Emelie, V., 2002. Suggested terms and definitions in photocatalysis and radiocatalysis. Int. J. Photoenergy. 4, 91-131.
- Sherwood, T.K., Shipley, G.H., Holloway, F.A.L., 1938. Flooding velocities in packed columns. Ind. Eng. Chem. 30, 765-769.
- Sing, K.S.W., Everett, D.H., Haul, R.A.W., Moscou, L., Pierotti, R.A., Rouquerol, J., Siemieniewska, T., 1985. Reporting physisorption data for gas/solid systems with special reference to the determination of surface area and porosity. Pure Appl. Chem. 57, 603-619.
- Skelland, A. H. P., 2006. Diffusional mass transfer. Malabar, Fla: R.E. Krieger Pub. Co.
- Stokke, J.M., Mazyck, D.W., Wu, C.Y., Sheahan, R., 2006. Photocatalytic oxidation of methanol using silica-titania composites in a packed-bed reactor. Environ. Prog. 25, 312-318.
- Stokke, J.M., 2008. Photocatalytic oxidation of hazardous air pollutants using silica – titania composites in a packed bed reactor. Ph.D. Dissertation, University of Florida.
- Stokke, J. M., Mazyck, D. W., 2008. Photocatalytic degradation of methanol using silica-titania composite pellets: effect of pore size on mass transfer and reaction kinetics. Environ. Sci. Technol. 42, 3808-3813.
- Tanaka, K., Capule, M., Hisanaga, T., 1991. Effect of crystallinity of TiO<sub>2</sub> on its photocatalytic action. Chem. Phys. Lett. 187, 73-76.
- Three Bond Co.,Ltd., 2004. Titanium-Oxide Photocatalyst. Three Bond Technical News No. 62. Tokyo, Japan.
- Treybal, R.E., 1980. Mass Transfer Operations, 3rd Ed., Chem. Eng. Series. New York: McGraw-Hill.

- Turchi, C.S., Ollis, D.F., 1990. Photocatalytic degradation of organic water contaminants: mechanisms involving hydroxyl radical attack. *J. Catal.* 122, 178-192.
- United States Environmental Protection Agency (USEPA), 1995. Method 524.2 "Measurement of purgeable organic compounds in water by capillary column gas chromatography/ mass spectrometry." Edited by JW Munch.
- United States Environmental Protection Agency (USEPA), 2007a. An introduction to indoor air quality. Retrieved February 10, 2007, from <http://www.epa.gov/iaq/voc.html#Health%20Effects>.
- United States Environmental Protection Agency (USEPA), 2007b. Drinking water contaminants: National primary drinking water regulations. Retrieved February 12, 2007, from <http://www.epa.gov/safewater/contaminants/index.html#organic>.
- United States Environmental Protection Agency (USEPA), 2007c. Clean Air Act. Retrieved February 20, 2007, from <http://www.epa.gov/air/caa/>.
- Ultra – Violet Products (UVP) Inc. Guide to Optical Radiation Measurements. Application Note AN – 1167.
- Wang, J.H., Ray, M.B., 2000. Application of ultraviolet photooxidation to remove organic pollutants in the gas phase. *Separ. Pur. Technol.* 19, 11-20.
- Weber, W. J. Jr., DiGiano, F.A., 1996. Process dynamics in environmental systems. Wiley Interscience, New York, NY.
- Xu, Y., Langford, C.H., 2000. Variation of Langmuir adsorption constant determined for TiO<sub>2</sub>-photocatalyzed degradation of acetophenone under different light intensity. *J. Photochem. and Photobiol. A: Chem.* 133, 67–71
- Yue, B., Zhou, Y., Xu, J., Wu, Z., Zhang, X., Zou, Y., Jin, S., 2002. Photocatalytic degradation of aqueous 4-chlorophenol by silica-immobilized polyoxometalates. *Environ. Sci. Technol.* 36, 1325-13.
- Zhang, R.B., 2005. Photodegradation of toluene using silica-embedded titania. *J. Non-Crys. Solids.* 351, 2129-2132.
- Zou, L., Luo, Y., Hooper, M., Hu, E., 2006. Removal of VOCs by photocatalysis process using adsorption enhanced TiO<sub>2</sub>-SiO<sub>2</sub> catalyst. *Chem. Eng. Proc.* 45, 959-964.

## BIOGRAPHICAL SKETCH

Christina Akly was born in Santa Cruz, Bolivia to Bethsy Flores and Salomon Akly. She grew up in her country of origin and came to the United States in 2001 to pursue her undergraduate degree in environmental engineering sciences at the University of Florida, where she graduated *sum cum laude* in May 2005. After completing her degree, she was offered a fellowship to continue her education in UF, and she received a non-thesis master's in 2007 and a doctorate in August 2009, both in environmental engineering with a focus in potable water treatment using advanced oxidation technologies. Her doctorate degree was performed under the guidance of her advisor Dr. Paul A. Chadik.